Development of a water vapor isotope ratio infrared spectrometer and application to measure atmospheric water in Antarctica

Janek Landsberg

THÈSE

Pour obtenir le grade de

DOCTEUR DE L'UNIVERSITÉ DE GRENOBLE

préparée dans le cadre d'une cotutelle entre l'Université de Grenoble et le Rijksuniversiteit Groningen

Spécialité : **Physique appliquée**

Arrêté ministériel : 7 août 2006

Présentée par

Janek Landsberg

Thèse dirigée par **Prof. Dr. Erik Kerstel, LIPhy, UJF Grenoble et Prof. Dr. Harro Meijer, CIO, Rijksuniversiteit Groningen**
et codirigée par **Dr. Daniele Romanini, LIPhy, UJF Grenoble**
préparée au sein du **Laboratoire interdisciplinaire de Physique**
dans le cadre de l' **Ecole Doctorale de Physique, Grenoble**

Developpement d'un spectromètre laser OF-CEAS pour les mésures des isotopes de la vapeur d'eau aux concentrations de l'eau basses

Thèse soutenue publiquement le **12 décembre 2014** devant le jury composé de :

Prof. Dr. Erik Kerstel, Directeur de thèse
Prof. Dr. Harro Meijer, Directeur de thèse
Dr. Daniele Romanini, Co-directeur de thèse
Dr. Amaelle Landais, Rapporteur
Prof. Dr. Thomas Leisner, Rapporteur
Prof. Dr. Thomas Röckmann, Examinateur
Prof. Dr. Howard Levinsky, Examinateur
Dr. Harald Saathoff, Examinateur
Prof. Dr. Ton Schoot-Uiterkamp, Examinateur

Development of an OF-CEAS laser spectrometer for water vapor isotope measurements at low water concentrations

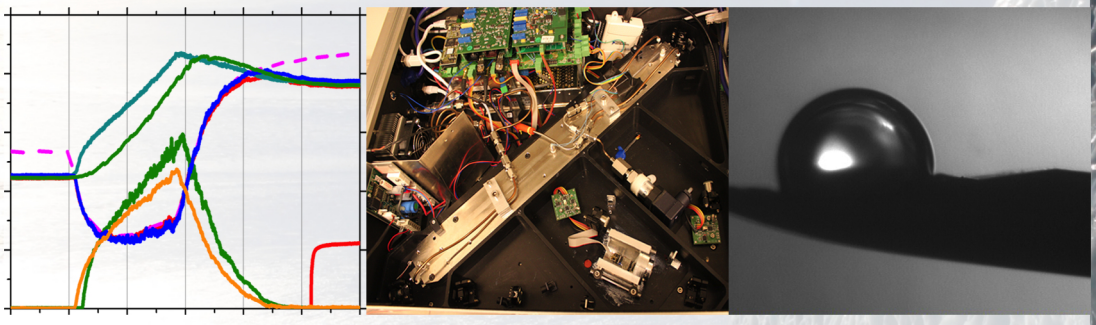

Felix Janek Landsberg

A Université de Grenoble I and Rijksuniversiteit Groningen double degree PhD thesis

Development of an OF-CEAS laser spectrometer for water vapor isotope measurements at low water concentration

A PhD thesis completed in a co-tutelle arrangement
between the J. Fourier University (Grenoble I)
and the University of Groningen

Felix Janek Landsberg

Book cover: Meike Kloster-Landsberg and Felix Janek Landsberg:

Background photo: view from the slope of Jutulhogget near Troll station, Antarctica

Front (left to right): $H_2{}^{16}O$ behavior during an ice cloud formation in the AIDA cloud chamber, the interior of the OF-CEAS instrument SIRI, droplet formation on the tip of a syringe

Back (left to right): An electronic card of the OF-CEAS instrument, Troll station, main building, bubbler calibration set-up

ISBN (E-book): 978-90-367-7447-5
ISBN (book): 978-90-367-7448-2

Published by SmartPrinting solutions - http://sps-print.eu - Gouda, The Netherlands

The work presented in this thesis received support from:

Netherlands Organization for Scientific Research (NWO) under project number NAAP 851.20.0045

University of Grenoble installation funding E. Kerstel

Additional funding from RUG resources

NSF, DFG GEPRIS and EUROCHAMP-2 (ISOCLOUD campaign)

Norwegian Polar Institute (logistics Troll campaign)

university of groningen

Development of an OF-CEAS laser spectrometer for water vapor isotope measurements at low water concentration

PhD thesis

to obtain the degree of PhD at the
University of Groningen
on the authority of the
Rector Magnificus Prof. E. Sterken
and in accordance with
the decision by the College of Deans.

This thesis will be defended in public on

Friday 12 December 2014 at 09.00 hours

by

Felix Janek Landsberg

born on 27 May 1982
in Freiburg im Breisgau, Germany

Supervisors
Prof. H.A.J. Meijer
Prof. E.R.T. Kerstel

Co-supervisor
Dr. D. Romanini

Assessment committee
Prof. J.-F. Doussin
Prof. M.A. Herber
Prof. E. Lacot
Prof. T. Leisner

ISBN: 978-90-367-7448-2

Acknowledgments

The dissertation presented in the following would not have been possible without the scientific, personal and financial support of quite a number of people and organizations, whom I would like to thank especially in the following.
First of all, I want to thank my supervisor in Grenoble, Erik Kerstel, for his strong support, his good ideas and helpful propositions throughout the years of this thesis.
Many thanks also to Daniele Romanini, my co-supervisor, who always had valuable comments and a helpful hand, especially concerning all problems related to the OF-CEAS technique.
I also would like to thank my supervisor in Groningen, Harro Meijer, who supported me - due to the fact that I spent the majority of my thesis in Grenoble - often per distance and via e-mail and always showed a great interest in the advancement of my thesis.
Un très grand merci à Samir Kassi, qui m'a aidé beaucoup avec une multitude des problèmes et modifications concernant le logiciel LabView pour faire tourner les instruments et avec des problèmes concernant l'instrument OF-CEAS. Je voudrais aussi remercier Thibault Desbois, qui m'a aidé beaucoup, spécialement au début de ma thèse en m'introduisant dans la technique OF-CEAS et en me forçant de faire cet introduction en Français, cela m'a beaucoup aidé á améliorer mon Français!
Je voudrais aussi remercier Serge Béguier, qui m'a assisté avec les problèmes informatiques et qui a fait plusieurs logiciels indispensables dans LabView et merci aussi á Jean-Luc Martin qui m'a aidé patiemment avec des problèmes électroniques. Merci aussi à mes co-doctorants Marine Favier et Mathieu Casado, qui ont pris le relais avec les instruments developpés dans cette thèse, qui se sont occupés des expériences dans les dernières semaines de ma thése et qui ont pris soin que les instruments seront utiliser dans le futur. Bernard Chelli Ponce de Leon et Michel Thijs, qui ont fait des stages avec moi, m'ont aidé avec des traveaux dans le laboratoire et Bernard aussi pendant une campagne de mesure à Créteil, merci beaucoup aussi pour cela.
Je voudrais aussi dire merci à tout l'àtelier méchanique au LIPhy, qui m'a aidé beaucoup avec la fabrication des pièces méchaniques compliqués et souvent avec des conseils quand j'ai fabriqué

des pièces moi-meme.
Merci aussi à tout l'équipe LAsers, Molécules et Environnement (LAME) du LIPhy pour l'intégration chaleureux dans l'équipe et beaucoup des discussions fructueux.
I would also like to thank the IMK-AAF group of the Karlsruhe Institute of Technology for their support during four measurement campaigns at the AIDA cloud chamber in Karlsruhe. Especially thanks to Harald Saathoff, Ottmar Moehler and Naruki Hiranuma for a very friendly and valuable collaboration and many good ideas concerning our joint experiments. A special thanks to Jan Habig, former PhD student in the IMK-AAF group, with whom I spent numerous weeks of shared work, both in Grenoble and Karlsruhe and had many fruitful discussions.
A great thanks also to Liz Moyer, Eric Stutz, Kara Lamb, Lazlo Sarkozy and Ben Clouser from the Department of Geophysical Science of the University of Chicago for the good collaboration during the measurement campaigns in Karlsruhe, thanks a lot Kara for the modelling and data, Eric for the joint work with our calibration systems, both in Karlsruhe and Grenoble and Liz for very helpful comments.
Thank you to Benjamin Kühnreich, Steven Wagner and Volker Ebert for the joint work at the AIDA cloud chamber and particularly thanks to Benjamin for several stimulating and helpful discussions, both during the campaigns and afterwards.
Je voudrais aussi remercier Amaelle Landais, Olivier Cattani et Fréderic Prie du Laboratoire des Sciences du Climat et de l'Environnement (LSCE) á Gif-sur-Yvette pour la collaboration. Olivier m'a donné des conseils indispensables sur le developpement du système de calibration et m'a généreusement prêté un système de calibration pour la campagne de mesure en Antarctique. Merci beaucoup à Amaelle et Fréderic pour la campagne de mesure conjoint á Créteil et les discussions scientifiques avant et après.
Tusen takk also to the Norwegian Polar Institute, without whom the measurement campaign to Antarctica would never have been possible. I would especially like to thank Elisabeth Isaksson and Kim Holmén for the pre-organization and Ken Pederson and Per Erik Hanevold for the help during my stay at Troll station. In this context, I also would like to thank Chris Lunder from the Norwegian Institute for Air research (NILU), who generously provided me with environmental data for the measurement period at Troll.
For the financial support, I would like to thank the Netherlands Organisation for Scientific Research (NWO) for the funding of three years of my PhD thesis in the framework of a NAAP project, including the measurement campaign to Troll and various scientific instrumentation. Thanks also to the University UJF of Grenoble I for the funding of scientific equipment under the Kerstel installation grant and the Rijksuniversiteit Groningen for the financing of an additional year of my thesis. Concerning the ISOCLOUD campaign, I am thankful to have indirectly participated of the NSF and DFG GEPRIS funding as well as of EUROCHAMP-2 funding for the travel expenses.
Apart from the scientific and financial support, I would like to thank a number of additional people for their personal support during the time of my thesis. A very great thank you to my wife

Meike Kloster-Landsberg, who supported me in every way during my entire thesis and without whom many parts would have been much more difficult or even impossible. I also would like to thank my family and Meike's family for their support during all this time and their sympathy in all aspects.
Finalement, je voudrais aussi remercier Mustapha Bouali et l'ensemble vocal de Grenoble, avec qui j'ai passé beaucoup de temps très agréable pendant mon temps à Grenoble, à la fois musicalement et personnellement. La musique m'a ressourcé chaque fois.

Summary

In recent years, the measurement of water isotopologues has become increasingly important for atmospheric research. Due to the influence of climatic conditions on the isotope ratios, the isotopic composition of water stored in the ice in Antarctica and the Arctic can be used as paleothermometers to reconstruct past climate changes [1]. The measurement of changes of the isotopic composition of water vapor in the atmosphere can be used to study the global hydrolocal hydrologic cycle [2] and to refine atmospheric circulation models [3].

Whereas the conventional method for water isotope measurements, Isotope Ratio Mass Spectrometry (IRMS), is not adapted for in-situ continuous measurements of water vapor isotopes, the recent development of laser spectrometers offers a comparably easy and robust method to conduct in-the-field research with good time resolution [4–7]. However, until now, most optical instruments require relative high humidity levels with water concentrations of at least several 1000 ppmv, which excludes measurements in some of the most interesting regions for water isotope research, such as the upper atmosphere and the central regions of Antarctica.

In this work, we present a novel infrared laser spectrometer based on Optical Feedback Cavity Enhanced Absorption spectroscopy (OF-CEAS), specifically designed to measure the four isotopologues $H_2\,^{16}O$, $H_2\,^{18}O$, $H_2\,^{17}O$ and $HD\,^{16}O$ under very dry conditions, at water concentrations of some hundred to only tens of ppmv. The instrument developed during this thesis shows a much higher measurement stability over time compared to previous OF-CEAS instruments with optimum integration times of up to several hours and a very long effective path length of more than 30 km. At water concentrations around 80 ppmv, a precision of 0.8‰, 0.1‰ and 0.2‰ for δ^2H, $\delta^{18}O$ and $\delta^{17}O$ respectively could be achieved with an integration time of 30 min and of 12‰, 1.1‰ and 3.2‰ with 4s averaging. At the optimum water concentration of approx. 650 ppmv, the precision for δ^2H, $\delta^{18}O$ and $\delta^{17}O$ is 0.28‰, 0.02‰ and 0.07‰ respectively, with averaging times of 30 to 60 min.

An investigation of the overall performance of the instrument is presented and we specifically discuss the problem of a dependence of the isotope measurements on the water concentration at

which a measurement is carried out. As main source of the concentration dependence, pattern noise is identified and a detailed analysis of the noise sources is given.

Furthermore, a new calibration system for water vapor isotope measurements, the Syringe Nanoliter Injection Calibration System (SNICS), is introduced, which was developed in the framework of this thesis to offer a more reliable and stable means for the calibration of water vapor isotope measurements. This calibration system is based on the continuous injection of water into an evaporation chamber with two nanoliter syringe pumps and is able to generate standard water vapor in a range of 5 to 15 000 ppmv. A model simulation of the water injection is presented and shows a good agreement with experimental results.

Subsequently, a first employment of the OF-CEAS spectrometer at the Norwegian research station of Troll in Antarctica is discussed. Data from a three-week period from February and March 2011, during which the spectrometer continuously measured water vapor isotopologues in the atmosphere at the research station, is shown and problems and possibilities are discussed.

Finally, the Isocloud project, an international project to study (super)saturation effects at the AIDA cloud chamber of the Karlsruhe Institute Technology in Germany, is introduced, in which we participated with both the spectrometer and the calibration instrument. Experimental data of the four measurement campaigns is presented, preliminary results are discussed. We conclude with a discussion of the optimum measurement protocol and give an outlook for the future.

Résumé

Au cours de ces dernières annés, la mesure des isotopologues de l'eau est devenue de plus en plus importante dans le domaine des sciences de l'atmosphère. La composition isotopique de l'eau conservée dans la glace en Antarctique et en Arctique peut être utilisée comme un paléothermomètre permettant de comprendre les changements passés du climat [1] du fait de l'influence des conditions climatiques sur les rapports isotopiques. La mesure des variations de la composition isotopique de la vapeur d'eau dans l'atmosphère peut servir à étudier le cycle hydrologique global de la terre [2] et à raffiner les modèles de circulations atmosphériques [3].

La Spectrométrie de Masse des Rapports Isotopiques (plus souvent connu par son acronyme anglais IRMS), qui est la méthode conventionnelle pour la mesure des isotopes de l'eau, n'est pas adaptée aux mesures en continu et in-situ des isotopes de vapeur d'eau. C'est grâce au développement récent des spectromètres laser, qu'il existe maintenant une méthode simple et robuste pour effectuer des recherches sur le terrain avec une bonne résolution temporelle [4–7]. Cependant, jusqu'à présent la plupart des instruments optiques usuels exigent des niveaux d'humidité relativement élevés avec des concentrations d'eau supérieures à 1000 ppmv, ce qui exclut les mesures dans certaines des régions les plus intéressantes pour l'étude des variations isotopiques dans l'eau, telles comme les couches élevées de l'atmosphère ou les régions centrales de l'Antarctique.

Ce travail à pour but d'introduire un nouveau spectromètre laser infrarouge basé sur la technique d'Optical Feedback Cavity Enhanced Absorption spectroscopy (OF-CEAS). Il a été conçu spécialement pour la mesure des quatre isotopologues $H_2\,{}^{16}O$, $H_2\,{}^{18}O$, $H_2\,{}^{17}O$ et $HD\,{}^{16}O$ dans un environnement sec avec des concentrations d'eau de quelques centaines à seulement quelques dizaines de ppmv. L'instrument développé dans le cadre de cette thèse montre une stabilité de mesure supérieure aux instruments OF-CEAS précédents, avec des temps d'intégration optimaux pouvant aller jusqu'à plusieurs heures et une longueur de trajet optique effective de plus de 30 km. Pour des concentrations d'eau d'environ 80 ppmv , une précision de 0.8‰, 0.1‰ et 0.2‰ a été atteinte respectivement pour δ^2H, $\delta^{18}O$ et pour $\delta^{17}O$ avec un temps d'intégration de

30 minutes et de 12‰, 1.1‰ and 3.2‰ avec une moyenne effectuée sur 4s. Pour la concentration d'eau optimale de 650 ppmv, la précision pour δ^2H, δ^{18}O et δ^{17}O est de 0.28‰, 0.02‰ et de 0.07‰, avec une durée d'accumulation de 30 à 60 minutes.

La performance globale de l'instrument est analysée et le problème de la dépendance des mesures isotopiques vis-à-vis de la concentration d'eau avec laquelle l'expérience est effectuée est étudié en détail. La présence d'un motif fixe spectral est identifiée comme étant la source principale de bruit et est analysée en détail. En outre, un nouveau système de calibration pour des mesures d'isotopes de vapeur d'eau, le Syringe Nanoliter Injection Calibration System (SNICS), est présenté. Ce système a été développé dans le cadre de cette thèse afin de disposer d'un moyen fiable et stable pour la calibration des mesures des variations isotopiques de la vapeur d'eau. Le système de calibration est basé sur l'injection continue d'eau dans une chambre d'évaporation avec deux pousse-seringues au nanolitre. Il est capable de générer une vapeur d'eau standard entre 5 et 15000 ppmv. Une simulation modélisée de l'injection d'eau, qui est en bon accord avec les expériences, est présentée. Ensuite une première utilisation du spectromètre OF-CEAS dans la station de recherche norvégienne (Troll) en Antarctique est exposée en détail. Les données enregistrées pendant une période de trois semaines de Février à Mars 2011 sont présentées et discutées, en particulier celles relatives aux problèmes de calibration rencontrés avec un système de calibration rudimentaire construit sur place. Pendant cette période le spectromètre a mesuré en continu les isotopologues de vapeur d'eau dans l'atmosphère sur le site de la station. Pour conclure, nous présentons le projet Isocloud, un projet international ayant pour but d'étudier des effets de (super)saturation en utilisant la chambre à nuages AIDA du Karlsruhe Institute of Technology en Allemagne. Notre spectromètre et le système de calibration faisaient partie de ce projet. Les données expérimentales de quatre campagnes de mesure sont présentées et des résultats préliminaires sont discutés. Nous concluons en présentant un protocole optimal de mesure optimal ainsi que par une discussion des perspectives pour le futur.

Samenvatting

De bepaling van de isotopensamenstelling van waterdamp heeft zich in de afgelopen jaren ontwikkeld tot een steeds belangrijker analytisch instrument in atmosferisch onderzoek. De invloed van klimaatfactoren op de isotoopverhoudingen maakt dat de isotopensamenstelling van water opgeslagen in Antarctisch en Arctisch gletsjerijs gebruikt kan worden als een paleo-thermometer in de reconstructie van klimaatveranderingen in het verleden [1]. De isotoopverhoudingen in waterdamp in de atmosfeer levert informatie over de (zoet-) water kringloop [2] en is een belangrijk gegeven voor de verdere ontwikkeling van atmosferische circulatie modellen [3]. Daar waar de conventionele meetmethode voor de bepaling van isotoopverhoudingen, Isotopen Ratio Massa Spectrometrie (IRMS), niet geschikt is voor "in-situ" bepaling van isotoopverhoudingen in waterdamp, bieden recente methoden gebaseerd op laser spectrometrie de mogelijkheid om op relatief eenvoudige en robuuste instrumentatie te bouwen voor meting in het veld met hoge tijdsresolutie [4–7]. Echter, de meeste van deze optische instrumenten vereisen een relatief hoge luchtvochtigheid met water concentraties van tenminste enkele duizenden ppmv (volumeconcentratie in delen per miljoen), waardoor metingen in enkele van de meest interessante regio's op aarde, zoals in de hogere atmosferische lagen of in centraal Antarctica, onmogelijk zijn. Dit proefschrift beschrijft de ontwikkeling van een innovatieve infrarood laser spectrometer welke gebruik maakt van de methode van Optical Feedback Cavity Enhanced Absorption Spectroscopy (OF-CEAS) voor de kwantitatieve bepaling van de vier waterisotopologen $H_2\,^{16}O$, $H_2\,^{18}O$, $H_2\,^{17}O$ en $HD\,^{16}O$ in zeer droge lucht bij waterconcentraties van enkele honderden tot slechts tientallen ppmv's. Het door ons ontwikkelde instrument, vergeleken met eerdere OF-CEAS instrumenten, wordt gekenmerkt door een veel langere meetstabiliteit in de tijd met een optimale middelingstijd tot enkele uren en een grote gevoeligheid ten gevolge van de extreem lange optische weglengte van ruim 30 km. Bij een waterconcentratie van 80 ppmv is de meetprecisie 0.8‰, 0.1‰ en 0.2‰ voor d2H, d18O en d17O, respectievelijk, bij middeling over 30 min, en 12‰, 1.1‰ en 3.2‰ bij middeling over 4 s. Bij de optimale waterconcentratie van ongeveer 650 ppmv is de precisie voor δ^2H, $\delta^{18}O$ en $\delta^{17}O$, respectievelijk, gelijk aan 0.28‰, 0.02‰ en 0.07‰ bij

middeling over 30 tot 60 min. We presenteren een algemene karakterisering van het instrument, alsook een gedetailleerde beschrijving van de afhankelijkheid van de isotopenmetingen van de waterconcentratie bij welke de metingen worden uitgevoerd. Als belangrijkste oorzaak van deze concentratieafhankelijkheid wijzen we naar het gestructureerde karakter van de instrumentele ruis op de achtergrond (basislijn) van het waterspectrum welke gebruikt wordt voor de bepaling van de isotopenverhoudingen. Het effect van dit 'patroonruis' op de metingen is verder onderzocht. Teneinde de spectrometer te kunnen kalibreren is een luchtstroom met een stabiele waterconcentratie en isotopensamenstelling vereist. Omdat bekende methoden voor de productie van een dergelijke vochtige luchtstroom niet voldoende betrouwbaar en stabiel bleken te zijn bij de door ons gewenste lage waterconcentraties, is in het kader van dit proefschrift een alternatief instrument ontwikkeld genaamd SNICS (voor Syringe Nanoliter Injection Calibration System). Dit systeem is gebaseerd op twee commerciële nanoliter spuitspompen teneinde waterconcentraties van 5 tot 15 000 ppmv te kunnen genereren met een zo laag mogelijke consumptie van de vaak kostbare water isotopen standaarden. Een simpel model geeft een goede kwantitatieve beschrijving van geïnduceerde veranderingen in zowel concentratie als isotopenverhoudingen. Vervolgens wordt een uitgebreide beschrijving gegeven van de eerste toepassing van de spectrometer in Antarctica, op het Noors station Troll, waarbij data van een periode van 3 weken in februari en maart van 2011 worden gepresenteerd. Tot slot bespreken we de deelname van de spectrometer en zijn kalibratie apparatuur aan het internationale project ISOCLOUD ter bestudering van (super) saturatie effecten tijdens wolkvorming in de AIDA simulatiekamer van het Karlsruhe Institute of Technology. We laten experimentele data van 4 meetcampagnes en de eerste resultaten zien. We besluiten met een bespreking van de optimale meetstrategie en geven een blik op de toekomst.

Contents

Introduction

Atmospheric water vapor is the most important greenhouse gas and responsible for approximately 60% of the natural greenhouse effect [8]. The spatial distribution of water vapor and the partitioning between vapor and liquid phase play an important role in the radiative balance of the atmosphere [9, 10]. Phase transitions between vapor and liquid or solid phase are determining cloud formation and precipitation, and present the basic mechanism of atmospheric energy transport.

The relative abundances of the different stable isotopologues of water are sensitive to the conditions at which phase changes, and evaporation and condensation in particular, take place. The isotopic composition of precipitation at higher latitudes is related to air temperature [11–13]. Because of this, water isotopic ratios offer a unique possibility to study processes that would otherwise remain hidden. Water isotopic ratios can be used as tracers of the atmospheric water cycle [14] and for the study of convective processes in the atmosphere [15–18]. Due to the influence of climatic conditions on the isotope ratios, the isotopic composition of water stored in the ice in Antarctica and the Arctic can be used to reconstruct past climate changes [1, 19, 20].

Conventionally, isotope ratio measurements are conducted by means of Isotope-Ratio Mass Spectrometry (IRMS) . Because of elaborate and time consuming preparation of the samples and the impossibility of in-situ measurements (cf. also 2.1), optical spectroscopy is increasingly used as alternative, especially when continuous and in-field measurements are required. In recent years, diverse laser spectrometers based on different optical techniques have been introduced (e.g. the references [4–7, 10], as well as section 2.4 of this thesis for a more detailed discussion) and successfully applied. However, to the best of our knowledge, so far no instrument has been able to measure isotope ratios in very dry conditions (< 50 ppmv) encountered in the upper atmosphere, with a sufficiently high precision to resolve microphysical processes responsible for some of the most interesting mechanisms in Earths atmosphere, such as supersaturation.

This thesis was initiated in the framework of the Dutch National AntArctic Research Program (NAAP) and funded to a large extend by the Netherlands Organization for Scientific Research

(NWO). Additional funding was given by the the Integration of European Simulation Chambers for Investigating Atmospheric Processes (EUROCHAMP-2). Local funding was generously provided by the Université Joseph Fourier (UJF). The goal was to develop a novel infrared laser spectrometer to measure stable water isotopes and the subsequent application to climate research, specifically by measuring water vapor isotopes in the Antarctic atmosphere.
After a first measurement campaign to Antarctica, an additional focus was set on the development of a robust and reliable calibration set-up for very low water concentration calibrations of isotopic measurements. Increased attention was also given to a more in-depth study of noise characteristics of the spectrometer itself. Furthermore, the application of the instrument was expanded to study mechanisms encountered in the atmosphere. These investigations were carried out at the cloud chamber AIDA in Karlsruhe, Germany in the framework of the so-called Isocloud project.
In chapter 1, a general introduction to the terminology of water vapor isotopologues is given, explaining the underlying mechanisms and principles. In chapter 2, we give an overview of the traditional and recent methods used to study water vapor isotopologues and in chapter 3, the principles and layout of the laser spectrometer developed in this thesis are explained.
Chapter 4 explains how the data recorded with the laser spectrometer is analyzed and converted to concentration and isotope ratio values. Furthermore, the precision and accuracy of the instrument are discussed. A procedure for the calibration of the data is introduced in chapter 5. In chapter 6, different calibration instruments are introduced that were used and partly developed during the thesis to put the isotopic measurements on an absolute scale.
In chapters 7 and 8, we finally present the application of the laser spectrometer to different scientific questions. In chapter 7 the study of atmospheric moisture in Antarctica at the Norwegian research station Troll is presented and in chapter 8, the investigation of ice cloud formation in stratospheric air that was done in the framework of the Isocloud project in the atmospheric climate chamber AIDA in Karlsruhe, Germany.

Chapter 1

Isotope terminology

1.1 Saturation water vapor pressure

In a mixture of different gases, each specific component behaves as if it would alone occupy the entire volume filled by the mixture. Because of this, not the total pressure but the partial pressure of each component is determining if a molecule is present at a certain temperature in purely gaseous form or partially as a condensate. The partial pressure above which condensation sets in, is called the saturation pressure.
In the case of water, the relation between saturation pressure and temperature has been investigated by several groups and different expressions have been established. Because of different heat capacity and molar volume, the saturation pressure of water above ice and above water at the same temperature are different and independent relations have to be used for the two cases. The most commonly used relations are the equations of Goff [21, 22]. More recently, a formulation based on an integration of the Clapeyron equation was established by Murphy and Koop [23]:

$$\begin{aligned} p_{water} &= \exp\left(54.842763 - 6763.22/\mathrm{T} - 4.210\ln(\mathrm{T}) + 0.000367\mathrm{T}\right. \\ &\quad + \tanh[0.0415(\mathrm{T} - 218.8)](53.878 - 1331.22/\mathrm{T} \\ &\quad \left. -9.44523\ln(\mathrm{T}) + 0.014025\mathrm{T})\right) \qquad (1.1) \\ p_{ice} &= \exp(9.550426 - 5723.265/\mathrm{T} + 3.53068\ln(\mathrm{T}) - 0.00728332\mathrm{T}) \qquad (1.2) \end{aligned}$$

with T in Kelvin and p in pascal. The equation for saturation pressure above water is valid for $123 < T < 332$ K and the equation for ice for $T > 110$ K.
If the partial pressure of water is higher than the saturation pressure, this is called supersaturation. The phenomena of supersaturation is quite common in the absence of nucleation centers (e.g. aerosols) on which the vapor can condense or freeze out, but has also been observed when nucleation centers are present (discussed in more detail in chapter 8). The saturation parameter

$$S = \frac{p_{H_2O}}{p_{saturation}} \qquad (1.3)$$

is used to express the degree of saturation, with supersaturation for $S > 1$.

1.2 Isotopes

Atoms consist of a nucleus surrounded by electrons. The nucleus is composed by protons and neutrons. The protons are positively charged and determine by their number (the atomic number), which chemical element the atom belongs to. The neutrons carry no electric charge and determine along with the protons, which have approximately the same mass, the mass of an atom. The sum of the number of protons (Z) and neutrons (N) in a nucleus is the nuclear mass number:

$$A = Z + N \tag{1.4}$$

The common notation to describe a specific nucleus of element X is:

$${}^{A}_{Z}X_{N}$$

Two atoms of the same element (same number of protons) but a different number of neutrons, are called isotopes. Many elements have two or more stable and naturally occurring isotopes. Apart from stable isotopes, some elements also have unstable (radioactive) isotopes that only have a small chance of natural occurrence.
In the case of hydrogen, two stable isotopes exist: ^{1}H and $^{2}_{1}H_{1}$ (also called deuterium). A third isotope $^{3}_{2}H_{2}$ (tritium) is radioactive. Oxygen has three stable isotopes, the most abundant ^{16}O and two rare isotopes, ^{18}O and ^{17}O.
In the case of molecules with different isotopic composition, one differentiates between isotopomers and isotopologues. Isotopomers have the same number of each isotopic atom but differ in their position. The term is a contraction of 'isotopic isomer' [24]. Isotopologues are molecular entities that differ only in isotopic composition (number of isotopic substitutions) [24], e.g. $H_2\,{}^{16}O$, $HD\,{}^{16}O$, $H_2\,{}^{18}O$ and $H_2\,{}^{17}O$.

1.2.1 Isotope ratios

Isotope abundances are generally reported as ratio of the less abundant isotope and the most abundant isotope:

$$R = \frac{\text{abundance of rare isotope}}{\text{abundance of abundant isotope}} \tag{1.5}$$

The isotope ratio normally has a superscript before the ratio symbol R to indicate which isotope is considered [25]. For example:

$${}^{2}R(H_2O) = \frac{[HD^{16}O]}{2[H_2^{16}O]} \tag{1.6}$$

The factor 2 in the denominator accounts for the two equivalent positions of the hydrogen atom in the water molecule.

It is common to report isotope ratios not in absolute numbers but in respect to a reference sample or standard. One of the reasons for this is that the absolute ratios are in general less relevant than changes in the ratios because of phase transitions or molecular changes. Another reason is that most of the instruments capable to measure isotope abundances are not suitable to measure absolute ratios but rely on the comparison with a reference sample [25].
As the change of the isotope ratios during the transitions is often very small, the change of the isotope ratio of a sample A is normally reported relative to the ratio of a reference sample r as a permil deviation:

$$\delta_{A/r} = \frac{R_A}{R_r} - 1 \quad (\times 10^3‰) \tag{1.7}$$

In the case of water, the standards used as international references, are Vienna Standard Mean Ocean Water (VSMOW) and Standard Light Antarctic Precipitation (SLAP) [26]. The absolute isotope ratios for VSMOW have been determined to:

$$\begin{aligned} {}^2H/{}^1H &: (155.75 \pm 0.08) \cdot 10^{-6} \text{ [27]} \\ {}^{18}O/{}^{16}O &: (2005.20 \pm 0.45) \cdot 10^{-6} \text{ [28]} \\ {}^{17}O/{}^{16}O &: (379.9 \pm 0.8) \cdot 10^{-6} \text{ [29]} \end{aligned} \tag{1.8}$$

The absolute isotope ratios for SLAP have only been measured with a comparable precision for ${}^2H/{}^1H$ [27]:

$${}^2H/{}^1H = (89.12 \pm 0.07) \cdot 10^{-6}$$

and have been calculated for ${}^{18}O/{}^{16}O$ based on the isotope ratio relative to VSMOW [30, 31]:

$${}^{18}O/{}^{16}O = (1893.91 \pm 0.45)$$

As the water standards VSMOW and SLAP are nearly depleted, two new international standards, VSMOW2 and SLAP2 have been provided by the Hydrology Laboratory of the International Atomic Energy Agency (IAEA) in Vienna. δ^2H for VSMOW2 and $\delta^{18}O$ for VSMOW2 and SLAP2 are, within the measurement precision, identical to those of VSMOW and SLAP, respectively. However, $\delta^2H = -427.5 \pm 0.3‰$ for SLAP2 and thus measurably different from $\delta^2H = -428‰$ of SLAP [26, 30].

1.2.2 Fractionation

Because of the differences in mass and size of the atomic nuclei of two isotopes of the same element, two isotopologues have slightly different physical and chemical properties. Because of the higher mass, a heavier isotopologue has a lower mobility than a lighter one. This leads to a lower diffusion velocity of the heavier isotopologues as well as a smaller chemical reactivity, which depends significantly on the collision frequency with other molecules [25]. In addition, the heavier molecules often have a higher binding energy than the lighter ones because of a larger atomic diameter.
Because of the different properties of the isotopes, the isotope ratios can change during a chemical reaction or a phase transition. As an example, during evaporation of water, the most abundant and light isotopologue $H_2^{16}O$ preferentially evaporates, resulting in isotope ratios that are lower in the vapor phase compared to that in the liquid source water.
The difference in the isotopic composition of two compounds in equilibrium ($A \Leftrightarrow B$) or before and after a physical or chemical transition ($A \rightarrow B$) can be described with the isotope fractionation factor, which is defined as:

$$\alpha_A(B) = \alpha_{B/A} = \frac{R_B}{R_A} \tag{1.9}$$

As the change of the isotope ratios is often very small ($\alpha \approx 1$), one often uses the fractionation instead, which is defined as $\epsilon = \alpha_{B_A} - 1$ (normally reported in permil).

In general, we distinguish between two kinds of fractionation, equilibrium fractionation and kinetic fractionation.
Equilibrium fractionation describes the difference in isotope ratios between two states that are in thermal equilibrium, i.e. in a system with no net fluxes. It can be shown [32, 33] that the fractionation factors of two molecules can be related to the ratio of the respective partition functions, a detailed discussion is however beyond the scope of this work.
In the case of water, the equilibrium fractionation factors are only dependent on temperature and not on pressure. For the phase change ice to vapor, the most commonly used equation for δ^2H was determined by Merlivat [34] in 1967 and is valid for $-40\ °C \leq T \leq 0\ °C$:

$$\ln \alpha_{ice-vapor}(^2H/^1H) = -9.45 \cdot 10^{-2} + \frac{16289}{T^2} \tag{1.10}$$

with T in Kelvin. For the phase change between liquid and gas phase water for δ^2H, and for both phase changes, ice-vapor and liquid-vapor for $\delta^{18}O$, the generally used equations were

formulated by Majoube [35, 36]:

$$\ln \alpha_{liquid-vapor}(^2H/^1H) = -52.612 \cdot 10^{-3} - \frac{76.248}{\mathrm{T}} + \frac{24.844 \cdot 10^3}{\mathrm{T}^2} \quad (1.11)$$

$$\ln \alpha_{ice-vapor}(^{18}O/^{16}O) = -28.224 \cdot 10^{-3} + \frac{11.839}{\mathrm{T}} \quad (1.12)$$

$$\ln \alpha_{liquid-vapor}(^{18}O/^{16}O) = -2.06667 \cdot 10^{-3} - \frac{0.4156}{\mathrm{T}} + \frac{1.137 \cdot 10^3}{\mathrm{T}^2} \quad (1.13)$$

with T in Kelvin. These equations are valid for -34 °C $\leq T \leq 0$ °C for $\alpha_{ice-vapor}(^{18}\mathrm{O}/^{16}\mathrm{O})$ and 0.75 °C $\leq$ T $\leq$ 91.6 °C for the phase change liquid-vapor.

Kinetic fractionation on the other hand describes an irreversible process, with a removal of molecules from the vapor phase e.g. because of diffusion. If one assumes that molecules are removed due to diffusion from the boundary layer between liquid and vapor phase, the kinetic fractionation factor can be expressed as [32, 37, 38]:

$$\alpha_{kin} = \frac{R_w}{R_e} = \frac{\alpha_{diff}\alpha_{eq}(1-h)}{1-\alpha_{eq}h(R_v/R_w)} \quad (1.14)$$

with α_{eq} the equilibrium fractionation factor, h the relative humidity, R_v the isotope ratio of the vapor, R_w the isotope ratio of the liquid and α_{diff} the diffusion fractionation factor accounting for differences in the diffusivities of the different isotopologues, with e.g. α_{diff}^{18O}:

$$\alpha_{diff}^{18} = \left(\frac{D_{\mathrm{H_2}\,^{16}\mathrm{O}}}{D_{\mathrm{H_2}\,^{18}\mathrm{O}}}\right)^n$$

with $D_{\mathrm{H_2}\,^{16}\mathrm{O}}$ and $D_{\mathrm{H_2}\,^{18}\mathrm{O}}$ the molecular diffusivity of $\mathrm{H_2}\,^{16}\mathrm{O}$ and $\mathrm{H_2}\,^{18}\mathrm{O}$, respectively. The exponent n depends on the ratio of turbulent to moelcular diffusion and is one if for no turbulences.

In the case of ice crystal formation in clouds, supersaturation can often be encountered, which also results in non-equilibrium conditions with kinetic fractionation (cf. also chapter 8). Jouzel and Merlivat [39] attribute this to the fact that the crystallization is diffusion limited, which means that crystallization occurs relatively fast but new water molecules have to be "re-supplied" to the crystallization zone by diffusion, which means that the crystallization zone is more depleted in the heavier HD ^{16}O, $\mathrm{H_2}\,^{18}$O and $\mathrm{H_2}\,^{17}$O molecules, which condense resultingly more slowly. As a consequence, the vapor becomes more enriched in the heavier isotopologues compared to the equilibrium case. The effective fractionation in this case can be described as [39]:

$$\alpha_k = \frac{S}{\alpha_e D/D'(S-1)+1} \quad (1.15)$$

with S the saturation parameter (equation (1.3)) and D/D' the ratio of the diffusion coefficient of the abundant isotopologue over that of the rare water isotopologue. Based on [40], this leads to

$$\alpha_k(\delta^2 H) \approx \frac{S}{1.0251\alpha_e(S-1)+1} \tag{1.16}$$

$$\alpha_k(\delta^{18} O) \approx \frac{S}{1.0285\alpha_e(S-1)+1} \tag{1.17}$$

$$\tag{1.18}$$

Alternatively, the kinetic fractionation in this case can be described with [39]:

$$\alpha_{kin} = \frac{\alpha_{eq}\alpha_{diff}(S-1)+1}{S} \tag{1.19}$$

with the definition of the parameters as above. This equation clearly shows the effect of the supersaturation and the diffusivities of the different isotopologues on the relation of kinetic and equilibrium fractionation.

Fractionation that occurs in an open system with an immediate removal of evaporated water, is described by the so-called Rayleigh fractionation. It is generally encountered when a dry gas flux removes the water vapor from the evaporation zone. Because of the continuous removal of a larger fraction of lighter isotopologues, the δ value of the remaining liquid becomes increasingly enriched and consequently the δ value of the vapor. The principle of this fractionation is demonstrated in figure 1.1, which is based on a similar figure from [25]. Let N be the number of the most abundant isotopic molecules, which is approximately equal to the total number of molecues, and R the isotope ratio of rare to abundant isotopologue. The number of the rare isotopic molecule is thus $N_{rare} = R \cdot N$. At each time step, $-dN$ molecules are evaporated from the liquid volume. If we neglect the the number of other rare isotopic molecules, which is true to a good approximation, we can write the mass balance of the rare isotopologue as:

$$\frac{R}{1+R}N = \frac{R+dR}{1+R+dR}(N+dN) - \frac{\alpha_{eq}R}{1+\alpha R}dN \tag{1.20}$$

Because of the small abundance of the rare isotopologue, we can approximate the total number of molecules with the number of the most abundant isotopic molecule. We thus equal all denominators with $1+R$. Equation 1.20 then becomes

$$RN = (R+dR)(N+dN) - \alpha R dN \tag{1.21}$$

If we now neglect the product of the differentials, $dRdN \approx 0$, we can separate the two variables and integrate the equation with the boundary condition $R = R_0$ for $N = N_0$. This leads to

$$\frac{R}{R_0} = \frac{N}{N_0}^{\alpha-1} \tag{1.22}$$

with R_0 the original isotopic composition of the liquid and N_0 the initial total number of molecules in the liquid.
In figure 1.2, the increasing enrichment of the liquid due to continuous removal of isotopically lighter water vapor is shown for a typical case for δ^2H.

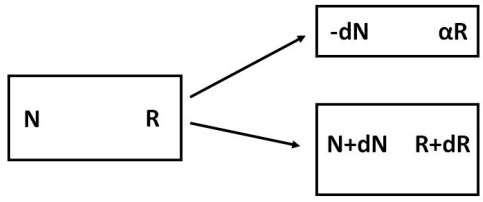

Figure 1.1: Schematics of the Rayleigh process, with N the number of the most abundant isotopic molecule, R the isotope ratio of the liquid and α the fractionation factor between liquid and vapor phase.

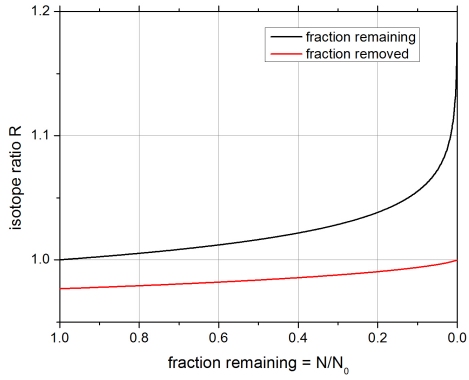

Figure 1.2: During the evaporation process, the liquid becomes increasingly enriched in the heavier isotopes as lighter isotopes evaporate preferentially and the isotope ratio increases (black line). Consequently, the average isotope ratio of the fraction that was already evaporated (in red), increases until it logically matches the initial isotope ratio of the liquid when all water is evaporated.

These different fractionation processes give a first idea, how natural occuring transitions behave and can be described mathematically. Of course more complex fractionation processes can occur, with a composition of the different fractionation mechanisms described above or with additional sources and sinks of water vapor, requiring more intricate and detailed models.

1.2.3 Delta values as proxies

Because of the dependence of fractionation processes on climatic conditions such as temperature and humidity levels, the delta values can be used as proxies of weather and climate changes. While δ^2H and δ^{18}O can be used as proxies of past temperature changes [41], the two parameters

can be combined in the so-called deuterium excess parameter (d-excess), defined as [14]:

$$\text{d-excess} = \delta^2 H - 8 \times \delta^{18} O \tag{1.23}$$

The d-excess provides additional information on variations of past temperature and evaporative conditions [42, 43] and is affected by relative humidity.
Additional information can also be captured by the ^{17}O-excess, which combines δ^{17}O and δ^{18}O in the following manner [44]:

$$^{17}\text{O-excess} = \ln(1 + \delta^{17} O) - 0.528 \ln(1 + \delta^{18} O) \tag{1.24}$$

The variation in ^{17}O-excess in water is relatively independent of temperature and is mainly dependent on kinetic fractionation effects [45]. It is therefore a strong indicator of the relative humidity in the source region, where water was evaporated [45, 46]. Whereas d-excess measurements have been routinely carried out since several years (see e.g. [1, 43, 47], the measurement of ^{17}O-excess has only recently gained increased attention. This is mainly due to the fact that very precise measurements are required (^{17}O-excess is generally expressed in per meg), which had not been possible until recently [48, 49].
Risi et al. [3] present a comparison of an isotopic general circulation model (LMDZ) with measurements of d-excess and ^{17}O−excess in different meteoric water samples, water vapor at Southern Ocean transects and polar ice cores. Whereas the model behavior agrees relatively well for δ^2H for differences between the last glacial maximum (LGM) and the present day distribution in Antarctica, the model is not yet well adapted to reflect the behavior ^{17}O-excess. The authors ascribe this mainly to the fact that the integration of ^{17}O-excess into the models remains still difficult because of missing experimental data. In addition, they point out that ^{17}O-excess seems to be more sensitive to a large range of parameters than d-excess, including mixing along distillation trajectories.
Measurements of ^{17}O-excess in ice cores from various sites in Antarctica [50, 51] show that the evolution of ^{17}O−excess is largely dependent on the location. Whereas a relatively large increase of 20 ppm in ^{17}O−excess can be observed in ice from the last deglaciation at the inner continental site of Vostok, it remains almost constant at the coastal site of Talos Dome. Whereas Winkler et al. [50] attribute this to a larger influence of oceanic moisture source regions on the ice at coastal Antarctic sites, Schoenemann et al. [51] propose kinetic isotope effects during snow formation under supersaturated conditions as the principal reason. Because of presumably large influences of local effects on ^{17}O−excess in continental Antarctic ice, Winkler et al. [50] propose to rather use ^{17}O−excess in coastal East Antarctic ice cores as a proxy for relative humidity.
Based on a comparison of d-excess, δ^{18}O and δ^2H measurements with environmental parameters such as temperature and pressure from a 1.5 year period at the Bermuda Islands, Steen-Larsen et al. [52] show that the largest influence on d-excess can effectively be allocated to relative humidity. Contrary to previous assumptions, they didn't observe an impact of wind speed on

d-excess, but observed a strong correlation with wind direction, which might be due to different source regions of the water vapor.

Due to the improved precision of recent laser spectrometers, d-excess and $^{17}O-$excess measurements become increasingly important and feasible, and a better understanding of the complex mechanisms governing these second-order parameters is only a question of time, when more experimental data sets from various places on Earth will help to refine the theoretical description.

Chapter 2

Measurement of isotopes

2.1 Mass spectrometry

For more than 50 years, Isotope Ratio Mass Spectrometry (IRMS) has been the conventional method to measure isotope ratios. Current IRMS instrumentation offers not only very high precision measurements, but also a relatively high throughput of samples.
Unfortunately, this technique has several disadvantages that make measurements of condensable gases or highly adsorbing molecules such as water very difficult. In the case of water vapor isotopes, the measurement can not be done directly on the water molecules, but has to be preceded by a chemical transfer of the isotope in question to a molecule that can be analyzed directly. In the case of ^{18}O, the transfer is typically done between H_2O and CO_2 in an equilibrium process involving the bicarbonate reaction, which normally requires several hours to reach equilibrium [53]. An accurate measurement of ^{17}O in H_2O by the CO_2 equilibration method is practically impossible because $^{17}O\ ^{12}C\ ^{16}O$ appears in the same mass channel as the more abundant $^{16}O\ ^{13}C\ ^{16}O$. Accurate measurements of ^{17}O and ^{18}O can be made following the method of Barkan and Luz[44]. Instead of CO_2, CoF_3 is used as reagent to fluorinate water samples enabling the determination of $\delta^{18}O$, as well as $\delta^{17}O$, by IRMS on O_2. In the case of ^2H, different methods exist, including the reduction to hydrogen gas at an elevated temperature with a suitable reducing agent [54–56] and on-line pyrolysis of water in combination with a continuous-flow IRMS [57, 58].
Most of these techniques require a very accurate temperature regulation and relatively large sample quantities (typically 4-5 mL)[53], which are not always available. In addition, the chemical transfer is usually very time consuming and thus makes real-time analysis practically impossible. Moreover, since the ^{18}O and ^2H isotopic ratio determinations are not carried out simultaneously on the same sample, one risks to introduce uncorrelated errors in the two measurements.
In the case of water vapor isotope measurements, an additional drawback of IRMS is that the vapor first has to be collected in the form of liquid water or ice, which can for example be done via cryogenic trapping[59] or with a molecular sieve [60]. However, apart from the risk to change the isotope ratios during the trapping or recovery of the water, this also seriously limits the temporal resolution and renders monitoring of fast isotope changes virtually impossible.

2.2 The optical alternative: Stable Isotope Ratio Infrared Spectroscopy

An alternative for the measurement of water vapor isotope ratios is offered by different optical measurement techniques. In the near- and mid-infrared region of the electro-magnetic spectrum, the different water isotopes show a number of highly characteristic rotational-vibrational transitions (figure 2.1). If the vapor and total pressure are sufficiently low, the individual molecular transitions can be easily resolved and attributed to a specific water isotopologue.

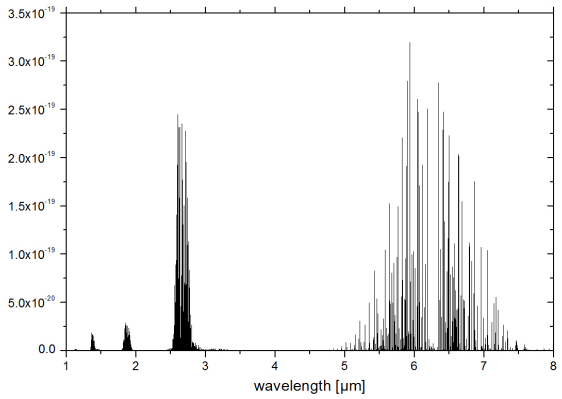

Figure 2.1: Simulated absorption spectrum of water in the infrared, based on the HITRAN2012 database [61]. The width of the individual ro-vibrational transitions are too small to be visible on this scale.

The simplest method to analyze a gas sample, is direct absorption spectroscopy. A light beam with intensity I_0 and frequency ν_0 that passes through an absorption cell of length l, filled with an absorbing medium of concentration c experiences an attenuation of the intensity due to light absorption by the gas molecules. This attenuation is described by the Lambert-Beer Law, which is valid in the linear absorption regime:

$$I = I_0 \exp(-\alpha(\nu)l) \tag{2.1}$$

The dimension of I and I_0 is power per unit area. The frequency dependent absorption coefficient $\alpha(\nu)$ can be calculated by

$$\alpha(\nu) = \sigma(\nu)n \tag{2.2}$$

with n the molecular number density and $\sigma(\nu)$ the molecular cross section, which depends on the frequency ν through the line profile function $g(\nu - \nu_0)$:

$$\sigma = Sg(\nu - \nu_0) \tag{2.3}$$

Combining equations 2.2 and 2.3 we get:

$$\alpha(\nu)\ l = S\ g(\nu - \nu_0)\ n\ l \tag{2.4}$$

The line profile function $g(\nu - \nu_0)$ depends on pressure and temperature and is normalized: $\int_{-\infty}^{\infty} g(\nu)d\nu = 1$. The line strength S of the absorption transition is an important spectroscopic property of the absorbing species. S depends on the transition dipole moment, which is a purely molecular property, and on the number of molecules in the lower level of the transition, which can be described by the Boltzmann distribution. It is thus also dependent on the temperature, which strongly influences the population distribution over the rotational levels of the ground vibrational state. For a given transition, the temperature dependence can be described by the following equation [62]:

$$S(T) = S(T_0) \cdot \frac{Q(T_0)}{Q(T)} \cdot \frac{e^{\frac{E''}{kT}}}{e^{\frac{E''}{kT_0}}} \cdot \frac{1 - e^{-\frac{E' - E''}{kT}}}{1 - e^{-\frac{E' - E''}{kT_0}}} \tag{2.5}$$

with $S(T_0)$ the line strength at reference temperature T_0 [Kelvin], and E'' and E' the lower and upper state energy, respectively. k is Boltzmann's constant and $Q(T)$ the ro-vibrational partition function of the molecule, which can be approximated by a temperature dependent third order polynomial [63]. The penultimate term accounts for the ratio of Boltzmann populations, whereas the last term describes the effect of stimulated emission, which in the infrared can usually be neglected. Equation 2.5 assumes a static gas cell with constant number density. At constant pressure instead of constant volume, the right hand side of equation (2.5) has to be extended with the term T_0/T, which is proportional to the number density. This is the usual case for the spectrometer of this thesis, in which the gas flows through the gas cell at a constant pressure.
Depending on how the absorption coefficient is defined, the line strength S is expressed in different units. A convenient choice, and the one used for the HITRAN database, is to express the line strength S in cm/molecule, the number density in molecules/cm^3, the optical path length in cm, and the width of the optical transition in wavenumbers (cm^{-1}).

Although the absorption of light by a molecule happens at well defined frequencies, the absorption is not infinitely narrow but takes place in a frequency range around these central frequencies due to different broadening mechanisms. This results in a line shape of each spectral line, which is described by the above mentioned line profile function $g(\nu - \nu_0)$ and takes into account different physical phenomena that contribute to the spectral broadening.

2.3 Optical Spectroscopy Techniques

Different optical techniques have been developed for spectroscopic measurements, of which we will introduce some of the most important in the following.
A technique that exploits the Beer-Lambert law, is direct absorption spectroscopy [5, 7, 64–66], also termed Tunable Diode Laser Absorption Spectroscopy (TDLAS) when the laser in question is either a lead-salt or a semiconductor diode laser. In order to increase the sensitivity of this method, while maintaining a small footprint of the spectrometer, the optical path can be folded between two refocusing mirrors, creating a multiple-pass cell (MPC). Different configurations have been developed over the years, the most common of which are the White cell [67, 68] and the Herriot cell [5, 64, 69]. The wavelength of the laser is tuned over one or several absorption lines by a change of the laser current so that their absorption profile can be measured by registering a decrease in the transmitted light level.
An alternative spectroscopic method offering much larger effective path lengths is Cavity Ring Down Spectroscopy (CRDS), which is based on the measurement of the decay rate of light injected into an optical cavity formed by two or more high reflectivity mirrors. In the following, we give a short and simplified introduction to CRDS, a more detailed and refined picture can be found for example in [70, 71].
When light is injected into the cavity, it travels back and forth between the mirrors. At each reflection on one of the cavity mirrors, the intensity of the light splits into three parts. The largest part is reflected back into the cavity, which is expressed with the Reflectance R of the mirrors (present-day cavity mirrors typically have values of $R > 0.99$). Another part is transmitted through the mirror, described by the Transmittance T and the remaining part is lost due to absorptions and scattering in the mirror itself (the Loss L). Because of energy conservation, the relation between R, T and L is:

$$\mathcal{R} + \mathcal{T} + \mathcal{L} = 1 \tag{2.6}$$

The intensity of the light transmitted through the optical cavity can be measured with a photodetector behind one of the cavity mirrors. If the light injection is interrupted, either because a pulsed laser is used or because of an interruption of a continuous wave (CW) light source, the transmitted light intensity shows an exponential behavior:

$$I(t) = I_0 e^{-\frac{t}{\tau}}$$

The so-called Ring-Down (RD) time τ does not depend on the amplitude of the light pulse and is thus not affected by intensity fluctuations of the light source. In the following we will give a simplistic description of the CRDS in the so-called broad-band or ballistic approach. Later we will correct the results obtained in this manner such that they can be applied to our case of CW narrow-band excitation of the cavity. A more complete description can be found in [71]. After

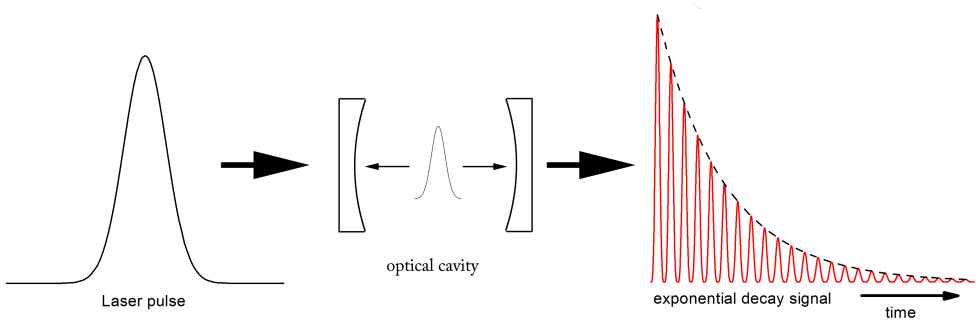

Figure 2.2: Ping-pong or ballistic model of pulsed CRDS: a short laser pulse is injected into a cavity. At each reflection, only a portion of the light is reflected, while another portion is transmitted and a part is lost due to absorption in the sample cell and in the mirror. This leads to an exponential decrease of the transmitted signal, measured by a photodiode behind the cavity (figure based on a graph from [72])

a first passage through the cavity, the initial intensity I_{in} is attenuated to:

$$I_0 = \mathcal{T}^2 e^{-\alpha l} I_{in} \tag{2.7}$$

with α the absorption coefficient of the absorbing medium in the cavity. After n round trips, the intensity measured by a photodetector can be calculated with:

$$I(t) = I_0 e^{-2n(-\ln \mathcal{R} + \alpha l)} \tag{2.8}$$

We can now replace the discrete number of passes n by the time the light spends in the resonator, $t = 2 \cdot l \cdot n/c$, which brings equation 2.8 to a continuous form:

$$I_{rd} = I_0 \exp\left(\frac{ct}{l}(-\ln \mathcal{R} + \alpha)\right) \tag{2.9}$$

The decay time constant (ring-down time) can be written as:

$$\tau = \frac{1}{c(-\ln R + \alpha l)} \tag{2.10}$$

When an absorber is present in the measurement cell, the decay rate of the light intensity is increased and the ring-down time decreases. The measurement of the ring-down can be converted into an absorption coefficient by subtracting the ring-down rate of the empty cavity from the ring-down rate of the cavity with an absorbing sample:

$$\alpha = \frac{1}{c}\left(\frac{1}{\tau} - \frac{1}{\tau_0}\right) \tag{2.11}$$

where τ_0 is the ring-down time for the empty cavity.
An important measure of the performance of an optical spectrometer is the minimum absorption, which can be measured. In CRDS instruments, this is determined with:

$$\alpha_{min} = \frac{1}{c}\left(\frac{1}{\tau_0 - \Delta t_{min}} - \frac{1}{\tau_0}\right) \approx \frac{\Delta\tau_{min}}{c\tau_0^2} \tag{2.12}$$

with $\Delta\tau_{min}$ the minimum measurable difference between τ and τ_0.
As indicator of the absorption measuring performance of an instrument, one generally states the Noise-Equivalent Absorption (NEA) [73], which is the minimum detectable absorption coefficient that can be distinguished from empty cavity losses during a one second measurement interval with 1 sigma uncertainty, per square root of the data-acquisition rate f:

$$NEA = \left(\frac{1}{f}\right)^{1/2} \frac{\Delta\tau_{min}}{c\tau_0^2} \tag{2.13}$$

In the case where white noise dominates the measurement statistics, which is generally the case for short acquisition times, the noise decreases with the inverse square root of time. This is the reason for the dependency on the square root of the data-acquisition rate in equation (2.13).
In addition to the behavior of the intensity with time, we also have to consider the relation of intensity and frequency encountered in optical spectrometers. In a cavity with two mirrors with same reflectivity R, the intensity of the transmitted radiation can be calculated with the Airy formula, when excitation of other transverse modes than TEM_{00} is ignored (see e.g. [74]):

$$I_T(\nu) = I_0(\nu)\frac{(1-\mathcal{R})^2}{(1-\mathcal{R})^2 + 4\mathcal{R}\sin^2(\Phi/2)} \tag{2.14}$$

with ν the input frequency of the radiation and Φ the phase difference between two successively reflected partial waves inside the cavity, which is $\Phi = \frac{4l\pi\nu}{c}$. The Airy formulas are calculated by taking the wave-like nature of light into account and interferences are considered as a given light wave propagates back and forth inside of a cavity.
The transmitted intensity is maximum when the denominator of equation (2.14) is minimum, which is the case when the sine is zero. This is the case for

$$\frac{2\pi}{c} l\nu = m\pi \tag{2.15}$$

and

$$\nu_m = m\frac{c}{2l} = m\Delta\nu_l \tag{2.16}$$

$\Delta\nu_l$ is the frequency interval between two resonances and is called Free Spectral Range (FSR). It depends on the distance l between the mirrors.

Because of this behavior, an optical cavity works as a filter with maxima only for frequencies, which fulfill the condition from equation (2.16).
For each frequency that follows equation (2.16), the length of a round trip of the light in the cavity corresponds to a multiple of the wavelength, corresponding to a longitudinal mode of the optical cavity. This relation ensures constructive interference of a reflected light wave when it overlaps with itself after a full round trip in the cavity. Apart from these longitudinal modes with nodes only in axial direction, there are also modes with nodes in x- and y-dimension (in Cartesian coordinates) and radial dimension (cylindrical coordinates), respectively. The collectivity of modes is called Transverse Electromagnetic Modes (TEM_{mnq}) , with subscripts m, n, and q for the number of nodes in the respective dimensions (q is the longitudinal number of modes and often omitted). An example of different TE-modes is shown in figure 2.3.

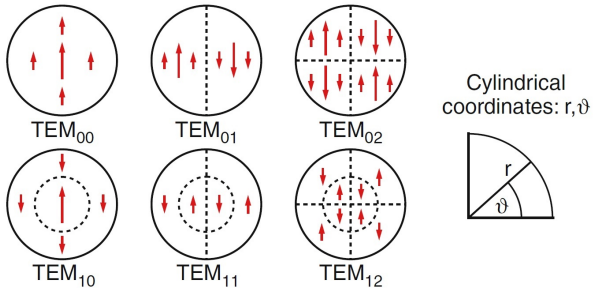

Figure 2.3: Schematic representation of the electric field distribution for the vertical polarization case in the xy-plane in the resonator in cylindrical coordinates, figure from [74])

The Full Width Half Maximum (FWHM) of the resonance given in equation (2.14), is [71]:

$$\Delta\nu_c = \frac{c}{2\pi l}\frac{1-\mathcal{R}}{\sqrt{\mathcal{R}}} \tag{2.17}$$

The width of a cavity mode thus depends on the mirror reflectivity and on the cavity length l. The ratio of the FSR and the width of a cavity mode is defined as the Finesse $\mathcal{F}$:

$$\mathcal{F} = \frac{\Delta\nu_{FSR}}{\Delta\nu_c} = \frac{\pi\sqrt{\mathcal{R}}}{1-\mathcal{R}} \tag{2.18}$$

Note that this formulation is true for a linear, but not a V-shaped cavity, where the equation has to be modified. It is an indicator of how well separated and narrow the cavity modes are. A graph showing the transmittance for different reflectivities $\mathcal{R}$ (based on a figure from [74]) is shown in figure 2.4. With increasing reflectivity, the cavity modes become increasingly narrow.

Instead of measurements of the ring-down time for the determination of the absorption coefficients, it is also possible to consider steady state conditions with a continuous light injection. This leads to Cavity Enhanced Absorption Spectroscopy (CEAS) techniques.

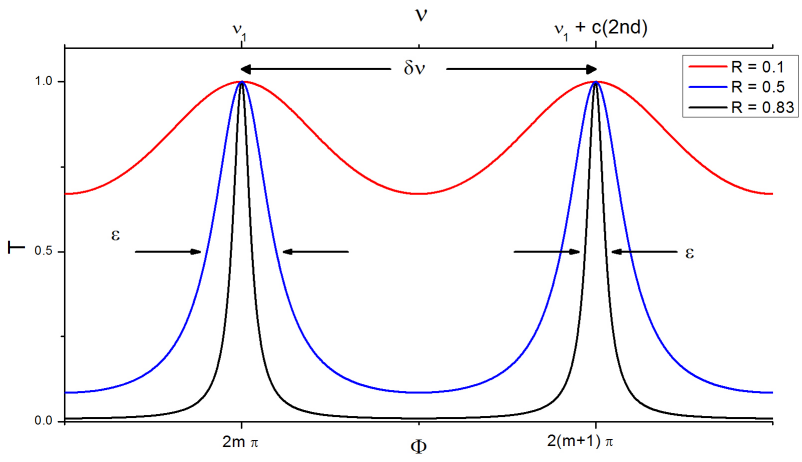

Figure 2.4: The cavity transmittance (equation (2.14)) for reflectivities of $\mathcal{R} = 0.1$, 0.5 and 0.83. At higher reflectivities (corresponding to higher Finesse), the FWHM ϵ becomes smaller and the individual cavity modes are much better separated (figure based on a similar figure from [74])

In CEAS, laser light is coupled into the cavity and the intensity of the light leaking out of the cavity is detected. The frequency of the laser should be in resonance with one of the cavity modes. Instead of following the decay of the light in the cavity in real time, the temporal integration of the total transmitted intensity, which depends on the attenuation of the light trapped within the cavity by an absorbing sample, is measured. Because of the continuous measurement, no rapid interruption of the laser is required. The largest challenge in this technique is to obtain a high efficiency of injection of the laser into the cavity. At higher finesse of an optical cavity, the transmission mode envelope of the cavity becomes narrower and the injection of the light into the cavity becomes more difficult.

Various implementations of CEAS exist, amongst which we want to mention Integrated Cavity Output Spectroscopy (ICOS) and Optical Feedback Cavity Enhanced Absorption Spectroscopy (OF-CEAS).

An implementation of ICOS is off-axis integrated cavity output spectroscopy (OA-ICOS) [4]. In this technique, the laser beam is aligned off-axis into a cavity with large astigmatic, dielectric mirrors (typically around 5 cm). Because of this alignment, the beam is launched into an intracavity trajectory folding onto itself only after a larger number of up to 100 round trips. Because of this, the laser beam has lost its coherence and possesses a random phase with respect to new incoming radiation, which results in zero average interference [71]. This results in a set-up with basically no resonances and the laser is not locked to the cavity modes [75]. In OA-ICOS, a large number of TEM_{mn} modes are excited and contribute to the detection of the absorbing gas. This renders the instrument quite insensitive to vibrations. In parallel to the gas cell, a portion of the laser light is guided to an etalon and reflected at the two surfaces. At each time the length of the etalon corresponds to a multiple of the laser wavelength, constructive interference occurs

and a photodiode measuring the etalon reflections records a maximum in the intensity. In this way, a frequency comb is generated and can be used to determine the tuning rate of the laser. A drawback of this technique is that due to the large number of reflections at the cavity mirrors, the transmission through the cavity is extremely reduced and a laser with relatively high output power and very sensitive detectors - often cooled to low temperatures - have to be employed. In addition, because of the relatively large mirrors, the sample volume is at least one order of magnitude larger than in CEAS techniques using on-axis cavity injection.

In the OF-CEAS technique, a portion of the light inside the cavity is sent back to the laser source and efficiently couples the laser frequency to one of the modes of the cavity. This technique is used for the instrument developed in this thesis and will be explained in more detail in section 2.5.

2.4 State-of-the-art

In recent years, several optical instruments based on the spectroscopic techniques described above, have been introduced for the measurement of water vapor isotope ratios.
A direct absorption spectrometer was introduced by Kerstel et al. [64] as early as 1999 (after a development phase that had started in 1995). It measured the isotopic composition of water using a Color Center Laser (or Farbe Center Laser, FCL) around 3662 cm^{-1} (2.73 µm) and at an effective path length of approx. 20 m in a spherical mirror Herriot MPC with a base-length of 43 cm. Their instrument was used for the determination of the isotopic composition of liquid water samples. A 10 µl water sample was introduced into an evacuated gas cell and measured in parallel to a reference cell containing an isotope standard. At partial pressures around 13 mbar, precisions of 0.7, 0.3 and 0.5‰ were reached for δ^2H, $\delta^{17}O$ and $\delta^{18}O$, respectively, for an average over 15 laser scans, corresponding to approx. 30 min total measurement time.
Webster et al. [5, 76] reported measurements of the water isotopic composition in the upper troposphere lower stratosphere (UTLS) with a TDL spectrometer called ALIAS, which is equipped with an MPC and a quantum cascade laser (QCL) emitting at 6.7 µm. At water concentrations around 80 ppmv, they report uncertainties for the delta values of approximately 50‰ over a pressure range of 75 - 300 mbar.
A TDLAS using a LN2-cooled lead-salt laser, commercialized by Campbell Scientific Inc., was used by Lee and co-workers [65, 66], to measure atmospheric water vapor isotopologues at 6.7 µm with a precision of 2‰ for δ^2H and 0.12‰ for $\delta^{18}O$, with 1 h averages at 5600 ppmv, and 1.1‰ and 0.07‰ at 15,000 ppmv for δ^2H and $\delta^{18}O$ respectively.
More recently, an MPC equipped direct absorption spectrometer, measuring at 2.66µm was described by Dyroff et al. [7]. This instrument uses 2f wavelength modulation and on-board calibration to two isotope standards to arrive at an accuracy of 2‰ for δ^2H and $\delta^{18}O$ at a water concentration of 600 ppmv. At 100ppmv, a detection limit of 4.5‰ and 1.2‰ for δ^2H and $\delta^{18}O$,

respectively was reported for 60s averaging.
An instrument based on a QCL-equipped OA-ICOS was described by Sayres et al. and successfully employed for isotope measurements in the upper troposphere and lower stratosphere [10]. Their instrument achieved a precision of 0.14 ppmv for the H_2O concentration, whereas at a water concentration of 5 ppmv a precision of 50‰ and 30‰ for δ^2H and $\delta^{18}O$, respectively, was demonstrated.
OA-ICOS is also used in the commercial instruments of Los Gatos Research (LGR). The LGR instruments first became commercially available in 2006. Newer versions of the instrument have been presented and discussed by different research groups [48, 77, 78]. Aemisegger et al. [78] report a precision of 0.02‰ with 7 min averaging for δ^2H and of 0.01‰ for $\delta^{18}O$ with 30 min averaging with a later version of the Water Vapor Isotope Analyzer (WVIA-EP) at water concentrations around 15,700 ppmv. For measurements including $\delta^{17}O$, Berman et al. [48] state for the Triple Isotope Water Analyzer (TIWA-45EP) a combined precision and accuracy of 0.07‰ and 0.03‰ for $\delta^{18}O$ and $\delta^{17}O$, respectively, in a water concentration range of $2 - 4.5 \times 10^{16}$ molecules/cm^3 (17,500 to 40,000 ppmv), for measurements averaged over four separate injections of liquid water samples.
A particularity of the Picarro WS-CRDS spectrometer is that it uses a three-mirror ring cavity. The calibration of the frequency scale requires the use of a custom made wavelength monitor [79]. For one of the later versions of the Picarro instruments, the L2130-i, Aemisegger et al. [78] report at 15,700 ppmv a precision of 0.02‰ with 170 min averaging for δ^2H and 0.006‰ with 100 min averaging for $\delta^{18}O$. With 5 s averaging, the reported precision is 0.83‰ and 0.22‰ for δ^2H and $\delta^{18}O$, respectively.
More recently, Steig et al. [49] presented a modification of the Picarro instrument (model L2140-i), which was specifically designed to measure $\Delta^{17}O$ with high precision. It uses two lasers to measure $\delta^{18}O$ and $\delta^{17}O$ at 7193 cm^{-1} and reaches precisions of 0.015‰ for both $\delta^{18}O$ and $\delta^{17}O$ and of 0.01‰ for $\Delta^{17}O$, with 1200 s averaging at water concentrations around 20,000 ppmv.
Although several of the above described techniques demonstrate very good performance with high stability and precision, none of the instruments, with the exception of the Harvard ICOS [10] and the ALIAS instrument [5], is well adapted to measure water isotopologues with sufficiently high precision under very dry conditions with $H_2O < 1000$ ppmv. Because of a large volume (around 1m^3) and large mass, the Harvard ICOS is, however, not particularly well-suited for wider spread use.

In order to be able to measure under very dry conditions, one could decrease the noise level, which is for example done in modulation techniques such as noise immune cavity enhanced optical heterodyne molecular spectroscopy (NICE-OHMS), which was most profitably used in Lamb-Dip experiments [80]. However, this technique is very complex and not suitable for Doppler-limited spectroscopy.
Another possibility would be to use stronger ro-vibrational transitions, which can be found in

the mid-infrared region at 2.7 µm and 6.7 µm. This is done in the Harvard ICOS instrument [10], the ALIAS instrument [76] and as well in the ISOCLOUD in-situ isotope instruments (see chapter 8). In the case of H_2O, the gain is approximately one order of magnitude, and is offset by less sensitive MIR detectors and mirrors with lower reflectivity, resulting in higher noise level and/or shorter effective path lengths.
Finally, a viable alternative solution is to increase the effective absorption path length, which can be achieved by the use of higher reflectivity coatings on the cavity mirrors of a CRDS or CEAS system.

2.5 Optical feedback cavity enhanced absorption spectroscopy (OF-CEAS)

Most of the previously described cavity enhanced absorption spectroscopy techniques suffer from inefficient and noisy cavity injection due to changes in the laser frequency and linewidth, which is in general much larger than the width of a single cavity mode. As mentioned above, this becomes a major problem when using very high finesse cavities, in which the coupling is even more difficult because of the correspondingly narrower cavity mode width.
In the case of OF-CEAS, a portion of the light (optical feedback) travelling inside the cavity is send back to the laser source, which results in a coupling of the laser to one of the cavity modes, which in turn leads to a narrowing of the laser line width to below that of the cavity mode transmission [81].

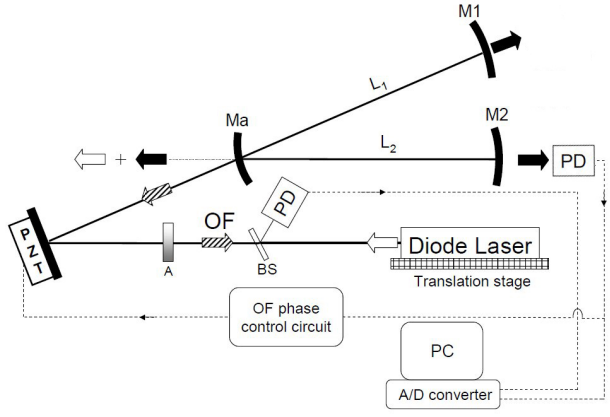

Figure 2.5: Schematics of a typical OF-CEAS set-up with a V-shaped cavity (figure from [82]

A schematic of a typical OF-CEAS set-up with a V-shaped cavity is shown in figure 2.5. The light from a diode laser is injected into a V-shaped cavity via a set of different optical components. The V-shape of the cavity efficiently avoids that a direct reflection from the folding

mirror at the apex of the cavity (labeled M_a) is sent back to the laser and ensures that only light reflected at mirror M_1 inside the cavity returns as optical feedback (OF) to the laser. A photodetector (PD) with a beamsplitter (BS) is used to monitor the injected laser intensity, whereas a signal detector behind the cavity measures the cavity output. An attenuator (A), e.g. a linear polarizer, between the cavity and the laser is used to adjust the level of feedback to the laser.

As the laser is scanned over a frequency range, it is slowed down due to the optical feedback and stays longer at the successive cavity frequencies (cf. figure 2.6). At higher feedback levels, the laser couples stronger to the cavity frequencies and the resident time for each frequency is extended.

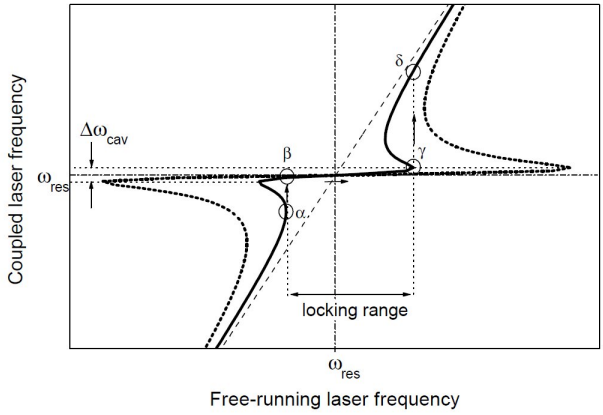

Figure 2.6: Figure from [82]. Frequency of the diode laser coupled by optical feedback to the V-shaped cavity, as a function of free running laser frequency, during the passage through a cavity mode for two different levels of feedback (solid and dotted lines for weak and strong feedback levels, respectively). The linear dashed line indicates the free running laser frequency, which is directly proportional to the laser current. Arrows in the plot indicate the path of the coupled laser frequency ($\alpha \rightarrow \beta \rightarrow \gamma \rightarrow \delta$ when the laser current is tuned and emphasize the longer residence time at the respective cavity frequency

The distance between the laser and the cavity equals L_2, the length of the second cavity arm. This ensures that constructive interference inside the laser cavity is obtained for all cavity modes, as the distance corresponds to an integer multiple of one-half the wavelength irrespective of the exact wavelength value (a detailed derivation can be found in [81]). To compensate for instabilities in the laser-cavity distance and cavity length due to temperature and mechanical variations or disturbances, a mirror between laser and cavity is mounted on a piezo element, controlled by a feedback loop. The error signal for the feedback loop is obtained by analysis of the symmetry of the transmission profiles of the cavity modes.
For the configuration described here above and used in our spectrometer, in which the laser to cavity distance equals L_2, modes for which the cavity round trip is an even or odd multiple of one-half of the wavelength (from now on simply called even and odd modes), experience a

slightly different reflection coefficient at the folding mirror, which results in a small difference in the ring-down time associated with the odd and even modes [81, 82]. However, this difference can easily be corrected for in the data analysis, as the difference remains constant over the small tuning range of the laser wavelength.

An OF-CEAS spectrum is finally recorded by determining the maxima of successive $TEM_{0,0}$ cavity mode profiles in the raw OF-CEAS signal (cf. figure 2.7) and normalizing them with the signal of the reference detector. At the end of each laser scan, the laser is interrupted for a little more than the duration of one cavity mode to measure a ring-down on one cavity mode. These RD measurements are used to calibrate the transmission signal and to convert the spectra to absorption units, based on the (approximated) relation:

$$\frac{\sqrt{H_k}}{\tau_k} = \frac{\sqrt{H_m}}{\tau_m} \tag{2.19}$$

with the cavity modes k and m, τ_k the ring-down time of mode k, and H_k the measured intensity ratio at mode k. A derivation of this relation can be found in [81]. This approximation is very good under typical CEAS conditions, and even in the limit of relatively strong absorption. In

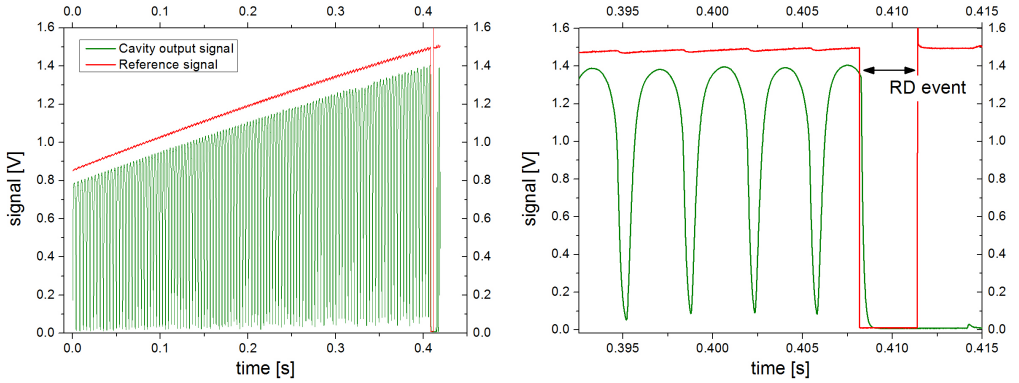

Figure 2.7: Exemplary OF-CEAS signal, a) signal over the entire laser scan b) at the end of each scan the laser is interrupted to record a RD event to convert the recorded spectra to absorption scale

table 2.1, the most important characteristic dimensions like the FSR and Finesse are compared for a linear cavity and a V-shaped cavity.

	Linear Cavity	V-shaped cavity
FSR	$c/(2L)$	$c/2(L_1+L_2)$
ring-down time empty cavity	$\tau_0 = \frac{L/c}{1-\mathcal{R}}$	$\tau_0 = \frac{L_1+L_2}{2c(1-\mathcal{R})}$
ring-down time with absorber	$\tau = \frac{-L/c}{1-\mathcal{R}+\alpha L}$	$\tau = \frac{L_1+L_2}{2c(1-\mathcal{R}+\alpha(L_1+L_2))}$
Finesse	$\frac{\pi\mathcal{R}}{1-\sqrt{\mathcal{R}}}$	$\frac{\pi\mathcal{R}}{1-\mathcal{R}^2}$
max. transmission for lossless cavity	$\approx \frac{1}{(1+\frac{\mathcal{L}}{\mathcal{T}})^2}$	$\approx \frac{1}{4}\frac{1}{(1+\frac{\mathcal{L}}{\mathcal{T}})^2}$
$H(\alpha \to 0, \mathcal{L}+\mathcal{T} \ll 1)$		

Table 2.1: FSR, ring-down time, Finesse and maximal transmission for linear and V-shaped cavity as a function of reflectivity $\mathcal{R}$, transmittance $\mathcal{T}$, and the length of the cavity arm(s) L (linear cavity), and L_1 and L_2 (V-shaped cavity), respectively. c is the speed of light.

2.6 Absorption scale linearity

As mentioned above, in direct absorption techniques, the molecular absorption coefficient α is obtained in a very straightforward manner from the Lambert-Beer-Bouguer law:

$$\alpha = -\frac{1}{l}\ln\left(\frac{I_t}{I_0}\right)$$

with I_t the transmitted intensity, I_0 the incoming light intensity and l the effective path length. In the case of OF-CEAS, the relation between molecular absorption and intensity is more complicated. As described in detail in [6, 81] and briefly summarized in the following, the relation between α and the transmitted intensity in OF-CEAS allows the measurement of isotope ratios over a much larger concentration range than in direct absorption spectroscopy.
In the case of a V-shaped cavity with cavity arm lengths l_1 and l_2, filled with an absorber with absorption coefficient $\alpha_m = \alpha(\omega_m)$ at the center of a cavity mode, the cavity transmission is described with an Airy-shaped transfer function whose maximum at frequency ω_m is given by [82]:

$$H_{max}(\alpha_m) = \left[\frac{\mathcal{T}\exp(-\alpha_m l_1/2)}{1-\mathcal{R}^2\exp(-\alpha_m(l_1+l_2))}\right]^2 \tag{2.20}$$

The effective mirror transmission and reflectivity coefficients $\mathcal{T}$ and $\mathcal{R}$ are $\mathcal{T} = (\mathcal{T}_a\mathcal{T}_1)^{1/2}$ and $\mathcal{R} = (\mathcal{R}_a)^{1/2}(\mathcal{R}_1\mathcal{R}_2)^{1/4}$ with the subscript a indicating the folding (apex) mirror and 1 and 2 the mirrors at the end of the two cavity arms (the transmitted intensity is calculated for mirror 1).

In general, all three mirrors are from the same batch and are virtually identical. As the angle between the two cavity arms is very small, the reflectivity is practically the same as for normal incidence and the reflection and transmission coefficients can be considered equal for the three mirrors.
Equation 2.20 is valid for cavity injections by a perfectly monochromatic field slowly passing through resonance. This is generally true in the case of OF-CEAS, as the laser tuning is sufficiently slow to assure full cavity buildup during frequency locking by optical feedback, which also results in a laser line width narrowing to well below the cavity mode width.
Because of conservation of energy, the effective mirror losses due to absorption and scattering are given by $\mathcal{L} = 1 - \mathcal{R} - \mathcal{T}$. With this, it is easy to show with equation 2.20 that the maximum transmission for a completely lossless cavity ($\alpha = 0$ and $\mathcal{L} = 0$) reaches 25%:

$$H(\alpha \leftarrow 0,\, \mathcal{L} + \mathcal{T} \ll 1) \approx \frac{1}{4} \frac{1}{(1 + \frac{\mathcal{L}}{\mathcal{T}})^2} \tag{2.21}$$

Equation 2.20 is derived by squaring the sum of the amplitudes of the field transmitted through the mirror at the end of one cavity arm and not by summing the square of the amplitudes [82]. The summation of the intensities would not account for the resonance effect in OF-CEAS and is only valid in the case of a broadband incoherent source. This would result in substantially lower transmission of only $\mathcal{T}/4$.
If we approximate $\exp(-\alpha_m l_1) \approx 1$ in the numerator, it is possible to invert equation 2.20, following the derivation presented in [6] and [81]:

$$\alpha_m = \frac{1}{l_1 + l_2} \left[2\ln(\mathcal{R}) - \ln\left(1 - \frac{\mathcal{T}}{\sqrt{H_{max}}}\right)\right] \tag{2.22}$$

We further make the assumption $\mathcal{T}/\sqrt{H_{max}} \ll 1$, which is in general true as $\mathcal{T}$ is typically smaller than 100 ppm and very large absorptions are avoided, such that $H_{max} > 1\%$. With this, we can write

$$\alpha_k \approx \frac{2}{l_1 + l_2} \ln(\mathcal{R}) + \frac{\mathcal{T}}{(l_1 + l_2)\sqrt{H_{max}(k)}} \tag{2.23}$$

If we write $\ln(\mathcal{R}) \approx 1 - \mathcal{R} = \mathcal{T} + \mathcal{L}$, it becomes evident that the first term on the right hand of equation (2.23) is $-\gamma_0$, the loss per unit length for the empty cavity. We can than write:

$$\frac{\gamma_k}{c} = \alpha_k - \frac{2}{l_1 + l_2} \ln(\mathcal{R}) = \alpha_k + \frac{\gamma_0}{c} \approx \frac{\mathcal{T}}{(l_1 + l_2)\sqrt{H_{max}(k)}} \tag{2.24}$$

The total loss coefficient γ_k can be determined experimentally by fitting $\exp(-\gamma_k t)$ to a ring-down event, which can be produced by an abrupt interruption of the laser once the maximum injection for mode k has been reached. The CEAS spectrum can then be obtained in absolute absorption units, apart from an offset due to the empty cavity losses (γ_0), by calculating

$1/\sqrt{H_{max}(m)}$ for all modes m and then multiplying by the factor $(\gamma_k/c)\sqrt{H_{max}(k)}$ determined by the ring-down measurement at mode k. It should be underlined that the absorption-scale calibration procedure can also be performed in the presence of intracavity absorption. The calibration of CEAS measurements in absolute absorption units does not require a measurement of the ring-down time for an empty cavity. An investigation of the accuracy of the normalization is discussed in detail in [81].

For a typical OF-CEAS cavity with ring-down time of 20 µs, the relative error due to the normalization procedure is smaller than 100 ppm for cavity transmissions larger than 10% of the maximum value ($H > 0.1$). This would correspond to an absorption coefficient of 4×10^{-6}/cm or, considering a typical noise level of 4×10^{-10}/cm, to a dynamic range of four decades. For a higher finesse cavity such as the one used in our spectrometer, the accuracy of the normalization is even better. For cavity transmissions larger than 5%, the relative error for a cavity with ring-down times of 130 µs would be smaller than 50 ppm.

Chapter 3

OCEAS instrument design

In this chapter, the OF-CEAS laser spectrometer, SIRI (Spectromètre Infrarouge des Rapports Isotopiques), developed within the framework of this thesis, is described. A first OF-CEAS spectrometer for water vapor isotope measurements was introduced by Kerstel et al. in 2006 [6], an improved version was described by Iannone et al. in 2009 [83]. With the novel spectrometer SIRI, we specifically aimed for an instrument able to measure water vapor isotopes in very dry conditions with water concentrations well below 500 ppmv as encountered in Antarctica and the upper atmosphere. This requires an instrument with much higher sensitivity and stability and could be achieved with the design detailed in the following. In addition, we refer to our publication in Optics Letters [84], which can be found in appendix C. Please note that for the purpose of the Optics Letter publication, the instrument developed in this work and referred to as SIRI throughout this entire thesis was named HiFi (for High Finesse Spectrometer) to offer a more international name.

3.1 Optical Layout

The laser source used in the laser spectrometer SIRI is, as in the predecessor IRIS, a distributed feedback (DFB) diode laser (obtained from either LaserComponents or Nanoplus) with a typical maximal output power of 10mW. For the different spectral regions (discussed in detail in section 3.6), various lasers were used.

The cavity mirrors (from Layertec GmbH) have a radius of 1 m and a wedge of 1°. With an empty cavity, these mirrors yield a ring-down time of 150 µs (at 7184 cm^{-1}, which is more than a factor seven higher than in previous instruments and requires an even more precise alignment of the optical set-up. The ring-down time corresponds to a reflectivity of 99.9989% (1-R=11 ppm) and leads to a cavity with a finesse of approx. 144,000 (a standard linear cavity of the same external length using the same mirrors would have $\mathcal{F} \approx 288,000$). This high finesse results in an effective path length of nearly 45 km and is necessary to be sensitive enough to measure at very low water concentrations.

Instead of using very high reflectivity mirrors, it would have been possible to change from the near-infrared into the mid-infrared (MIR) at 2.7 µm, which would have resulted in transitions that are approx. a factor 10 stronger. However, apart from the currently still lower reflectivities

of mirrors for the MIR, this would also have required the use of less sensitive photodetectors. The gain of stronger transitions would thus have been canceled out or even overcompensated by these disadvantages.
In our instrument, the photodetectors are InGaAs detectors (Hamamatsu) wired in the back of the detector, which reduces the risk of optical fringes induced by parasitic reflections on the wires.
To correct the measurements for water absorption occurring outside of the gas cell, the path lengths outside the cavity for reference and signal photodiode were matched. This becomes especially important when the sample measured in the gas cell is much drier than the ambient air.

3.2 Mechanical layout

The instrument is mounted in a thermally insulated aluminum casing, which has a volume of approx. 45 l and a weight of 25 kg and is thus easily transportable. The core of the spectrometer is an additionally insulated triangular base mounted on four metallic springs on which the optical set-up is installed. The V-shaped cavity consists of two arms of 50 cm under an angle of 0.94°. Other than previous versions, the gas cell is other than in previous versions now machined from a single stainless steel bloc, which reduces the risk of leaks.

3.3 Flow system

An important factor influencing the response time of an instrument, is the so-called memory effect. Due to for example adsorption of water to the walls of tubing and cavity of the instrument or small dead volumes that are not efficiently exchanged with new gas, the time response of an optical spectrometer can sometimes be in the order of several minutes.
To reduce the memory of our system, the electropolished stainless steel of the gas cell is now additionally coated with a fluoroaliphatic polymer (Cytonix FluoroPel 800A).
Because of the very low water concentrations, special attention was paid to the gas inlet system to reduce memory effects. All inlet tubing is coated O'Brian tubing, and a Siltek treated inlet filter (Restek) is used to protect the system against contamination from larger particles. The pressure is regulated to 35 mbar by a Siltek treated pressure controller (Bronkhorst) at a flow rate of approx. 150 sccm. The gas cell has channels with a diameter of 5 mm, which results in a volume of 18.6 ccm and therefore in a gas exchange time of only 0.18 s.
During in field deployment of the instrument, additional O'Brien tubing is used for the inlet and is temperature stabilized to approximately 50°C with an auto-regulating heating band (Horst).

3.4 Data acquisition and storage

The entire instrument is controlled by a C program on a ARM9-based micro-controller (ATMEL), which is also used for the data acquisition in combination with a analog/digital converter. Communication with the ARM9 is established via an Ethernet connection with a Labview (National Instruments) based program, which is also used to control the instrument. Data analysis is done on-line with the same Labview program in combination with a C based analysis program incorporating the Minuit library of CERN [85]. The signal of the two photodiodes is digitized by a 16 bit A/D converter with 60 000 points per channel. Due to the high ring-down times, which result in very long residence times for each single mode in the cavity, a scanning frequency of 1.96 spectra per second was chosen, corresponding to approximately 3.5 ms per single mode. The scanning frequency is thus a factor three smaller than in the predecessor IRIS. However, instead of one ring-down event per second, the laser is now interrupted for approximately 3.5 ms (400 data points) at the end of each scan. Housekeeping data such as cavity temperature and pressure are recorded with 12 bit and averaged over 10 consecutive acquisitions before being written to file.

3.5 System control and house keeping

A large improvement has been made in the temperature stability of the system compared to previous versions. Whereas IRIS was stabilized to 35.5 ± 0.5°C by an on/off regulation, the temperature of the instrument is now regulated in a two step system to 45°C with mK-precision and a drift of less than 0.5 mK over 200 min (see figure 3.1).. The air temperature in the entire instrument is regulated to 38 ± 0.1 °C with a PID regulated TEC (Supercool) in combination with two mixing fans. Furthermore, the temperature of the optical triangle is stabilized at 45 °C with additional heating bands , which are regulated with a PID loop via a pulse width modulation (PWM). The temperature sensor used for the regulation is a very low drift Pt1000, which is read out with 16 bit resolution.
To avoid additional electronic heat in the insulated box due to the power supply, the instrument is powered by a commercially available 220W single output desktop power supply. Because of two additional Pt1000 temperature sensors that are freely suspended in the inlet and outlet stream of the cavity, it is also possible to correct measurements for fluctuations of the gas temperature. This becomes especially important if atmospheric measurements with large variations of the air temperature (e.g. day-night cycle) shall be done. Due to the different temperature dependency of the single absorption lines, this can become crucial when isotope ratios should be determined with high accuracy. The pressure in the cavity is stable within the microbar level (better than 10 µbar) for several hours (cf. figure 3.1b).

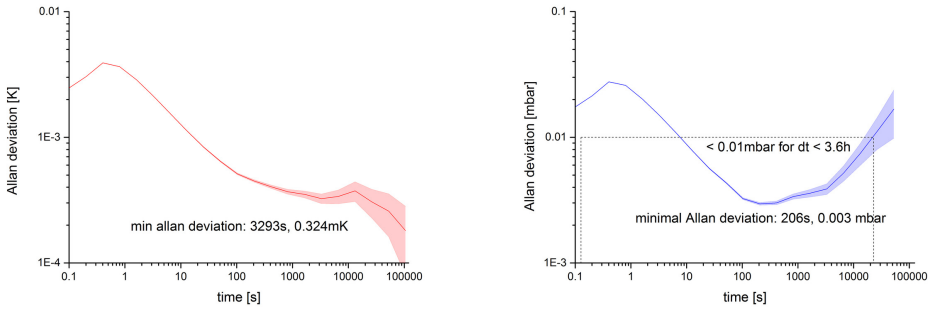

(a) (b)

Figure 3.1: Allan variances of temperature and pressure in the instrument. The sensors used for the Allan variances are independent sensors and not used for the regulation. The stability of the cell temperature is better than 1 mK, the maximum at 1 s is due to the read-out of the sensor. The pressure is regulated with a precision of better than 10 µbar over a time of 3.6 h

3.6 Choice of spectral ranges

Depending on the specific requirements of the measurements, different spectral regions in the near infra-red were selected for the measurements. For most of the measurements, a spectral region around 7184 cm^{-1} was chosen that was also used in previous instruments [6, 83] and is also used by commercial instruments [78, 86]. As can be seen in an exemplary spectra in this region (figure 3.2), this region is suited for measurements of all of the four isotopologues $H_2{}^{16}O$, HD ^{16}O, H_2 ^{18}O and H_2 ^{17}O. Because of a relatively large number of additional weak absorption

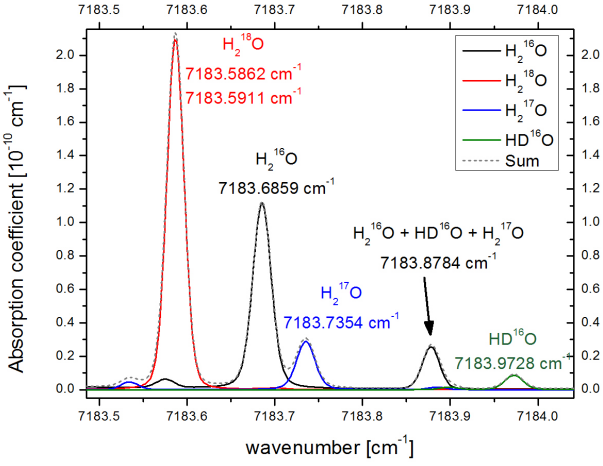

Figure 3.2: Simulated spectrum at 7184cm^{-1}, 1 ppmv H_2 ^{16}O, spectral information from the Hitran database [61]

lines and several methane absorption lines in this spectral region, the analysis of the spectral data is more difficult than in other spectral regions.
An alternative, for measurements in which $H_2\,^{17}O$ is of no or little interest, is the spectral region around 7200 cm^{-1} in which the absorption lines of the three isotopologues $H_2^{16}O$, $HD\,^{16}O$ and $H_2\,^{18}O$ are better separated (figure 3.3). This region, which we used for some of our measurements, is also the region of choice of the most common version of the instruments of Los Gatos Research Inc. [78]. For measurements at very low water concentrations ($<$ 40 ppmv),

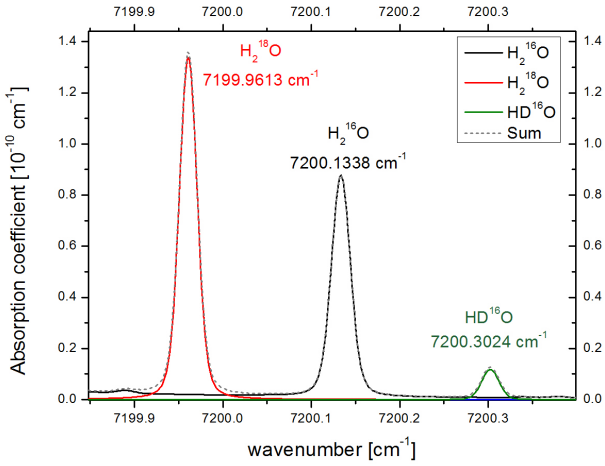

Figure 3.3: Simulation of a spectrum at 7200cm^{-1} and 1 ppmv $H_2\,^{16}O$; spectral information from the Hitran database [61]

we chose an alternative spectral region around 7286 cm^{-1} (cf. figure 3.5), which includes an $H_2\,^{18}O$ absorption line that is nearly a factor 4 stronger and an $H_2^{16}O$ line that is more than a factor 50 stronger than in the above mentioned regions. In addition, the region around 7286 cm^{-1} enables the measurement of δ^2H with spectral lines of $H_2\,^{16}O$ and $HD\,^{16}O$ at 7280 cm^{-1}. With the available laser (Nanoplus GmbH), the two region could be reached by selecting the appropriate temperature of the laser chip. In table 3.1, the wavenumber, intensity and temperature dependence of the line strength for the principal absorption lines [61] is shown for the different spectral regions used in our measurements. For the spectral region around 7286 cm^{-1}, the change of the wavelength region additionally results in an increase of the ring-down time of the instrument due to a higher reflectivity of the cavity mirrors (cf. figure 3.4). With ring-down times of up to 180 µs, this configuration results in a significantly increased sensitivity in the low water vapor concentration range (see chapter 8).
This spectral range was not used in our instrument but we adapted a different OF-CEAS spectrometer that was initially built in our laboratory by J. Habig of the Karlsruhe Institute of Technology [87].

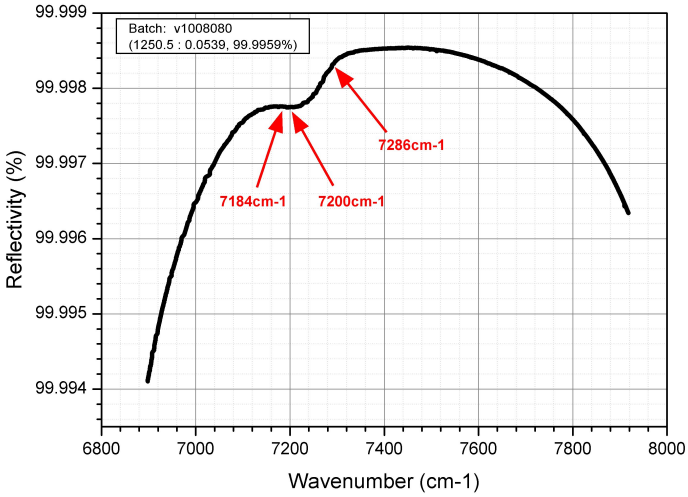

Figure 3.4: The reflectivity of our cavity mirrors vs. the wavenumber (measurements by S. Kassi, LIPhy, UJF). The reflectivity is higher for the region 7286 cm^{-1} proposed for measurements of $\delta^{18}O$ at very low water concentrations compared to the spectral regions used before.

isotopologue	wavenumber $[cm^{-1}]$	intensity $[cm^{-1}/(molecule \times cm^{-2})]$	temperature dependence %/°C
$H_2\ ^{16}O$	7183.6858	3.67×10^{-24}	0.0593
$H_2\ ^{18}O$	7183.5892	4.54×10^{-24}	0.133
$H_2\ ^{17}O$	7183.7355	1.16×10^{-24}	-0.688
$HD\ ^{16}O$	7183.9728	3.385×10^{-25}	-0.609
$H_2\ ^{16}O$	7200.1338	3.268×10^{-24}	-0.398
$H_2\ ^{18}O$	7199.9613	4.434×10^{-24}	-0.0365
$HD\ ^{16}O$	7200.3024	3.514×10^{-25}	-0.155
$H_2\ ^{16}O$	7286.0508	2.049×10^{-22}	-0.244
$H_2\ ^{18}O$	7285.7703	3.442×10^{-23}	-0.709
$H_2\ ^{16}O$	7280.4842	2.735×10^{-23}	-0.103
$HD\ ^{16}O$	7280.5569	7.383×10^{-25}	-0.787

Table 3.1: Principal absorption lines in the investigated spectral regions [61]

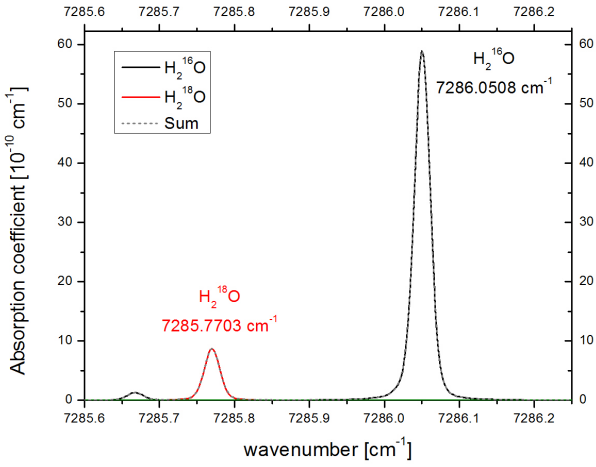

(a)

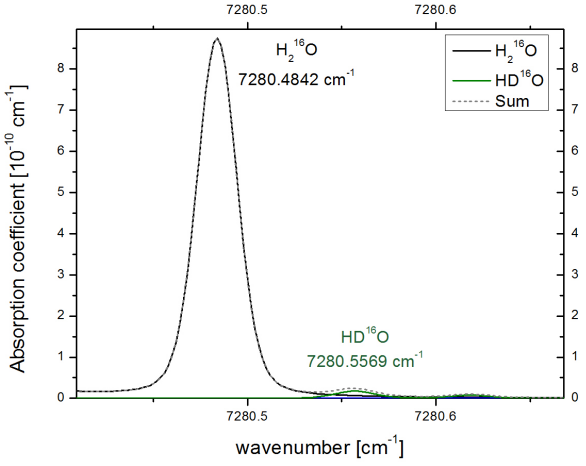

(b)

Figure 3.5: Simulation of spectra at a) 7286 cm^{-1} and b) 7280 cm^{-1}, respectively. Spectral information from the Hitran database [61].

Chapter 4

Data analysis procedures

To retrieve concentrations and isotope ratios from a measurement, a theoretical model is generally fit to the experimental spectra. For the synthetic spectra, different models can be used, that take different factors responsible for line broadening into account.
If the pressure of the gas sample is very low ($p \leq 0.5$ mbar), the line width of the spectral lines is dominated by the Doppler line width. It takes into account the effect that the frequency at which a molecule with a velocity component along the trajectory of the light beam absorbs and emits electromagnetic radiation is slightly shifted. As the velocity of the molecules in a gas is due to thermal motion, this change in the absorption frequency leads to a Gaussian line shape [88]:

$$I(\nu) = I_0 \exp\left[-\left(\frac{2\ln(2)(\nu-\nu_0)}{\gamma_D}\right)\right] \tag{4.1}$$

with γ_D the FWHM of the Gaussian function:

$$\gamma_D = \frac{\nu_0}{c}(8k_B T \ln(2)/m)^{1/2} \tag{4.2}$$

with ν_0 the center frequency of the absorption in Hz, c the speed of light, k_B Boltzmann's constant, T the temperature in Kelvin and m the mass of the molecule in kg.
At higher pressures, the collision between molecules in the gas can lead to a reduction of the lifetime of the molecule's upper energy state, which according to Heisenberg's uncertainty principle leads to an increased linewidth. The line shape in this case is described by a Lorentzian function [89]:

$$I(\nu) = I_0 \frac{2\pi\gamma_C}{(\nu-\nu_0)^2 + (\pi\gamma_C)^2} \tag{4.3}$$

$$\tag{4.4}$$

with γ_C the FWHM of the Lorentz function. At higher pressures ($p \geq 1000$ mbar), the collisional broadening is the dominant mechanism and the profile can be described relatively well by a purely Lorentzian line shape [90]. At intermediate pressure (0.5 mbar $\leq$ p $\leq$ 1000 mbar), the line shape is often approximated with the Voigt profile, which is a convolution of a Gaussian

and a Lorentzian profile. The normalized Voigt profile can be written as [91]:

$$\Gamma_V(\nu) = \frac{\gamma_C}{\pi^{3/2}\gamma_D^2} \int_{-\infty}^{+\infty} \frac{e^{-y^2}}{\left(\frac{\nu-\nu_0}{\gamma_D} - y\right)^2 + \left(\frac{\gamma_C}{\gamma_D}\right)^2} dy \tag{4.5}$$

and has in a first approximation a FWHM γ_V of [92]:

$$\gamma_V \approx 0.5346\gamma_C + \sqrt{0.2166\gamma_C^2 + \gamma_D^2} \tag{4.6}$$

However, the Voigt profile is only an approximation, as it does not take into account further mechanisms that influence the line shape of a spectral lines. In reality, the Doppler profile of the spectral lines is narrowed because of collisions between the active molecules and molecules in the buffer gas, which result in a reduced free path length (to below the wavelength of the infrared radiation) and consequently in a smaller velocity of the molecules.
Two different models have been developed to take this narrowing, the so-called Dicke effect, into account. The Rautian and Sobel'man model (in the following Rautian profile)[93] and the model of Galatry (Galatry profile)[94]. These two models take into account the Doppler broadening, the Dicke narrowing and the collisional broadening. Whereas the Galatry model assumes that the mass of the active molecule is much heavier than the mass of the molecules of the carrier gas (and consequently many collisions are required to induce a notable velocity change), the model of Rautian and Sobel'man supposes the contrary, namely that the perturber is much heavier than the active molecule (and a single collision suffices) [90, 93, 94].
As in our case, the active molecule is in general lighter than the carrier gas molecules, we will focus here on the Rautian profile. This profile can be expressed as [90]:

$$\gamma_R(\gamma_D, \gamma_C, z) = \frac{1}{\gamma_D\sqrt{\pi}} \Re\left[\frac{W(\gamma_D, \gamma_C + z)}{1 - \sqrt{\pi} z W(\gamma_D, \gamma_C + z)}\right] \tag{4.7}$$

with

$$W(\gamma_D, \gamma_C, z) = \frac{i}{\pi} \int_{-\infty}^{\infty} \frac{e^{-t^2}}{(\frac{\nu-\nu_0}{\gamma_D} + i(\frac{\gamma_C}{\gamma_D} + z) - \frac{t}{\sqrt{\ln(2)}})} dt \tag{4.8}$$

and the narrowing parameter z:

$$z = \frac{\beta_C}{\gamma_D} \tag{4.9}$$

with β_C the coefficient of collisional narrowing (given in cm^{-1}).

4.1 Analysis of experimental spectra

For the analysis of our experimental spectra, a simulated spectrum based on the Rautian line profile is fit to the experimental data. The line positions of the different absorption lines were taken from determinations with high sensitivity CW-Cavity Ring Down Spectroscopy done by Leshchishina et al. [95] and the frequency scale of the measured spectrum was scaled linearly to match this theoretical spectrum, effectively determining the FSR of our OF-CEAS cavity. The Gaussian line widths (Doppler broadening) were calculated for the different isotopologues based on the gas cell temperature and then fixed for all spectra. Lorentzian widths (pressure broadening) and the Dicke parameters (motional narrowing) were fit once over an exemplary measurement and kept constant throughout the measurements. The relative intensities of different absorption lines from the same isotopologue were fixed, thus yielding only one free parameter for intensity per isotopologue. Note that of different temperature dependencies of the strengths of different absorption lines, this grouping should only be done with a very good temperature stabilization, which is present in our spectrometer. In addition to the group intensities for each isotopologue, an additional parameter accounts for a possible mode shift of the entire spectra, which can occur due to small temperature fluctuations of the gas or gas cell temperature. To take into account additional absorption lines of methane in the same spectral region, these lines were introduced as an additional species in the model spectrum, with an additional fitted group intensity parameter. The absorption frequencies of methane were taken from measurements of Campargue et al. [96], whereas we determined the relative intensities and Lorentzian line widths of the strongest methane absorption lines in a measurement on a diluted methane sample. The methane absorption does not play an important role for higher water concentrations but becomes an important factor at lower water concentrations (500 ppmv and below). The baseline is fit with neighboring strong water absorption lines outside the measurement range, and an additional third order polynomial.
The quality of the fit, and consequentially an important factor of the instrumental performance, is determined by the residual on the fit. Throughout the water concentration range, in which we can measure with SIRI, the RMS of the residual on the fit is below 8×10^{-11} cm^{-1} (at 2 Hz measurements). At water concentrations below 500 ppmv, the NEAS of the instrument is typically around 6×10^{-11} cm^{-1}Hz$^{-1/2}$, which is an improvement by a factor of almost 7 compared to the predecessor instrument IRIS.

4.2 Precision

In the case of an absolutely stable system, the precision of the measurements would continuously improve with increasing integration time. However, in the real world instrument stability is limited, for example because of temperature or pressure drift or mechanical disturbances.

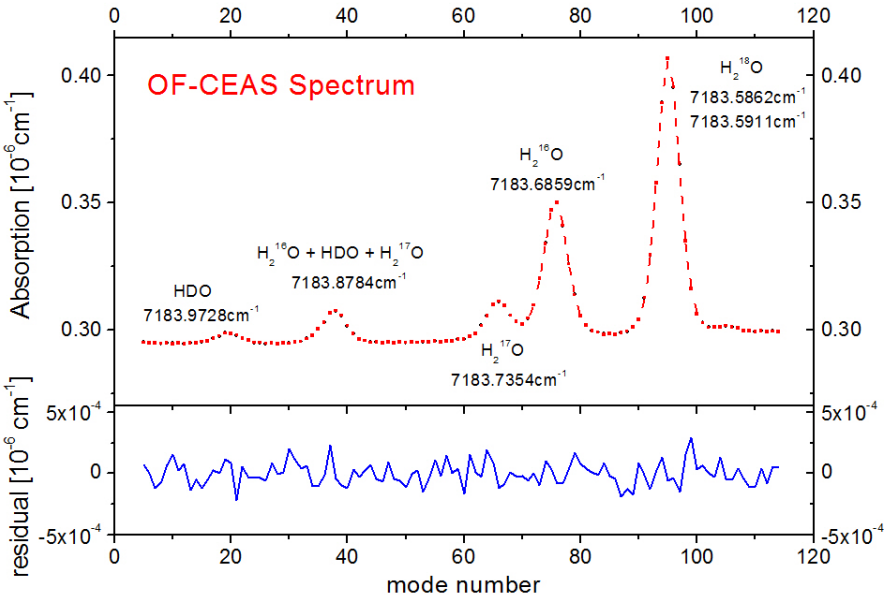

Figure 4.1: A single experimental spectrum, recorded in 0.51 s at 500 ppmv H_2O. The RMS of the residual (bottom panel), is 8×10^{-11} cm^{-1}

Because of these drifts, longer averaging is only beneficial up to the level where instrumental drift becomes noticeable.

The optimum integration time can be effectively determined with an Allan-Werle-plot. The Allan-Werle-plot was first introduced to the field of laser-based trace gas detection to reveal low frequency drift phenomena [97] and later adapted to characterize instrumental stability [98]. To determine the stability of SIRI and its level of precision, long time measurements at different water concentrations were made. A gas bottle was filled with a mixture of dry synthetic air and a calculated amount of a local water standard to a given water concentration. This standard gas bottle was then connected to the OF-CEAS instrument for long time ($>$ 8h) stability measurements. This measurement was repeated with different water concentrations in the range from 20 ppmv to 1500 ppmv. Measurements with a bottle filled with a standard water gas mixture is a well adapted approach for long term stability measurements as it offers a very stable moist air supply and is very easy to use. Most importantly, Kerstel et al. [6] showed that fractionation in the bottle can be neglected under the conditions encountered in our experiments, with partial pressures well below saturation.

Figure 4.2 shows Allan-Werle plots for the isotope ratios of the three isotopologues HDO, $H_2\,^{17}O$ and $H_2\,^{18}O$ from measurements at different water concentrations that were done with standard gas bottles as described above.

In the case of δ^2H, the best precision $\sigma_{opt} = 0.12‰$ is reached in $\tau_{opt} = 36.4$ min and at a water concentration of 1500 ppmv. For δ^{18}O the optimum integration time is also $\tau_{opt} = 36$ min,

but the best precision is at H_2O= 600 ppmv and for $\delta^{17}O$ the best results are achieved with τ_{opt} = 70 min at 1500 ppmv and σ_{opt} = 0.064‰. Because of fast natural isotope variations, it is not always possible to integrate the measurements for more than 30 min. Because of this, the precision that can be achieved in shorter time is also a very important measure. In table 4.1, the precisions at the different water concentration measurements shown in figure 4.2, are given for T = 4 s (8 data points) averaging and for the Allan optimum integration time T_{opt}. With 4 s averaging, the time resolution is still sufficient to study fast isotopic processes, but the precision is nearly a factor of three better than for non-averaged (0.5 s) measurements. As can be seen in

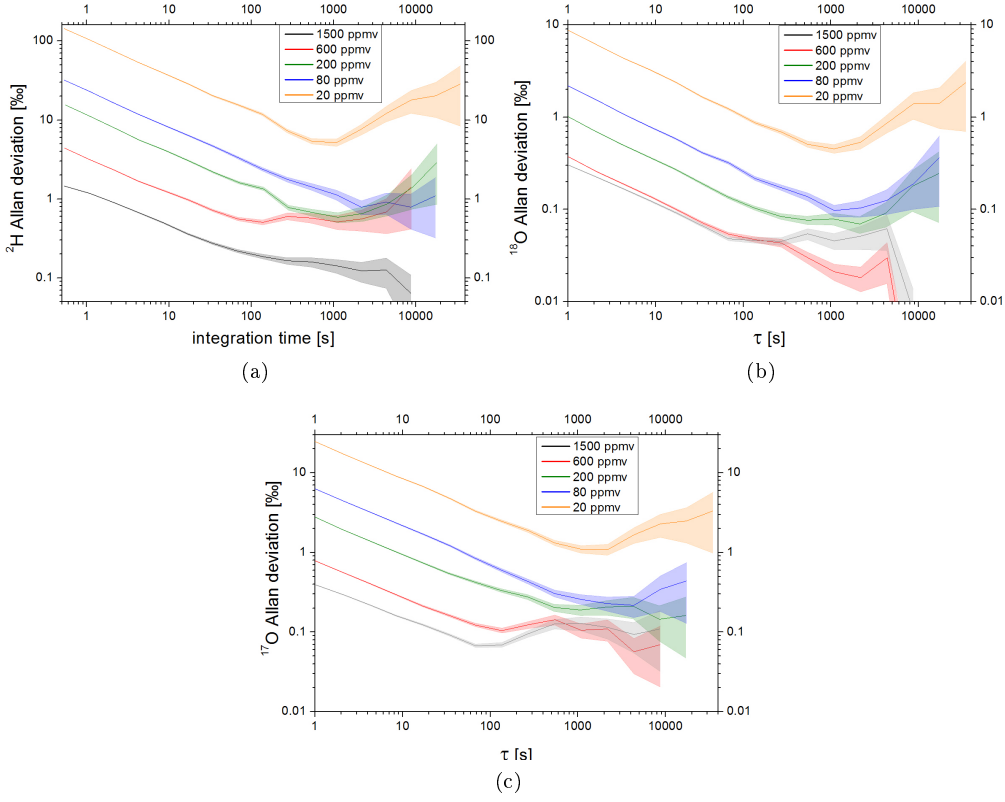

Figure 4.2: Allan deviation for the three isotopes

figure 4.3, the precision of the measurements in a water concentration range from 200ppmv to 2000ppmv remains approximately the same for all three isotopologues. For δ^2H, the precision is always better than 0.8‰, for $\delta^{17}O$ better than 0.15‰ and for $\delta^{18}O$ better than 0.1‰. A detailed discussion of the precision of our instrument can be found in [84], which is included in the appendix of this thesis. In the letter, the instrument is named HiFi (High Finesse Instrument) to avoid confusion with the name of the previous instrument IRIS.

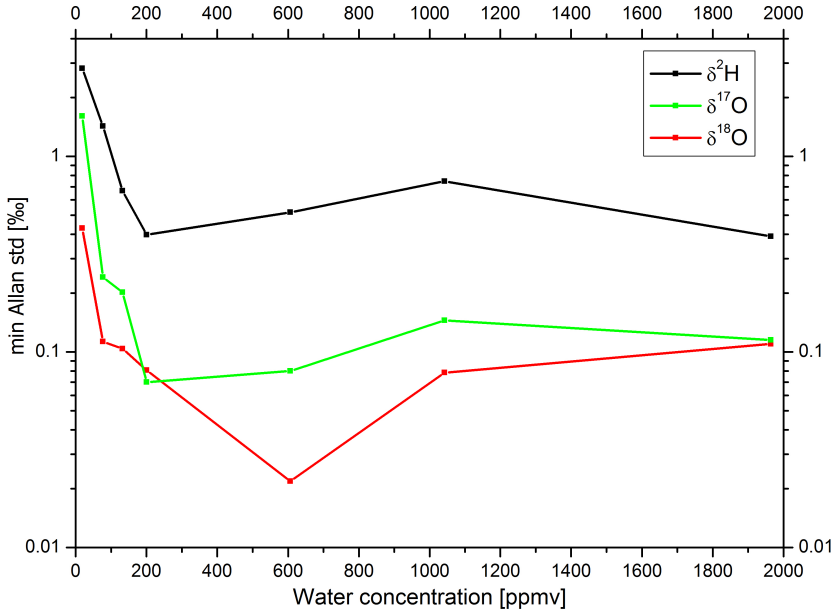

Figure 4.3: Minimum Allan deviation vs. H2O

Table 4.1: Measurement Precision as a Function of the Water Mixing Ratio for Different Averaging Times

H_2O [ppmv]	$\sigma(^2H)$ (4 s) [‰]	$\sigma(^2H)$ (T_{opt}) [‰]	$\sigma(^{18}O)$ (4 s) [‰]	$\sigma(^{18}O)$ (T_{opt}) [‰]	$\sigma(^{17}O)$ (4 s) [‰]	$\sigma(^{17}O)$ (T_{opt}) [‰]
20	54	5	4.4	0.5	12	1.1
80	12	0.8	1.1	0.1	3.2	0.2
190	5.5	0.6	0.5	0.07	1.4	0.19
420	2.7	0.5	0.27	0.05	0.7	0.16
610	1.7	0.5	0.18	0.02	0.4	0.1
770	1.1	0.28	0.18	0.04	0.3	0.07
1470	0.7	0.12	0.17	0.05	0.22	0.07

4.3 Noise analysis

To estimate the performance of the fitting routine used to analyze our data and to investigate factors that can influence the analysis of the data, synthetic spectra were generated with a Labview based simulation program. For the simulation, the C-based routine that is also used for the fitting analysis of the data was incorporated into the Labview program. All generated spectra were simulated with a Rautian line profile. Gaussian and Lorentzian widths as well as the Dicke parameter were set to the average values that were obtained from fits to experimental spectra. The relative intensities of the different lines of the same isotopologue were fixed. To simulate changes in the water concentration only, the intensities of all spectral lines of water were equally scaled. The baseline of the simulated spectra consists of a second order polynomial, superimposed with Gaussian white noise. To compare synthetic and experimental data, simulations were done with Gaussian noise of the same size as the fit residual of the experimental spectra and the intensity of the spectral lines was also matched.
In figure 4.4, the Allan-Werle plot of an experimental run at 80 ppmv H_2O with a residual of $7.1 \cdot 10^{-11}$ cm^{-1} is shown together with that of synthetic data simulating the same conditions. Surprisingly, the experimental data yield an Allan deviation that is more than two times lower than of the synthetic data. A histogram over the residuals of 30 subsequent spectra of the measurement used for the Allan-Werle plot (figure 4.5) shows that the experimental noise is indeed Gaussian distributed, as would be expected for uncorrelated, normally distributed white noise.

With pure white noise, averaging of several spectra reduces the residual of the fit (σ_{avg}) with the square root of the number of averaged spectra (N):

$$\sigma_{avg} = \sigma_0 \cdot \frac{1}{\sqrt{N}}$$

Whereas the simulated data follows the $1/\sqrt{N}$ behavior, the residual of the fit to the experimental data clearly does not tend towards zero, but instead levels off at a value of about $6 \cdot 10^{-11}$ cm^{-1} (figure 4.6). Clearly, a large fraction of the noise is not susceptible to averaging. Indeed, if we compare the fit residual of a single spectrum with that of the fit to the average of five or twenty spectra (figure 4.7), we see that the structure of the residual remains very similar, independent of the number of averaged spectra. This means that a large fraction of the noise in our measurements is not fast changing white noise but slowly varying structured noise, possibly caused by multiple, weak optical fringes [98].

Larger fringes are typically caused by parasitic reflections of the laser beam and can be efficiently reduced by catching these reflections with optical traps or improvements in the optical alignment, which was efficiently done in our set-up. Smaller fringes, e.g. due to backscattering on the optical surfaces in the beam path, are primarily due to scattering of light on the optical elements in the beam path and are virtually impossible to remove [99]. This structured noise

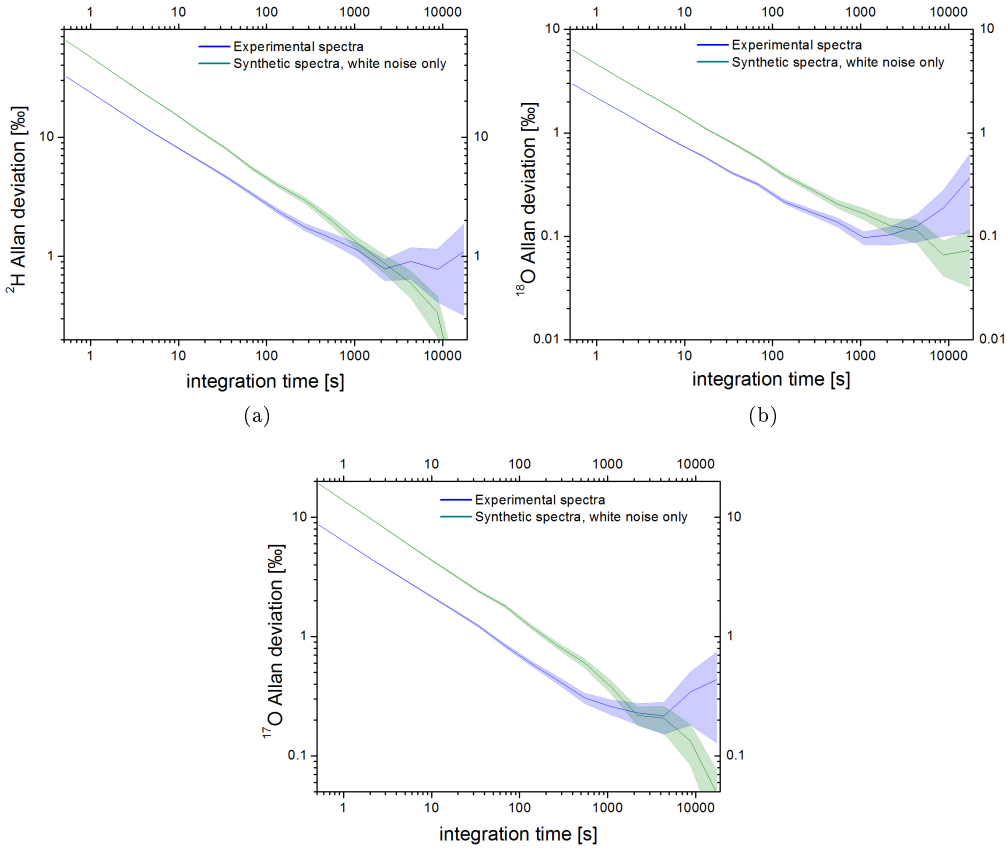

Figure 4.4: Allan-Werle plot of a measurement at 80ppmv compared to a simulated measurement at the same water concentration for a) δ^2H b) δ^{18}O and c) δ^{17}O. Both, simulated and experimental spectra have a RMS deviation of 7×10^{-11}cm^{-1}/s on the fit.

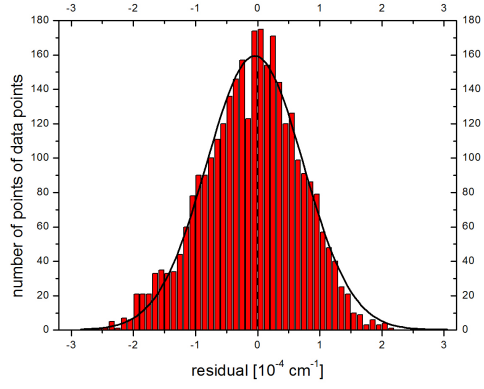

Figure 4.5: A histogram over the residuals of 30 subsequent spectra shows that the noise is following a Gaussian distribution (in black)

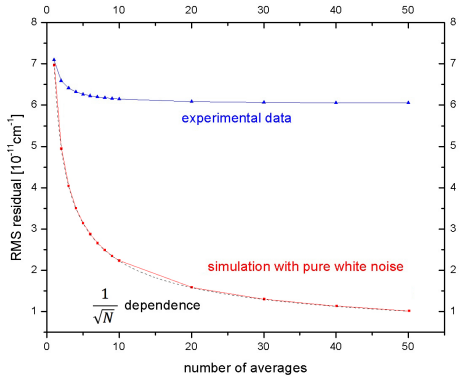

Figure 4.6: The residual of the spectral fit vs. the number of spectra averaged (in black). In red, the behavior for random white noise is depicted. When averaging over several spectra, the residual of the fit does decreases much slower than for random white noise.

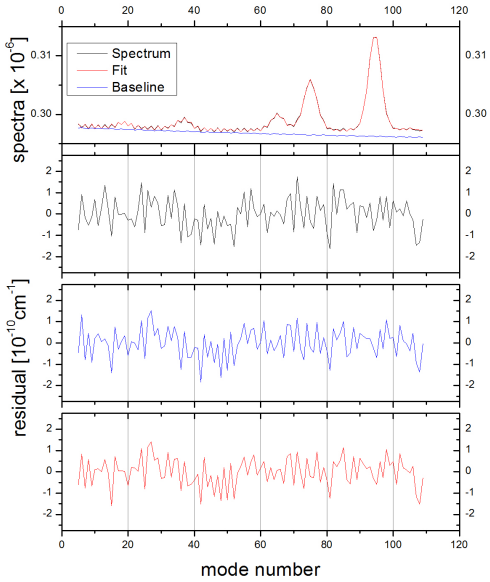

Figure 4.7: Comparison of the fit residual without averaging (second panel, in black), with the residuals of a fit to a spectrum averaged over 5 (third panel, in blue) and 20 individual spectra, respectively (bottom panel, in red). The shape of the residual remains nearly unchanged, independently of the number of averages. The noise pattern is thus not random white noise but systematic time-invariant noise.

is highly correlated between subsequent spectra and results in a smaller variation of the fit on a short time scale than the fast changing white noise. Because of this, the Allan-Werle plot for the experimental data starts at much lower values than the corresponding plot for synthetic data with the same level of (fast changing white) noise. To take the more stable noise source in the generation of synthetic spectra into account, an additional Gaussian distributed noise is added once to the baseline of the synthetic spectra and kept constant throughout the entire simulation. By changing the relative amount of the structured noise to the entire noise level, it is thus possible to adapt the simulation to the measurements and to estimate the contribution and influence of structured noise on the real measurements.
With an increasing contribution of time-invariant noise to the total noise of the simulation, the standard deviation of the delta values decreases and can be matched to the real measurement. With an RMS of the structured noise that is 1.5 times the RMS of the fast changing white noise, the simulated Allan-Werle plot is in very good agreement with the experimental data (cf. figure 4.8). Of course, for longer integration times, the synthetic Allan deviation continues to decrease, whereas the precision of the real measurement is limited by instrumental drift and increases again. The RMS of time-invariant noise was set to 6×10^{-11} cm^{-1} and the RMS of variable noise to 4×10^{-11} cm^{-1}. For the summation of these two independent noise distributions, the quadrature of the two sources has to be added, resulting in an overall RMS of the residual of $\sigma_{tot} = \sqrt{6^2 + 4^2}$ cm^{-1} = 7.2 cm^{-1} and a contribution of the structured noise to the overall noise, which is 6 cm^{-1}/7.2 cm^{-1} $\approx$ 83%.

In figure 4.9, the RMS of the residual versus the number of averaged residuals is shown just as in figure 4.6, but this time including the corresponding behavior for the synthetic data with 83% structured noise. The RMS of the simulation with structured noise is slightly larger than for the experimental data but perfectly reproduces the behavior for different averaging. Because of the large contribution of slowly changing structured noise in the measurements, the fluctuations between subsequent spectra is smaller than would be expected from the residual on the fits. In fact, the (short) time precision that can be achieved in the measurements would be equal to the precision of measurements with the white noise component only. The structured noise, which remains virtually constant, permanently biases the model fit to the spectrum and is therefore reflected in the accuracy of the measurement and not the precision.

4.4 Photodetector linearity

A possible problem that is well known in spectroscopic studies is photo detector non-linearity [100, 101], that is, the signal voltage has a nonlinear dependency on the incident power. A non-linearity would have large effects on our measurements, as a change of the emitted laser power would result in an apparent change of the water concentration and of the apparent isotope ratios, as was shown by Kerstel et al. [102].

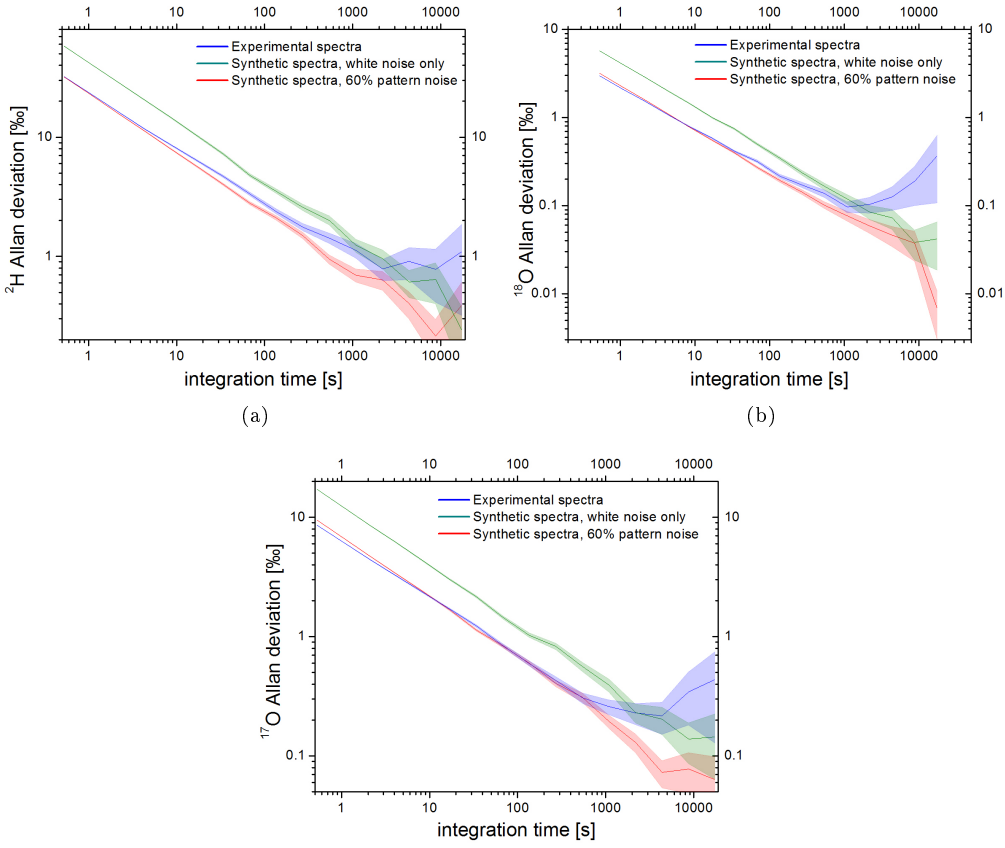

Figure 4.8: The Allan-Werle plot of figure 4.4 now including the deviation for a simulation with 60% structured noise and the same overall noise level. Whereas the simulation with random white noise only shows much larger deviations than the experiment, the simulation with 60% structured noise perfectly matches the experimental data.

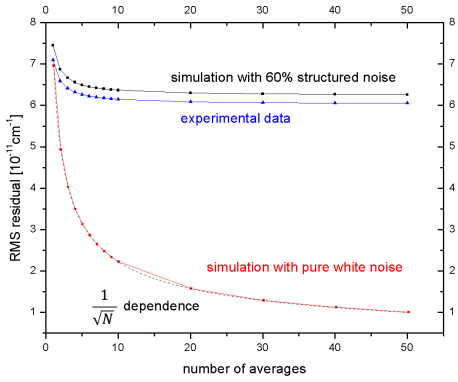

Figure 4.9: The residual of the spectral fit vs. the number of spectra averaged (in black). In red, the behavior for random white noise is depicted. When averaging over several spectra, the residual of the fit does decreases much slower than for random white noise.

One possibility to check for a non-linearity of the photo detectors is to measure a constant sample with the spectrometer and change only the laser power. If the detectors show a non-linear behavior, this would result in a change of the measured concentrations, since the baseline of the measurement (corresponding to a high detector signal) and the peaks of the absorption lines (corresponding to low detector signal), would be affected differently by the change of the laser power, provided that the absorption is relatively strong. In addition, the reference channel may be affected because of the change in laser power with detuning of the laser. In our case, however, this change is approximately 20% over the span of one spectrum, whereas the absorption depth of the stronger line(s) in the spectrum can be well over 50%, depending of course on the water concentration. However, a change of the laser power in our instrument can not be done by computer and would require to open the instrument to make the necessary changes to the laser current driver. This would also lead to a perturbation of the instrument stability, in particular of the temperature stabilization, which could in its turn introduce changes or instabilities in the measurements.

Because of this we examined a possible non-linearity of the detectors on several ring-down events, which are performed at the end of each laser scan to scale the absorption spectra (see also chapter 3). When the laser is interrupted at the end of a scan, the light intensity normally decays exponentially.. This ringdown event is carried out in a spectral region with little or no gas absorption in order to avoid possible line saturation effects (see paragraph 4.5) and because in this case the ringdown time is long, and can thus be measured more accurately. Now, if the output voltage of the photo detectors has a non-linear component, the measured decay will not be purely exponential.

The dependency of the signal voltage of the detectors on the incident light intensity including a

non-linear component can be described by the following relation:

$$V(t) = V_0 + I(t) + \epsilon I(t)^2$$

With $I(t) = I_0 + A\exp\left(\frac{t-t_0}{\tau}\right)$ this leads to:

$$\begin{aligned} V(t) &= V_0 + I_0 + \epsilon I_0^2 + A(1+2\epsilon I_0)\exp\left(-\frac{t-t_0}{\tau}\right) + \epsilon\exp\left(-\frac{2(t-t_0)}{\tau}\right) \\ &= V_0' + A'\exp\left(-\frac{t-t_0}{\tau}\right) + \epsilon\exp\left(-\frac{2(t-t_0)}{\tau}\right) \end{aligned} \tag{4.10}$$

In figure 4.10, a typical ring-down event recorded at the end of each laser scan, is shown. For the non-linearity check, we averaged over 30 subsequent ring-down events to further reduce the noise on the measurement. In figure 4.10a, the fit of an ordinary exponential decay and the residual of this fit are shown. The reduced chi-square of the fit is $\chi^2_{red} = 8.8 \times 10^{-9}$ and gives a ring-down time of $\tau = 119.25 \pm 0.01$ µs. The residual of the fit is uniform and does not show any deviations during the ring-down event.
In figure 4.10b, the same ring-down event fit with an additional quadratic term (equation 4.10) is given, assuming a non-linearity of the photo detectors. The fit has a reduced chi-square of $\chi^2_{red} = 8.1 \times 10^{-9}$ and results in a ring-down time of $\tau = 119.41 \pm 0.03$ µs. The coefficient of the non-linearity term $\epsilon = (-1.8 \pm 6.0) \times 10^{-3}$ and thus is equal to zero within the error limits. In both figures, the ring-down event is shown on a logarithmic vertical scale. The curve deviates from a straight line for lower signals because of the non-zero background signal of the photo detector. As an ordinary exponential function matches the ring-down event very well and the additional quadratic term is within the error equal to zero, it can be concluded that the photo detectors show a non-linearity that is well below the measurement precision of the instrument, and the concentration and isotope ratio measurements are not affected.

4.5 Power saturation

Measurements with the OF-CEAS technique rely on the linear dependence of the absorbed power on the incident laser intensity. However, if the population density of the absorbing level is noticeably diminished due to the absorption of laser radiation, saturation of the transition can occur and the relation of absorbed power and incident intensity is no longer purely linear. Saturation of a transition is reached when the depletion of a level due to relaxation becomes comparable to the absorption induced population of the same level, that is, the number of molecules that are excited from the ground state to an upper state is comparable to the number of molecules that go back to the ground level [74]. A larger laser power leads to a stronger depletion of the ground level of a transition, whereas a larger number of molecules in the gas cell (higher pressure) results in collision induced relaxation of the upper level. The intensity at

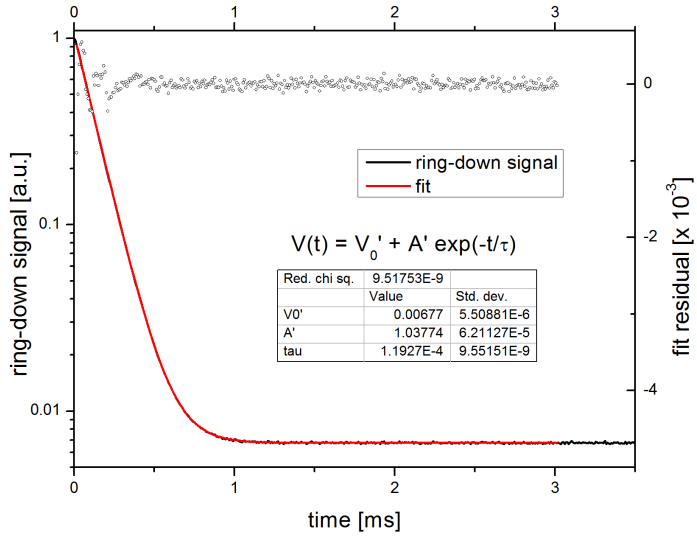

(a)

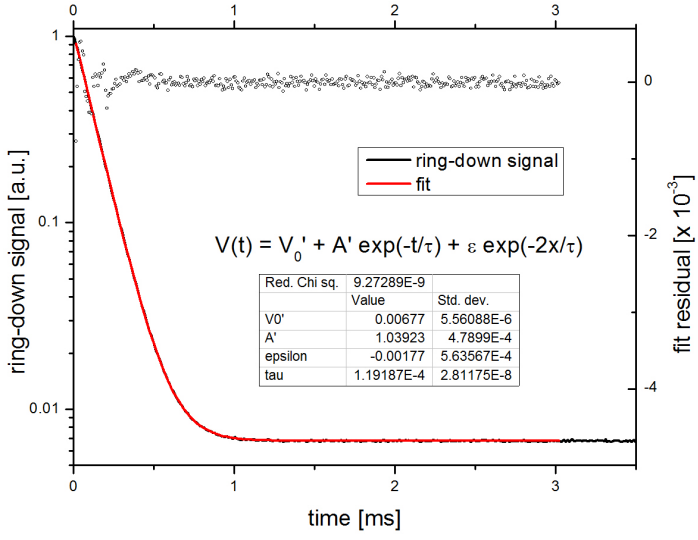

(b)

Figure 4.10: An average of 30 ring-down events, fit with a) an ordinary exponential decay and b) assuming a non-linearity of the photo detectors. Note that the ring-down signal deviates from a straight line in the logarithmic plot at the end of the measurement. This is due to the detector background, which is larger than zero.

which saturation of a transition occurs can be calculated with [103]

$$I_s = \frac{ch}{3}\frac{\Gamma^2 k^3}{A} \tag{4.11}$$

with c: speed of light, h: Planck constant, A: the Einstein coefficient of the transition, k: the wave vector and Γ the full width at half maximum (FWHM) of a transition, which takes in the Voigt profile also into account the effect of collisional relaxation. The dependence of the saturation intensity on the pressure in the gas cell is taken into account via the FWHM of the absorption line, which is larger for higher pressure and approaches the Doppler FWHM for very low pressures.

To investigate if saturation of one or several absorption lines occurs in our instrument, we analyze ring-down events measured at the central frequency of the absorption lines of the investigated wavelength region. As observed by Romanini et al. [104] and Giusfredi et al. [103], a ring-down is no longer single exponential, when saturation of a transition occurs as the degree of saturation diminishes with diminishing intra-cavity intensity and the intensity ultimately becomes smaller than the saturation intensity of equation (4.11). The Einstein coefficients of the transitions investigated in our OF-CEAS spectrometer are shown in table 4.2. As a larger Einstein coefficient corresponds to a lower saturation intensity (equation (4.11)), the absorption line of $H_2^{18}O$ at 7183.5859 cm^{-1}, which has the largest Einstein coefficient, would be the first absorption line affected by saturation effects. To estimate if power saturation occurs in our measurements,

isotopologue	wavenumber [cm^{-1}]	Einstein coefficient [s^{-1}]
$H_2^{16}O$	7183.685800	0.0566
$H_2^{18}O$	7183.585780	23.12
$H_2^{17}O$	7183.735450	11.53
$HD^{16}O$	7183.972790	1.853
$H_2^{16}O$	7200.133840	0.0094
$H_2^{18}O$	7199.961310	5.52
$HD^{16}O$	7200.302440	11.48

Table 4.2: Einstein coefficients of the transitions investigated in SIRI (from [61])

we compare the intracavity intensity I_c with the saturation intensity (equation (4.11)). The intracavity intensity can be calculated with

$$I_c = (\frac{\mathcal{F}}{\pi} \cdot I_0) \cdot \eta \tag{4.12}$$

with $\mathcal{F}$ the cavity finesse, I_0 the intensity of the injected light and η the portion of I_0 injected into the TEM_{00} modes. The intensity of the laser is in our case approx. $2 \cdot 10^{-3}$ W/cm^{-2} and the injection efficiency into the TEM_{00} modes around 20%. With a finesse of 288,000 (cf. section 3.1), this leads to $I_c = 1.833 \cdot 10^6$ kg/s^3.

For the saturation intensity (equation (4.11)), we need to know the FWHM of the transition,

which we can obtain from our fit model to the experimental data. For the $H_2\,{}^{18}O$ absorption at $k = 7183.58578\ \mathrm{cm}^{-1}$, the Gaussian FWHM is 615 MHz and the Lorentzian FWHM approx. 98 MHz. We approximate the FWHM with the Gaussian linewidth, thus underestimating the saturation intensity. With this and the Einstein coefficient from table 4.2, the saturation intensity is $I_s = 8.087 \times 10^8\ \mathrm{kg/s^3}$, which is more than a factor 440 larger than the intracavity intensity. In our measurements, power absorption can thus be neglected.

For an additional experimental verification, we also investigate if power saturation occurs by looking at ring-down events performed directly on an absorption line. As mentioned above, power saturation would result in ring-down curves that are no longer single exponential. Unfortunately, it was not possible to study the saturation effects on this line as no laser for this wavelength region was available at the time of these measurements (nor could it be purchased and delivered fast enough). Instead, the saturation was investigated on the $HD^{16}O$ absorption at $7200.3024\ \mathrm{cm}^{-1}$. This line has an Einstein coefficient that is half as large as that of the $H_2\,{}^{18}O$ line. However, the absorption for this line is more than a factor 15 weaker, which means that the ring-down time is longer and can be measured more precisely.

For the study of saturation effects, the pressure in the cavity was reduced to 2.7 mbar. This reduces the density of molecules in the cavity and therefore also the relaxation of excited levels due to collision with other molecules, effectively lowering the saturation intensity level (cf. equation (4.11)).

To determine the ring-down more precisely, instead of one single ring-down measurement, 30 subsequent ring-down events were averaged. The averaged measurement is shown in figure 4.11 on a logarithmic scale together with a single exponential fit. The fit gives a ring-down time of $\tau = 141.01 \pm 0.1$ µs and has $\chi^2_{red} = 1.3 \times 10^{-8}$. In the fit residual, a larger deviation is visible for the beginning of the ring-down measurement, which could be an indication of possible saturation effects. However, this larger residual is also visible for ring-down measurements performed on the baseline (cf. figure 4.10), where power saturation can not occur. In addition, the calculation of the saturation intensity for the $HD\,{}^{16}O$ absorption line for a pressure of 2.7 mbar gives $I_s = 8.627 \cdot 10^8\ \mathrm{kg/s^3}$ and a ratio of saturation intensity and intracavity intensity of $I_s/I_c = 470$. Therefore, we can conclude that no saturation of the transitions occur in our measurements, which are done at a pressure of 35 mbar, which further increases the saturation intensities for the different transitions.

4.6 Matrix effects

Apart from gas pressure and temperature, the line profiles of the spectral lines also depend on the buffer gas used in the experiment. As explained above, the collisions between the molecules of interest and the carrier gas lead to a pressure broadening of the absorption line, which is described by the Lorentzian line width. However, this broadening is not only dependent on pressure but also on which gas is used as carrier, as the interactions are different for different

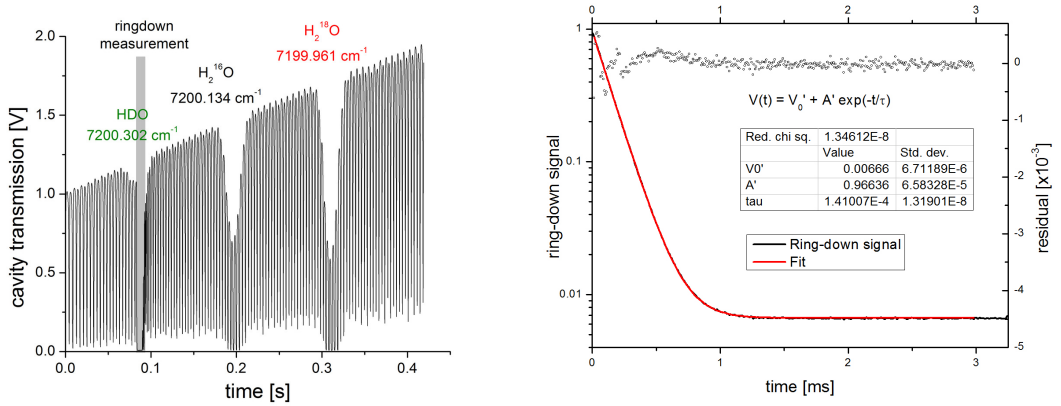

(a) (b)

Figure 4.11: A ring-down measurement on the absorption line of $HD^{16}O$ at 7200.3024 cm^{-1} (a), fit with a single exponential decay function (b) The residual on the fit shows a small deviation in the beginning of the ring-down, which can also be found in ring-down events performed on the baseline of the spectrum.

molecules.

This becomes important if different carrier gases are to be used in the experiments. The Lorentzian widths of the spectral lines depend on the buffer gas that is used and a different parameter file for the spectral fit has to be used for each of the gases. Because of this, different carrier gases for calibration and measurement have to be avoided, and if possible precisely the same relative abundances of different molecules should be used.

Two measurements under exactly the same conditions but with different carrier gases are shown

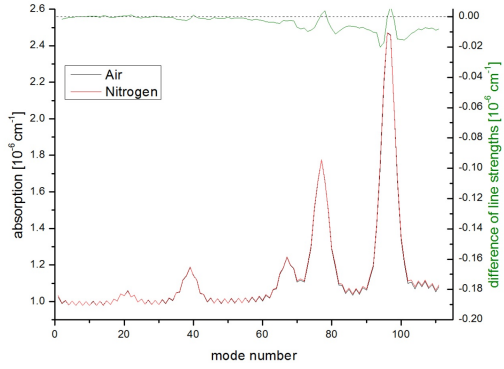

Figure 4.12: Comparison of two experimental spectra measured at the same conditions but with different carrier gases. In black a measurement in air is shown and in red, a measurement in nitrogen. The difference between the two spectra is given in green (right scale).

in figure 4.12. For the two measurements, synthetic air (20% oxygen, 80% nitrogen), and pure

nitrogen, respectively were used as carrier gases.
The difference of the line widths in different carrier gases is due to differences in the relaxation of the excited states due to different collisional rates. To estimate the different line widths, we make the (simplistic) assumption that the different collisional widths are only due to differences of the mean free path lengths (MFP) for the two matrices, which determine the collisional rate. The MFP can be calculated using the molecular diameter [105]:

$$l = \frac{k_B T}{\sqrt{2}\pi d^2 p} \tag{4.13}$$

with k_B Boltzmann's constant, T the temperature in Kelvin, d the diameter of the gas molecules in meters and p the pressure in Pascals. The MFP difference is thus determined by the square of the different molecular diameters. The molecular diameters of Nitrogen and Oxygen are 370 pm and 358 pm, respectively. For the conditions in our experiments (35 mbar, 45 °C), this leads to MFP lengths of 2.06 µm and 2.2 µm for N_2 and O_2, respectively. For synthetic air with 20% oxygen and 80% nitrogen, the MFP is of the same ratio, which results in an MFP of 2.09 µm. The collisional rate in the carrier gas and therefore also the Lorentzian width of the spectral lines is proportional to the inverse of the MFP. The Lorentzian line widths for N_2 should thus be approx. 1.5% larger than for synthetic air.
A more detailed study by Moretti et al.[106] reveals that for a more complete picture, other properties, like the different rotational states have to be taken into account as well. The authors propose that the different collisional rates are likely due to different quadrupole moments, which play an important role in the dipole-quadrupole interaction occurring during the collision between H_2O and N_2 or O_2. For the $H_2\,^{18}O$ line at 7183.59 cm^{-1} in our spectrum, they report a collisional broadening coefficient of 2.26(1) MHz/Torr in N_2, and of 0.99(4) MHz/Torr in O_2, which leads to a broadening coefficient of 1.99(2) MHz/Torr in synthetic air and an approx. 11% larger Lorentzian line width in N_2 compared to air.
In figure 4.12, two spectra from measurements with a lower finesse instrument of the same sample at $[H_2O] \approx$ 5900 ppmv, is shown for measurements with the two different carrier gases. As can be seen in the difference between the spectra in synthetic air and the spectra in nitrogen, the difference between the two spectra more negative at the wings of the absorption lines and positive for the line maxima (most visible for the two strongest lines). This indicates that the line widths are a bit larger for the nitrogen buffer gas than for synthetic air. In addition, the difference shows a negative slope and is more negative for larger mode numbers. This is due to a very strong $H_2^{16}O$ absorption line, which is in close proximity to the end of the measured spectral region (corresponding to approx. mode 220). Because of the stronger broadening in nitrogen, the wing of this absorption line also has a larger influence in nitrogen than in air. A fit to the absorption lines with fixed Gaussian line widths and free Lorentzian line width indicates Lorentzian line widths that are approx. 4.5% larger for N_2 than for synthetic air, which is in relative good agreement with the value given by Moretti et al.[106], especially regarding the fact

that we use a Rautian line profile, whereas Moretti et al. assume a Voigt profile of the line.
It is difficult to estimate the error that would be made in the isotope determination, if different carrier gases would be used for calibration and measurement or if a parameter file with Lorentzian widths for another matrix is used. Erroneous line widths are partly compensated by other parameters in the spectral fit, which makes a simple estimate of the error impossible. In addition, we found that different carrier gases can also result in a change of the concentration dependence of the isotope ratios. In conclusion, the use of different gas matrices should be avoided and if possible, desiccated sample air instead of synthetic air should be used for calibrations. Due to measurements at very low water concentrations, this was not always possible in our measurements, as most desiccants do not permit to dry air to concentrations below 100 ppmv. Instead, we had to use dry synthetic air. However, the error made because of different molecular composition is in this case negligible. Earth's atmosphere consists of 78.08% N_2, 20.95% O_2 and 0.97% trace gases and water [107]. The synthetic air is specified with $20 \pm 1\%$ O_2 and $80 \pm 1\%$ N_2. The line width difference because of differences of the gas matrix is thus smaller than 0.07% and does not result in visible changes of the residual in our measurements.

4.7 Conclusion

With SIRI, the NEAS at water concentrations below 500 ppmv is typically $6{\cdot}10^{-11}$ cm^{-1} $Hz^{-1/2}$, an improvement by a factor of almost 7 compared to the previous instrument IRIS, which is equal to the ratio of the finesses.
Due to the new temperature regulation, the cavity temperature is stabilized at 45°C with a drift smaller than 0.5 mK over 3.6 h. Over the same time, the drift in cavity pressure is smaller than 10 µbar. This increased stability results in optimum integration times of up to 70 min (for longer integration times drift degrades the precision), compared to longest optimum integration times of approx. 5 min in IRIS.
In conclusion, the new instrument achieves similar or better results in terms of measurement precision compared to our previous OF-CEAS water isotope spectrometer, as well as compared to most commercial water vapor spectrometers but at a water concentration that is approximately an order of magnitude lower. The NEAS of $5.7{\times}10^{-11}$ cm^{-1} $Hz^{-1/2}$ (or $5.4{\times}10^{-12}$ cm^{-1} $Hz^{-1/2}$ when normalized per spectral element) is among the lowest values reported for near-infrared CEAS so far, with the exception of NICE-OHMS (with its much smaller tuning range) and the lowest for CEAS with a base length below 50 cm.
The improved stability time can be used to increase the precision on a single measurement before drift starts dominating the noise. It also enables longer uninterrupted recording before recalibration needs to be carried out [98].

Chapter 5

Data Corrections and Calibration

As described in chapter 1, the measurement of isotope ratios is never a measurement of absolute values but always done relative to well-known calibration standards. The recommended procedure of the International Atomic Energy Agency (IAEA) to calibrate isotope measurements is to measure two isotope standards and make a linear correction of the measured isotope delta values [26, 108]:

$$\delta_s^{(cal)} = \delta_1^{(t)} + \left(\delta_s^{(m)} - \delta_1^{(m)}\right) \times f \tag{5.1}$$

with

$$f = \left(\delta_2^{(t)} - \delta_1^{(t)}\right) / \left(\delta_2^{(m)} - \delta_1^{(m)}\right) \tag{5.2}$$

with 1, 2 and s for isotope standard 1 and 2, and the unknown sample, respectively, and the superscripts (m), (cal) and (t) indicating measured, calibrated and true isotope delta (determined independently, e.g. by IRMS measurements).

In many optical spectrometers, however, the isotope ratios of the same sample, measured at different concentrations, are dependent on the concentration at which they are measured [109–113]. Although the measurement should result in the same isotope ratio, independent of the concentration at which it was measured, this is often not the case and an additional correction of the isotope measurements for the concentration has to be made.

The reason for the concentration dependence of the isotope ratios is not always evident and often has different reasons in different instruments. Early measurements with the color center laser, dual gas cell, liquid water isotope ratio spectrometer developed in the mid-90's at the university of Groningen required a correction for the difference in the amount of water injected into the reference and sample gas cells. This effect was understood as due to a differential pressure broadening between the sample and reference cells, and could be quantitatively described with a simple model [64].

Tuzson et al. [109] propose amongst other things instrumental non-linearity, non-unity gain factors and potential cross-coupling effects as potential reasons. Cross-coupling between different spectral lines in the measurement because of overlapping wings of the absorption lines, can be very pronounced in spectra with many different absorption lines, where the separation of the individual lines is not always straightforward. Additional sources can be uncertainties in

the spectral baseline and the tails of very strong absorption lines that are close to the spectral window used for the measurements.

In the case of our instrument, strong $H_2\,{}^{16}O$ absorption lines close to the spectral region used

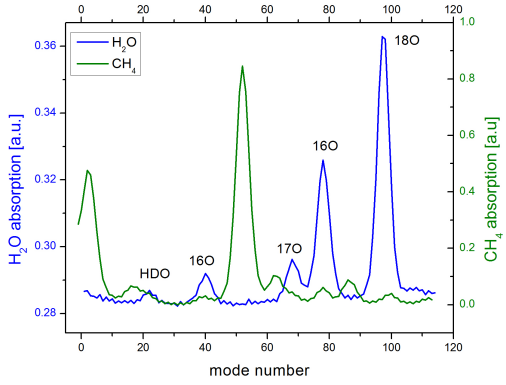

Figure 5.1: Water (blue) and methane (green) spectra measured at 7184 cm^{-1}. The measurement of H_2O was done at 350 ppmv and the CH_4 measurement at an enhanced concentration of approx. 1700 ppmv to localize additional methane absorption lines in the spectral range measured with our instrument. To improve the result of our data fitting, the different absorption lines were included into the model spectra fit to our data. At natural abundance ($<$ 2 ppmv) the methane peaks are generally not visible in the spectrum.

for the measurements are taken into account in the model spectra fit to the experimental data. Furthermore, additional measurements in the spectral region were made on Methane samples at an enhanced concentration of approx. 1700 ppmv, to take weaker Methane absorption lines into account as well (cf. figure 5.1). These absorption lines are at natural abundances ($<$ 2 ppmv) generally hidden in the water absorption spectra. After careful generation of the model spectra and different fit approaches, we found that the main source for the remaining concentration dependence of the isotope ratios is structured and time-invariant noise in the measurement, discussed in more detail in section 4.3.

In figure 5.2, the isotope ratio measurements as a function of the water concentration are shown for two synthetic data sets, which were simulated as described in section 4.3. Both simulations were done with an RMS of the residual of $7.8 \times 10^{-11} cm^{-1}$ and the concentration of the different isotopes was varied by changing the amplitudes of the individual spectral lines. The relative change of all amplitudes was identical, such that the isotope ratios should remain constant.

In one simulation, the noise was Gaussian white noise only, which was recalculated with a fresh start of the random number generator for each spectrum. In the other simulation, 83% was time-invariant structured noise as previously observed in the measurements. Whereas the isotope ratios in the measurement with white noise only (figure 5.2, in red) show almost no variation with changing water concentration, the measurement with structured noise (in black), shows a strong dependence of the isotope ratios on the water concentration. At very low water

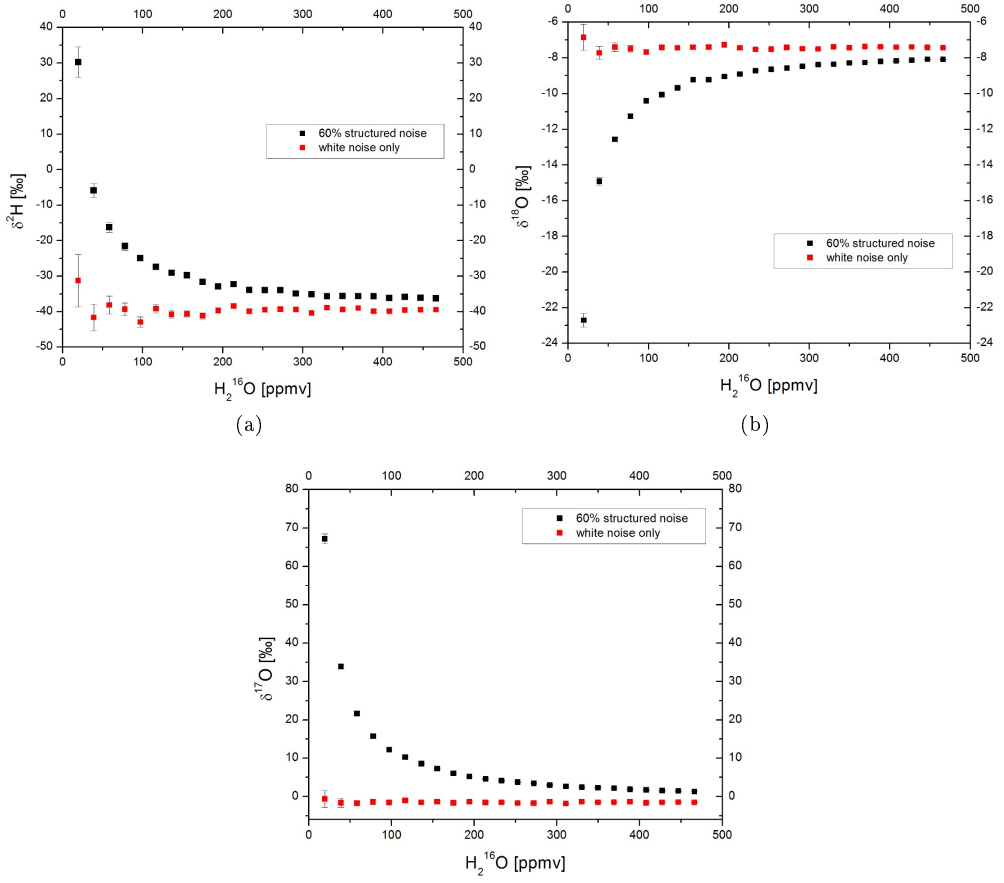

Figure 5.2: Comparison of the isotope ratios of two synthetic data sets with varying water concentrations. a) δ^2H, b) δ^{18}O and c) δ^{17}O. In the case of pure white noise (in red), the isotope ratios show essentially no dependence on the water concentration in the measurement. In a measurement with 83% structured noise (in black, see also section 4.3), the concentration dependence becomes very pronounced for all three isotopologues.

concentrations, the absorption lines become weaker and the influence of the structured noise on the measurement becomes even more pronounced. Because of this, the isotope ratios show very large deviations for lower water concentrations and almost no deviation for larger concentrations.

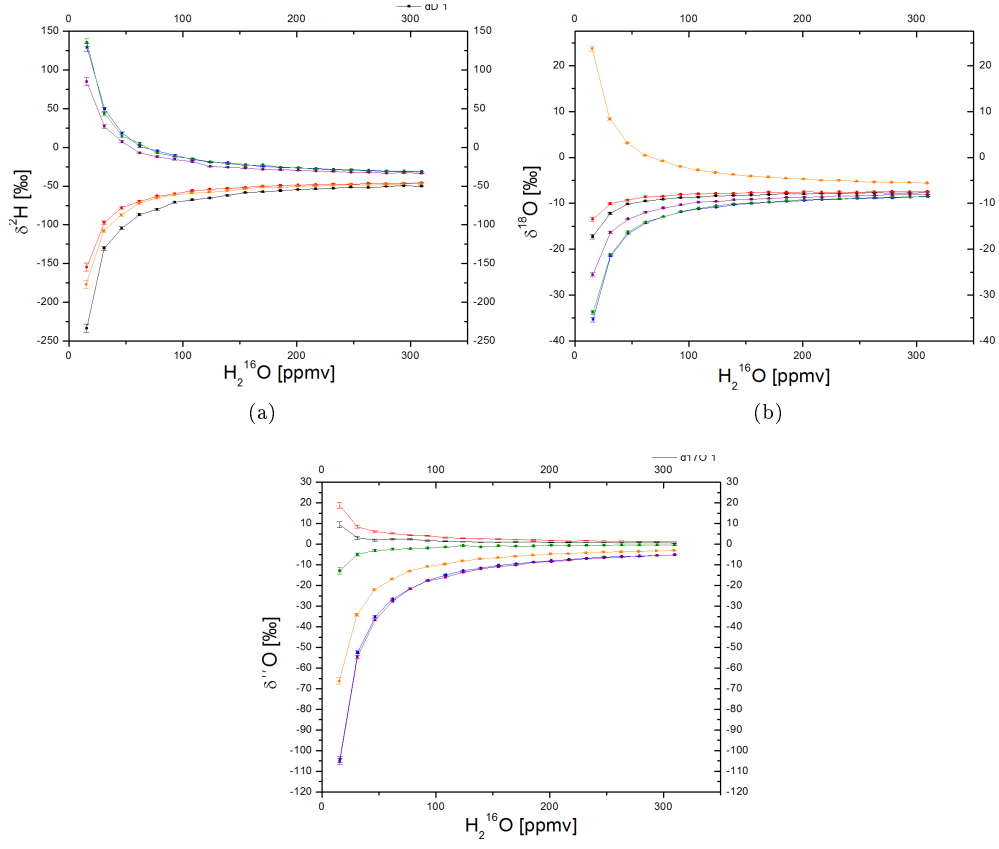

Figure 5.3: Comparison of six simulations with 60% (randomly generated) structured noise. The pattern of the structured noise has a large influence on the concentration dependence of the isotope ratio. Between different simulations, the concentration dependence even changes the sign because of the difference in the structured noise.

In figure 5.3, the isotope deltas from the fit of six different simulations with varying water concentrations are shown. The simulations were all done with 60% structured noise and were identical apart from the structured noise, which was each time randomly generated Gaussian distributed noise. The difference in structured noise results in changes of the concentration dependence of the isotope ratios and can even lead to a change of the sign of the dependency between different simulations. If the pattern of structured noise changes, the concentration de-

pendence also changes and a correction for the concentration dependence becomes very difficult. In general it is thus not possible to assume a time-invariant concentration dependence of the isotope ratios. Frequent calibrations at different water concentrations are necessary to account for changes of the noise pattern in the measurements.
However, the extreme case of a complete change of the structured noise pattern, as generated in the simulations, does normally not occur and the real changes are much smaller. In figure 5.4, calibration measurements over a 16-day period during a measurement campaign are shown for ${}^{2}R_{sample}/{}^{2}R_{VSMOW}$ and ${}^{18}R_{sample}/{}^{18}R_{VSMOW}$ measurements at 7200 cm^{-1}. Because of the strong isotopic enrichment, the values are given in ratios instead of permil. As can be seen, the concentration dependence only changes slightly between different measurements, which means that the shape of the pattern noise stays very similar throughout the entire measurement campaign. At water concentrations around 600 ppmv, the RMS deviation from the average concentration dependence is 10‰ for ${}^{2}R_{sample}/{}^{2}R_{VSMOW}$ and 1.5‰ for ${}^{18}R_{sample}/{}^{18}R_{VSMOW}$. At very low $H_2{}^{16}O$ concentrations around 10 ppmv, the RMS deviation increases to 160‰ and 35‰ for ${}^{2}R_{sample}/{}^{2}R_{VSMOW}$ and ${}^{18}R_{sample}/{}^{18}R_{VSMOW}$, respectively.

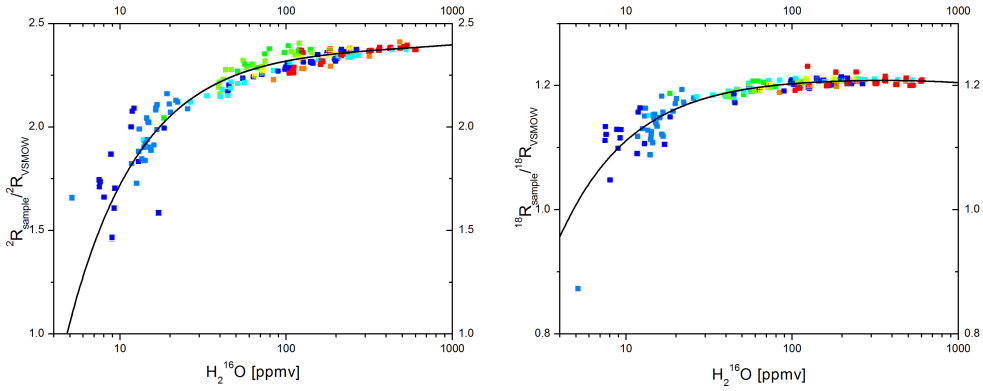

(a) (b)

Figure 5.4: Calibration measurements over a 16-day period during a measurement campaign. The isotope ratios are plot versus water concentration for a) ${}^{2}R_{sample}/{}^{2}R_{VSMOW}$ and b) ${}^{18}R_{sample}/{}^{18}R_{VSMOW}$. The different colors indicate different calibration measurements. The concentration dependence remains very similar for all measurements, indicating that in real experiments the function describing the dependence remains virtually unchanged over time.

5.1 Calibration strategy

Because of the concentration dependence, the calibration of our measurements has to be done in two steps. First, the isotope ratios have to be corrected for the water concentration effect and second, a calibration of measured versus true delta values has to be carried out.

In the following, our calibration strategy is illustrated on a set of three isotope measurements done at 7184 cm^{-1}. First, a measurement of the isotope standard GS48 was done using the SNICS calibrated water vapor generator (see section 6.2) at different water concentration steps. Subsequently, a measurement with varying water concentration of the standard GS22 was done, which serves here as our "unknown" water sample. Finally, a measurement of GS50 as second calibration standard was done at different water concentrations. This sequence enables us to calibrate the measured values for the "unknown" GS22 sample on the isotopic scale defined by the local standard materials GS48 and GS50, whose isotopic compositions bracket that of GS22. This is thus similar to the IAEA-recommended procedure for calibration to the VSMOW-SLAP scale (see beginning of this chapter).
Over each concentration step of the measurements, the average of the water concentration and the isotope ratios was calculated. As an example, we show the measurement of GS22 in figure 5.5 for (a) water concentration and (b) isotope deltas. For each concentration step, unstable periods were excluded. The light gray boxes in the figure indicate the sections over which averages were calculated.

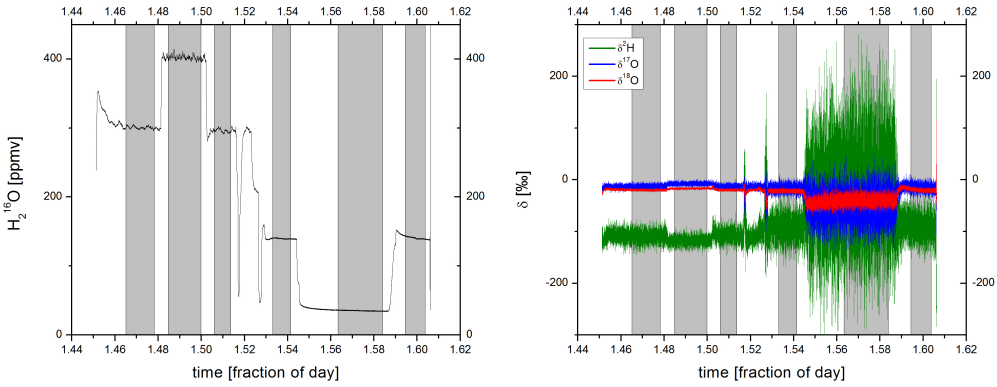

(a) (b)

Figure 5.5: Measurement of water concentration variation of the standard GS22 generated with SNICS. The light gray boxes indicate sections over which averages were calculated for the calibration.

In figure 5.6, the average delta values are plot against the water concentration for (a) δ^2H, (b) δ^{18}O and (c) δ^{17}O, clearly showing the dependency on the amount of water in the measurements. Whereas the relation is almost linear for larger water concentrations, it is non-linear for concentrations below 150 ppmv.

We found that the concentration dependence is best described with a linear term in combination with a hyperbola:

$$\delta([H_2\,{}^{16}O]) = \delta_0 + m \times [H_2\,{}^{16}O] + \frac{b}{[H_2\,{}^{16}O]} \tag{5.3}$$

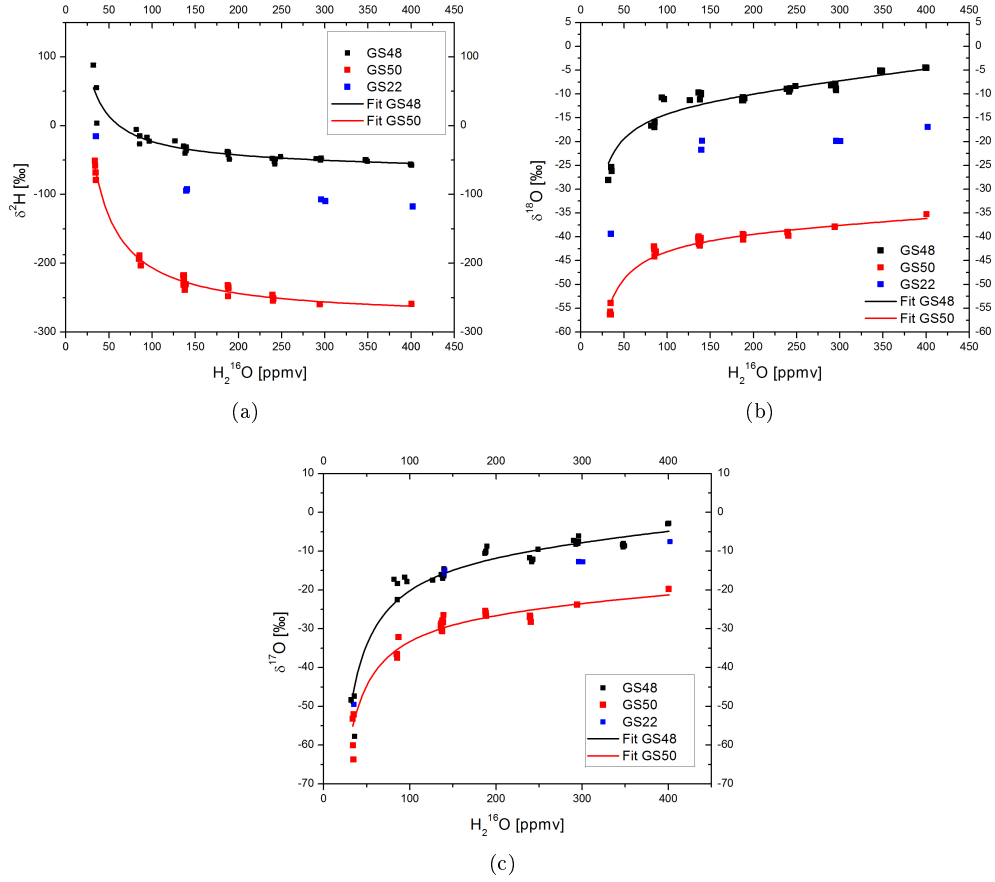

Figure 5.6: Delta values averaged over each concentration step of the two calibration measurements with GS48 and GS50 (data not shown) and the measurement of GS22 (figure 5.5). For higher water concentrations, the relation between water concentration and delta values is practically linear whereas it is strongly non-linear for lower abundances. The two calibration measurements are fit with a combination of hyperbola and line (black and red line). The fit results are given in table 5.1

For each isotopologue, the function of equation (5.3) is fit independently to the two calibration measurements of GS48 and GS50. The data is weighted with the standard error of the data points. The fit is shown in figure 5.6, the resulting parameters are given in table 5.1. The

Standard	Isotope	δ_0	b	m
GS48	δ^2H	-58 ± 5	3619 ± 459	-0.02 ± 0.01
	δ^{18}O	-12 ± 2	-416 ± 125	0.021 ± 0.004
	δ^{17}O	-9 ± 3	-1302 ± 248	0.018 ± 0.007
GS50	δ^2H	-282 ± 7	7489 ± 504	0 ± 0.02
	δ^{18}O	-38.8 ± 0.8	-529 ± 64	0.01 ± 0.002
	δ^{17}O	-24 ± 2	-1069 ± 145	0.013 ± 0.005

Table 5.1: Fit parameters of the function on the concentration dependence for all three isotope deltas for the standards GS48 and GS50

parameters of the function are different for the two isotope standards, which is not surprising as the error that is made in the estimation of the concentration of the different isotopes is larger for weaker absorption lines and thus more pronounced for stronger depleted isotope standards. This is especially pronounced for δ^2H, where the fit on GS50 indicates a much stronger non-linear concentration dependence than for GS48. Whereas the difference in the relative abundance between the two standards is smaller than 3% for $H_2{}^{18}O$ and smaller than 2% for $H_2{}^{17}O$, it is larger than 24% for δ^2H (cf. table A.A.1). For δ^{18}O and δ^{17}O, the difference in the fit parameters is smaller than the uncertainty on the parameters and one globally valid function could be assumed to correct the concentration dependence.

The concentration dependence of an unknown sample is determined from the concentration dependence determined in the two calibration measurements. We assume that the function for the sample measurement can be determined as a linear combination of the parameters δ_0, b and m of the fit functions determined in the calibration measurements. The relative contribution of the two results is determined by the difference in the delta values of the two standards and the unknown sample. For the parameter b, this is for example:

$$b_s = b_1 + (b_2 - b_1) \times \frac{\delta_s - \delta_1}{\delta_2 - \delta_1} \tag{5.4}$$

with subscripts 1, 2 and s indicating standard 1 and 2 and sample, respectively and δ and b the isotope delta and parameter b of the same isotopologue. As the concentration dependence is much less pronounced for higher water concentrations, we propose to use the isotope deltas at the highest available water concentration in the measurements.

In our case, the highest concentration at which the two standards and the sample were measured is 400 ppmv. The three delta values at 400 ppmv in the three measurements are given in table 5.2. The linear combination of the concentration dependency functions of the two calibration measurements results in correction functions for the sample measurement with parameters δ_0, b and m as shown in table 5.3. The concentration dependence calculated from the linear combi-

isotope	GS48	sample (GS22)	GS50
δ^2H [‰]	-57.3	-117.7	-261.3
δ^{18}O [‰]	-4.6	-17.0	-35.9
δ^{17}O [‰]	-2.8	-7.5	-19.8

Table 5.2: The measured delta values for the two calibration measurements of GS48 and GS50 and the sample measurement (GS22) at the highest water concentration in the measurements (400 ppmv).

Isotope	δ_0	b	m
δ^2H	-124 ± 6	4765 ± 472	-0.01 ± 0.01
δ^{18}O	-23 ± 1	-461 ± 101	0.017 ± 0.003
δ^{17}O	-13 ± 3	-1238 ± 219	0.017 ± 0.006

Table 5.3: Correcting function for the concentration dependence for the sample measurement (GS22) originating from a linear combination of the functions from the two calibration measurements

nation of the calibration is shown together with the averaged isotope measurements of figure 5.6 in figure 5.7. In light red, the error on the correction based on the uncertainty of the parameters is given. The adjustment function for the sample measurement calculated from a linear combination of the correction functions for the two calibration measurements agrees well with the measurement at different water concentrations of the isotope deltas for the sample measurement of GS22. With the functions describing the concentration dependency of the delta values for the two water standards (equation (5.3) and table 5.2) and the sample (table 5.3), the isotope measurements can be corrected for variations of the water concentrations. This correction is done by subtracting the linear and hyperbolic concentration dependence from the measured delta values:

$$\delta_{corr.} = \delta_{meas.} - \frac{b}{H_2^{16}O} - m \times H_2^{16}O \tag{5.5}$$

The adjusted isotope ratios are shown in figure 5.8 for all three isotopologues. The correction results in delta values that show no longer a dependency on the water concentration. For very low water concentrations ($<$ 50 ppmv), the correction is more problematic due to the large deviation from a linear dependency and shows larger uncertainties. The horizontal lines in the plots indicate the average delta values calculated over all water concentrations of the measurements, excluding concentrations below 50 ppmv because of the larger uncertainties.

The averaged measured delta values for the three measurements along with the real deltas are shown in table 5.4. After the correction of the concentration dependency, a calibration of measured versus true delta values can be done, assuming a linear relation between true and measured deltas (cf. equations 5.1 and 5.2).
In figure 5.9, a plot of real versus measured delta values is shown for δ^2H, δ^{18}O and δ^{17}O

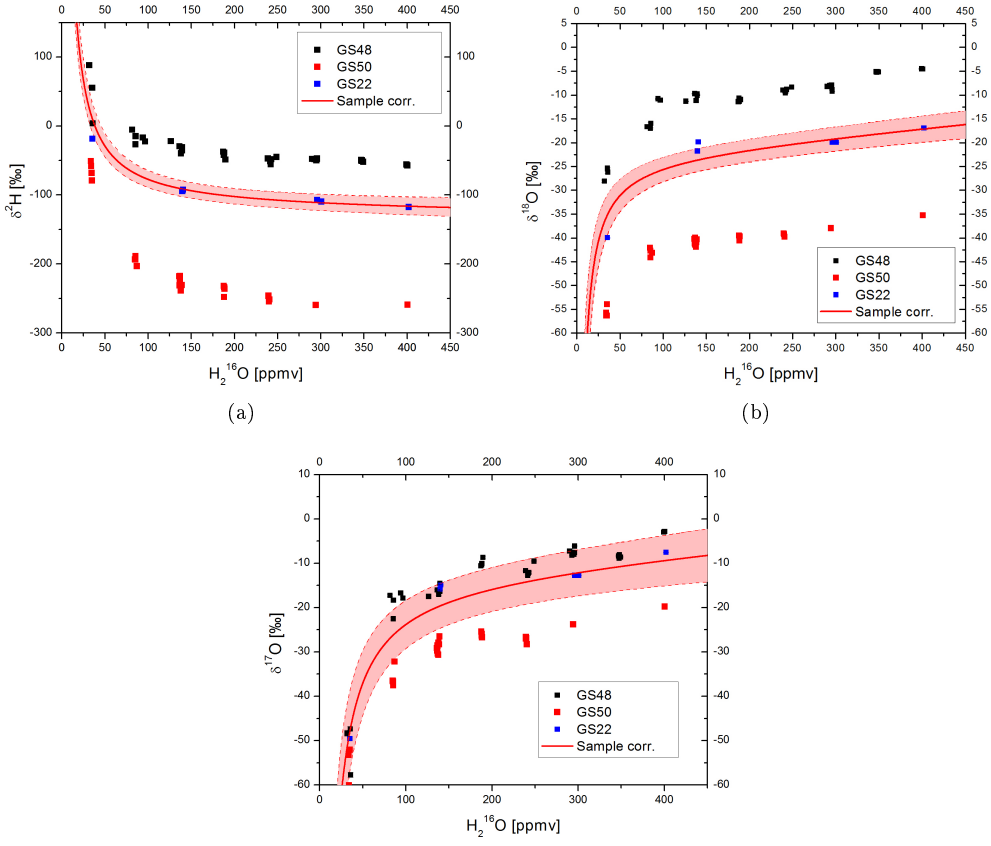

Figure 5.7: The adjustment function for the unknown sample (here GS22) determined from a linear combination of the adjustment functions from the calibrations for a) δ^2H, b) δ^{18}O and c) δ^{17}O. The light red area indicates the uncertainty of the function based on the standard deviation of the fit parameters. The adjustment function agrees well with the concentration dependency of the sample measurement.

	GS48	GS50	GS22
δ^2H true	-43.3 ± 0.3	-276.7 ± 0.3	-113.5 ± 0.3
δ^2H meas.	-57.4 ± 0.8	-281.5 ± 1.2	-124.2 ± 1.2
δ^{18}O true	-6.52 ± 0.03	-35.01 ± 0.03	-15.29 ± 0.03
δ^{18}O meas.	-12.0 ± 0.3	-38.6 ± 0.2	-21.8 ± 0.9
δ^{17}O true	-3.45 ± 0.02	-18.64 ± 0.02	-8.1 ± 0.02
δ^{17}O meas.	-8.4 ± 0.4	-23.8 ± 0.3	-11.3 ± 1.1

Table 5.4: Correcting function for the concentration dependence for the sample measurement (GS22) resulting from a linear combination of the functions from the two calibration measurements

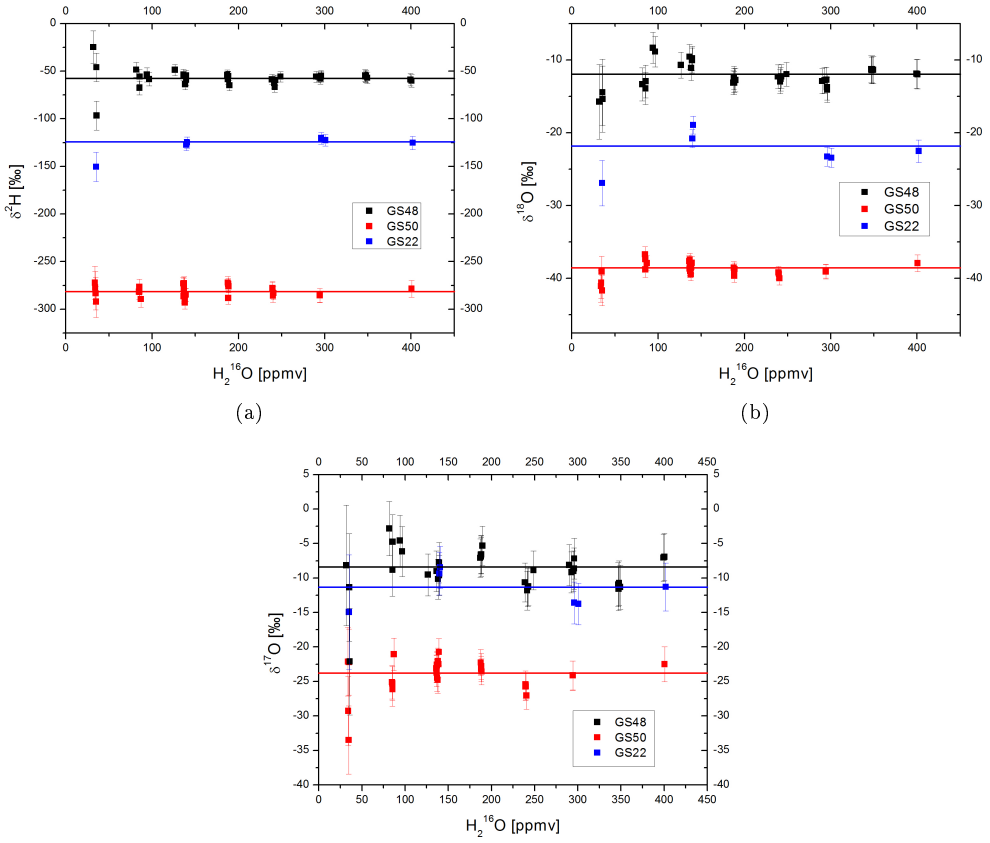

Figure 5.8: The averaged delta values from the two calibration and the sample measurement corrected for the concentration dependency. a) δ^2H b) δ^{18}O and c) δ^{17}O. The horizontal lines indicate the average delta values calculated for all measurement points with $H_2\,^{16}O > 50$ ppmv. Lower water concentrations are excluded because of much higher uncertainties due to the large contribution of the non-linearity in the concentration dependence function

along with the linear calibration function. The delta values are also plot for GS22, the sample measurement, to show the quality of the concentration correction and calibration procedure. Within the error on the calibrated deltas, they agree well with the true values.

For the calibration of our measurements, this results in:

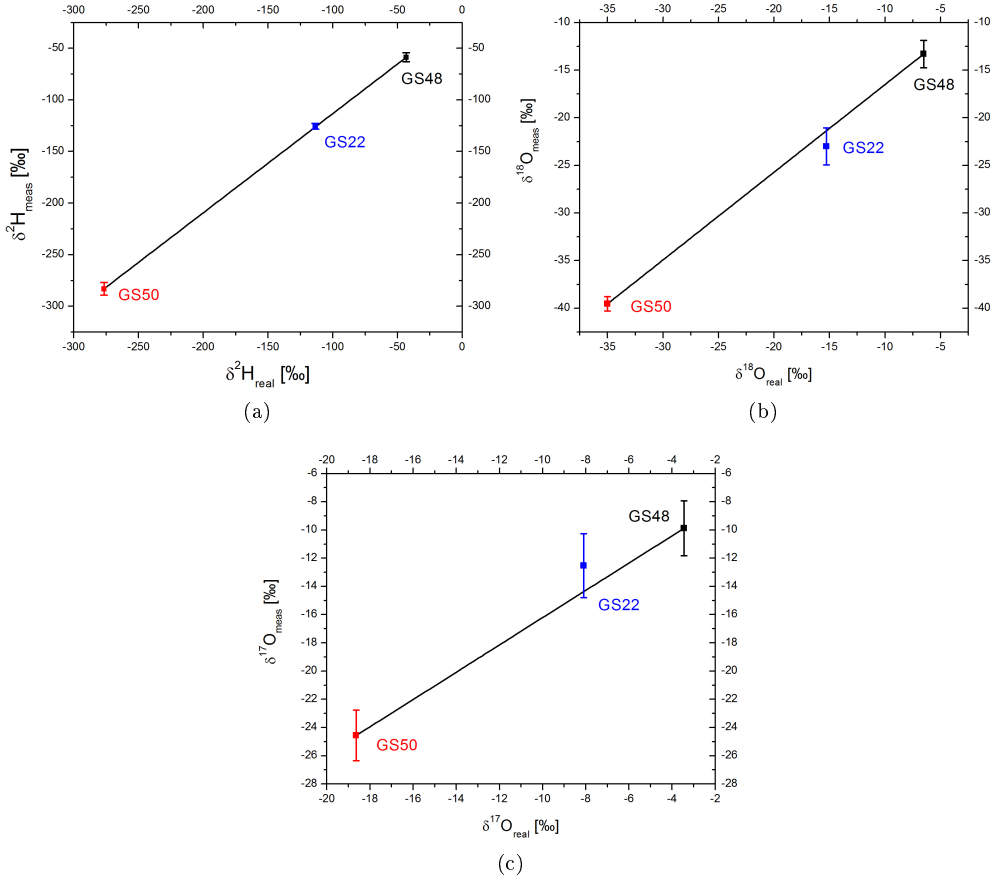

Figure 5.9: Plot of the measured delta value corrected for the water concentration dependence against the true delta value for a) δ^2H, b) δ^{18}O and c) δ^{17}O for the two calibration measurements with GS48 and GS50, averaged over all concentration steps above 50 ppmv. The error bars represent the 1-sigma standard deviation of the measured values. The GS22 value agrees for all three isotopes with the value given by the GS48-GS50 calibration lines.

$$\delta^2\mathrm{H}^{(c)} = 16.5 + 1.0415 \times \delta^2\mathrm{H}^{(m)} \tag{5.6}$$

$$\delta^{18}\mathrm{O}^{(c)} = 6.3 + 1.07153 \times \delta^{18}\mathrm{O}^{(m)} \tag{5.7}$$

$$\delta^{17}\mathrm{O}^{(c)} = 4.9 + 0.9889 \times \delta^{17}\mathrm{O}^{(m)} \tag{5.8}$$

with superscripts (c) and (m) for calibrated and measured values, respectively. The calibrated delta values, corrected for the concentration dependence, are shown in figure 5.10, with horizontal

lines indicating the true delta values of the respective isotope standards. Within the errors, the calibrated delta values agree well with the true values.

To better appreciate the accuracy of the calibration, the RMS deviation from the true value as

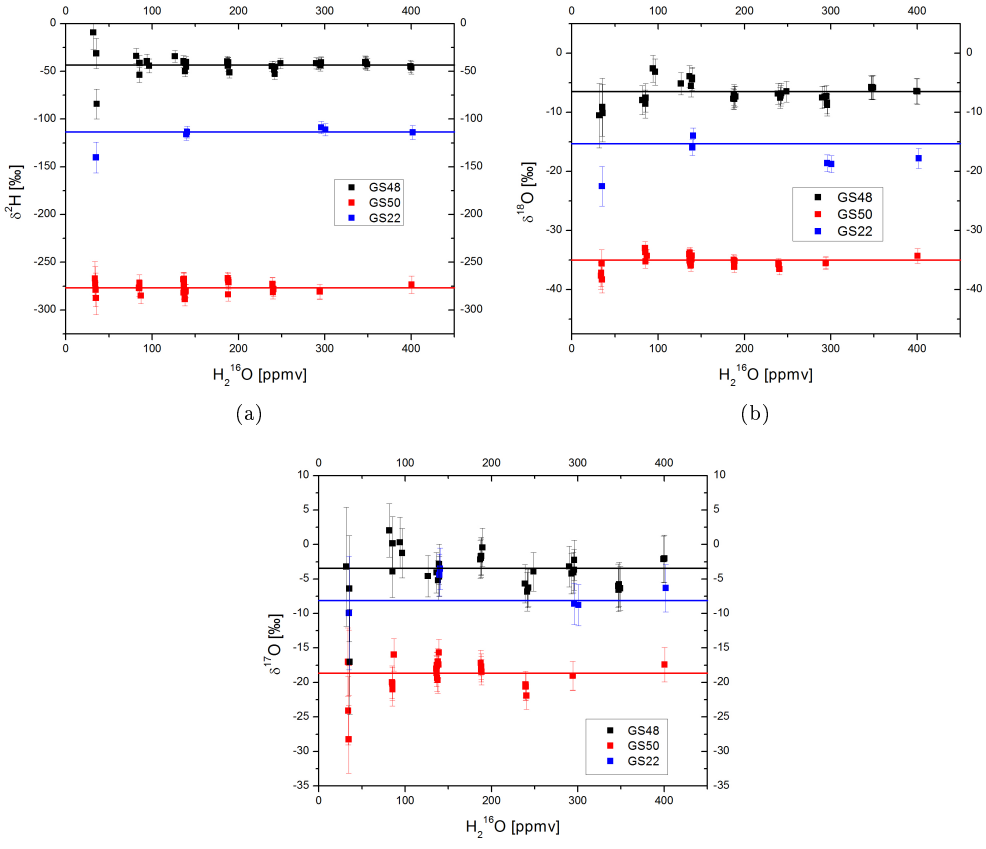

Figure 5.10: Calibrated delta values of the measurements, corrected for the concentration dependence, against the measured water concentration. The horizontal lines indicate the true isotopic composition of the different water standards.

a function of the water concentration is shown in figure 5.11. For water concentrations larger than 50 ppmv, the standard deviation is smaller than 10‰, 4‰ and 5‰, for δ^2H, δ^{18}O and δ^{17}O, respectively. For concentrations below 50 ppmv, the error increases because of the large non-linearity in the concentration dependence. For higher concentrations, the concentration dependence is less pronounced (cf. figure 5.4) and the error stays below the errors calculated here.

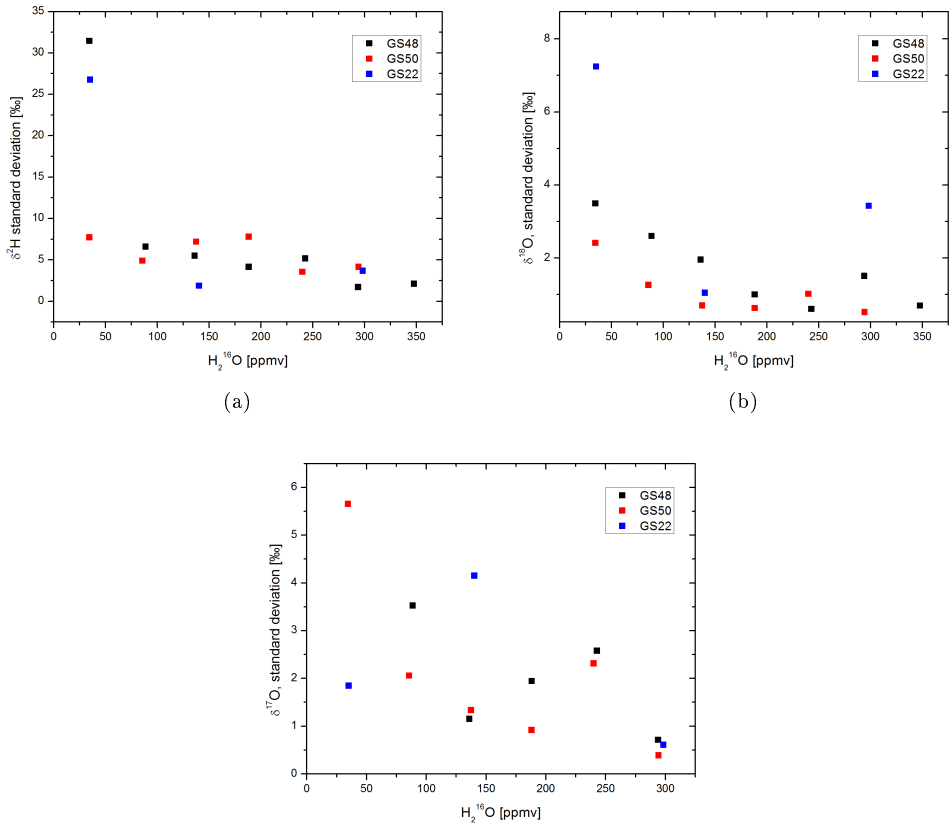

Figure 5.11: RMS deviation from the true value as function of the water concentration for the (a) δ^2H, (b) δ^{18}O, and (c) δ^{17}O isotope ratios.

5.1.1 Concentration dependence in other spectral ranges

In the spectral range at 7200 cm^{-1}, with absorption lines of $H_2\,{}^{16}O$, HD ^{16}O and $H_2\,{}^{18}O$, the concentration dependence of the delta values is also best described with equation (5.5). An ensemble of different calibration measurements at 7200 cm^{-1} averaged for each concentration step, is shown in figure 5.12 in a log-lin-plot. The non-linearity is comparable to that observed in the 7184 cm^{-1} region. A strongly enriched isotope standard (BEW2) was used. The change of the spectral region from 7184 cm^{-1} to 7200 cm^{-1}, which has better separated absorption lines, does not reduce the concentration dependency of the measurements. This might be an indication that the major source of the concentration dependence are strong absorptions outside the recorded spectral window, which dominate the baseline shape and can be found in both of the spectral regions.

In figure 5.13a, a plot of ${}^2R_{sample}/{}^2R_{VSMOW}$ versus the water concentration is shown for

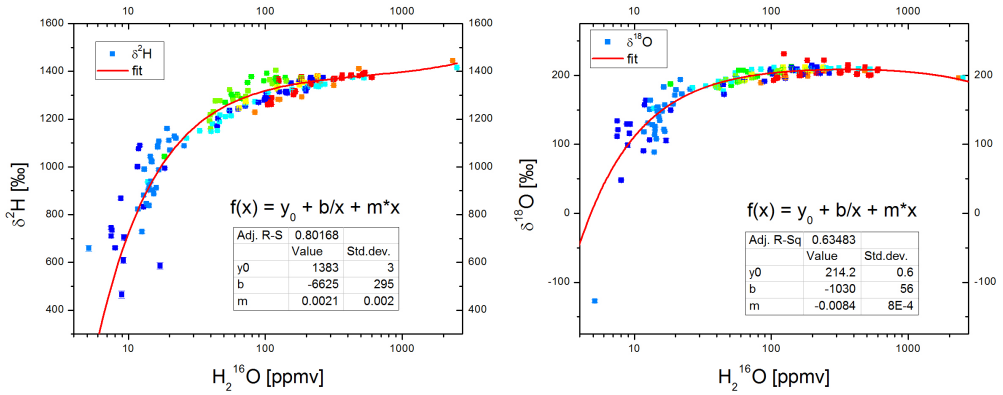

Figure 5.12: Set of a) δ^2H and b) $\delta^{18}O$ averaged over different water concentration steps from measurements at 7200 cm^{-1}. The different colors indicate different calibration measurements. As at 7184 cm^{-1}, the concentration dependence is best described with equation (5.5).

measurements at 7280 cm^{-1}. The water concentration dependency is less pronounced in this spectral region and can be approximated with a linear function. At any given concentration, the spread in the measurements is larger than the correction that would be applied.

Figure 5.13b shows ${}^{18}R_{sample}/{}^{18}R_{VSMOW}$ versus $H_2\,{}^{16}O$ for measurements at 7286 cm^{-1}. As explained above, this spectral range is well suited to low water concentration measurements (section 3.6) and in fact no measurements above 50 ppmv were possible due to saturation of the absorption signal on the strong transitions in this region.. A possible water concentration dependence is smaller than the measurement error at any given water concentration and can thus be safely neglected.

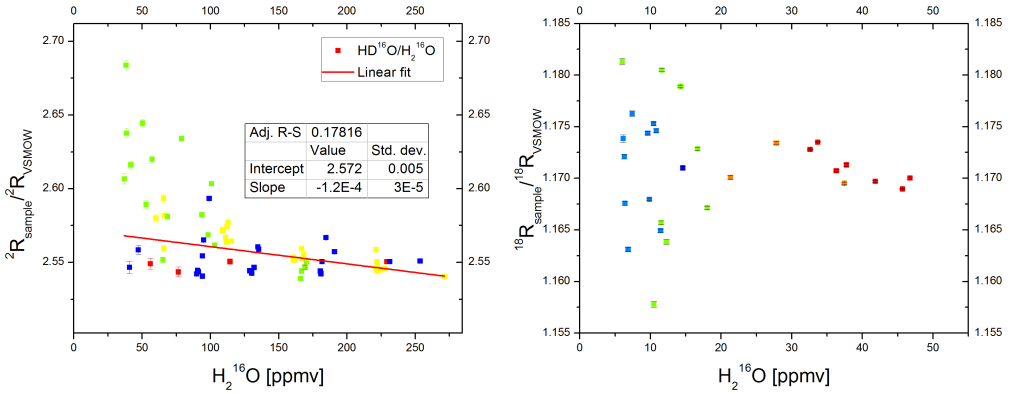

(a) (b)

Figure 5.13: Average a) $^{2}R_{sample}/^{2}R_{VSMOW}$, measured at 7280 cm^{-1} and b) $^{18}R_{sample}/^{18}R_{VSMOW}$, measured at 7286 cm^{-1} for different water concentration steps. The different colors indicate different calibration measurements. At 7280 cm^{-1}, the concentration dependence of $^{2}R_{sample}/^{2}R_{VSMOW}$ can be approximated with a linear relation. For measurements at 7286 cm^{-1}, a possible concentration dependence of $^{18}R_{sample}/^{18}R_{VSMOW}$ is smaller than the uncertainty at one concentration and no correction is applied.

Chapter 6

Calibration instruments

The measurement of isotope ratios is never an absolute measurement but is always done in comparison with measurements of known samples, called isotope standards. These additional calibration measurements are necessary to correct for instrumental artifacts like non-linearity or a dependence of the isotope ratios on the concentration at which they are measured [114]. In addition, small changes of temperature and pressure inside the absorption cell can influence the measurement and lead to a change in the measured isotopic composition.
Depending on instrument stability and the dependency of the isotope ratios on the concentration, a protocol with frequent calibration measurements of different isotope standards measured at one or different concentrations has to be established.
For these measurements, well determined isotope standards have to be used to enable an intercomparison of the measurements made with different instruments and to calibrate the values to the scale determined by VSMOW and SLAP (see section 1.2.1). Normally, the measurements calibrated with respect to laboratory standards, which in turn have been calibrated by IRMS with respect to the international standard materials VSMOW and SLAP.
Generally, these standards are distributed and stored as liquid water, whereas the optical spectrometers analyze vapor phase water. Therefore, a procedure is required to transform liquid water standards into water vapor without changing the isotopic composition, or alternatively with a change of the isotopic composition that can be determined independently of the spectrometer. If the liquid water is evaporated only partially, fractionation of the isotopes occurs and the isotopic composition in the vapor phase water no longer corresponds to the composition of the liquid water. In addition, one would like to vary the amount of water in the gas phase to be able to make isotope measurements at different concentrations and study the effect of these changes on the isotope ratios.
Not least because of the increased importance of optical spectrometers, a number of different calibration instruments has been developed. Several groups [65, 115, 116] propose to use a Dew Point Generator (DPG) to inject small amounts of water into a dry air stream and calculate the isotope ratios based on Rayleigh distillation curves. However, in these calibrations, the temperature has to be measured very precisely to determine the occurring fractionation and with smaller water reservoirs, the liquid water becomes increasingly enriched in the heavier isotopologues. In addition, these calibrations often require long time to stabilize and equilibrate and are typically done for 12 to 24h. An alternative way for the measurement of different liquid samples is the

injection of a small amount of liquid water into a heated chamber and to measure the pulse of the evaporation [117]. In combination with an autosampler, this procedure is well adapted to automatically measure larger numbers of liquid water samples. However, for continuous measurements of vapor phase water and small amounts of water, this method is not well suited.
Another possibility is to simply fill a pressurized tank with a mixture of a water standard and dry air, as was demonstrated in our group [6]. This works well as long as the dew point temperature of the water in the tank is lower than ambient air temperature. A drawback is that the isotopic composition could be affected by surface effects inside the tank. Iannone in his PhD work [118] established that with selected tanks that were previously conditioned with isotopically the same water, the isotopic fractionation was smaller than the measurement precision. The remaining drawbacks then are that the isotope range that can be covered is limited, that the water concentration is not easily varied, that the tank preparation is time consuming, and finally that the tank is big and heavy.
Alternatively, Iannone et al. [119] and later Sturm and Knohl [120] demonstrated the successful implementation of a Microdrop calibration system. With a piezoelectric micrdroplet generator, sub-microliter volumes of water are injected into a dry air stream. Because of the small volume, the water is immediately evaporated and no fractionation occurs. With an unheated evaporation chamber, this method can be used to generate water concentrations between 12 and 3500 ppmv. The Microdrop calibration system, which was also used for measurements of this thesis, is described in more detail in section 6.1.
A calibration instrument, developed by Lee and co-workers [65, 66], allows for a more easily adjusted water concentration. This device, called a dripper by the authors, uses a syringe pump to continuously inject water with a syringe pump into a heated evaporation chamber and transported to the spectrometer by a dry air stream. By changing the water injection rates between 1 and 12 µl/min, the water concentration can be varied between 800 and 30,000 ppmv.
Similar devices were built by Gkinis et al.[121] and Tremoy, Cattani et al. [122]. In the latter devices, a stream of liquid water of approximately 0.5 µl/min is generated with a syringe pump. From the main sample line, a small fraction is split-off and directed through a fused silica capillary towards a hot oven, stabilized at 170°C with a PID-controlled heater. The capillary has an inner diameter of 100 µm, which imposes a back pressure and efficiently reduces the water injection into the evaporation chamber. Through the chamber, a dry air flow is guided and transports the water vapor to the spectrometer. Whereas the calibration device of Gkinis et al. works reliable between 17,000 and 22,000 ppm, the instrument of Tremoy, Cattani et al. was tested between 2000 and 30,000 ppmv. After an adaption to lower water concentrations, this set-up was also employed in our measurements (see chapter 7).
A very robust system that has seen wide-spread use and convinces because of its simplicity is the so-called bubbler [37, 52, 123–127]. A dry nitrogen or air flow is guided through a larger volume (typically several liters) of liquid water, often through a diffusor to create smaller gas bubbles. While the bubbles rise through the water column, the gas inside the bubble becomes saturated

in water. The temperature inside the water container is stabilized and monitored. Because of this, it is possible to calculate the isotope ratios in the water vapor, assuming equilibrium fractionation during the phase change (section 1.2.2,[35, 36]). To vary the water concentration, the saturated gas flow is subsequently combined with a variable dry gas flow. As long as a large liquid water volume is used, the increasing enrichment of the liquid phase is often negligible and well below the measurement precision. However, it also means that large amounts of standard water have to be used. In addition, an additional error is introduced because of the indirect determination of the isotopic composition of the vapor phase based on the assumption of equilibrium fractionation.

Apart from calibration systems developed by individual groups, there are also commercial versions available. The Standard Delivery Module (SDM) in combination with a Vaporizer (Picarro Inc.) is based on two syringe pumps injecting a small continuous water flow into an evaporation chamber, heated to 140 °C [78, 122, 128], through which a dry air stream is guided. Due to the high temperature in the injection chamber, water is evaporated at the meniscus of the needle and after a short equilibration time, the isotope ratio of the vapor phase equals that of the liquid standard water. Because of the two syringe pumps, automatized calibrations with two standards can be performed. Another method is used by the Water Vapor Isotope Standard Source (WVISS, Los Gatos Research)[114]. In this device a nebulizer aspirates liquid water from a 0.5 l water reservoir and injects small water droplets into an evaporation chamber, heated to 80 °C. Following the evaporation, the humid air is mixed with a variable dry air flow. With an injection rate of 50µl/min H_2O and an additional dry air flow of up to 5 l/min, concentrations between 2500 and 25,000 ppm can be achieved[114].

Recently, Gkinis et al. introduced an ultrasonic concentric nebulizer, which has been used for the isotopic analysis and calibration of ice cores [129].

Several of the above mentioned calibration set-ups proved to work reliably and generate water vapor at different concentrations without fractionation. However, to the best of our knowledge, no reliable and robust option exists for the calibration at water concentrations below 500 ppmv. Some of the instruments could potentially be adapted to produce lower water concentration by an increase of the air flow through the evaporation chamber, or by subsequent dilution of the humidified air stream with dry air (see also the calibration discussion in chapter 7). This, however, results in a large consumption of costly and often limited standard water, and/or requires a large amount of air dried to a level that is not easily obtained in an on-line drying technique (e.g., using Drierite™). In addition, the air flow can not be greatly increased as this would result in turbulent flow, which reduces or destroys the stability of the injection. Also, with an air flow rate of 5 standard liters per minute (slm), the water injection would still need to be lower than 2 µl/min to reach a water mixing ratio lower than 500 ppmv..

6.1 Microdrop injector

An instrument that allows the generation of very low water concentrations is the microdrop generator [130], which was first introduced for water vapor measurements by Iannone et al. in 2007 [131] and was later also used by other groups [120, 123]. With their microdrop generator, Iannone et al. [119] were able to generate water mixing ratios ranging from 12 to 7600 ppmv using a commercial piezo-electric droplet generator (Microdrop GmbH, model MD-K-130) to generate subnanoliter water droplets injected into a stream of dry synthetic air or nitrogen. Due to the small size of the water droplets, evaporation is immediate and no fractionation occurs. The microdispenser technology used for the generation of microdroplets is based on the same principle as common inkjet printer nozzles [132, 133]. Around a glass capillary with inner diameter 30 µm, a piezo ceramic tube is mounted. When a voltage pulse is applied to the piezoelectric component, the capillary tube is contracted and the liquid inside is ejected as a droplet. For the generation of a droplet, the contraction of the glass capillary has to generate sufficient inertia to overcome surface tension and viscous forces. By changing the pulse width and intensity, it is possible to adjust to a specific droplet size. The pulse frequency determines the number of droplets per time and therefore the water concentration. A series of photographs showing the generation of a water droplet is shown in figure 6.1, taken from [119]. In the middle of the droplet generator, the glass capillary can be seen. In the third image, the ejection of the droplet is shown, which is followed by a retraction of the remaining water back into the capillary.

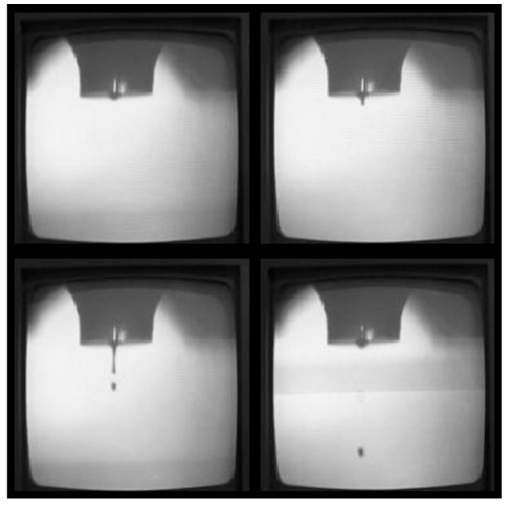

Figure 6.1: Generation of a microdrop with the piezo injector. In the third image, the droplet is ejected and the remaining water column retracts back into the glass capillary.

6.2 Syringe Nanoliter Injection Calibration System

Because the existing calibration instruments were not adapted to generate water concentrations as low as several tens of ppmv and the failing of the microdrop generator during the preparation of our Troll measurement campaign (see chapter 7), an alternative calibration system, the Syringe Nanoliter Injection Calibration System (SNICS), based on very low injection rate syringe pumps was developed in the framework of this thesis. It was developed to offer a more robust and fully automatized method to regularly calibrate water vapor isotope ratio measurements at low volume mixing ratio (vmr) with liquid water standards. An additional goal was to waste as little standard water as possible, thus requiring water injection rates as low as several tens of nl per minute to match the optimal concentration range of our OF-CEAS spectrometer.
A schematic of the calibration instrument is shown in figure 6.2a. At the core of SNICS are two high precision syringe pumps (Harvard Apparatus) that can inject two different standard waters into separate evaporation chambers 6.2b. A dry carrier gas is connected to both of the injection chambers. Because of two upstream installed mass flow controllers (MFC, Bronkhorst), the flow rate through each of the chambers can be individually adjusted. Behind each evaporation chamber, an electronic three-way-valve is connected, which allows to select, which of the two evaporation lines is connected to the OF-CEAS spectrometer. Typically, one of the two injection lines ("measurement line") is connected to the OF-CEAS spectrometer, whereas the other one ("waste line") is connected to a supplementary vacuum pump. In front of the outlet to the OF-CEAS spectrometer, an upstream pressure regulator (Bronkhorst) has been installed, behind which a vacuum pump is connected. This enables setting the gas flow rate in the measurement line independently of the flow rate through the spectrometer and to stabilize the pressure in the measurement line. The difference between incoming and outgoing flow is automatically compensated by an additional flow to the vacuum pump.
To provide stable conditions also in the waste line, a proportional valve with an additional vacuum pump downstream, is connected to the other exit of the two three-way-valves. With this valve, the pressure in the waste line is typically adjusted to the same pressure as in the measurement line.
Because of the two independent lines, it is for example possible to initialize a stable injection of two different standards at the same time and to quickly switch between the two standards by simply changing which of the evaporation chambers is connected to the spectrometer. Alternatively, it is also possible to inject the same water standard in both lines but at different water concentrations to investigate water concentration dependencies.
An additional three-way-valve at the outlet to the spectrometer allows to also connect a sample gas and to quickly change between calibration and measurement. To increase the stability of the device, the entire calibration set-up is mounted into a thermally insulated 19 inch box, which is stabilized in temperature with a PID regulated peltier in combination with two mixing fans (Laird Technology, Supercool). In addition, this makes the calibration set-up easily trans-

portable. The read-out of flow and pressure as well as the control of flow, pressure and electronic valves is done via two data acquisition cards (National Instruments, Measurement Computing). The syringe pumps are connected to a computer through a built-in USB port.
For the combined read-out and control of all components of the calibration set-up, we developed a new Labview program. This program allows to run fully automatized calibration cycles with changes in gas flow and water injection rates as well as changes between the two injection lines.

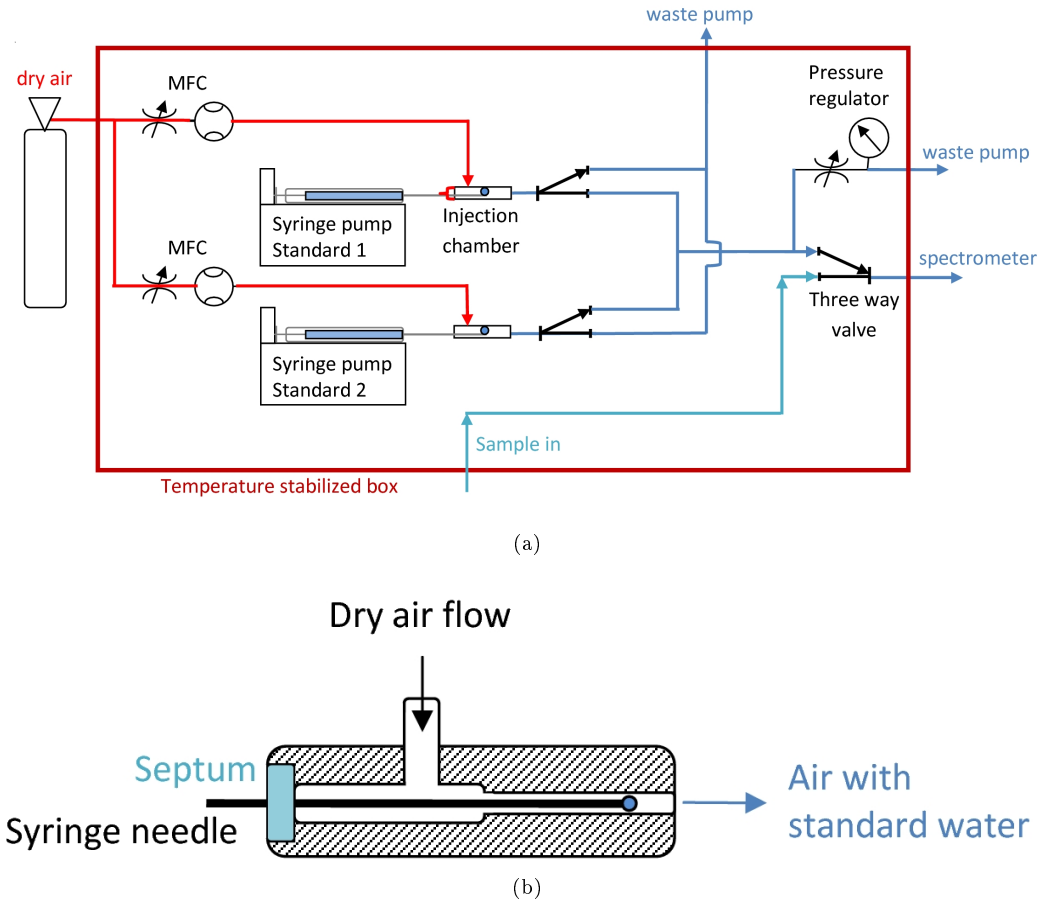

Figure 6.2: Schematics of SNICS (a) and the flow chambers in which the water is evaporated (b)

6.2.1 Modeling of the syringe injection

In figure 6.3, the tip of a syringe needle with a water droplet during a stable calibration run is shown. The water exiting at the tip of the syringe needle does not immediately evaporate upon injection from the standard reservoir inside the syringe but builds a droplet from which

evaporation occurs. To good approximation the evaporation rate will be proportional to the exposed surface area of the droplet. Therefore, initially the evaporation rate is smaller than the supply rate of water from the reservoir through the needle (Hamilton Company™, gauge 26, internal diameter = 0.464 mm) and the droplet will grow in size. Steady-state will be reached when the evaporation rate equals to water supply rate. In the following paragraphs we will derive equations describing the dynamics of the droplet and its isotopic composition.
We assume the droplet on the syringe needle from which water is evaporated to be a spherical cap (cf. figure B.1a) with volume V_{drop}. The evaporation from a droplet inevitably results in isotope fractionation between this volume and gas phase water. However, as the syringe injection gives a constant supply to the droplet, always yielding the same isotope ratio, in steady state conditions, this leads to an equilibrium with an enriched water droplet such that the liquid-vapor fractionation renders the isotopic composition of the vapor phase equal to that of the water supplied from the syringe, as will be shown below.

As evaporation occurs at the surface layer of the droplet only, the surface will be strongest

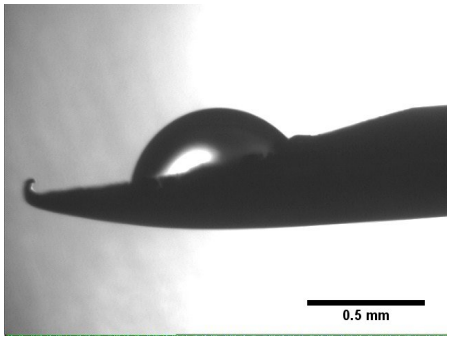

Figure 6.3: Image of the syringe needle tip with a droplet during a calibration run

enriched in the heavier isotopes with a gradient of the isotope ratio perpendicular to the surface, which is determined by the diffusivity of the heavier isotopes. The inhomogeneity of the water droplet in the different isotopes can be estimated by the average distance a (heavy) water molecule has traveled in the droplet due to diffusion. The diffusion length L can be calculated with [134]:

$$L = 2\sqrt{Dt}$$

with D the diffusion coefficient and t time. The diffusion coefficients of HDO and $H_2\,^{18}O$ in water have been measured to be $2.34 \cdot 10^{-9}$ m^2/s and $2.66 \cdot 10^{-9}$ m^2/s, respectively [135], yielding the diffusion lengths for 1s of 110 µm and 117 µm. They are thus of the same order of magnitude as the radius of the droplet and we can make the assumption that the entire droplet and not just a surface layer is becoming enriched in the heavier isotopes.
Because of injection rates as low as 100 nl/min, the diffusion velocity is comparable, but opposite

in sign, to the velocity of the water flux injected with the syringe. We thus have to determine if the diffusion is large enough to change the isotopic composition in the syringe itself. The syringe needle, which is generally used for the calibrations, is a 26 gauge needle with 51 mm length (Hamilton) and 464 µm inner diameter. The speed of the flux inside the needle at 100 nl/min is thus

$$v_{flux} = \frac{100 \text{ nl/min}}{A_{needle}} = 12 \text{ µm/s}$$

with A_{needle} the internal cross section of the needle. To calculate the penetration depth in the needle of the diffusing heavier isotopologues, we equate the diffusion length and the distance crossed of the injection flow

$$2\sqrt{Dt} = t \cdot v_{flux}$$

which leads for $H_2\,{}^{18}O$ to

$$t = \frac{4D}{v^2} = 74 \text{ s}$$

The penetration depth inside the needle is thus

$$L_{needle} = t \cdot v_{flux} = 0.9 \text{ mm} \tag{6.1}$$

This corresponds to an enriched volume of 114.57 nl inside the needle. With a total length of 51 mm of the needle, this is however less than 2% of the needle length. We thus conclude that the isotope ratio in the syringe volume itself is not changed.

Instead of an isotope ratio gradient inside the droplet, we assume an enriched surface layer volume and a core volume with the isotope ratio of the water standard (figure 6.4). This means that the syringe calibration system is built of three different water volumes:
1) the syringe reservoir with constant isotope ratio R_0 of the given water standard and a flow rate $\Phi_0(t)$, which is determined by the injection speed of the syringe pump.
2) the core volume of the droplet, which has a time dependent volume $V_C(t)$ and constant isotope ratio $R_C(t) = R_0$.
3) The surface layer of the droplet with volume $V_S(t)$ and isotope ratio $R_S(t)$, which is influenced by the evaporation from the surface layer and a continuous supply of the isotope standard from the core volume V_C. For the surface volume, we assume a constant thickness d, which is determined by the diffusion of water molecules in the surface layer. For small d, we can approximate V_C to be the surface area A_S multiplied with the thickness of the layer:

$$V_S(t) = A_S(t) * d \tag{6.2}$$

Alternatively to the volume of equation (6.2), the volume can be taken equal to the entire droplet volume, which would be the limiting case for large diffusion coefficients with a sufficiently high flow speed in the needle to avoid back diffusion into the syringe reservoir.

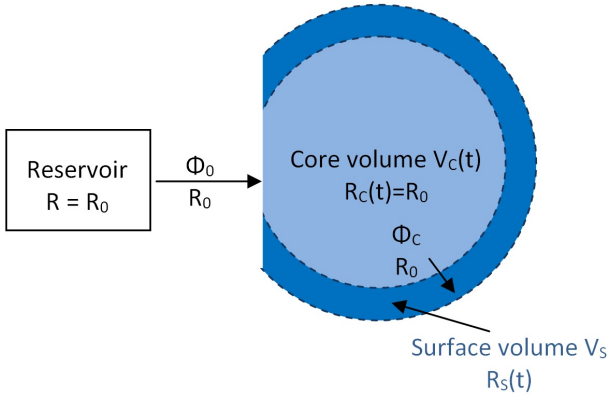

(a)

Figure 6.4: Modelling approach for the water injection with SNICS. Water from the syringe reservoir is injected into a core volume V_c with identical isotopic composition. From the core volume, the water is transported to an enriched surface volume V_s with isotopic composition $R_s(t)$.

A detailed discussion of the model can be found in chapter B, here we only present the results. Based on our modelling approach, the isotope ratio of the enriched surface layer can be calculated by

$$R_S(t) = \frac{\psi(t)}{1+\psi(t)} \tag{6.3}$$

and the isotope ratio of the vapor phase with

$$R_e(t) = R_S(t) \cdot \alpha_V \tag{6.4}$$

6.2.2 Comparison with experimental data

In the following, we will now compare the results of the theoretical model described above, with real experimental data.
Other than the model, the experimental data is smoothed because the response time of the OF-CEAS spectrometer. To include this response into our model, we filter the model output by a double-exponential time response. The two time constants of the exponential were determined in transition experiments with the real instrument and were set to $\tau_1 = 30$ s and $\tau_2 = 300$ s. In addition, the two exponential functions were weighed differently, with a ten times larger amplitude of the fast time response.

6.2.3 Calibration with two syringe pumps

The use of two different injection lines offers the possibility to quickly change between two different water standards or between different concentrations of the same water standard without the penalty of an additional time delay because of the time required to reach a new steady state of the injection module. In figure 6.5, a measurement with regular changes between the two injection lines is shown. One syringe pump was used to inject a slightly depleted standard (GS48), whereas the other syringe was filled with a strongly enriched standard (BEW2).

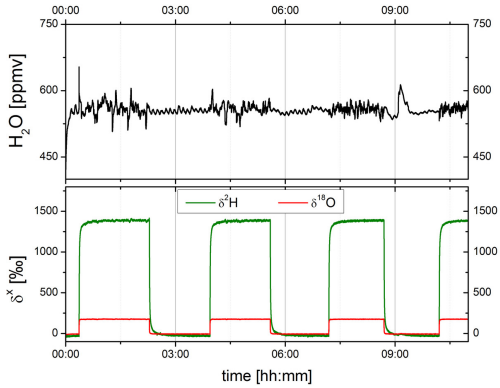

Figure 6.5: Measurement using the two separate injection lines in SNICS. One syringe injected a slightly depleted water standard (GS48), whereas the other syringe was filled with BEW2, a strongly enriched standard. Using the two different lines, it is possible to make much faster changes of water concentration or water standard than would be possible with only one syringe pump

In figure 6.6, a calibration run with the 100-µl syringe under constant conditions is shown. The water injection rate was set to 150 nl/min and the air flow rate to 300 sccm, resulting in a mean water concentration of around 660 ppmv. Whereas the isotope ratios are very stable throughout the calibration run, an oscillation with amplitude 2.2 ppmv, thus 0.33% of the water concentration, can be observed in the water concentration measurement. A Fast Fourier Transform (FFT) of the water concentration measurement yields an oscillation period of 424 s. With an injection rate of 150 nl/min, this corresponds to an injected volume of 1.06 µl. Taking the inner diameter of 1.46 mm of the syringe into account, this corresponds to a distance of 633 µm covered by the plunger of the syringe during one oscillation. This value matches very well the distance of 635 µm that is specified for one full revision of the lead screw of the syringe pump [136]. The oscillation is thus caused by inhomogeneities of the turning of the lead screw of the syringe pump. It is also present with the second syringe pump and changes its period and amplitude if a smaller or larger syringe is used. In the isotope ratios of the same measurement, this oscillation is not visible and neither is it in the FFT of the isotope ratios. In general, the oscillations of the water concentration are small enough to not affect the isotope ratios. In cases,

where it is visible in the isotope ratios (e.g. when a larger syringe is used), averaging of the isotope ratio over the entire oscillation period is recommended.

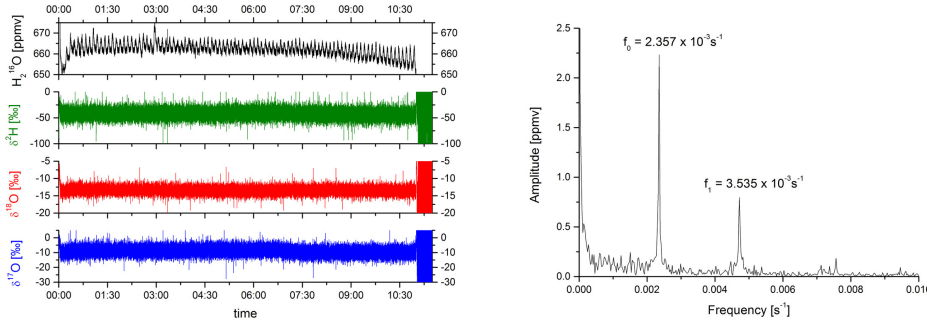

(a) (b)

Figure 6.6: Calibration run for one water concentration, with 150 nl/min water injection and an air flow rate of 300 sccm. (a) Water concentration and isotope ratios during the entire calibration run. The water concentration shows an oscillation, which is caused by a variation of the injection rate due to the syringe pump (b) FFT of the water concentration, yielding an amplitude of 2.2 ppmv and a frequency of 2.357×10^{-3}Hz of the oscillation, leading to a period of 424 s which corresponds exactly to the period of revolution of the lead screw of the syringe pump. The amplitude of the oscillation is thus smaller than 1% of the total water concentration.

In figure 6.7, a calibration run with a constant air flow of 180 sccm and water injection rates between 10 and 130 nl/min is shown. In figure 6.7a, the non-averaged water concentration measurement is shown together with the water concentration calculated from water injection and air flow rates. The light gray curve shows the entire measurement data whereas the black indicates the data used to average over each concentration step. In the raw data, four sudden drops in the water concentration are visible. These disruptions are due to the formation of air bubbles at the connection from syringe to needle and which disturb because of their larger compressibility. The formation of air bubbles can be avoided following a more careful syringe filling procedure, in which the syringe is filled with a small disposable syringe from the back and the plunger is inserted only afterward. In figure 6.7b, the average water concentration of each injection step has been plot against the calculated water concentration. The relation between calculated and measured water concentration is perfectly linear. The intercept of 10 ppmv is due to residual water in the carrier gas, whereas the slope of 1.029 probably originates from uncertainties in both the Hitran parameters for the intensities of the absorption lines (for the $H_2{}^{16}O$ line at 7183.6858 cm^{-1}, the uncertainty is 5 - 10% [61, 137]) and the uncertainties in the air flow measurement (0.6%, [138]) and the water injection rate (0.35%, [139]).

As mentioned in the model of the syringe injection (section 6.2.1), the very low water injection rates used with SNICS result in injection velocities that are of the same order of magnitude as the diffusion velocities of the molecules. Based on the estimate given above, the diffusion

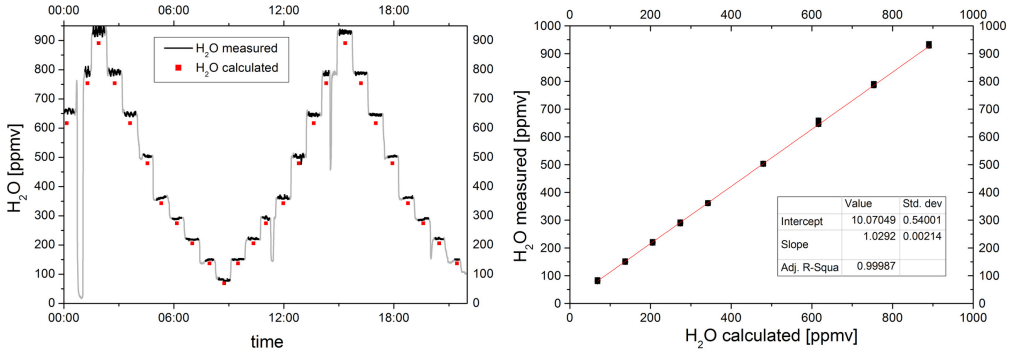

(a) (b)

Figure 6.7: Long term calibration measurement with different water injection steps to change the water concentration. a) the raw H2O measurement compared to the calculated water concentration based on water and air flow rates. b) The linear fit of the averaged water concentration at each calibration step versus the calculated water concentration shows a perfectly linear dependence.

however does not lead to a change of the isotopic composition of the water reservoir in the syringe itself.

In the case of diffusion velocities that are larger than the injection velocity in the syringe needle, the water in the syringe would become increasingly enriched throughout a calibration run. If this would be the case, the water vapor would also show an increase of the heavier isotopologues during the calibration. For an experimental investigation, several measurements were made with a stable injection of water over the entire syringe volume. In order to calibrate the measurements and to separate instrumental drift from a gradual change of the isotopic ratios in the syringe volume, we frequently switched from SNICS to an injection of the same standard with the piezo injector ([119]), in which no fractionation of the water throughout a measurement occurs. Changes between the two calibration methods were done by a change of the injection line, in both lines the water injection and a stable air flow were maintained over the entire measurement.

A measurement with regular switching between SNICS and piezo injector is shown in figure 6.8, with a) the water concentration during the measurement and b) δ^2H. Throughout the calibration, instrumental drift leads to a decrease of the isotope ratio for both calibrations but the isotope ratio for the syringe injection shows no systematic difference or change over time compared to the piezo injections. This means that no change of the relative isotopic abundances or a change smaller than the instrumental drift occurs during the syringe calibrations.

In conclusion, the new Syringe Nanoliter Injection Calibration System offers a robust and precise alternative to other calibration methods such as bubblers or piezo injector and can be used for long measurements for instrumental characterization as well as for normal inter-measurement calibration runs at one or several concentrations with up to two different water

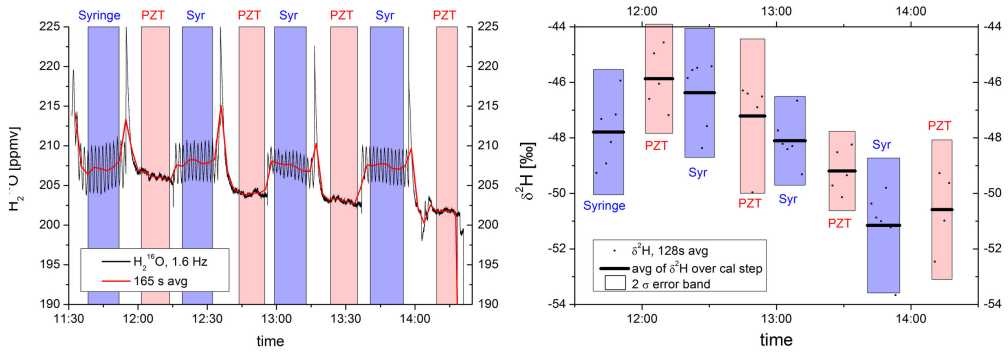

(a) (b)

Figure 6.8: A calibration run with regular changes between injection of the same water standard by piezo injector and SNICS.

standards. The buildup of a water droplet and the time until equilibrium with stable isotope ratios can take several minutes. As soon as equilibrium is reached, the isotope ratio in the vapor phase is identical to the isotope ratio of the water standard and no fractionation inside the syringe reservoir occurs due to diffusion. By changing between two different syringe injection lines, faster changes between different concentrations or standards is possible. In the current set-up, operator invention is still required to refill the syringes. However, we plan to remedy this drawback by equipping the system with a system with a 3-way liquid flow valve immediately following the syringe, either directing the syringe output towards the needle, or enabling the syringe to be refilled from a closed standard water reservoir. The refilling is possible with the syringe pump model used in SNICS, which offers a withdraw mode.

Chapter 7

Water vapor isotopologues in Antarctica

In the context of a globally warming climate it is crucial to study the climate variability in the past and to understand the underlying mechanisms [140]. Precipitation deposited on the polar ice caps provides a means to retrieve information on temperature changes (through the paleo-temperature dependence of the isotopic composition of the ice) and atmospheric composition (of gas stored in bubbles in the ice) on time scales from one to almost one million years, with sub-annual resolution in the most recent centuries [141]. However, it is now widely recognized that the calibration of the paleo-thermometer is highly problematic. For this reason attempts to model the global water cycle, including the isotope signals, are ongoing with the aim of providing a more physical basis of the isotope - temperature relation. Currently, there is a large divergence in the results obtained by different modeling strategies. The missing link in these model studies is their forcing by experimental data on the pre-deposition isotopic composition of the vapor phase compartment of the hydrological cycle. We propose to measure the isotopic composition of moisture carried towards and deposited on Antarctica, in order to constrain the numerical models. For these reasons we have developed the OF-CEAS spectrometer described in this thesis and measured water vapor isotopologues in Antarctic air. The instrument was first operated at the Antarctic Research station Troll, to continuously measure in-situ the three stable isotope ratios of atmospheric water vapor.
The Norwegian Research station of Troll is located in Queen Maud Land, Antarctica (72°01'S, 2°32'E, 1275 m a.s.l.) at approximately 220 km from the Antarctic coast. Troll station is one of the few stations located at the slope of the Antarctic ice sheet, which is exposed to varying influence from the Antarctic plateau and the Southern Ocean [142]. Because of this it is ideally suited to study the transportation of humid air from the ocean to the Antarctic plateau as well as continental transportation of atmospheric moisture.
The main complex of the research station is built on ground rock, whereas the air field is located on the blue ice at approximately 7 km from the main station (cf. figure 7.1).

7.1 The Antarctic spectrometer design

During the Antarctic campaign, the instrument was measuring at 7184 cm^{-1}, allowing simultaneous measurements of $H_2^{16}O$, $HD^{16}O$, $H_2\,^{18}O$ and $H_2\,^{17}O$. The general design of the instrument

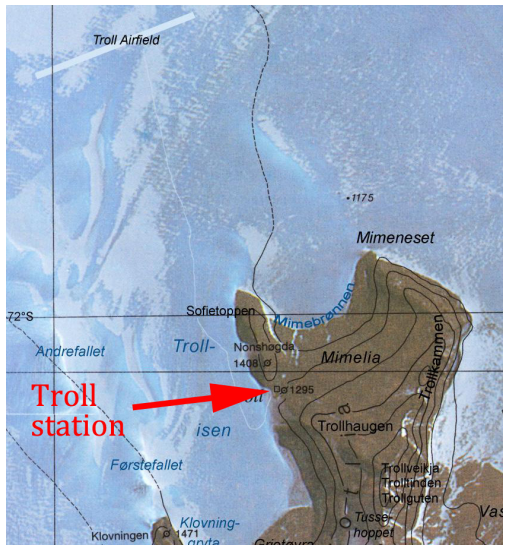

Figure 7.1: The location of Troll research station. The main complex of the station is placed on submontane rock, whereas the air field is 7 km from the main station on the blue ice (map provided by the Norwegian Polar Institute)

is as described in chapter 3. However, some differences will be discussed in the following. During the measurement campaign, the instrument was powered by two internal switching power supplies (Mean Well RD-125 and TDK Lambda LS75), providing 5V and 24V and 15V, respectively. Instead of a Bronkhorst flow controller (cf. chapter 3), the pressure inside the instrument was stabilized with an adjustable vacuum pump at the exit of the instrument (KNF 84.4ANDCB), controlled with a PID loop regulating the cavity pressure. The flow was regulated with a sonic nozzle at the inlet of the instrument. The sonic nozzle is basically a tube which has on the upstream side a convergent cross section and a smooth rounded outlet section with a small opening in the center through which the flow has to pass. Because of this restriction, the flow is accelerated to supersonic speed in the opening and the flow rate through the nozzle becomes a linear function of the inlet pressure and independent of the downstream pressure [143], as long as the downstream pressure is significantly smaller than the inlet pressure ($p_{in} > 1.4 \times p_{out}$). With an inner diameter of the nozzle of 100 µm and atmospheric pressure at the inlet, the flow was regulated to 110 sccm during the campaign.

A photograph of the Antarctic OF-CEAS set-up is shown in figure 7.2 with the beam path indicated in yellow and some of the optical elements highlighted in red. The ring-down time, which was in a later version of the instrument increased to up to 150 µs for this wavelength region, was limited to 80 µs because of the lower reflectivity of the mirrors that were used.

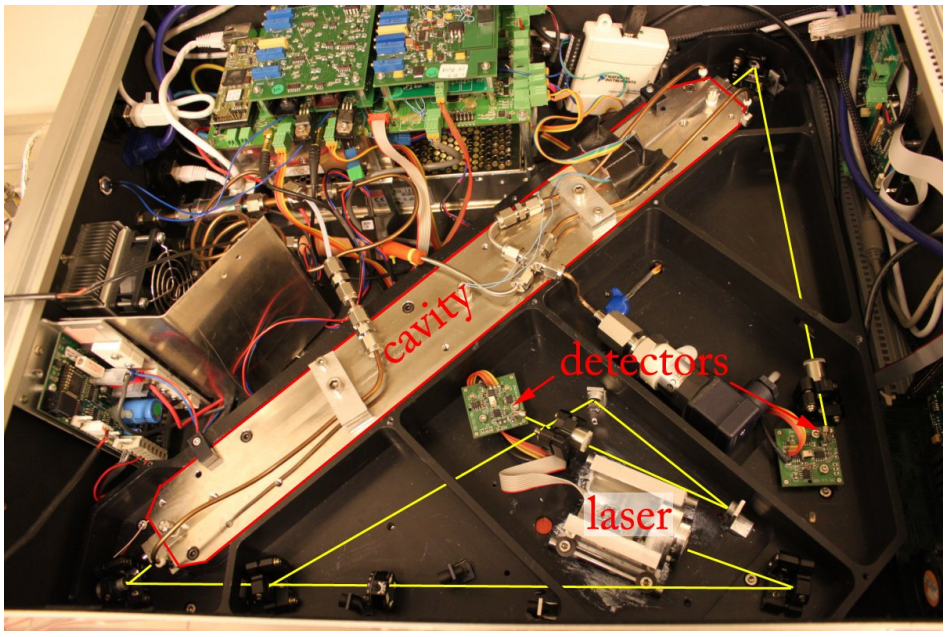

Figure 7.2: The OF-CEAS spectrometer design used during the Antarctic mission. In yellow, the beam path is indicated.

7.2 Local set-up

Because of the requirement of a sufficient power supply and an insulated measurement container, we were bound to install our measurement set-up in the close vicinity to the main complex of the station. To be the least influenced by emissions of the station itself, the spectrometer was installed in a small insulated container approximately 200 m from the main building and situated at the border of the station arrangement (see figure 7.3). The measurement inlet tubing was directed in west-north-west direction. Whereas in the winter half-year, winds are most of the time coming from North-East and East-South-East, the wind direction in the summer months is more fluctuating, but with a median around 30° [142]. In figure 7.4, a polar diagram of wind at Troll Station during the measuring period in January and February 2011 is shown, the data was provided by the Norwegian Institute for Air Research (NILU). Approximately 40% of the time, the wind was coming from a corridor of 22.5° to 135°, corresponding to the direction of main buildings of the station. Another 40% of the time, wind was coming from South and West (157.5° to 337.5°), and 20% of the time from North, which is the direction of minor station buildings. To avoid contamination of the collected air sample by the operation of the research station, it would have been better to measure at a larger distance of the station buildings. Unfortunately, because of the necessity of a power source and local infrastructure, neither this nor a measurement location to the north east of the station was possible.

Figure 7.3: Photography of the arrangement of Troll station, with an arrow indicating the container used for our set-up throughout the measurement campaign. On the bottom of the figure, a compass has been added to indicate cardinal directions.

The spectrometer was installed on a table inside the container, which had a size of approximately 2 x 2.5 x 2 m and a volume of 10 m^3. The inlet tubing was a Silcotek treated stainless steel tubing connected to the outside via a venting slot in the wall of the container. To avoid freezing or clogging of the tube, it was constantly heated to approx. 50°C with a self-regulating heating band (Horst GmbH) and thermally insulated. To avoid snow entering directly into the inlet tubing, a small plastic cover was mounted around the inlet (figure 7.5).
Because of the small size of the measurement container, solar heating during day time in combination with the heat generated by the electronics, in particular by the heating band and the heating of the calibration device (see section 7.3.1), led to an increased temperature of up to 30°C in the room. Together with the heat generated by the internal power supply of the OF-CEAS spectrometer, this led to problems in the temperature stabilization of the spectrometer itself, which could not be sufficiently cooled. This problem was largely solved by installing an air fan in front of one of the venting slits of the container, which decreased the temperature in the container to below 20°C. In addition, the temperature inside the spectrometer was increased from 35°C to 40°C to increase the difference to room temperature.

7.3 Calibration procedure

7.3.1 Syringe pump calibration

Because of pre-campaign problems with a proper functioning of the piezo injector (section 6.1, [119]), an alternative calibration method was used during the campaign in Antarctica. For the

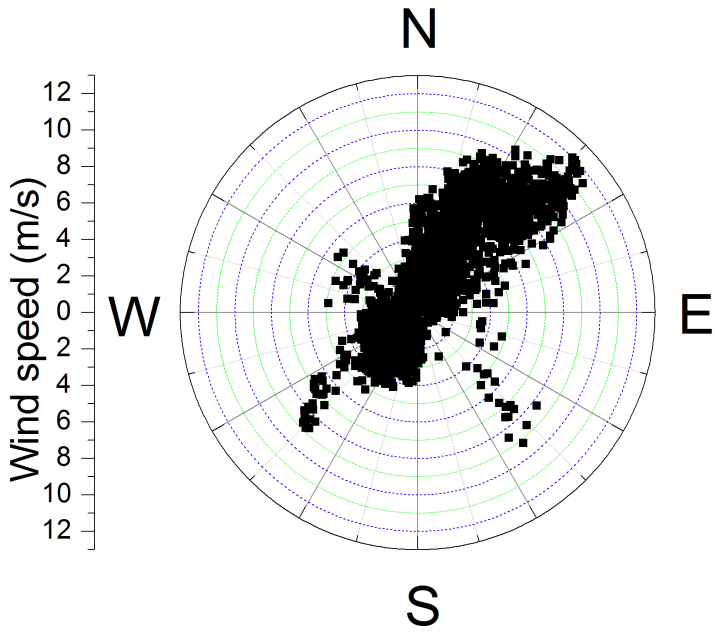

Figure 7.4: Polar diagram of wind at Troll Station during the measuring period in January and February 2011. The wind was often coming from North-East with interim winds from South-West.

campaign, a syringe pump based calibration system, developed by Olivier Cattani from the *Laboratoire des Sciences du Climat et de l'Environnement* (LSCE) was employed.

A schematics of this system is shown in figure 7.6. On the syringe pump (Legato 100, kdScientific), a 60 mL syringe is injecting close to the minimum injection rate of the pump (typically 13.3 µL/min). The water is pushed through 1/16 inch PEEK tubing and split into two streams to reduce the rate that is injected into the evaporation chamber. Part of the injected water is send to a waste bin, whereas the other portion is injected via a heated capillary (100 µm inner diameter, approx. 10 cm length) into a glass chamber (150 ccm) that is heated to 140°C. Because of complete evaporation of the injected water at the tip of the capillary, no fractionation occurs. An adjustable dry gas flow, either dry synthetic air from a bottle or ambient air, dried within a cartridge with a desiccant (Drierite), is connected to the injection chamber. The air flow through the glass chamber is maintained by the spectrometer itself in combination with an additional pump with a flow regulator connected in parallel. The adjustable flow to the secondary pump also offers a further possibility to regulate the water concentration in the calibration system more precisely. Typically, the total gas flow through the evaporation chamber is set to 2 l/min.

This calibration system was designed to work with commercially available spectrometers, which typically measure several 10,000 ppmv and more than 50% of the injected water is sent

Figure 7.5: The inlet for atmospheric air during the measurement campaign. The coated tubing was heated to 50°C and thermally insulated. A plastic cover around the inlet avoided perturbations because of snow fall

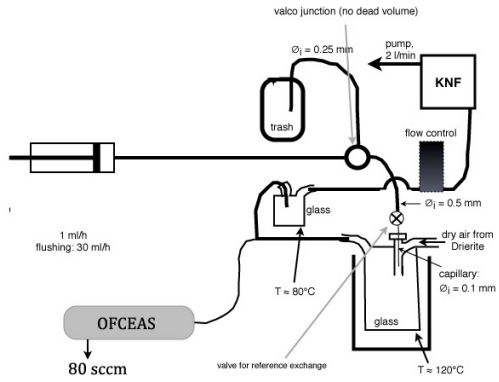

Figure 7.6: The LSCE calibration system, based on a syringe pump

to the evaporation chamber. As our OF-CEAS spectrometer measures in a range of 200 ppmv $< H_2O <$ 4000 ppmv, the water injection rate has to be reduced much further. With an air flow rate of 2 slm, a water concentration of 1000 ppmv corresponds to an injection rate of 1.5 µL/min, thus only 11% of the total water injection rate, whereas the remainder has to be send to the waste line.

During prior test measurements in the lab, the LSCE calibration system worked quite reliable and showed only small fluctuations of the water concentration during the calibration runs. However, during field employment, the calibration turned out to be very sensitive to small changes in the conditions in the measurement container. The adjustment of the water flow fraction to the waste, which is the most sensitive part of this calibration system, proved to be nearly impossible in the field. Even a small change of the height of the end of the waste tubing, which results in a small pressure change in the tubing, led to a large disturbance of the water concentration. In addition, the fact that the temperature in the measurement container could not be stabilized led to further instabilities.

As mentioned above, the calibration system was designed to provide much higher water concentrations than measured with our spectrometer and the need to drastically reduce the water injection rates resulted in a much larger sensitivity of the system stability to the change of any one parameter. Because of the large sensitivity of the calibration system to the exact settings, it had to be precisely set before each calibration run and often became unstable after some minutes of relatively stable water injection.

In figure 7.7, two exemplary calibration runs with the syringe injection system during the Antarctic mission are shown. In figure 7.7a, a calibration with the Groningen standard GS48 is shown and in 7.7b, a calibration with the standard GS22. Although the water concentrations were relatively stable (amplitude of oscillations on $H_2O < 100$ ppmv), strong variations and periodic oscillations of the delta values are apparent. These oscillations are due to the formation of small water droplets on the tip of the capillary, which occurred probably because of pressure fluctuations inside the evaporation chamber, induced by a variation of the air flow through the chamber. Because of larger fractionation factors and a stronger memory effect, they are more pronounced in δ^2H than in $\delta^{18}O$.

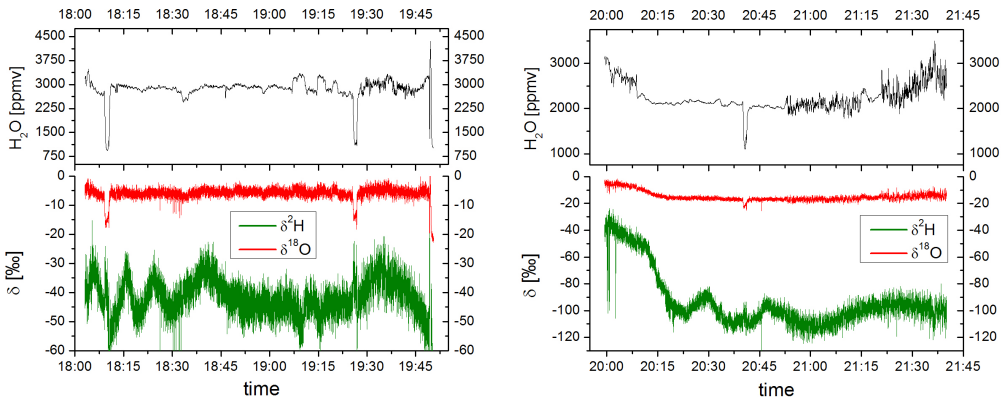

(a) Calibration with GS48

(b) Calibration with GS22

Figure 7.7: Exemplary relatively stable calibration with the syringe calibration system used in Troll

7.3.2 Bubbler

Because of the high sensitivity and instability of the syringe calibration system during the campaign, we eventually decided to knock together a bubbler as a simpler and more robust alternative calibration system. As explained in chapter 6, the principle of the bubbler is based on the saturation of an initially dry gas flow guided as bubbles through a volume of liquid water. Due to a relatively large transit time (several seconds), the gas bubbles get saturated in water and an equilibrium between liquid water and gas phase water can be assumed. The temperature

of the water column was measured, such that the corresponding water saturation vapor pressure [23] and equilibrium fraction factor [36] could be determined. The first gives the water mixing ratio when combined with the measured pressure above the water column, whereas the second quantity gives the vapor phase isotopic ratio when combined with the liquid phase isotopic ratio. For this reason, samples of the water inside the bubbler were taken at the beginning, as well as at the end of the experiment and analyzed by IRMS.
As the bubbler used here, had to be assembled in the field, it is a relatively simple version compared to other implementations [37, 52, 123–127].
A schematics is shown in figure 7.8. The inlet pressure of the bubbler was regulated with a combo

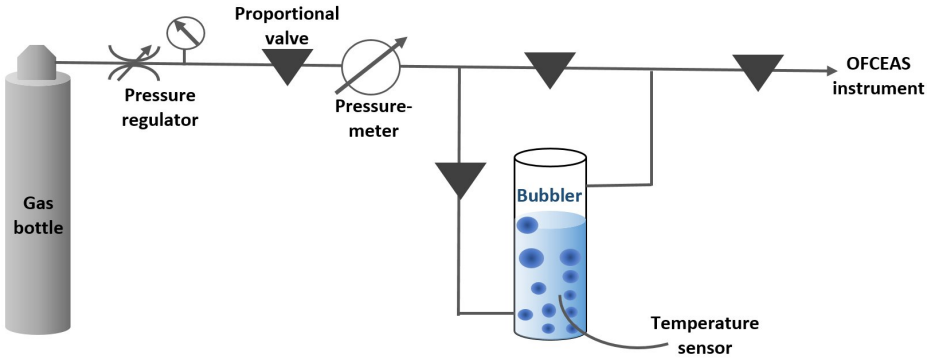

Figure 7.8: Schematics of the Bubbler calibration system used during the Antarctic campaign

pressure regulator (VICI Valco Instruments Co. Inc.) to approx. 1.5 bar. The regulation of the dry air flow and the flow through the water, was done with two manual proportional valves and the flow was measured with two electronic flow meters (Honeywell 3300). The downstream pressure was measured with an electronic pressure meter (Honeywell) and read-out with an electronic DAQ card (National Instruments USB6009).
The bubbler was built from an empty Drierite cartridge filled with local water melted from the ice layer surrounding the research station. The temperature of the bubbler was measured with an electrically isolated NTC thermistor (BetaTHERM Sensors) inside the water reservoir. The read-out, by measuring the voltage (supplied by the DAQ card) over a 10kΩ resistance connected in parallel to the thermistor, yielded a precision of 3 mK and accuracy 0.2 K.
The entire flow through the bubbler system was guided to the OF-CEAS instrument. Because of this, a change of the water concentration made an adaption of both the dry air flow rate and the flow rate through the bubbler necessary to again match the flow of the spectrometer.
As only one water was available in sufficient quantities to fill a bubbler for the calibration, it was not possible to do a two-standard calibration and apply a linear correction of the delta values as recommended e.g. by the International Atomic Energy Agency [26]. Instead, only a scaling factor was calculated to correct the measured delta values from the calibrations and yield the

real values. This factor was calculated from the isotope ratios:

$$f_{cor.} = \frac{R_{real}}{R_{meas} \times R_{VSMOW}} \tag{7.1}$$

with R_{real} the real isotope ratio, R_{VSMOW} the isotope ratio of VSMOW, and R_{meas} the measured isotope ratio.

Whereas the first calibrations with the bubbler were done at one water concentration only, all later calibrations were done at three different water concentrations to take a possible water concentration dependence of the isotope ratios into account (cf. chapter 5).

Because of the fractionation between liquid and gas phase water, the reservoir becomes increasingly enriched in the heavier isotopologues. Consequently, this enrichment has to be taken into account for the calibration measurements. To evaluate if the enrichment in our case has to be accounted for, we make an estimate of the enrichment throughout the campaign.

The bubbler reservoir was filled with approx. 0.57 l H_2O. Over the entire measurement period, a flow through the bubbler volume was maintained for a total of 91 h and interrupted, when no calibration measurements were done. During this time, the average water concentration generated by the bubbler was 1814 ppmv, which corresponds at a gas flow rate of 100 sccm to a water injection rate of 145.8 nl/min. The amount of water evaporated over the entire measurement period is thus 91 h $\cdot$ 145.8 nl/min = 0.8 ml.

For the average water temperature of 16.85 °C in the bubbler, the fractionation factor for δ^2H and δ^{18}O (ratio of isotopic composition in vapor and liquid phase) are calculated to be 0.945, and 0.99 respectively [144].

We can thus calculate the increasing enrichment of the liquid water reservoir assuming Rayleigh Fractionation (cf. section 1.2.2,[145]):

$$\frac{R}{R_0} = f^{\alpha-1} = \left[\frac{0.55 - 0.8 \cdot 10^{-3}}{0.55}\right]^{\alpha-1} \tag{7.2}$$

For δ^2H, this leads to $1 - \frac{R}{R_0} = -0.08‰$ and for δ^{18}O to $1 - \frac{R}{R_0} = -0.01‰$, indicating that the change in the isotope ratios of the reservoir water is smaller than the measurement precision, if one assumes that the isotopic composition of the bubbler water is equal to VSMOW and $R_0 = 1$. As the water is collected in Antarctica, it is depleted in the heavier isotopes and the difference is even smaller.

An independent measurement of the reservoir water by IRMS, done by H. Jansen of the Center for Isotope Research in Groningen on a sample of pre-campaign and post-campaign water, shows indeed no difference in the isotope ratios of the two water samples. This measurement yielded δ^2H= −348.6‰ and δ^{18}O= −43.57‰ for the pre-campaign water and δ^2H= −348.6‰ and δ^{18}O= −43.52‰ for the post-campaign water, confirming the above estimate to within the measurement accuracies (resp. 0.3‰ and 0.1‰ for δ^2H and δ^{18}O). Consequently, no correction for this effect was required.

The isotope abundances in the water vapor were calculated assuming equilibrium fractionation between liquid and gas phase with the fractionation factors based on the formulation of Horita and Wesolowski [144] and using the water temperature measurement. The average water temperature inside the bubbler was 16.8 ± 1.5°C, which corresponds to delta values of -401.4‰ and -53.08‰ for δ^2H, and δ^{18}O, respectively. The maximum water temperature during the measurement campaign was 20°C and the minimum 11.8°C, corresponding to variations of the isotope abundance in the vapor phase water in a range of $\delta D_{max} - \delta D_{min} = -399.3 + 404.9‰ = 5.6‰$ and $\delta^{18}O_{max} - \delta^{18}O_{min} = -52.81 + 53.53‰ = 0.72‰$. Throughout an individual calibration run, the change of the water temperature was maximal much smaller, and always less than 2 °C.

7.3.3 Calibration measurements at Troll Station

Because of the temperature sensor mounted in the gas stream inside the cavity (cf. section 3.5), the gas flow temperature is recorded. During the measurement campaign, the gas temperature inside the cavity was on average equal to 39.0 °C, with a six-σ variation of 12.3 °C (see figure 7.9). The cavity temperature was 40.2°C with a six-σ variation of 4.8 °C. The quite high variation of the cavity temperature is partly due to problems with the read-out of the temperature sensor, which led to a partial erroneous read-out of the temperature (the spikes observed in figure 7.9). The real cavity temperature is thus more stable than the figure of 4.8 °C suggests, with actual variations limited to less than 0.9 °C.

The large variations of the gas flow temperature are strongly correlated with external conditions

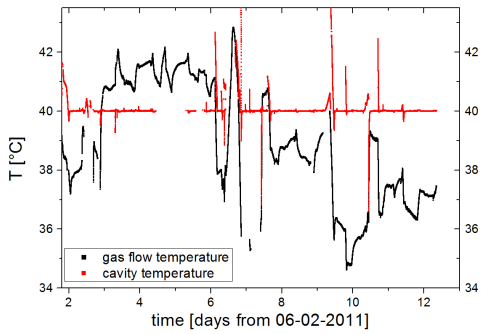

Figure 7.9: The cavity and gas temperature inside the instrument for the measurement period in Antarctica. The gas temperature is much more sensitive to external influences than the temperature of the large cavity.

like ambient air temperature and wind speed. This is probably related to insufficient thermal insulation of the inlet tubing, which resulted in larger variations in the self-regulated heating of the tubing and subsequently in stronger fluctuations of the gas temperature. Because of the large

gas temperature variations, all measurements have been post-corrected for the ("Boltzmann-")variation of the absorption line strengths induced by the temperature changes. In figure 7.10, an example of the effect of the gas temperature correction is shown for $\delta^{17}O$, for which the temperature dependence is strongest (cf. table 3.1). In figure 7.10a the uncorrected and corrected measurements are compared for a single calibration run and in figure 7.10b, all calibrations over an 11-day period are shown for $\delta^{17}O$. In both cases, the correction clearly results in a decrease in the delta value variation and underlines the importance of this correction.

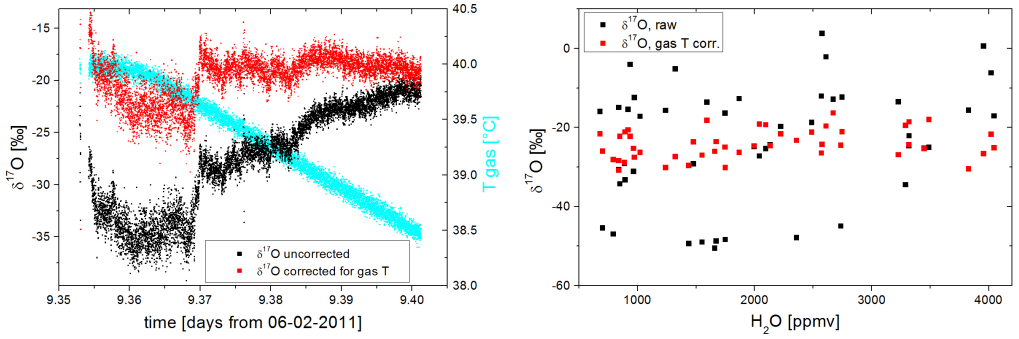

(a) (b)

Figure 7.10: Correction of the isotope measurements, exemplarily shown for $\delta^{17}O$. In a) the correction is shown on an individual calibration run and in b) the correction for the entire measurement period is shown, both showing the strong effect of the gas temperature on the isotope ratios.

In figure 7.11, an exemplary calibration measurement is shown. Each calibration was done for approximately one hour and consisted of three concentration steps. Calibrations were done once in the morning (around 7:30 am) and once in the evening (around 7:30 pm). In figure 7.12, the isotope deltas for all calibration measurements during the Troll mission from 08-02 till 18-02 (11 days) are shown, averaged over each stable concentration step and corrected for the temperature dependent fractionation inside the bubbler.

The total variation of the delta values in the calibrations for the entire measurement period, after correction for gas temperature variations, is 25‰ for $\delta^{2}H$, 14.5‰ for $\delta^{17}O$ and 8.7‰ for $\delta^{18}O$. These relatively large differences are mainly due to instrumental drift, induced by temperature instabilities inside the measurement container. Another reason is a water concentration dependence of the isotope ratios that is visible for all three isotopologues (see also chapter 5). The behavior of $\delta^{2}H$ and $\delta^{17}O$ with the water concentration changes between different calibration runs and sometimes its slope even changes sign. We suppose that the changing behavior of this dependency is a result of residual optical fringes with a structure that changes on the time scale of the measurements (approx. 1 day) that interfere with the absorption spectra and introduce deviations (see chapter 4 for a more detailed discussion). As the change of the con-

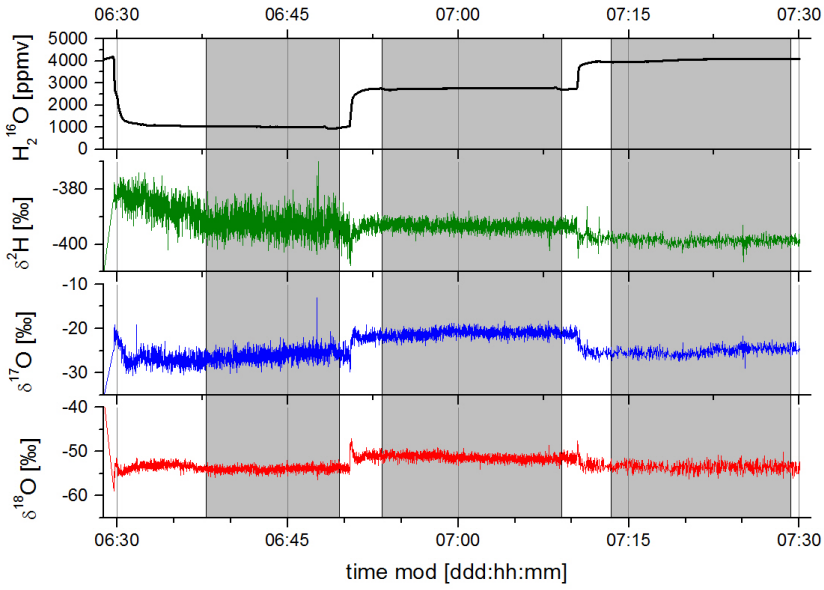

(a)

Figure 7.11: Exemplary calibration measurement with the bubbler

centration dependence between two calibration measurements proved impossible to predict, we decided not to attempt a correction of δ^2H and δ^{17}O.
For δ^{18}O (figure 7.12b), the water concentration dependence of the delta values reproduces between the different calibration runs. Because in general only three different water concentration steps were made per calibration, it would not be advisable to fit the concentration dependency of δ^{18}O with a higher order polynomial. We thus assume a linear dependency, which is determined with a fit to the ensemble of the calibration steps of all calibrations. We assume that the slope is constant for all calibration runs and thus fit a single global slope to all runs simultaneously. A linear fit to δ^{18}O yields a slope of $(2.3 \pm 0.2 \times 10^{-3})$‰/ppmv (figure 7.13a). In figure 7.13b, δ^{18}O of all calibration runs, corrected for the concentration dependence, is shown.

To estimate the instrumental drift throughout the measurement campaign, the average delta values for the concentration step closest to 1000 ppmv of all calibration runs are compared in figure 7.13. With an average time between two calibrations of 12.45h, the average difference between two calibration runs is 7.2‰ for δ^2H, 0.6‰ for δ^{18}O and 4.7‰ for δ^{17}O.

To estimate the uncertainty introduced in the measurements because of the concentration dependence, we take the average isotope ratios for all concentration steps and determine for each calibration run the difference between maximum and minimum isotope ratio for the two isotopologues. The average difference of the isotope values in a single calibration run is 7.4‰, 5‰ and 4.5‰ for δ^2H, δ^{18}O, and δ^{17}O respectively, with an average difference in water concentration of 2300 ppmv. When δ^{18}O is corrected for the concentration dependence with a linear dependency

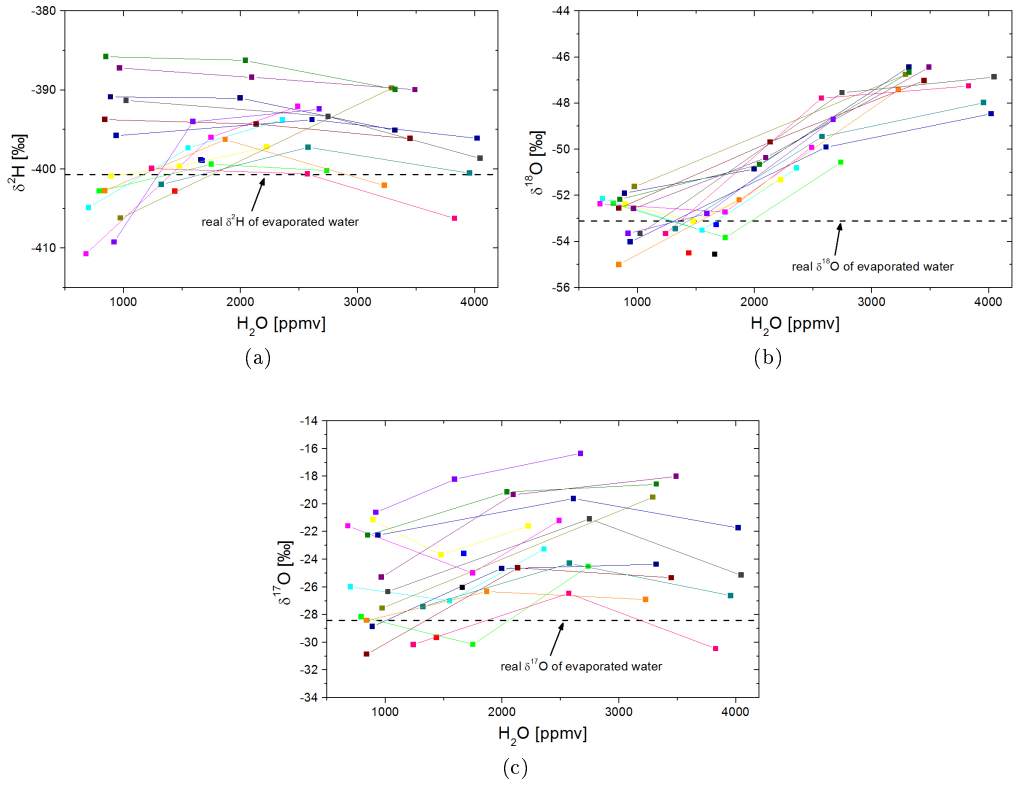

Figure 7.12: Average delta values over all calibration steps of the Bubbler calibrations from 08-02 till 18-02-2011, a) δ^2H, b) δ^{18}O and c) δ^{17}O.

as described above, the average difference in δ^{18}O decreases to 1.9‰. As the calibration runs always lasted more than one hour, these estimates also include a drift over the calibration run and will in reality be slightly smaller.

The large drifts in the delta values throughout the measurement campaign probably originate in instabilities in the OF-CEAS spectrometer during the campaign. As mentioned above, the temperature regulation of the spectrometer proved to be difficult because of too much heat generated by the electronics in the container and inside the instrument itself. The installation of a fan and the increased temperature in the spectrometer did improve the stability but also resulted in relatively large changes in the room temperature of up to 15 °C. As the continuous operation of the fan would have decreased the temperature too much, it could only be powered from time to time.

To calibrate the measurements, the average delta values were calculated for each calibration and the delta values of each measurement were scaled with the average factor from the two embracing calibrations.

Because of the relatively large uncertainties in the delta values, the δ^{17}O-excess, which is calcu-

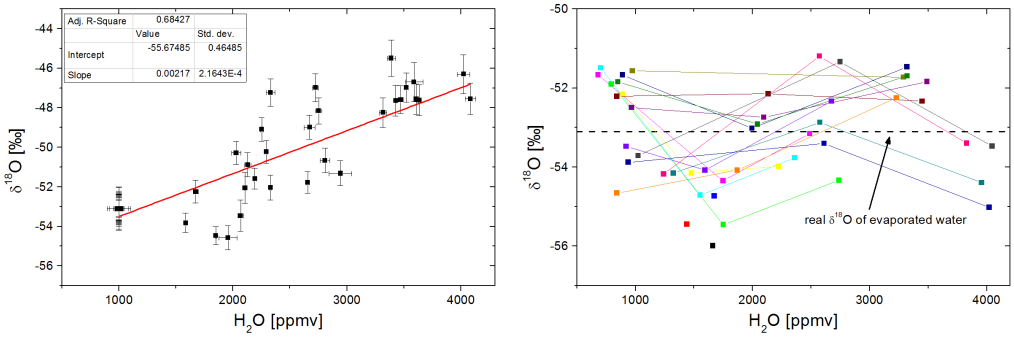

(a) Linear fit to correct for the concentration dependence of $\delta^{18}O$. The individual calibrations have been linearly corrected for the concentration dependence of the ensemble of all calibration

(b) $\delta^{18}O$ of the calibrations during the Antarctica mission, shifted as described in the text to be able to fit the concentration-shifted calibrations

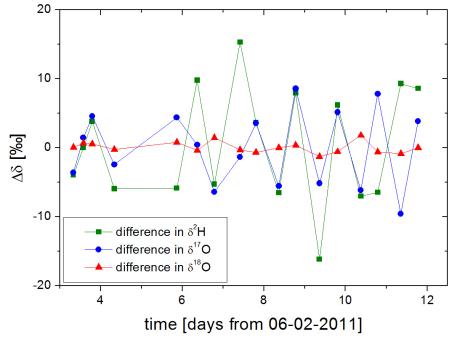

Figure 7.13: Estimation of the instrumental drift resulting in changes of the delta values between different calibration runs. For each calibration, the average delta values for the concentration step closest to 1000 ppmv is shown.s

lated with δ^{17}O-excess$= \ln(1+\delta^{17}O) - 0.528\ln(1+\delta^{18}O)$[44] and is usually given in per meg variation, is not reliable.

Because of its high uncertainty, δ^{17}O, which is generally only shown in combination and comparison with δ^{18}O in the form of δ^{17}O-excess, is not further considered.

7.4 Measurement

During some episodes of the measurements, the air flow temperature inside the cavity changed quite dramatically due to external influences. In figure 7.14, the gas temperature inside the cavity, measured inside the gas flow (section 3.5), is shown for a two day section, together with the temperature of the cavity, the temperature of the ambient air and the wind speed. Whereas

the cavity temperature stays relatively stable throughout the measurement, the gas temperature shows variations of more than 4°C, which are clearly correlated with the wind speed. These variations are surprisingly strong, if one takes into account that the air is guided through more than five meters of temperature stabilized 1/4 inch stainless steel tubing and additionally through a filter and 50 cm of 1/8 inch stainless steel tubing, mounted inside the temperature stabilized instrument itself.
These strong variations strongly underline the importance of independent gas temperature sensors inside laser spectrometers comparable to ours, to be able to correct for line strength changes due to variations in the gas temperature.
The water concentration and isotope ratio measurements shown in the following have therefore been corrected for the changes in the gas flow temperature, based on the temperature coefficients of the different absorption lines.

The water concentration and isotope ratios were quasi-continuously measured for a period of 11 days in February 2011, with small interruptions for calibration runs and smaller adaptions of the laser spectrometer. The water concentration, δ^2H and δ^{18}O measurement for this period are shown in figure 7.15 together with an air temperature measurement, friendly provided by C. Lunder from the Norwegian Institute for air research (NILU) .
Occasionally during the measurement period, the temperature approached highs close to 0 °C, which together with strong solar radiation, resulted in water concentrations of more than 4000 ppmv, which is close to the maximum our laser spectrometer could measure. In addition, the relatively mild temperatures resulted in sublimation and melting of the ice around the research station (see figure 7.17), and led temporarily to a strong component in the measured water vapor coming from local water instead of water vapor transported to Antarctica.

Because of the limitation imposed by a calibration procedure involving only one water standard, and the above mentioned drift and water concentration dependency, the delta values calibrated against the bubbler measurements exhibit a relatively large uncertainty.
Drift and water concentration dependency led to an δ^2H accuracy of approx. 12‰, and an accuracy of 4.4‰ for δ^{18}O. Because of this, a profound study and interpretation of the observed isotope ratio variations during the measurement period is not very useful.
However, because some atmospheric events were associated with very large changes in the isotopic ratios, which certainly are larger than the uncertainty of the measurements, it is still possible to examine if a correlation with atmospheric variations, especially in the source region, exist.
In figure 7.18, a measurement section of two days shows the water concentration, the delta values and the ^{2}H-excess. In addition, the air temperature and the wind speed, measured by NILU in a measurement container at 1309 m a.s.l., thus 34 m above the main building of the station and at a distance of approximately 200 m [142], is shown. Until approximately 11:00h on 16-02-2011

(10.46 on the time scale given in the figure), the isotope ratios are relatively stable, with δ^2H around -320‰ and $\delta^{18}O$ around -45‰. At 11:00h, both δ^2H and $\delta^{18}O$ show a rapid increase, δ^2H up to -280‰ and $\delta^{18}O$ to -32‰. At the same time the D-excess decreases. A decrease in the air temperature took place approximately one hour before the change of the isotope ratios and seems thus not be directly correlated with the change of the isotopic composition. However, a strong increase in wind speed seems to be strongly correlated with the change of D-excess. At approximately 18:00 on the same day, the wind speed decreases, whereas δ^2H and D-excess show a much slower transition and the transition for $\delta^{18}O$ happens around 3 hours later at approximately 21:00.
In addition to these strong changes, a temporary change of the wind direction that goes along with an increase of wind speed and occurred at T=11.15, directly translates into an increase of all isotope ratios and thus indicates a relatively large influence of the wind direction on the relative isotope abundances.

7.4.1 Backtrajectories

To determine if the observed change of the isotopic composition at 11:00 am on 16-02-2011 and the change back to the previous composition at approximately 18:00h for D-excess and 21:00h for $\delta^{18}O$ on the same day are related to a change of the source region of the atmospheric moisture, back trajectories were calculated with the online available Hybrid Single Particle Lagrangian Integrated Trajectory Model (HYSPLIT) of the National Oceanic and Atmospheric Administration (NOAA) [146, 147] using the Global Data Assimilation System (GDAS) meteorology archive. A set of back trajectories for the same time frame as the experimental data in figure 7.18, is shown in figure 7.19. For a better overview, the most important characteristics of each calculated back trajectory are given in table 7.1.
The strong transitions in the isotope ratios observed with our spectrometer, do not seem to be correlated with changes of the source region of the humid air, nor with the altitude of the air. Most of the time, the air stream is mainly passing over land and coming from altitudes around 1000 m above ground level. The rapid changes in the isotopic composition of the atmospheric moisture at Troll station seems thus to be more correlated with local conditions, such as wind speed and local re-evaporation.

7.5 Conclusion

The measurement campaign at Troll station showed that our laser spectrometer reliably measures water concentration and the two isotope ratios δ^2H and $\delta^{18}O$ with very good precision. Because of problems with the on-site calibration of the isotope ratios, the accuracy of the collected data is unfortunately not sufficient to draw detailed conclusions about atmospheric water

Table 7.1: Back trajectories for Troll station for 16-02-2011, simulated with the HYSPLIT model of NOAA [146, 147]

time [hh:mm]	source region	altitude of source [m]
04:00	land	1285
06:00	land	792
08:00	land	763
10:00	land	927
12:00	land	871
14:00	land	773
16:00	land	737
18:00	sea	773
20:00	land	877
22:00	land	1069
24:00	sea	6
26:00	sea	0

vapor transportation or to refine atmospheric circulation models. The water concentrations encountered during the measurements are well above the minimal concentrations that our instrument can measured with good precision, partially they were nearly too high.

A comparison of the isotopic measurements with back trajectory models revealed no correlation between the source region of the air mass and our isotopic measurements. A strong relation between the local wind speed and the isotope ratios of ambient air indicates that local phenomena probably govern the local water vapor composition. A possible explanation could be for example the strong eddy winds on the mountain range that resulted temporarily in wind speeds of more than 22 m/s during our measurement campaign. Furthermore, the strong solar radiation and high temperatures temporarily lead to strong evaporation of the local snow and strongly influenced and sometimes even governed the isotopic composition of the atmospheric water vapor.

In order to analyze atmospheric water transportation processes and to help to refine the theoretical modeling of these processes, we propose to conduct further measurement campaigns on the Antarctic high plateau, for example at the French Italian research station Dome Concordia. This station is located at (75°06'S, 123°21'E) at an altitude of 3,233 m a.s.l. [19, 148] The mean annual temperature of -49.8°C (measured in 2009) corresponds at an average pressure of 644.4 mbar [149] to a saturation water concentration of approximately 63 ppmv. In the summer months December and January, the temperature reaches values of up to -25°C and thus water concentrations of several hundreds of ppmv.

Our OF-CEAS spectrometer would thus be almost perfectly adapted to measure water vapor isotopologues in the harsh environment of the Antarctic high plateau. Because of the location on the high plateau, less eddy winds coming from inland regions are to expected and because of the cold temperatures, melting and evaporation of local water is less likely to influence the

composition of atmospheric moisture.
The occasionally large drifts of the instrument, caused mainly by temperature regulation problems and manifesting in relatively large differences in the isotope ratios between different calibration runs, were efficiently reduced with further improvements of the laser spectrometer after the measurement campaign. The operation temperature was further increased to 45°C and the internal power supply was replaced with an external one to reduce heat production inside the thermally insulated instrument.
Because of the difficulties encountered with the Piezo injector before the campaign and with the two other calibration systems in-the-field, a new and more robust system based on high-precision syringe pumps (section 6.2) was developed and offers a more reliable and automatized way to perform isotope calibrations during future measurement campaigns.

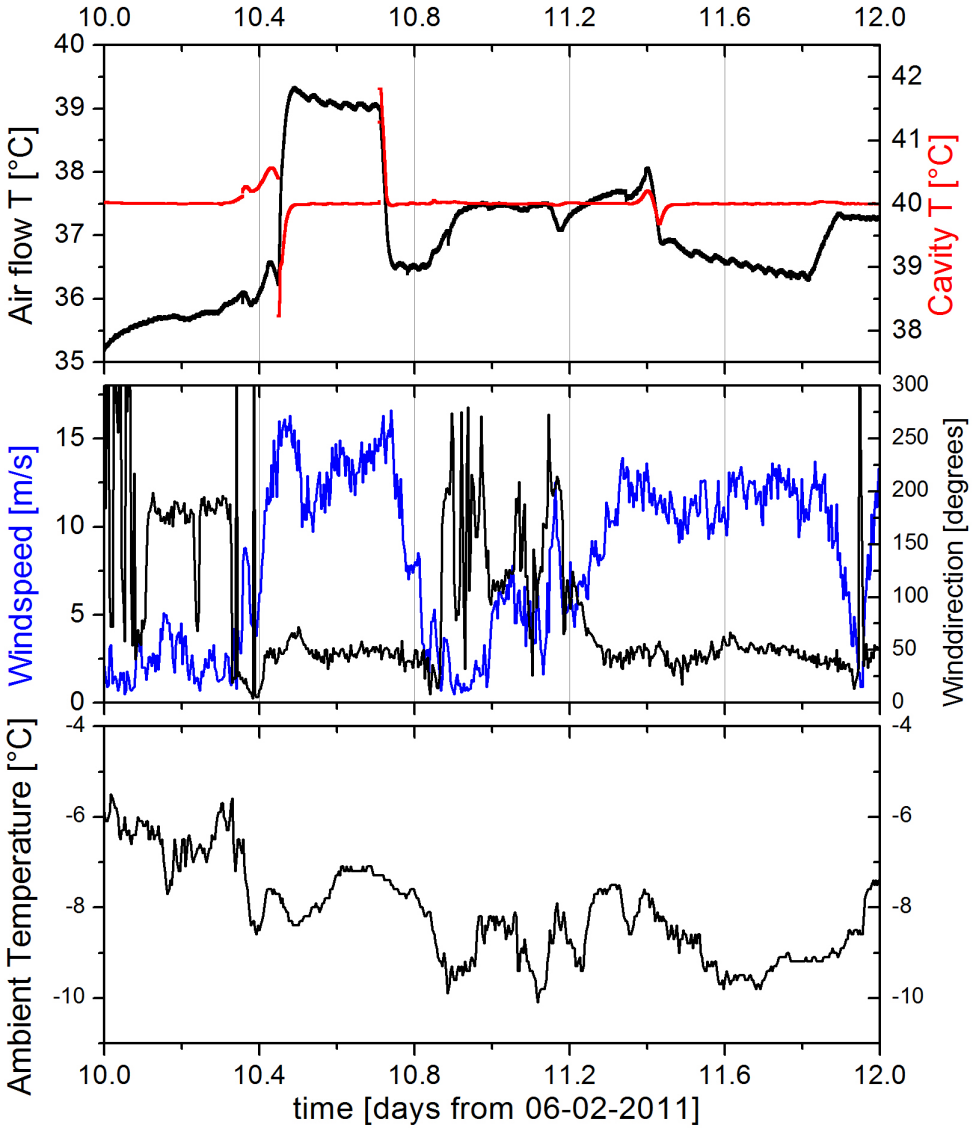

(a)

Figure 7.14: The gas flow temperature inside the OF-CEAS spectrometer was influenced by rapid changes in the ambient conditions. Apart from changes in the ambient air temperature, strong winds around the research station resulted in a large change of the air sample temperature. Other then the wind speed, the wind direction had no direct influence on the temperature. The data were post-corrected for the temperature variations.

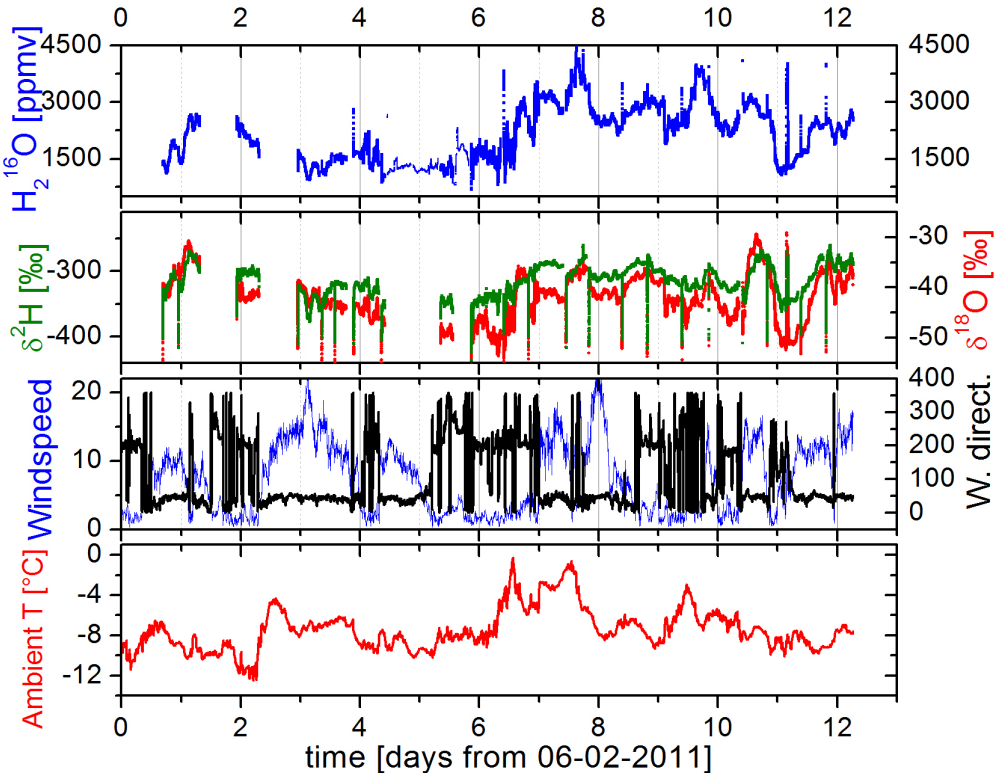

(a)

Figure 7.15: Quasi-continuous water concentration measurement at Troll Station during 11 days in February 2011. Interruptions are due to calibration runs with the bubbler and minor modifications of the OF-CEAS spectrometer. In the top panel, the water concentration is shown, in the second panel δ^2H and δ^{18}O. The third panel shows wind speed and wind direction and the bottom panel the ambient air temperature.

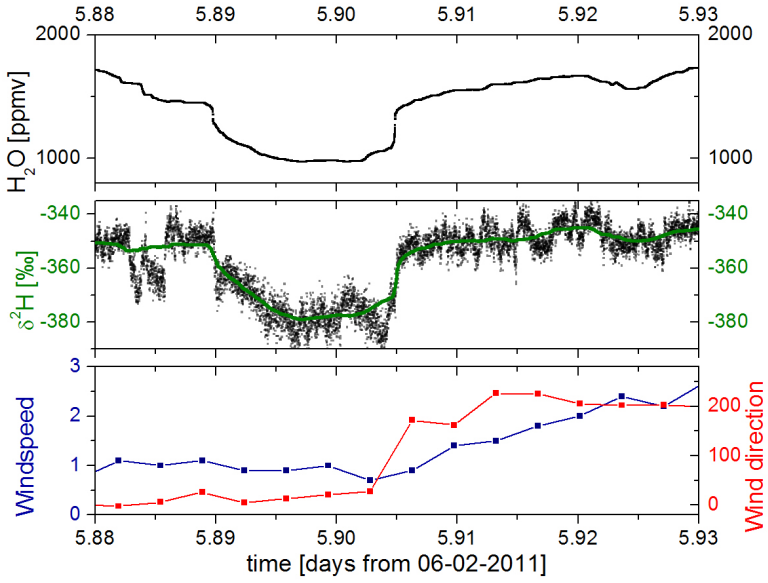

(a)

Figure 7.16: Zoom into an apparent spike in figure 7.15. The transition is relatively slow and lasts for more than 25 minutes, showing that the data is real and not an experimental artifact.

(a)

Figure 7.17: Continuously warm temperatures and strong solar radiation temporarily lead to a strong melting of the ice layer around Troll station, which resulted in higher water concentrations in the ambient air and a large contribution of local water vapor to the isotope ratios measured by our spectrometer

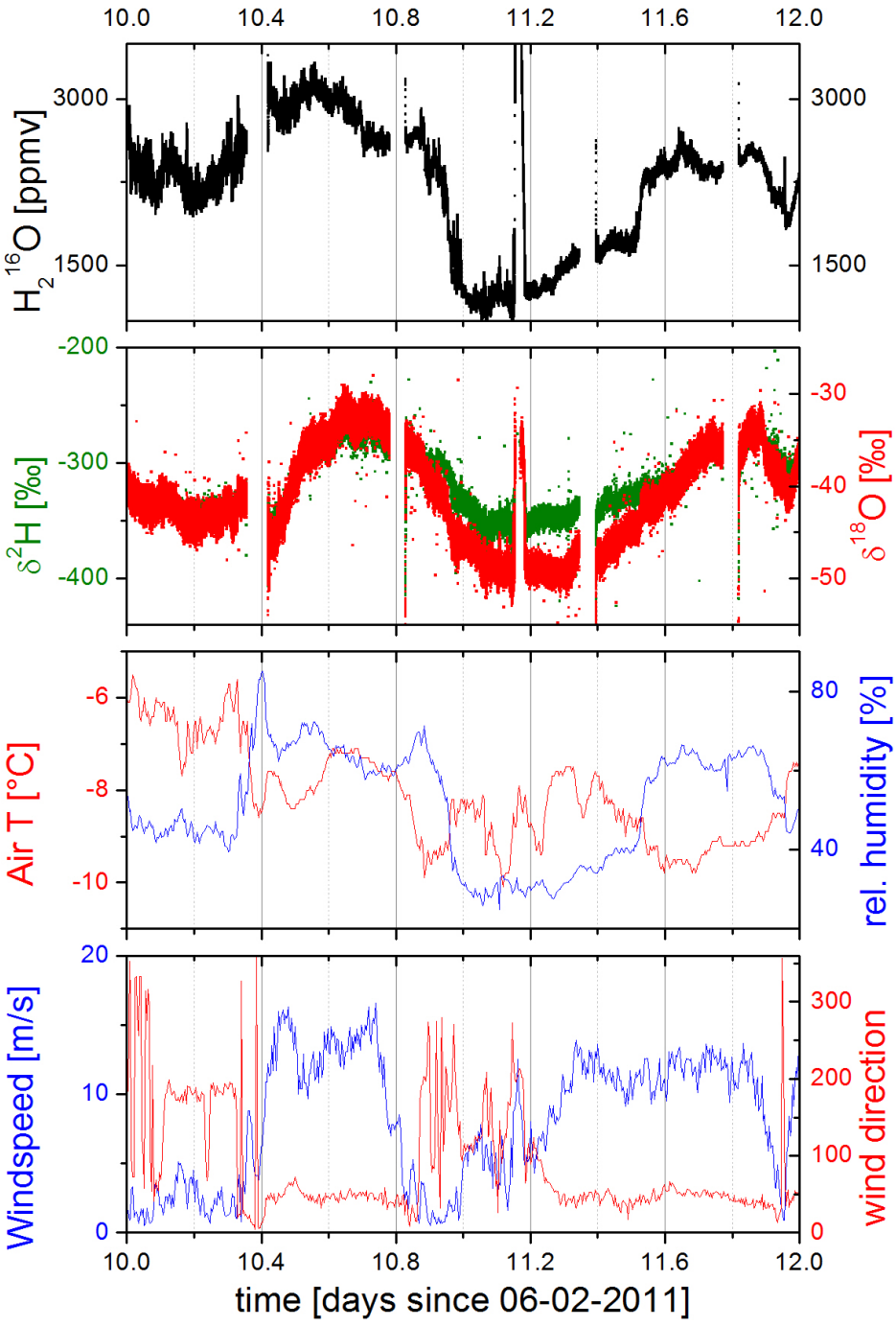

(a)

Figure 7.18: Section of two days (16-02 to 18-02) from the measurement at Troll Station in February 2011

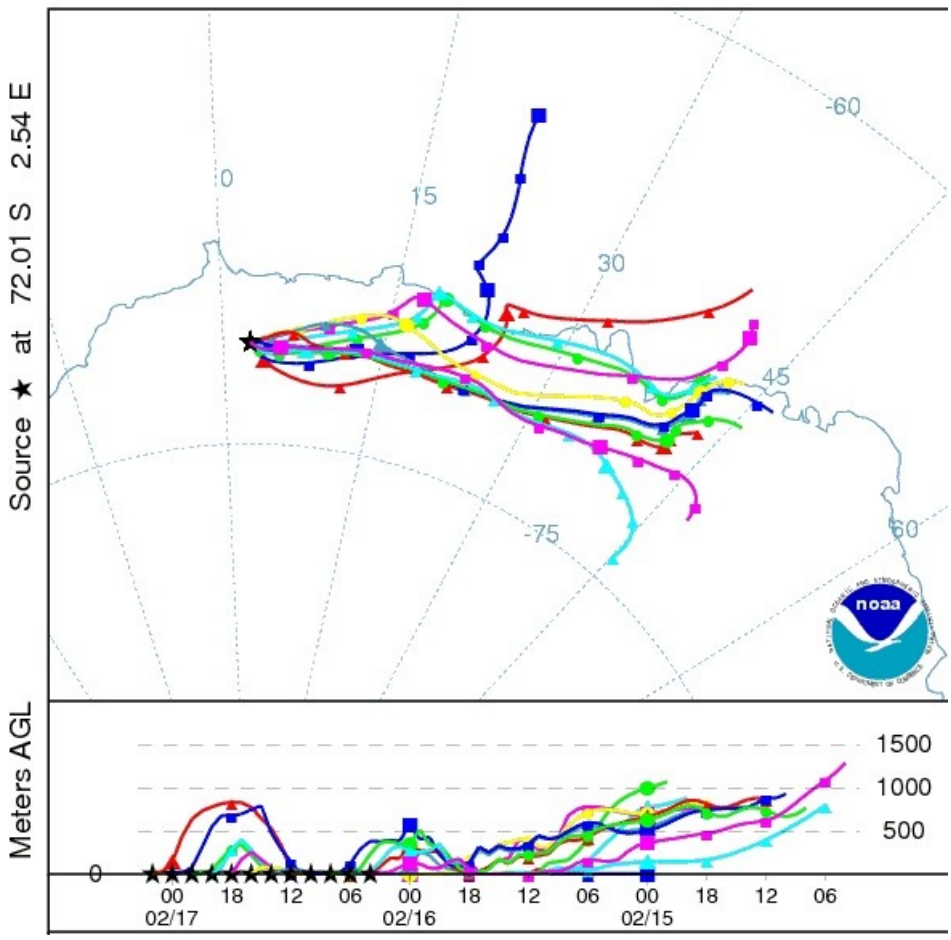

(a)

Figure 7.19: Back trajectories for Troll station for 16-02-2011, calculated with the HYSPLIT model of NOAA

Chapter 8
Water isotope fractionation in simulated ice clouds

Various measurements carried out in the coldest regions of the atmosphere revealed the occurrence of super-saturation (partial pressure of water above the saturation pressure) in the presence of ice crystals in the upper troposphere [150].

Super-saturation is a well-known phenomenon in the absence of nucleation centers. However, it can also occur in the presence of foreign nuclei that initiate heterogeneous freezing, or even in the presence of ice crystals. Two hypotheses have been forwarded to explain the latter case.

The first hypothesis is known as diffusion-limited super-saturation [151], while the second hypothesis is that of equilibrium-limited crystallization [152]. As these two mechanisms would leave a very distinct signature on the isotopic composition of the ice crystals and the atmospheric water vapor, measurements of the isotopic ratios can be exploited to determine their relative importance. A schematic representation of the two proposed mechanisms is given in figure 8.1. In the diffusion-limited case, crystallization, effectively reducing supersaturation to saturation, is limited by the diffusion time of the water molecules to the nuclei with heavier water isotopologues diffusing more slowly. This induces a negative gradient in the isotope abundances in the direction of the ice crystals. However, as the probability of adsorption is higher for heavier isotopologues, the crystals are still enriched in the heavier isotopes. At the same time, the relative humidity decreases in close proximity to the ice nuclei, as neighboring water molecules freeze out faster than new molecules can be replenished by diffusion.
The second possible mechanism, equilibrium-limited crystallization, assumes that the absorption capacity of the ice crystals is the limiting factor for the decrease of the degree of super-saturation. In this case, the different diffusion rates of the isotopologues do not affect the isotopic abundances in the ice crystal. Consequently, the heavier isotopologues would be more abundant in the crystals than in the case of diffusion-limited crystallization and neither isotope ratio nor relative humidity, would change in the proximity of the ice nuclei. By measuring the different water isotopologues separately in the gas phase, in ice crystals, and in the total water content in the ice cloud chamber, we aimed to investigate, which of the above mentioned mechanisms is primarily responsible for the super-saturation effects observed in the upper troposphere and to experimentally determine fractionation factors at very low temperatures.

Because of the difficult accessibility and very low water concentrations ($<$ 10 ppmv), measurements to investigate these mechanisms in situ are until now to the best of our knowledge not feasible. The AIDA cloud simulation chamber at the Karlsruhe Institute of Technology,

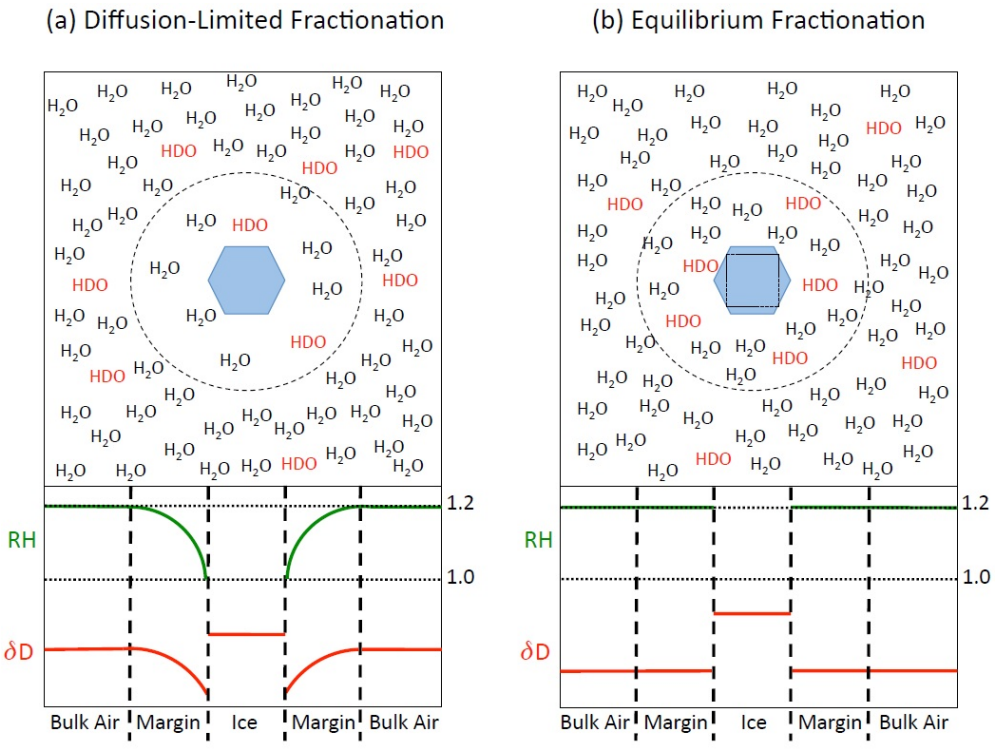

(a)

Figure 8.1: a) Diffusion-limited and b) equilibrium limited Fractionation can produce the same supersaturation. Due to different reasons for the supersaturation (see text), they produce distinct isotope signals, which can be used to determine, which mechanism is responsible. In the lower panel, the relative humidity in close proximity to the ice crystal is given in green and δD in red. Figure from E.J.Moyer [153]

Germany (KIT) was ideally suited for this study, as it enables producing the right conditions for super-saturation to occur during an expansion-driven cloud formation, and being equipped as it is with extractive sample ports and two in-situ long-path length optical absorption gas cells of the White design.

Ice cloud formation and the possible mechanisms were studied in the framework of the Isocloud project, an international collaboration funded by the National Science Foundation (`http://www.nsf.gov/`), the Deutsche Forschungsgesellschaft (`http://www.dfg.de`) and Eurochamp-2 (`http://www.eurochamp.org`) between the group of E. Moyer of the Department of Geophysical Sciences of the University of Chicago (UoC), the Institute for Meteorology and Climate Research Atmospheric Research of the KIT, the group of V. Ebert of the Center of Smart Interfaces, Technische Universität Darmstadt (TUD) and Physikalisch Technische Bundesanstalt (PTB) in Braunschweig, Germany and the LIPhy of the University of Grenoble as adjoint partner.

Gas phase water and isotopic composition was measured with two in-situ TDLAS spectrometers. The UoC developed a system that measured $H_2^{16}O$ and HDO at 2.65 µm (CHI-WIS) and the University of Darmstadt/PTB/KIT groups contributed with a similar instrument, called Isotope AIDA-PCI-in-cloud-TDL (ISO-APicT), described in detail in the dissertation of Jan C. Habig [87]), that measured $H_2^{16}O$ and $H_2^{18}O$ at 2.64µm. Both of these instruments will also be discussed in more detail in the PhD theses of K. Lamb (University of Chicago) and B. Kühnreich (Universität Darmstadt/PTB Braunschweig). We participated with the OF-CEAS spectrometer (SIRI) and the syringe calibration system developed in the framework of this thesis and supported the KIT with the operation of their OF-CEAS spectrometer (Resonatorverstärktes Wasserdampf Absorptions Spektrometer, Rewas-Iso), which was also built in Grenoble and which is based on our own spectrometer.
To measure the isotopic composition of the ice crystals, one of the OF-CEAS spectrometers was connected behind a pumped counter-flow virtual impactor (PCVI) [154] that separates ice particles larger than a set cut-off size from the gas flow. The PCVI is described in more detail in section 8.2. The second OF-CEAS spectrometer was directly connected to the cloud chamber and measured via an extractive heated tubing the isotopic composition of total water.
In addition to these four instruments, the already existent AIDA PCI extractive TDL (APeT) and a frost point mirror (MBW) measured total water concentration via an extractive line and a single pass in-situ TDL (SP-APicT) additionally measured the water concentration in the gas phase. A schematic representation of the experimental set-up is shown in figure 8.2, a list of the different instruments deployed during the Isocloud campaign and their most important characteristics are given in table 8.1.

8.1 General set-up

The AIDA cloud chamber is made of aluminum, has a diameter of 4 m and a height of 7.5 m with a volume of 84.5 m^3 and an inner surface of 103 m^2. A vacuum pump is connected to the top of the cloud chamber and is used to rapidly decrease the pressure in the chamber, which leads to an adiabatic expansion and thus a cooling of the contained air. At the bottom of the chamber, a fan is installed to homogenize the air inside the chamber. Close to the ground level, the PCVI is connected via an extractive tubing, behind which one of the OF-CEAS spectrometers was installed. The second OF-CEAS spectrometer was connected to Silcotek coatet 1/4 inch stainless steel tubing heated to 35 °C, that was installed approximately 135 cm above the base of the chamber. At a distance of 13 cm from the chamber walls, air was extracted through the tubing with a flow rate of 130 sccm. It would have been best, to connect this second OF-CEAS spectrometer at the same location at which the other extractive instruments measuring absolute water, were connected and at the same level of the chamber as the in situ instruments. Unfortunately, because of limitations of the local availability, this was not possible. Initially, the spectrometer was connected close to the top of the AIDA chamber, however this did not work

Table 8.1: A list of the different instruments deployed during the Isocloud campaigns.

Group	Instrument name	Wavelength region	Measured Isotopologues	Measured phase
UoC	CHI-WIS	2.65 µm	$H_2{}^{16}O$ and $HD{}^{16}O$	gas phase (in situ)
KIT,TUD/PTB	Iso-APicT	2.64 µm	$H_2{}^{16}O$ and $H_2{}^{18}O$	gas phase (in situ)
KIT	Rewas-Iso	1.39 µm (Isocloud 1 - 3) 1.37 µm (Isocloud 4)	$H_2{}^{16}O$, $HD{}^{16}O$, $H_2{}^{18}O$, $H_2{}^{17}O$ $H_2{}^{16}O$ and $HD{}^{16}O$ or $H_2{}^{16}O$ and $H_2{}^{18}O$	total water (extractive)
LIPhy	SIRI	1.392 µm (Isocloud 1 - 3) 1.389 µm (Isocloud 4)	$H_2{}^{16}O$, $HD{}^{16}O$, $H_2{}^{18}O$, $H_2{}^{17}O$ $H_2{}^{16}O$, $HD{}^{16}O$, $H_2{}^{18}O$	mostly ice phase (behind PCVI)
KIT	SP-APicT	1.37 µm	$H_2{}^{16}O$	gas phase (in situ)
KIT	APeT	1.37 µm	$H_2{}^{16}O$	total water (extractive)
KIT	MBW	not applicable	total water	total water (extractive)

well because of disturbances of the measurements due to strong vibrations of the metal frame on which the instrument had to be installed. Because of this, a location close to the bottom of the chamber, which provided more mechanical stability, was chosen.
At a height of approx. 4 m, two white cells are installed into which the two TDL spectrometers of the UoC and PTB/KIT groups were coupled. The PTB/KIT instrument, Isotope AIDA-PCI-in-cloud-TDL (ISO-APicT), a change between two different lasers was made possible to integrate the already existent facility TDL hygrometer APicT [155], which previously measured gas phase water on the same beam path of the White cell. An additional single pass TDL spectrometer (SP-APicT) was connected to the chamber at the same level as the other TDL spectrometers to independently measure the water concentration in gas phase.
In addition to the OF-CEAS spectrometer, total water concentration in the cloud chamber was measured by an extractive TLD spectrometer, ***AIDA PCI extractive TDL (APeT)*** and a chilled-mirror frost point hygrometer (MBW 373LX) [155] connected to the same heated extractive line either on the third level of the cloud chamber (approx. 6 m height) or on the second level (approx. 4.5 m height). The Isocloud project comprised four measurement campaigns that

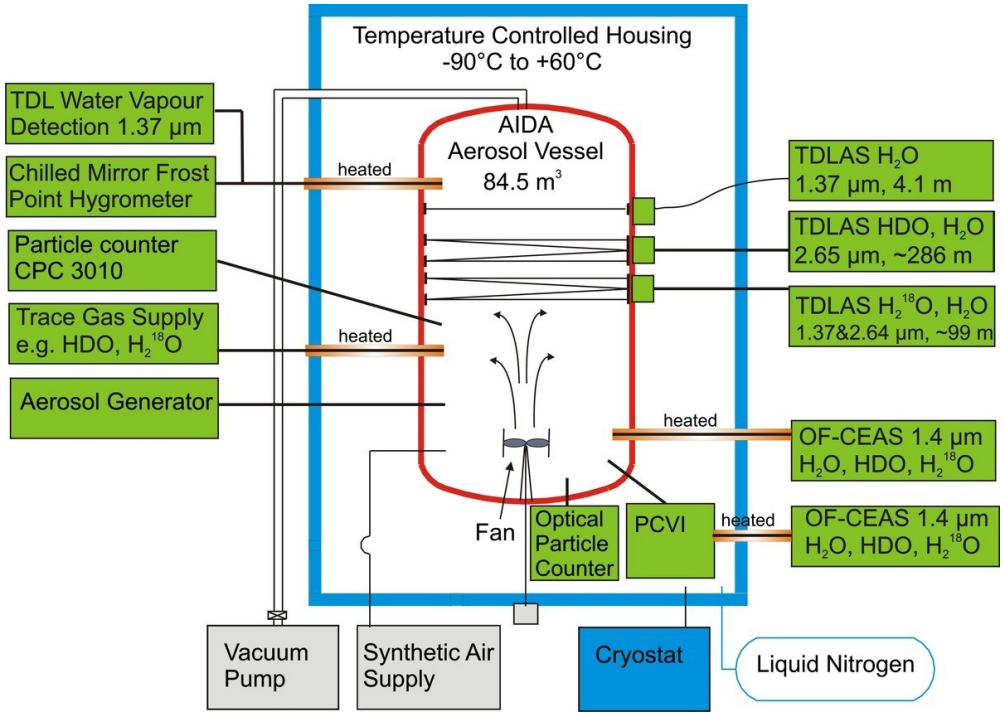

(a)

Figure 8.2: Experimental set-up at the AIDA cloud chamber during the Isocloud measurement campaigns, schematics by H. Saathoff (KIT). The OF-CEAS instrument behind the PCVI was typically SIRI.

were conducted in April 2012, June 2012, October 2012 and March 2013. The two OF-CEAS

spectrometers were in a very similar configuration for the first three campaigns and measuring at 1.392 µm, the wavelength region that was also used during the mission to Antarctica (cf. 7. For the last campaign, the KIT OF-CEAS spectrometer was adapted to be able to measure the $H_2^{18}O/H_2^{16}O$ ratio in very dry air as encountered in the stratosphere. These adaptions are described in more detail in section 8.1.1.
As the first two campaigns served mainly as trial campaigns to test the different optical instruments and to reveal where modifications and adaptions were necessary, the data presented in the following is from the last two measurement campaigns, Isocloud3 and Isocloud4.

8.1.1 Isocloud OF-CEAS

Whereas the configuration of our OF-CEAS spectrometer was very similar to the one also used for the Antarctic mission, several modifications were made between the campaigns to adapt the instrument to the very demanding conditions that were encountered during the measurements. As a decrease of the inlet pressure, as experienced by the spectrometer during the cloud simulation experiments would result in a changing flow with an ultrasonic nozzle, this flow restriction was completely removed from the instrument. In addition, the variable-speed pump, which was used to regulate the cavity pressure, proved to be too weak to provide a sufficient flow at the lower pressures. Because of this, a Restek coated Bronkhorst pressure regulator was installed upstream of the cavity and the variable-speed pump was replaced with an ordinary and larger membrane pump (KNF N813.5 ANE). With this modification, the flow through the instrument could be increased to 150 sccm and be kept constant, even as the inlet pressure descended to below 100 mbar.
For the last measurement campaign (Isocloud4), we replaced the laser in Rewas-Iso with a laser operating between 7278 and 7290 cm^{-1}. As mentioned in section 3.6, the absorption line of $H_2\,^{16}O$ is more than a factor 50, and the $H_2\,^{18}O$ line nearly a factor 4 stronger at 7286 cm^{-1} compared to the lines in the spectral regions at 7184 and 7200 cm^{-1}. Because of this, the concentration range of the modified instrument in which sub-permil precision for $\delta^{18}O$ can be achieved is significantly reduced to 1 ppmv $< H_2O <$ 60 ppmv. In addition to the measurement of $\delta^{18}O$, a spectral region around 7280 cm^{-1} allows the measurement of $\delta^{2}H$. Since, at natural abundance, in this region the HD ^{16}O line is about 40 times weaker than the major isotopologue line, it is especially appropriate for measurements of samples strongly enriched in HD ^{16}O, as were generated during the Isocloud campaigns. Two experimental spectra for the wavelength region at 7286 cm^{-1} and 7280 cm^{-1} are shown along with a fit to the data in figure 8.3. The spectrum of figure 8.3a was recorded at a water concentration of 23 ppmv and the spectrum of figure 8.3b at 90 ppmv.

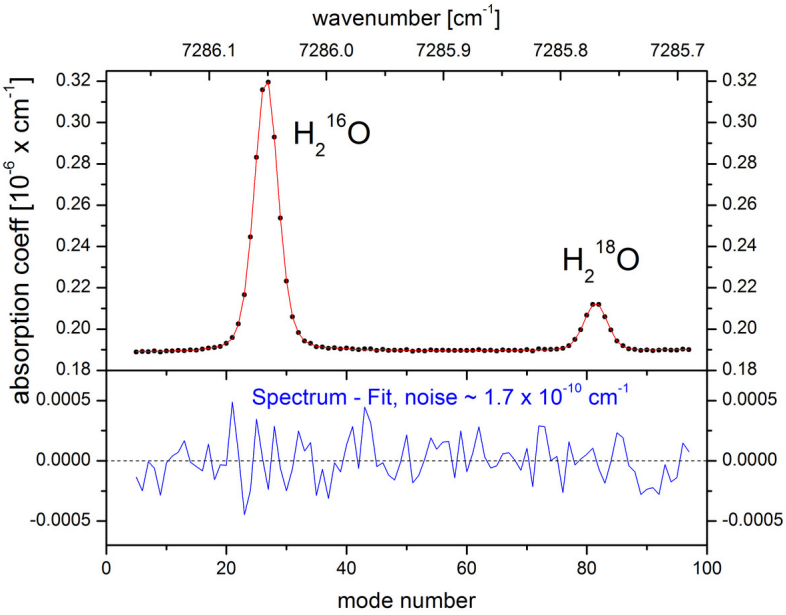

(a)

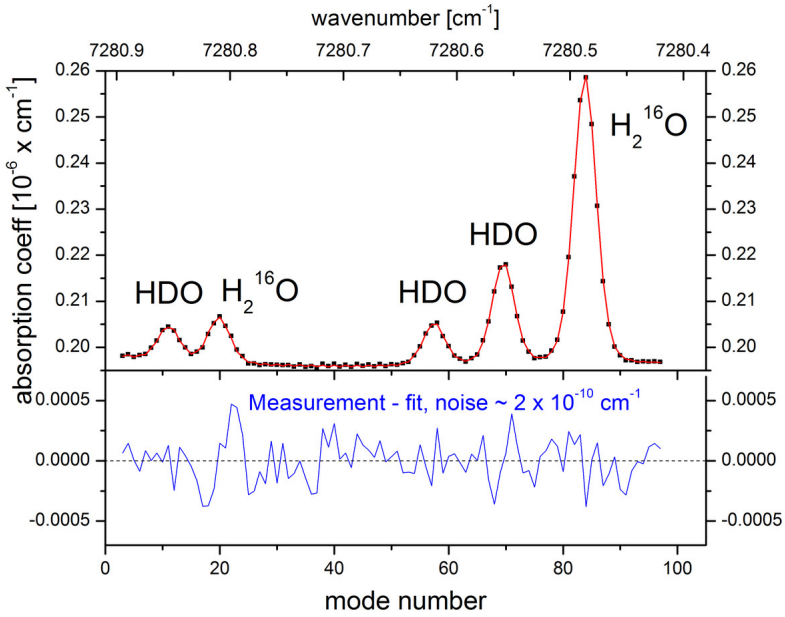

(b)

Figure 8.3: Experimental spectra measured with Rewas-Iso in the new wavelength range at a) 7286 cm^{-1} and b) 7280 cm^{-1}.

In figure 8.4, the Allan-Werle plot is shown for measurements of $\delta^{18}O$ at three different concentrations. At 16 ppmv, at the optimum integration time of 3740 s, a precision of 0.17‰ is obtained. With 1 s averaging, the precision is 4‰ at 16 ppmv and 15‰ at 5 ppmv.

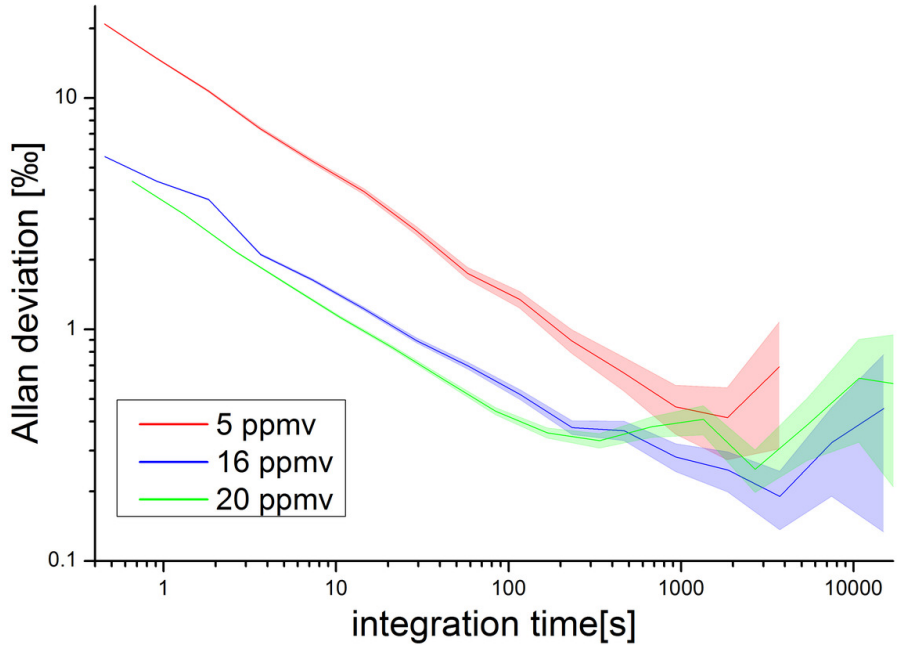

Figure 8.4: Allan deviation plot for Rewas-Iso in the $H_2^{18}O$ wavelength region. At H_2O = 16 ppmv, and an optimum integration time of 3740 s, the precision is 0.17 ‰

8.2 Pumped Counterflow Virtual Impactor (PCVI)

As a detailed discussion of the functioning of the PCVI would go well beyond the scope of this work, it is only briefly introduced here. A more thorough description can be found in [156–158]. In figure 8.5, a schematic representation of the PCVI is shown (from [158]). A sample flow (f_s) including particles - in our case the air from the cloud chamber - is drawn into the virtual impactor by a vacuum pump (indicated as pump flow in the figure). Supplemental counterflow (f_{cf}) of a particle-free gas, typically a dry synthetic air stream, is sustained to intertially remove smaller particles from the flow through the PCVI. Only particles above a certain mass and, because of same densities, above a certain size (the so-called cut size or cut-off size) traverse the counterflow because of their larger inertia and are separated from the bulk part of the sample flow. The particle-free counterflow consists of a fraction (the effective counterflow f_{ecf}) that is evacuated by the connected pump and another fraction (f_{of}) that serves as carrier gas for the separated particles in the output flow ($f_{cf} = f_{ecf} + f_{of}$).

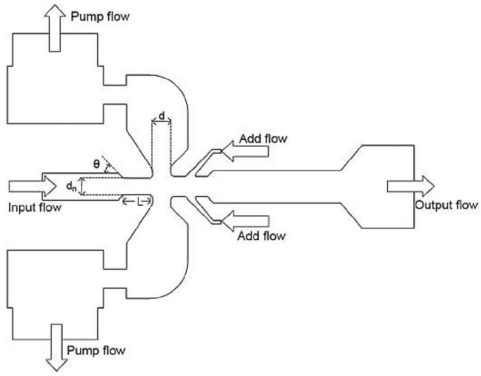

(a)

Figure 8.5: Schematics of the pumped counterflow virtual impactor (PCVI), figure from [158]

The cut size is typically defined as the size at which 50% of the particles are transmitted through the PCVI into the output flow [157]. It is mainly dependent on the ratio of volumetric effective counterflow and incoming sample flow, but also depends on other parameters such as input pressure, the pressure in the PCVI [158], viscosity of the air and density of the particles. As the incoming sample flow can be larger than the output flow of the PCVI, the separation of particles comes along with an enhancement of the sample concentration, which equals the ratio of sample flow and output flow. During the Isocloud campaigns, the cut size was typically around 2.5 µm and the enhancement factor in the water concentration 3.72. As described above, the separation in the PCVI depends on the inertia of the particles, which means that it requires constant particle speeds and thus a constant volumetric flow, independent of the pressure in the PCVI. However, the OF-CEAS instruments work with constant mass flows, which means that the volumetric flow increases at lower inlet pressures.
To maintain a pressure independent constant volumetric flow through the sample outlet of the PCVI with a constant mass flow through the OF-CEAS instrument behind, a mass flow controller was connected in parallel to the OF-CEAS. The flow through the MFC was then regulated such that the volumetric flow in the PCVI remained constant (cf. figure 8.6).

8.3 Calibration of total water and isotope ratios

8.3.1 Calibration of OF-CEAS

The total water concentration measurements of Rewas-Iso were calibrated against the water concentrations of APeT. For this, all sections of the measurements during the campaign with stable water concentrations, at which both APeT and REWAS-Iso were measuring total water, were used. Subsequently, the average for both instruments over each of these sections was calcu-

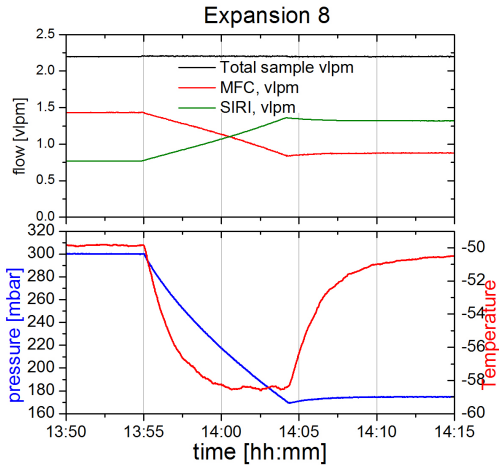

(a)

Figure 8.6: The volumetric flows at the sample outlet of the PCVI during an expansion experiment. As the mass flow through the OF-CEAS instrument stays constant, the volumetric flow increases with lower pressures. To sustain a constant total mass flow at the sample outlet, an MFC with a pump is connected in parallel to the OF-CEAS and the flow is decreased with lower pressure. Lower panel shows the pressure and temperature in the AIDA chamber for a typical expansion experiment.

lated. As REWAS-Iso was measuring in four different wavelength regions during the campaign (cf. 8.1.1), four different datasets were thus constructed.

As an example, in figure 8.7, the H_2O calibration is shown for the $H_2\,^{18}O$ wavelength region at 7286 cm^{-1}. A linear function was fit to the plot of the water concentration measured by Rewas vs. that measured by APeT and yielded an intercept of 0.1±0.07 ppmv and a slope of 0.76±0.01. The large difference with unity is due to an initially erroneous conversion factor from line profile to concentration in the fit file of the OF-CEAS spectrometer. The water concentrations of SIRI were not calibrated in Isocloud4 as SIRI was connected almost always behind the PCVI and no direct comparison could be made. Since SIRI measured in a same wavelength range that had been calibrated previously, this was also not necessary.

The isotope ratio measurements of Rewas-Iso and SIRI were calibrated with SNICS at least twice a day, once before the experiment in the morning and once after the experiment in the evening. Because of the limited time available for the calibrations, we decided to focus the calibration on the correction of the water concentration dependency and only one isotope standard was used for measurements at different water concentrations. In the case of SIRI, the concentration dependency was determined for a combination of the two calibrations before and after the measurement (cf. 5.1) and was used for the correction of the measurements. The variation between the two calibration measurements was in general comparable to the variation of measurement steps in the individual calibrations. For concentrations above 40 ppmv, the standard

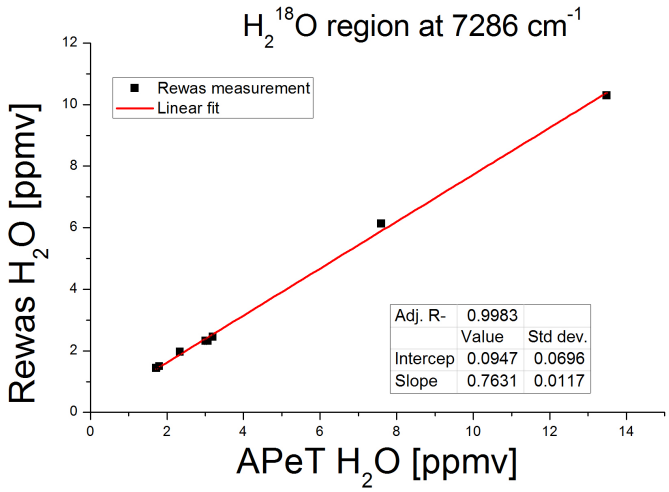

(a)

Figure 8.7: Calibration of the H_2O measurement of Rewas-Iso vs. APeT. For the calibration, all sections with stable conditions in the Isocloud4 measurements were identified and the average of $H_2^{16}O$ for APeT and Rewas-Iso were calculated and plotted against each other. The standard deviation on the measurement is smaller than the size of the data points.

deviation of the correction function is 18‰ for δ^2H and 2.1‰ for $\delta^{18}O$, for concentrations below this, the standard deviation becomes significantly larger because of the strong non-linearity of the concentration dependence.

8.3.2 Calibration of in situ measured HDO/H_2 ^{16}O ratios for CHI-WIS

For the Chicago-built in-situ TDLS water spectrometer CHI-WIS, the experimentally determined value of the deuterium isotope ratio

$$^2\tilde{R} = \frac{[\mathrm{HD}\ ^{16}\mathrm{O}]_{\mathrm{sample}}/[\mathrm{H_2}\ ^{16}\mathrm{O}]_{\mathrm{sample}}}{[\mathrm{HD}\ ^{16}\mathrm{O}]_{\mathrm{VSMOW}}/[\mathrm{H_2}\ ^{16}\mathrm{O}]_{\mathrm{VSMOW}}}$$

was calibrated against the (calibrated) $^{\mathrm{R}}$ of Rewas-Iso. Analog to the calibration of the water concentration for Rewas-Iso, all sections of the data with stable H_2O and R_{2H} were identified over the entire measurement period. As Rewas-Iso was not always measuring HDO, only those experiments were considered, in which an HDO measurement was available for both instruments. As all stable sections were used, the data include measurements at different pressures and before and after expansion experiments.

Different calibration strategies were studied in order to calibrate the isotope ratio $[HDO]/[H_2^{16}O]$ of CHI-WIS (in the following R_{CHIWIS}) with the calibrated measurements of Rewas-Iso. Amongst others, a separate calibration of $[H_2^{16}O]$ and [HDO] was tried. However, the best result is achieved

when a correction is applied to the isotope ratio directly, assuming a quadratic relation between R_{CHIWIS} and R_{Rewas}. The fit was weighted using the standard deviations of the Rewas-Iso data points only ($\omega_i = \frac{1}{\sigma_i^2}$), considering that the error on the Rewas data is typically of the same size as and occasionally up to 4 times larger than that of CHI-WIS data (cf. figure 8.8). The fit

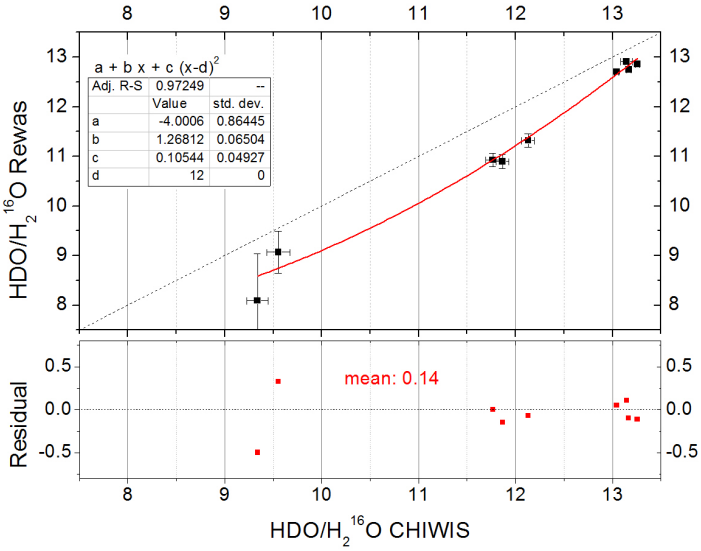

(a)

Figure 8.8: The deuterium isotope ratio measurements (12 in total) of Rewas-Iso plotted against those of CHI-Wis. The error bars represent 1σ standard deviations. A quadratic function was fit to the data to correct the CHI-Wis measurement with the calibrated measurement of Rewas-Iso.

gives the following relation:

$$R_{Rewas} = -4 + 1.27 \cdot R_{CHIWIS} + 0.11 \cdot (R_{CHIWIS} - 12)^2 \tag{8.1}$$

The residual of the fit indicates a difference of several hundred permil between the isotope ratios of CHI-WIS and Rewas-Iso after the calibration. This is because data from the entire Isocloud4 campaign was used for the calibration fit. Because of the small amount of stable measurement sections that could be compared, only a limited amount of data points was available and it was not possible to make one separate calibration for each measurement day. This means that the drift of the two instruments is also included in the fit and adds to the uncertainties. In addition, Rewas-Iso features a large uncertainty on the isotope ratios at very low (< 5 ppmv) water concentrations.

In figure 8.9, the effect of the R_{2H} calibration is exemplary shown for one experiment. In figure 8.9 a), the uncalibrated isotope ratio is shown for CHI-WIS and in b) the calibrated data. Although one calibration was done for the entire measurement campaign, the calibrated data agree within less than 100 permil, which is much smaller than the isotopic changes observed in

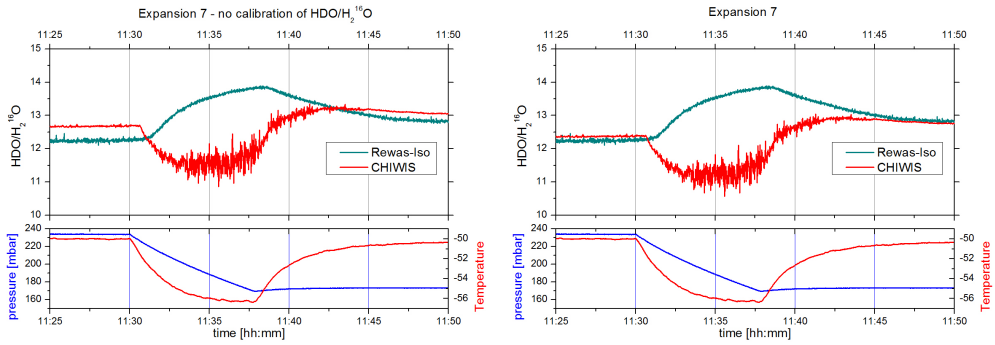

(a) (b)

Figure 8.9: Isotope ratio measurement ($HDO/H_2^{16}O$) of CHI-WIS and Rewas-Iso during the Isocloud4 campaign. a) CHI-WIS is not calibrated for drift. A difference of nearly 500‰ can be seen in the stable sections in the beginning and the end of the experiment, where both instruments should agree b) CHI-WIS data calibrated against Rewas-Iso measurements for the entire measurement campaign. The two instruments agree better than 100‰, which is much smaller than the overall change in the isotope ratios and corresponds to a relative error on the ratio R of approx. 1%.

the measurements, and corresponds to a relative measurement accuracy of 1% on the (enriched) deuterium ratio.

8.4 Typical expansion experiment

For the Isocloud campaigns, a standard experimental protocol was established to study ice cloud formation processes. At the beginning of a measurement day, water was added to the chamber air until the partial pressure was close to saturation pressure [23]. This water was strongly doped with HDO ($^2R = 10$ to 20) to enhance the otherwise relatively weak HDO signal.
An experimental run was started when the air in the cloud chamber was homogeneously mixed and the water concentration as well as the isotopic composition were stable.
For each expansion experiment, the pressure inside the chamber was decreased by evacuating chamber air with the vacuum pump connected to the top of the cloud chamber (cf. figure 8.10). Pressure drops were either from 300 mbar to 230 mbar, 230 mbar to 170 mbar or 300 mbar to 170 mbar, and took a few minutes to achieve.. The decrease of the pressure inside the chamber lead to an adiabatic cooling of typically 5-7 K of the chamber air.
As the partial pressure of water was close to saturation before the experiment, this decrease in temperature leads to supersaturation in the chamber air and, in the presence of ice-condensation nuclei, subsequently to the formation of an ice cloud.
As ice-condensation nuclei, different types of aerosol particles were used, amongst others Arizona Test Dust (ATD) and Sulfuric Acid (H_2SO_4). The degree of supersaturation that is reached

during an expansion experiment, as well as size and amount of formed ice can be influenced by the selection of a specific aerosol and the amount of aerosol particles that are added [159].
Throughout the measurement campaigns, expansion experiments with ice cloud formation were carried out at different initial chamber temperatures ranging from -40°C to -85°C, corresponding to water saturation vapor pressures of 12.8 Pa down to 0.024 Pa [23].
A typical expansion experiment is shown in figure 8.10. As discussed above, the three instruments SP-APicT, Chi-WIS and Iso-APicT measure in-situ gas phase water, in the case of Chi-WIS also including HDO, and for Iso-APicT including $H_2\,^{18}O$.

In the upper panel of figure 8.10, the different water concentration measurements are shown. MBW and APeT as well as Rewas-Iso measure total water via two different extractive lines, in the case of Rewas-Iso together with one ($H_2\,^{18}O$ or HDO; Isocloud4) or three (HD ^{16}O,$H_2\,^{18}O$ and $H_2\,^{17}O$; Isocloud3) of the rare water isotopologues. SIRI was connected behind the PCVI and measured ice phase water including the three rare isotopologues. The enhancement in the water concentration that occurs in the PCVI (discussed in section 8.2), was corrected for. Furthermore, the water concentrations corresponding to saturation vapor pressure is shown. When the vacuum pump is turned on, the pressure starts to decrease with approx. 0.22 mbar/s. At the same time, the air temperature decreases in less than 6 min more than 8.5°C (lower panel in figure 8.10). The decrease of air temperature also results in a decrease in saturation water vapor pressure. When a critical supersaturation is reached, water vapor starts to form ice particles on the present nuclei. The ice formation can be seen in an increase in total water (APeT, MBW and Rewas) and a decrease in water vapor (APicT and CHIWIS) in the upper panel of figure 8.10.
In the center panel, the isotope ratio $HDO/H_2^{16}O$ measurement for gas phase (CHI-WIS), total water (Rewas-Iso) and in the PCVI ice (SIRI) is shown. In the isotopic composition (center panel of figure 8.10), the crystallization results in a decrease of the isotope ratio $HDO/H_2^{18}O$ in gas phase water as the heavier isotopologues preferentially crystallize. The measurement of Rewas-Iso shows that total water becomes increasingly enriched during the ice cloud formation. If the water concentration and isotopic composition would change only due to the removal of chamber air by the vacuum pump, the isotope ratio in total water would remain relatively constant as all isotopes are practically removed homogeneously. The strong increase of the total water isotope ratio indicates a water flux from the chamber walls, with a strong isotopic enrichment compared to the chamber air.
The measurement of SIRI behind the PCVI shows an increase of the relative abundance of HDO in the ice phase, which is expected because of preferential crystallization of the heavier isotopologues. The isotope ratio does not decrease to the initial value of the carrier gas but remains highly elevated ($^2R > 10$). This is due to wall-adsorption that leads to a large memory effect at very low water concentrations. As the carrier gas is very dry, adsorbed HDO molecules on the walls are not efficiently replaced by $H_2^{16}O$ but only slowly released, leading to the high

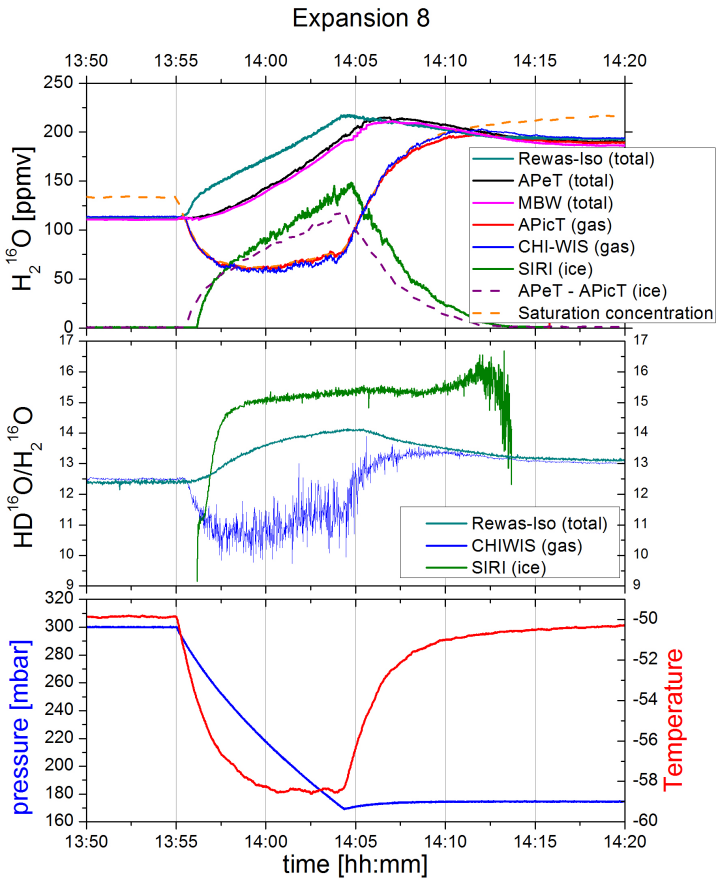

(a)

Figure 8.10: Upper panel: The different measurements of vapor phase, total water and ice phase behind the PCVI and the ice water content calculated as the difference of APeT and APicT measurement. The orange dashed line indicates the concentration corresponding to saturation water vapor pressure. Center panel: $HD^{16}O/H_2^{16}O$ for total water (Rewas-Iso), gas phase water (CHI-WIS) and behind the PCVI (SIRI). Lower panel: chamber pressure (in blue) and chamber air temperature (in red)

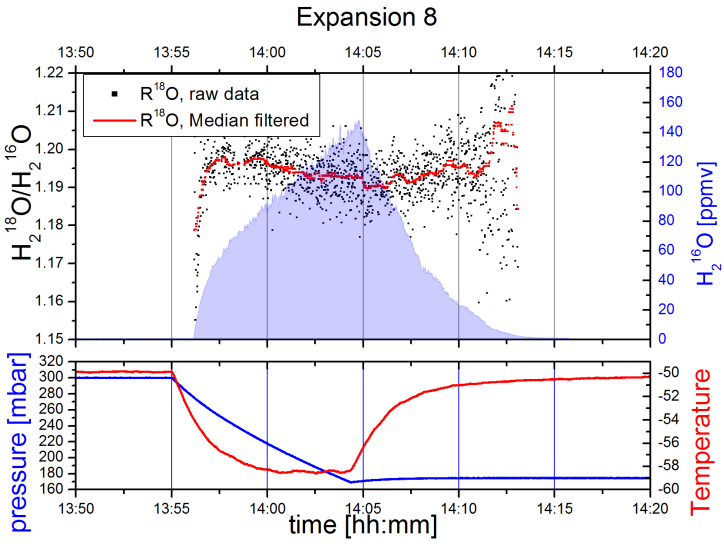

(a)

Figure 8.11: $\delta^{18}O$ measurement of the ice behind the PCVI during the experiment shown in figure 8.10. In the beginning of the ice formation, $\delta^{18}O/H_2^{16}O$ increases approx. 50‰. During the experiment, the change is smaller than the noise level.

isotope ratio values.

In figure 8.11, the ice phase $\delta^{18}O$ measurement of SIRI behind the PCVI is shown. To guide the eye, a smoothed curve with a Median filtering over 60 points (40 s) at a time is shown in red. In light blue, the corresponding $H_2^{16}O$ measurement is given. For this experiment, no total water $\delta^{18}O$ measurement is available, as Rewas-Iso was measuring HDO and $H_2^{16}O$ only. The Iso-APicT gas phase measurement of $H_2^{16}O$ and $H_2^{18}O$ is still being analyzed by our colleagues at Darmstadt university and not yet available at the time of this writing.

When the first ice arrives behind the PCVI, ^{18}R increases by approx. 50‰ from 1.15 to 1.2. During the approx. 16 min of the ice cloud expansion (from 13:57 h till 14:11 h), the change of the isotope ratio is within the noise band of the measurement and no trend can be identified. The initial increase in ^{18}R is probably due to a higher relative abundance of the heavier isotopologues in the water vapor inside the chamber compared to the dry synthetic air. As isotopic changes in the case of $\delta^{18}O$ are very small, possible changes could unfortunately not be resolved with our OF-CEAS spectrometer at the water concentrations measured during the Isocloud campaigns. In addition, the separation of the ice particles in the PCVI leads to a further smoothing of the signal, which makes the temporal resolution of the ice formation even more difficult. The strongest enrichment, which can be found in newly formed ice particles, can not be measured with the PCVI, as these particles are too small to be separated. During crystal growth, the ice becomes isotopically lighter due to a depletion of the gas phase in the heavier isotopologues.

8.4.1 Comparison of total water measurement of APeT/MBW and Rewas/SIRI

In figure 8.10, a significant difference between the total water measurement of APeT and MBW on one side and REWAS-Iso on the other side can be seen. Whereas the three H_2O measurements show differences smaller than 1 ppmv for the stable region before and after the pressure decrease, the measurement of REWAS-Iso indicates a more rapid and stronger increase in concentration than the two other instruments. This difference can be observed in practically all of the measurements, with REWAS-Iso always showing a stronger and faster response to the pressure decrease than APeT and MBW. In fact, the measurements of REWAS-Iso appear to be driven more directly by the pumping-induced pressure change.

A possible explanation for the differences between the total water concentrations measured by APeT and MBW on one extractive line compared to the water concentration measured by Rewas-Iso on another extractive line could be that the measurement of one or several of the instruments was affected by the temperature or pressure changes during an expansion experiment, either directly or because these introduced systematic errors in the instruments. It is also important to notice that REWAS-Iso is measuring with constant pressure and temperature inside the instrument, whereas APeT and MBW measure water number density at changing pressure and temperature, which in the case of APeT requires corrections for decreasing total air number density and increasing number density due to a drop of the temperature.
Systematic errors because of temperature or pressure changes would be obvious if the two instruments on the same extraction line would show different readings. However, the measurements of APeT and MBW, which were always connected to the same extraction line, are in relatively good agreement throughout the expansion experiments, especially as far as the overall shape of the water concentration changes is concerned. Furthermore, APeT and MBW also agreed with other instruments sampling at different positions of AIDA (also including level 1) during the intercomparison measurements of the AquaVIT campaigns 1 and 2 [155]. At the same time, the water concentration measured by Rewas-Iso and SIRI agree, when connected to the same extraction line. Figure 8.12 shows an example of the good agreement between APeT and MBW and between Rewas-Iso and SIRI for one experiment. This makes it highly unlikely that the problem is related to measurement problems with one of the instruments.

Furthermore, APeT measures the water concentration optically and MBW via a dew point mirror, thus by two very different techniques, and a common error between these two instruments can practically be excluded. In the case of Rewas-Iso and SIRI, both instruments measure the water concentration by the OF-CEAS technique. However, both instruments are measuring in different spectral regions with different temperature dependencies of the investigated absorption lines. In addition, both instruments are stabilized in cavity temperature, pressure and flow rate, which makes them virtually insusceptible to pressure and temperature changes in the AIDA chamber. Finally, the characteristics of the water concentration change measured by Rewas-Iso

during an expansion experiment does not change between the different spectral regions for HDO and $H_2\,^{18}O$ in which it was measuring during Isocloud4.

Therefore, the differences in the water concentrations have to be real, either because of in-

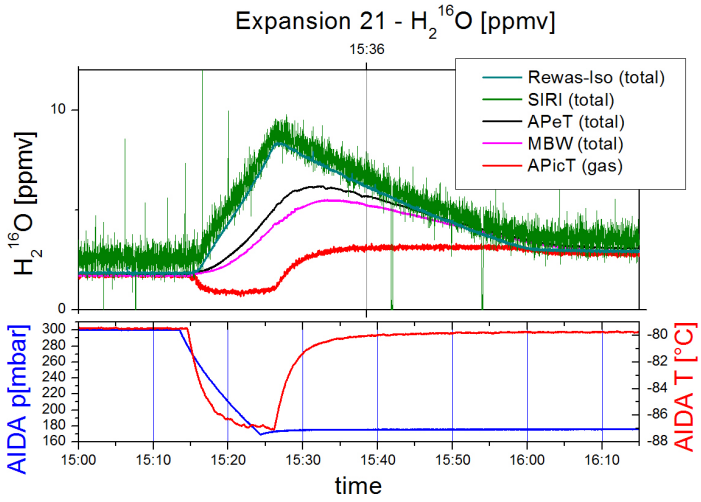

Figure 8.12: During the expansion experiments, the water concentration measured by (a) APeT and MBW are in good agreement, as are the measurements by Rewas-Iso and SIRI (b)

homogeneities in the cloud chamber itself or because of problems inside the extractive tubing. Because of the limited size of the cloud chamber, there is permanently an exchange of water inside the chamber with water on the chamber wall. Whereas this exchange reaches an equilibrium under stable conditions, an increased addition of water from the walls can be observed during the expansion experiments. In addition, a boundary layer close to the chamber wall is strongly influenced by the temperature of the chamber wall, which stays relatively constant during the pump-down experiments, in contrast to the gas temperature in the chamber. The extractive tubing through which Rewas-Iso was measuring during the campaigns samples the chamber air at a distance of 13 cm from the chamber wall, in contrast to the tubing of APeT and MBW, which extracts air at a distance of 30 to 40 cm from the wall.

Due to the smaller distance from the wall, the measurement of Rewas-Iso could thus be more affected by fluxes coming from the walls than that of the other two instruments. However, flow simulations of the conditions encountered in the AIDA chamber during evacuation and under stable conditions show that this is not the reason. This is also confirmed by the observed radial temperature profile in the chamber. In figure 8.13a, the horizontal gas temperature profile inside the chamber in proximity to the chamber wall is shown for the expansion 14 of 14-03-2013. Whereas the sensors at a distance of up to 30 mm from the wall show temperature readings that are very close to the wall temperature, the sensor at 100 mm is in good agreement with the mean gas temperature in the chamber. The chamber air appears to be already homogeneously mixed at this distance and the influence of a direct flux from the wall seem to be very small.

Because of this, a strong impact of the wall fluxes on the measurement in Rewas-Iso that would be necessary to explain the relatively large differences between APeT/MBW and Rewas-Iso appears very unlikely.

In addition to the different radial position, the two extraction points of APeT/MBW and

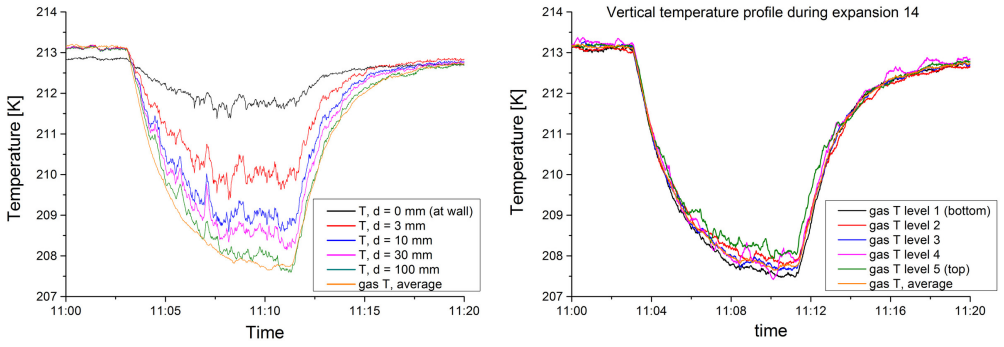

(a) (b)

Figure 8.13: a) The horizontal gas temperature profile in the AIDA chamber close to the chamber wall during an exemplary expansion. Temperature sensors were installed in thermal contact with the wall and at distances of 3, 10, 30 and 100 mm. As reference, the mean gas temperature, averaged over several sensors in the entire chamber is shown, b) The vertical gas temperature profile in the cloud chamber at the different access levels of the chamber

Rewas-Iso are also installed at different heights of the chamber (cf. figure 8.2). Whereas Rewas-Iso is measuring at 135 cm above the base of the chamber, APeT and MBW sample at a height of 6 m. As warm air has a lower density than cold air, warm air rises and there is a vertical temperature gradient in the AIDA chamber. This means that at the extraction point of APeT/MBW on the third level of the AIDA chamber, the temperature will be slightly higher than at the bottom, where Rewas-Iso is measuring (level 1). The vertical temperature gradient is shown exemplarily for the same expansion experiment as previously the horizontal temperature profile in figure 8.13b. There clearly is a difference of approx. 0.5 °C in the gas temperature at the top of the chamber compared to the bottom. The shape of the temperature change during the expansion is very similar on all levels, as are the absolute temperatures. This indicates that the chamber air is relatively well mixed in the entire chamber and differences between the different levels in the chamber are probably not an explanation for the differences between the two total water concentration measurements.

In figure 8.14, two subsequent expansion experiments are compared. In the first experiment, APeT and MBW were exceptionally connected to an extractive line on level 2 of the cloud chamber (approx. 4 m), whereas they were connected to their standard port on level 3 (6 m) in the second experiment. The different water concentrations in the two experiments can be explained by the different conditions during the two expansions (exp. 20 was a pump-down from 230 to 170 mbar and exp. 21 from 300 to 170 mbar). It is noteworthy that despite the different

extraction ports, the overall shape of the water concentration measurement by APeT is identical between the two different sampling heights. This indicates that the different shape of the water concentration measurements of APeT/MBW and Rewas-Iso is not due to a different sampling height.

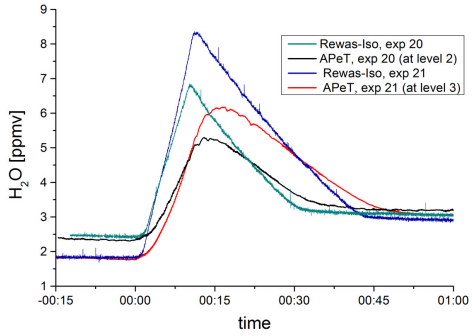

Figure 8.14: Comparison of two subsequent expansion experiments, in exp. 20 APeT and MBW were sampling at 4 m height and in exp. 21 at 6 m. Because of different measurement conditions, the water concentrations are not equal but the shape is identical for both measurement heights

Finally, the ridges inside the cloud chamber that improve its mechanical strength, could hamper a good mixing of the air closer to the walls. The ridges extend approximately 10 cm into the chamber, which is nearly the same distance at which Rewas-Iso is measuring. However, this hypothesis was excluded in an extensive chamber and instrumental intercomparison study (AquaVIT-1) done in the AIDA simulation chamber by Fahey et al. [160]. For experimental conditions similar to the conditions encountered during the Isocloud campaigns, they found that mixing ratio gradients are virtually non-existent.
CFD simulations and simultaneous measurements at various AIDA positions during the intercomparison campaigns AquaVIT 1 and 2 support our arguments against all of the above-mentioned hypotheses [161]. After excluding almost all possible chamber related reasons for the observed discrepancies, the cause may rather be related to the sampling system with a rather small flow of 150 sccm. The difference in the total water measurement of REWAS and APeT is well correlated with the pressure change and relaxes at constant pressure. Therefore, problems with the flow controller system or a dynamic leak seem possible causes for the observation. Despite numerous leak tests and other investigations, neither of these last two hypotheses could be confirmed. However, until now no flow simulations in the chamber were done for isotope changes and a problem due to incomplete mixing of the chamber air remains a possibility as well. The true cause of the discrepancy between the instruments on the lower and higher air extraction lines could thus not yet be revealed and remains speculation.

8.4.2 Ice phase measurements

In figure 8.15, the water concentration measurement of two expansions is shown (top panel) together with the particle density measured with two optical particle counters (OPC, WELAS 2100, second panel). The particle density is with approx. 500 cm^{-3} higher in figure 8.15b than in figure 8.15a (100 cm^{-3}), the water concentration is the opposite. Lower ice nuclei number concentrations at higher water concentrations allow the formation of fewer but larger ice crystals (about 100 µm) in experiment 8.15a compared to about 50 µm in experiment figure 8.15b.
Because of the larger particle sizes, the ice crystals grow more quickly to beyond the cutoff size of the PCVI and are thus sublimated in the sample air arriving in the OF-CEAS spectrometer. In the case of experiment 8 of figure 8.15a, the water concentration behind the PCVI continues to increase for approx. 70 s after the start of the experiment, whereas in experiment 15 (figure 8.15b), it takes approx. 40 s longer for ice crystals to be detectable by the OF-CEAS instrument. Note that this difference in ice crystal size is also visible in the onset behavior of the two different optical particle counters which have different lower detection limits.

In figure 8.16, an expansion experiment at -60°C is shown. In the top panel, the water concentration measurements with an initial water vapor concentration of 40 ppmv are shown. The center panel shows the ratio $HDO/H_2^{16}O$ in the vapor phase, total water in the gas phase, as well as in the ice phase as measured behind the PCVI. Due to heavier wall ice that is released during the pressure decrease, the HD $^{16}O/H_2$ ^{16}O ratio increased from 10.6 to 11.1 during the experiment. The isotope ratio measured by SIRI behind the PCVI increases in the beginning of the experiment (until 11:05 h), then decreases for approximately one minute, before it increases again, to level off at a higher than before the expansion, due to the above discussed wall-induced memory effect for HDO. The one-minute long decrease of the $HDO/H_2^{16}O$ ratio can be observed in several of the experiments (e.g. also in figure 8.10).
This dip in the isotope ratio is probably due to the increasing influence of wall ice throughout the expansion experiment. In the beginning, the ice is becoming progressively enriched because of a preferential crystallization of the heavier isotopologues. As the vapor phase becomes more depleted in the rare isotopologues, more $H_2^{16}O$ molecules crystallize and the isotope ratio of the ice decreases slightly. Because of highly enriched water coming from the walls, the total water isotope ratio increases again and as this water freezes, consequently also the isotope ratio of the ice crystals, leading to the observed behavior with a dip in the isotope ratio in the beginning of the experiment.

Figure 8.17 shows a measurement, in which Rewas-Iso was connected behind the PCVI. In addition to the expansion experiment, the AIDA air before and after the pump-down has been measured with Rewas-Iso directly connected to the AIDA chamber via heated tubing. These two data sets serve as an additional calibration of the measurement and allow comparing directly the isotopic compositions through the PCVI and inside the chamber air.
In the top panels of figure 8.17, the water concentration measurements are shown with a back-

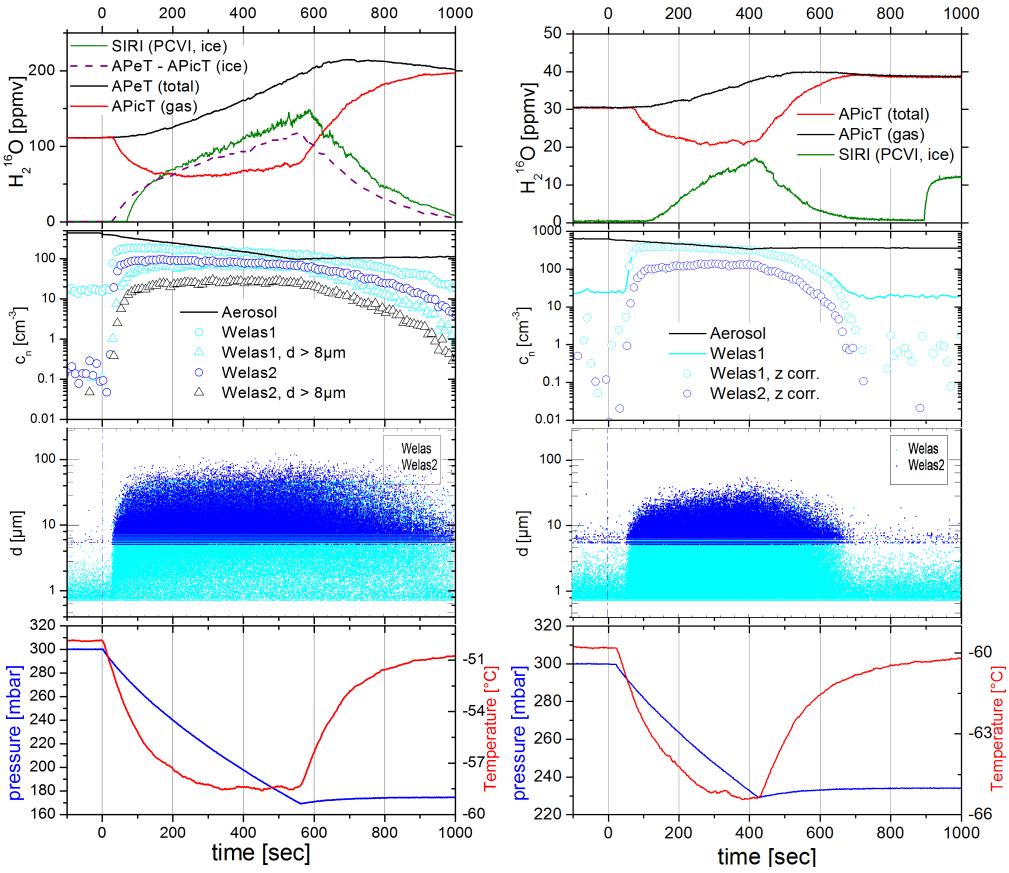

Figure 8.15: Two cloud expansion measurements (a) starting at -50 °C and with 100 particles/cm^{-3} and (b) starting at -60 °C and with 500 particles/cm^{-3}. Top panel: H_2O in gas phase, in the ice behind the PCVI and in total water. Second panel: Measurement of two OPCs (Welas and Welas2) of the particle density in the cloud chamber. Third panel: The maximal particle size in a) is nearly 100 µm compared to around 50 µm in b). Bottom panel: Pressure and air temperature during the experiment

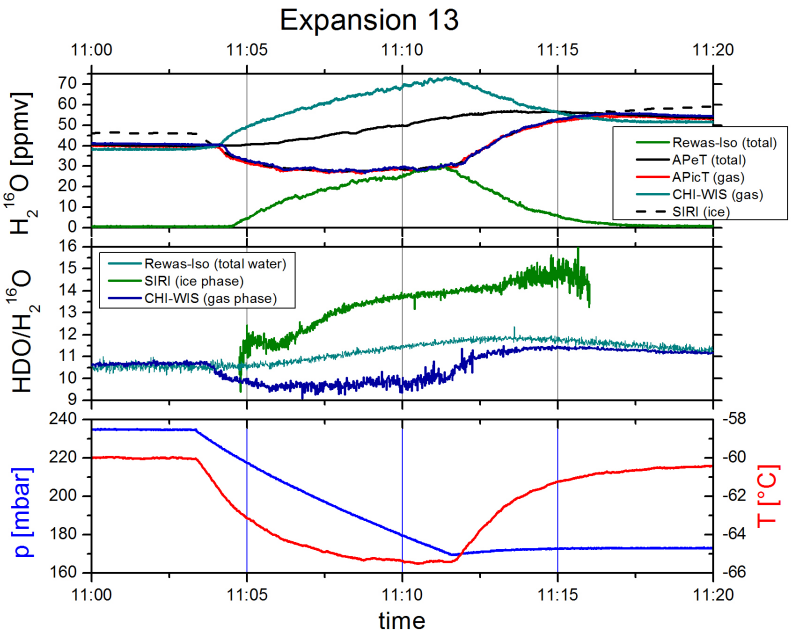

Figure 8.16: Expansion at -60°C. Top panel: Measurement of gas phase, total water and ice behind the PCVI. Center panel: HDO/$H_2^{16}O$ in gas phase, total water and ice. In the ice phase water, a small dip in the isotope ratio can be observed shortly after the beginning of the ice cloud measurement, which is probably related to the water dynamics in the cloud chamber. Bottom panel: Pressure and air temperature during the experiment

ground measurement before (left panel) and after the expansion (right panel). In the center panels, the corresponding $\delta^{18}O$ measurements of background and expansion are given and in the bottom panel, pressure and temperature during the expansion.

For a first estimate of the fractionation factor in the experiment, we assume a constant fractionation factor and only a transition from the vapor phase to ice, thus a Rayleigh fractionation process with one sink. We can then calculate the fractionation factor with the following formula (cf. 1.2.2 and [145]):

$$\frac{R}{R_0} = \left(\frac{N}{N_0}\right)^{\alpha-1} \tag{8.2}$$

with R and R_0 the current and initial isotope ratio and N and N_0 the current and initial water concentration, respectively. The $\delta^{18}O$ values are $3.5 \pm 0.8‰$ and $3.1 \pm 0.7‰$ for the chamber air before and after the expansion, respectively and $10.6 \pm 1.8‰$ for the ice phase behind the PCVI. The water concentration before the ice cloud formation was 8.12 ± 0.05 ppmv and the lowest water concentration during the expansion (measured with APicT) 5.65 ± 0.07 ppmv. For the fractionation coefficient α, we then get $^{18}\alpha = 1.018 \pm 0.014$.

This is only a first estimate, as no additional sinks and sources for water, such as the chamber

wall were taken into account. In addition, the measurement behind the PCVI risks to be biased as only ice crystals of a certain size can be measured. Even with the improved detection limit in Rewas-Iso of approx. 4‰ in $\delta^{18}O$ at water concentrations around 20 ppmv, the standard error made in the calculation of the fractionation factor (0.014) relatively high. A better estimation of the fractionation factors can be obtained by the comparison of in-situ measurements of the gas phase (ISO-APicT and CHI-WIS) with measurements of the total water (APeT, MBW and Rewas-Iso). In addition, a more complete model of the water fluxes in the cloud chamber has to be developed, as was done by Kara Lamb of the University of Chicago as part of her PhD thesis. A brief introduction of this model will be given in the next section, for more details we refer to the PhD thesis of K. Lamb and [162].

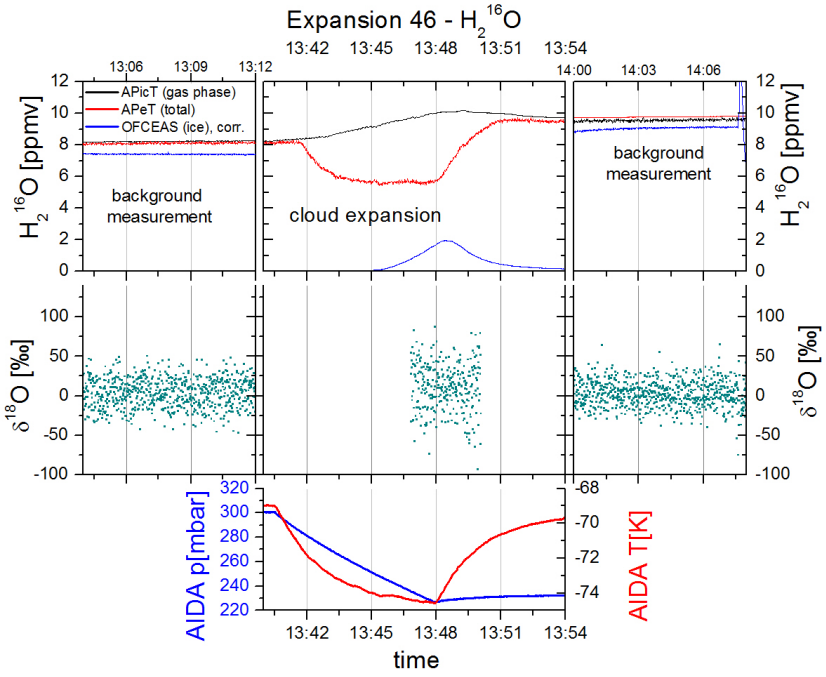

Figure 8.17: Expansion at very low water concentration. Top panel: water concentration measurement during the experiment (middle) and background measurements before (left) and after (right) the expansion. Middle panel: corresponding $\delta^{18}O$ measurements of background and expansions. Bottom panel: pressure and temperature during the expansion

8.5 Modeling of fluxes in the AIDA chamber

As the ice cloud formation experiments are done in a finite volume, we have to take into account interactions of the gas inside the chamber with the chamber wall and the removal of air from the chamber during the experiments.

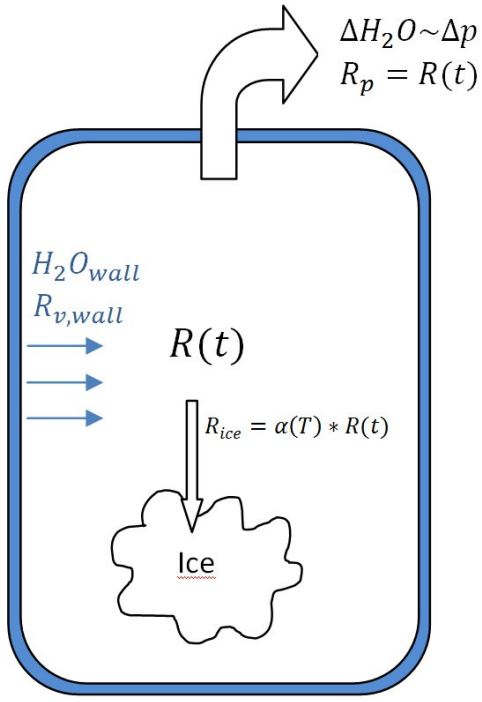

Figure 8.18: Schematics of the water and isotope fluxes included in the model

Figure 8.18 gives a schematics of the water fluxes that are simulated in the model. Three different fluxes of H_2O are assumed:
1) A reduction of $[H_2O]_{total}$ in the chamber because of the decrease in pressure:

$$\Delta [H_2O]_{pump} = [H_2O] \cdot \frac{dN}{N} \tag{8.3}$$

$$= [H_2O] \cdot \left(\frac{(p + \Delta p)T}{p(T + \Delta T)} - 1 \right) \tag{8.4}$$

As the chamber air is constantly stirred by a mixing fan, we assume a homogenous isotopic distribution throughout the chamber, and :

$$R_{pump} = R(t) \tag{8.5}$$

2) An exchange between vapor and ice phase due to crystallization and sublimation

$$\Delta [H_2O]_{ice} = [H_2O]_{total} - [H_2O]_{gas} \tag{8.6}$$

As total water the measurement of APeT is used and for water vapor the data from APicT. For the crystallization, Rayleigh distillation is assumed with (cf. section 1.2.2)

$$\frac{dR}{R} = (\alpha - 1)\frac{dN}{N} \tag{8.7}$$

As the gas temperature change during an experiment is typically of the order of only 4°C to 5°C during an ice cloud formation, a linear dependence of the fractionation factor α on the temperature can be assumed:

$$\alpha = a_0 + a_1 T \tag{8.8}$$

The offset a_0 is a free parameter in the fit and the slope a_1 is derived from the temperature dependence of the fractionation factor as described by Merlivat and Nief ([34], equation (1.10)). The result is however insensitive to whether the formulation of Merlivat and Nief is used or the formulation by Ellehøj [163].
α can be separated into kinetic and equilibrium fractionation (section 1.2.2,[39],[46]):

$$\text{with } \alpha = \alpha_{eq} \cdot \alpha_k \tag{8.9}$$

$$\text{and } \alpha_K = \frac{S}{1 + \alpha_{eq}\frac{D}{D'}(S-1)} \tag{8.10}$$

and the the equilibrium fractionation factor can subsequently be determined based on equations 8.8 and 8.10. The water that sublimates from ice to vapor is assumed to have the same isotope ratio it froze at.

3) A flux of $[H_2O]$ from wall ice into the chamber air:

$$\Delta\,[H_2O]_{wall} = \Delta\,[H_2O]_{total} - \Delta\,[H_2O]_{pump} \tag{8.11}$$

As the fraction of ice coming from the wall is much smaller than the total amount of wall ice, the isotopic composition of the wall ice can be assumed to be constant throughout an experiment. In addition, the change of the wall temperature is very small during the adiabatic expansions. Because of this, we can assume that the isotope ratio of the ice coming from the wall is practically constant:

$$R_{v,wall} = const. \tag{8.12}$$

The parameter $R_{v,wall}$ is fitted. A list of all input data and parameters used in the model is shown in table 8.2.

Table 8.2: Input data and parameters used in the isotope flux model

parameter	determination
$\Delta[H_2O]_{total}$	measured by APeT/MBW/Rewas-Iso
$\Delta[H_2O]_{gas}$	measured by APicT/SP-APicT/ISO-APicT
$\Delta[H_2O]_{pump}$	$= [H_2O] \cdot \frac{(p+\Delta p)T}{p(T+\Delta T)} - 1$
$\Delta[H_2O]_{ice}$	$= [H_2O]_{total} - [H_2O]_{gas}$
$\Delta[H_2O]_{wall}$	$= \Delta[H_2O]_{total} - \Delta[H_2O]_{pump}$
$R(t)_{gas}$	measured by CHI-WIS/ISO-APicT
$R(t)_{total}$	measured by REWAS-Iso
$R_{v,wall}$	const., free fit parameter
R_{pump}	$= R(t)_{gas}$
R_{ice}	$= \alpha(T) \cdot \alpha_{gas}$
$\alpha(T)$	$= \alpha_0 + \alpha_1 T$
α_0	const., free fit parameter
α_1	based on [34] or [163]

The ice, pumping, and wall flux components are determined for one second time intervals by interpolated data sets. The model is adapted to the experimental data with a Levenberg-Marquardt least squares fit.

In figure 8.19, the isotopic ratio measured by CHI-WIS is shown for a typical expansion experiment, along with the model fit (top panel). In the middle panel, the different water fluxes assumed in the model (see above) are given, showing the removal of chamber air as negative flux and a positive flux coming from the walls. The flux between vapor and ice is positive in the beginning, indicating a transition from vapor to ice phase when the air temperature decreases and water vapor saturation is reached. When the temperature increases at the end of the experiment, the vapor-ice flux is negative, representing the transition from ice phase to water vapor.
In the bottom panel, water concentrations measured by APeT and APicT are shown along with chamber pressure and air temperature, showing the typical behavior during the expansion experiments as described above.

Based on the model, equilibrium fractionation factors have been derived from the fit for a series of Isocloud experiments at different temperatures. The fractionation factors are shown in figure 8.20 and compared with previous results by other groups ([34, 127, 164–168]). The temperature dependence of fractionation factors derived from our experiments agree with previous investigations. The recent proposition of higher fractionation factors at temperatures below 250 K [127] is not confirmed.

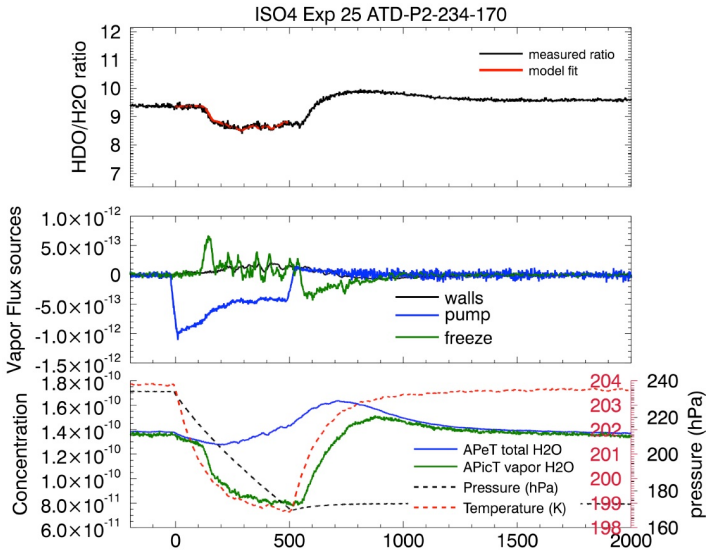

Figure 8.19: Figure from [162], Top panel: The isotopic ratio measured by CHI-WIS, along with the model fit. Middle panel: Model fluxes between ice and vapor (green), from the walls (black) and due to the removal of chamber air by the pump (blue). Bottom panel: Total and vapor phase water concentrations measured by APeT (blue) and APicT (green). In dashed red chamber air temperature and in dashed black pressure.

8.6 Summary of Isocloud

Although it was not yet possible to determine, which of the two mechanisms, diffusion-limited fractionation or equilibrium fractionation, is responsible for the supersaturation observed in the upper atmosphere, the Isocloud project yielded very promising results. It was possible to establish a measurement protocol to efficiently measure ice cloud formation at temperatures as low as -80°C in vapor phase, total water and ice phase simultaneously. Because of the isotope calibration of the external OF-CEAS spectrometers, we could calibrate the internal TDL spectrometers and reduce the relative error to $< 1\%$ on a very large isotopic enrichment. The ice phase was successfully measured with the OF-CEAS instruments behind the PCVI and a first comparison of the isotope ratios in all three phases could be done. Rewas-Iso could be successfully adapted to measure $\delta^{18}O$ with four times higher precision than before and at water concentrations as low as a few ppmv.

Because of undefined problems in the connection of Rewas-Iso to the AIDA cloud chamber, the total water measurement is unfortunately only partly exploitable and has to be treated carefully. If the observed differences between Rewas-Iso and APeT are due to fluxes from the chamber walls that are captured by Rewas-Iso due to the closer proximity to the walls, these measurements could for example be used to test the validity of the above described modeling approach of wall fluxes and could even be used to refine the model. At the time of this writing,

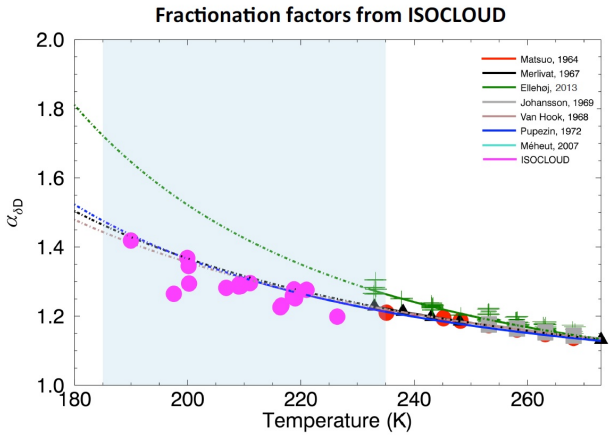

Figure 8.20: Figure from Kara D. Lamb, UoC: Comparison of the temperature dependence of fractionation factors derived from the (isotope) flux model in the AIDA chamber with previously published results. Pink dots represent fractionation factors inferred from ISOCLOUD measurements. Previously experimental results are shown with data as symbols and modeling results as lines (solid for experimental ranges and dashed for extrapolations). Our results agree with previous published data but not with the recently proposed increase of equilibrium fractionation factors for water vapor over ice.

this was however work in progress and could not be included.

The mechanisms for supersaturation could not clearly be identified because of limitations in the experimental set-up. Most importantly, the uncertainty in the total water measurement because of problems in the Rewas-Iso sample line make a precise determination of the isotopic composition of total water impossible. In addition, the measurement of ice phase water behind the PCVI only reflects a portion of the total ice phase. Due to the inevitable cut-off size of separated particles, smaller ice crystals are lost and are not detectable. Therefore, it is not possible to accurately determine the difference between the isotopic composition of gas phase water and ice phase water that would be necessary to further investigate the two possible explanations of supersaturation.

To overcome these limitations, for a next cloud campaign, several improvements could be made and would lead to an even better result and better intercomparibility of the different instruments. Rewas-Iso should be connected to the same outlet as the other two total water measurements, MBW and APeT, in order to eliminate any uncertainty concerning the sampling location and transfer of the sample through the extraction tubing. Regular measurements should be done at stable conditions inside the cloud chamber to calibrate the internal isotope measurements against the external (and previously calibrated) OF-CEAS spectrometers. The wavelength range of SIRI should be changed to the same range as Rewas-Iso, which is especially important for lower temperatures with very low water concentrations.

Finally, regular calibrations of the OF-CEAS spectrometers with the Syringe Nanoliter Injection

Calibration System should be made with two enriched standards approximately matching the isotopic composition inside the cloud chamber. This way, an additional uncertainty because of different isotopic composition of calibration and real measurements, can be eliminated.

Conclusion

In the framework of this thesis, we developed an OF-CEAS spectrometer that shows significantly better performance and stability than previous instruments based on the same technique. At water concentrations around 80 ppmv, the precision was 0.8‰, 0.1‰ and 0.2‰ for δ^2H, δ^{18}O and δ^{17}O, respectively with optimum averaging time (about 30 min). With 4s averaging, the precision is 12‰, 1.1‰ and 3.2‰. In the optimum measurement range of the instrument at water concentrations around 650 ppmv, precisions of 0.28‰, 0.02‰ and 0.07‰ can be achieved with averaging times of 30 to 60 min.

As limiting factor of the accuracy, a strong concentration dependence of the isotope ratio measurements was identified. Due to thorough investigations and optimization of the analysis procedure, the main source of this dependency was identified to be constant pattern noise in the measurements, which propagates in the isotope ratios and becomes especially prominent at low absorptions, corresponding to lower water concentrations. By comparing the experimental data with synthetic absorption spectra, we could conclude that approx. 83% of the baseline noise is due to slowly changing structured noise. The structured noise is assumed to originate from residual backscattering on multiple optical surfaces in the beam path and could not (yet) be removed.

We therefore propose a calibration strategy with two isotope standards. One standard should be measured at four different water concentrations before the measurement, with each step maintained for 30 min to determine the concentration dependence. In addition, the second standard should be measured at one water concentration to adapt the isotope scale, which is a much smaller correction than the correction for the concentration dependence. After the measurement, the second water standard should be measured at four different water concentrations and the first standard at only one concentration. This way, the correction function for the unknown sample can subsequently calculated as a linear combination of the individual functions of the two standards and possible drift can be corrected for by the additional one-concentration measurements of the other standard, respectively. In this way, calibration measurements are done

for approximately five hours per day and measurements of unknown samples can be done for approximately the same time between the two 2.5 h calibrations. If the water concentration only shows small variations during a measurement (no variations of more than 200 ppmv and no water concentrations below 80 ppmv), the number of concentration steps could be reduced to three or even two steps, thus shortening the time needed for calibration.

With the in this thesis established calibration and correction protocol, the demonstrated accuracy of the measurements for water concentrations above 80 ppmv is better than 10‰ for δ^2H, 4‰ for δ^{18}O and 5‰ for δ^{17}O. The time between the two calibrations should be sufficiently short to reduce additional uncertainties due to drift of the instrument. Based on the drift analysis with Allan-Werle plots, we recommend to run calibrations approximately every 6h.

If measurements should be done at lower water concentrations, the error made in the correction strongly increases due to an inverse dependency of the isotope ratios on the water concentration, which becomes very large for drier gas samples. At 50 ppmv, the accuracy is approx. 35‰, 8‰ and 10‰ for δ^2H, δ^{18}O and δ^{17}O, respectively.

For measurements of δ^{18}O at water concentrations as low as 5 ppmv, we successfully demonstrated the application of a modified OF-CEAS spectrometer, measuring at 7286 cm^{-1}. With this modified instrument, a precision better than 0.2‰ was demonstrated for δ^{18}O at water concentrations below 20 ppmv. In addition, due to much stronger absorption coefficients, the water concentration dependency of the isotope measurements are much smaller than in measurements at 7184 cm^{-1} and 7200 cm^{-1}.

As a novel calibration instrument, the Syringe Nanoliter Injection Calibration System (SNICS) was developed and used for calibration measurements in the lab and during several measurement campaigns at the AIDA cloud chamber in Karlsruhe. A theoretical model was established to better explain the operation of the syringe injection system and showed good agreement with the experimental results. In parallel measurements of SNICS and a microdrop injector, we could show that no fractionation occurs in the water inside the syringe itself and that the new system is well adapted for calibration measurements at water concentrations as low as several tens of ppmv.

Finally, the OF-CEAS spectrometer was successfully operated during measurement campaigns in Antarctica and at the cloud simulation chamber in Karlsruhe, Germany. Due to difficulties with the calibration in Antarctica, this data could not be fully exploited. However, due to its proper functioning under harsh conditions, we were able to show the promising perspective of using optical spectrometers for isotope measurements in the coldest region of the planet. With the cloud chamber experiments, we were able to show that the OF-CEAS technique is, after proper adaptions, capable to measure water isotope ratios even at water concentrations as low as several ppm and could thus also be successfully used for atmospheric studies, for example in the stratosphere.

In the near future, more experimental investigations will be done in order to reduce the water concentration dependence of the OF-CEAS spectrometer, which is at the moment the limiting

factor for a higher precision and accuracy of the measurements. One possibility that is going to be studied is the removal of the additional reference photo diode and to extract this information from the measurement of the signal photodiode. In this way, optical elements in the beam path such as the beam splitter, a lens in front of the reference photo diode and the photo diode itself could be removed, which would eliminate parasitic reflections and possible optical fringes in the measurements and could result in a reduced concentration dependence.

As it was shown in the framework of this thesis, the novel OF-CEAS spectrometer is well adapted to measure at very low water concentrations. The instrument can with proper calibration be used for measurements under extreme conditions as for example encountered in continental Antarctica. Next winter, it will probably be part of an upcoming measurement campaign at the French Italian Antarctic research station of Dome Concordia (75°06'S - 123°21'E). This campaign will be done in the framework of the European Research Council (ERC) Starting Grant project COMBINISO of A. Landais of Laboratoire des Sciences du Climat et de l'Environnement. At Dome Concordia, the mean air temperature is around -50.8°C [148], which corresponds at a mean pressure of around 650 mbar to water mixing ratios as low as 60 ppmv [169]. The calibration device, SNICS, can be used not only to calibrate the OF-CEAS instrument but also other, e.g. commercially available, instruments. It is also going to be used for the upcoming measurements at Dome Concordia.

The objective of these measurements and the ERC COMBINISO project in general is to establish a better description of the links between climate, hydrological cycle and stratospheric inputs over the last 100 years in Antarctica. For a correct use of water isotopes, it is important to better understand the relation between physical properties such as temperature and relative humidity and the fractionation factors. First measurements in a cloud chamber have thus been done to investigate kinetic fractionation factors during solid condensation at low temperature [170]. Further investigations will be done to determine water fractionation coefficients. These can be used to improve the description of cloud microphysics in isotopic models and will thus lead to a better understanding of isotope records in polar ice cores. To accomplish the goal of even more stable water vapor isotope measurements, a new water vapor isotope spectrometer based on the technique of Optical Feedback Frequency Stabilized Cavity Ring-Down Spectroscopy (OFFS-CRDS)[171] is currently being developed in this project to measure all three of the water vapor isotopes, $\delta^{18}O$, $\delta^{17}O$ and $\delta^{2}H$, and will be employed together with our OF-CEAS spectrometer.

Bibliography

[1] Jouzel, J ; Masson-Delmotte, V ; Cattani, O ; Dreyfus, G ; Falourd, S ; Hoffmann, G ; Minster, B ; Nouet, J ; Barnola, J M. ; Chappellaz, J ; Fischer, H ; Gallet, J C. ; Johnsen, S ; Leuenberger, M ; Loulergue, L ; Luethi, D ; Oerter, H ; Parrenin, F ; Raisbeck, G ; Raynaud, D ; Schilt, A ; Schwander, J ; Selmo, E ; Souchez, R ; Spahni, R ; Stauffer, B ; Steffensen, J P. ; Stenni, B ; Stocker, T F. ; Tison, J L. ; Werner, M ; Wolff, E W.: Orbital and millennial Antarctic climate variability over the past 800,000 years. In: *Science (New York, N.Y.)* 317 (2007), No. 5839, 793–6

[2] Hoffmann, G ; Werner, M ; Heimann, M: The water isotope module of the ECHAM atmospheric general circulation model: a study on timescales from days to several years. In: *J. Geophys. Res.* 103 (1998), No. D14, P. 16871–16896

[3] Risi, C. ; Landais, A. ; Winkler, R. ; Vimeux, F.: What controls the spatio-temporal distribution of D-excess and 17O-excess in precipitation? A general circulation model study. In: *Climate of the Past Discussions* 8 (2012), No. 6, 5493–5543

[4] Baer, D.S. ; Paul, J.B. ; Gupta, M. ; O'Keefe, a.: Sensitive absorption measurements in the near-infrared region using off-axis integrated-cavity-output spectroscopy. In: *Applied Physics B: Lasers and Optics* 75 (2002), No. 2-3, 261–265

[5] Webster, Christopher R. ; Heymsfield, Andrew J.: Water isotope ratios D/H, 18O/16O, 17O/16O in and out of clouds map dehydration pathways. In: *Science (New York, N.Y.)* 302 (2003), No. 5651, 1742–5

[6] Kerstel, E.R.T. ; Iannone, R.Q. ; Chenevier, M ; Kassi, S ; Jost, H.-J. ; Romanini, D: A water isotope (2H, 17O, and 18O) spectrometer based on optical feedback cavity-enhanced absorption for in situ airborne applications. In: *Applied Physics B* 85 (2006), No. 2-3, 397–406

[7] Dyroff, C. ; Fütterer, D. ; Zahn, A.: Compact diode-laser spectrometer ISOWAT for highly sensitive airborne measurements of water-isotope ratios. In: *Applied Physics B* 98 (2010), No. 2-3, 537–548

[8] Rozanski, K.: 18. Isotopes in atmospheric moisture. In: Aggarwal, Pradeep K. (Edt.) ; Gat, Joel R. (Edt.) ; Froehlich, Klaus F. (Edt.): *Isotopes in the Water Cycle - Past, Present and Future of a Developing Science*. 2005, Chapter 18. Isotop, P. 291–301

[9] Solomon, Susan: Stratospheric ozone depletion: A review of concepts and history. In: *Reviews of Geophysics* 37 (1999), No. 3, 275

[10] Sayres, David S. ; Moyer, E J. ; Hanisco, T F. ; St Clair, J M. ; Keutsch, F N. ; O'Brien, A ; Allen, N T. ; Lapson, L ; Demusz, J N. ; Rivero, M ; Martin, T ; Greenberg, M ; Tuozzolo, C ; Engel, G S. ; Kroll, J H. ; Paul, J B. ; Anderson, J G.: A new cavity based absorption instrument for detection of water isotopologues in the upper troposphere and lower stratosphere. In: *The Review of scientific instruments* 80 (2009), No. 4, 044102

[11] Dansgaard, W: The abundance of 18O in atmospheric water and water vapour. In: *Tellus* 5 (1953), No. 4, P. 461–469

[12] Epstein, S ; Mayeda, T: Variation of O18 content of waters from natural sources. In: *Geochimica et Cosmochimica Acta* 4 (1953), No. 5, 213–224

[13] Craig, H: Isotopic Variations in Meteoric Waters. In: *Science (New York, N.Y.)* 133 (1961), No. 3465, 1702–3

[14] Dansgaard, W: Stable isotopes in precipitation. In: *Tellus* 16 (1964), No. 4, 436–468

[15] Jouzel, J. ; Merlivat, L. ; Roth, E.: Isotopic study of hail. In: *Journal of Geophysical Research* 80 (1975), No. 36, 5015–5030

[16] Risi, Camille ; Bony, Sandrine ; Vimeux, Francoise ; Descroix, Luc ; Ibrahim, Boubacar ; Lebreton, Eric ; Mamadou, Ibrahim ; Sultan, Benjamin: What controls the isotopic composition of the African monsoon precipitation? Insights from event-based precipitation collected during the 2006 AMMA field campaign. In: *Geophysical Research Letters* 35 (2008), No. 24, L24808

[17] Lee, Jung-Eun ; Pierrehumbert, Raymond ; Swann, Abigail ; Lintner, Benjamin R.: Sensitivity of stable water isotopic values to convective parameterization schemes. In: *Geophysical Research Letters* 36 (2009), No. 23, L23801

[18] Kurita, Naoyuki ; Noone, David ; Risi, Camille ; Schmidt, Gavin A. ; Yamada, Hiroyuki ; Yoneyama, Kunio: Intraseasonal isotopic variation associated with the Madden-Julian Oscillation. In: *Journal of Geophysical Research: Atmospheres* 116 (2011), No. D24

[19] Augustin, Laurent ; Barbante, Carlo ; Barnes, Piers R F. ; Barnola, Jean M. ; Bigler, Matthias ; Castellano, Emiliano ; Cattani, Olivier ; Chappellaz, Jerome ; Dahl-Jensen, Dorthe ; Delmonte, Barbara ; Dreyfus, Gabrielle ; Durand, Gael ; Falourd, Sonia ; Fischer, Hubertus ; Flückiger, Jacqueline ; Hansson, Margareta E. ; Huybrechts, Philippe ; Jugie, Gérard ; Johnsen, Sigfus J. ; Jouzel, Jean ; Kaufmann, Patrik ; Kipfstuhl, Josef ; Lambert, Fabrice ; Lipenkov, Vladimir Y. ; Littot, Geneviève C ; Longinelli, Antonio ; Lorrain, Reginald ; Maggi, Valter ; Masson-Delmotte, Valerie ; Miller, Heinz ; Mulvaney, Robert ; Oerlemans, Johannes ; Oerter, Hans ; Orombelli, Giuseppe ; Parrenin, Frederic ; Peel, David a. ; Petit, Jean-Robert ; Raynaud, Dominique ; Ritz, Catherine ; Ruth, Urs ; Schwander, Jakob ; Siegenthaler, Urs ; Souchez, Roland ; Stauffer, Bernhard ; Steffensen, Jorgen P. ; Stenni, Barbara ; Stocker, Thomas F. ; Tabacco, Ignazio E. ; Udisti, Roberto ; Van De Wal, Roderik S W. ; Van Den Broeke, Michiel ; Weiss, Jerome ; Wilhelms, Frank ; Winther, Jan-Gunnar ; Wolff, Eric W. ; Zucchelli, Mario ; Members, Epica C.: Eight glacial cycles from an Antarctic ice core. In: *Nature* 429 (2004), No. 6992, 623–628

[20] Masson-Delmotte, V. ; Hou, S. ; Ekaykin, A. ; Jouzel, J. ; Aristarain, A. ; Bernardo, R. T. ; Bromwich, D. ; Cattani, O. ; Delmotte, M. ; Falourd, S. ; Frezzotti, M. ; Gallée, H. ; Genoni, L. ; Isaksson, E. ; Landais, A. ; Helsen, M. M. ; Hoffmann, G. ; Lopez, J. ; Morgan, V. ; Motoyama, H. ; Noone, D. ; Oerter, H. ; Petit, J. R. ; Royer, A. ; Uemura, R. ; Schmidt, G. A. ; Schlosser, E. ; Simões, J. C. ; Steig, E. J. ; Stenni, B. ; Stievenard, M. ; Broeke, M. R. d. ; Wal, R. S. W. d. ; Berg, W. J. d. ; Vimeux, F. ; White, J. W. C.: A Review of Antarctic Surface Snow Isotopic Composition: Observations, Atmospheric Circulation, and Isotopic Modeling*. In: *Journal of Climate* 21 (2008), No. 13, 3359–3387

[21] Goff, J. A.: Saturation pressure of water on the new kelvin scale. In: *Trans. Am. Soc. Heating Air-Cond. Eng.* 63 (1957), P. 347–354

[22] Goff, J. A.: *Saturation pressure of water on the new Kelvin scale. In Humidity and moisture: Measurement and control in science and industry.* Reinhold Publishing, New York, USA, 1965

[23] Murphy, D. M. ; Koop, T.: Review of the vapour pressures of ice and supercooled water for atmospheric applications. In: *Quarterly Journal of the Royal Meteorological Society* 131 (2005), No. 608, 1539–1565

[24] McNaught, A. D. ; Wilkinson, A.: *Compendium of Chemical Terminology, 2nd ed. "The Gold Book".* 2nd. Oxford : Blackwell Scientific Publications, 1997

[25] Mook, Willem G.: *Lecture Notes on Stable Isotope Hydrology.* Internatio. 2001. – 57 – 60 P.

[26] International Atomic Energy Agency: Reference Sheet for International Measurement Standards / IAEA. 2009 (May). – Scientific report. – 5 P.

[27] De Wit, J.C. ; Straaten, C.M. van d. ; Mook, W.G: Determination of the Absolute Hydrogen Isotopic Ratio of VSMOW and SLAP. In: *Geostandards Newsletter* 4 (1980), No. 1, P. 33–36

[28] Baertschi, P.: Absolute 18O Content of Standard Mean Ocean Water. In: *Earth and Planetary Science Letters* 31 (1976), P. 341–344

[29] Li, W. ; Ni, B. ; Jin, D. ; Chang, T.L: Measurement of the Absolute Abundance of Oxygen-17 in VSMOW. In: *Chinese Science Bulletin* 33 (1988), P. 1610–1613

[30] Wise, S.A. ; Watters, R.L.: Report of Investigation Reference Materials 8535, 8536, 8537 / National Institute of Standards & Technology. 2005. – Scientific report

[31] Gonfiantini, R. ; Rozanski, K. ; Stichler, W.: Intercalibration of Environmental Isotope Measurements: The Program of the International Atomic Energy Agency. In: *Radiocarbon* 32 (1990), No. 3, P. 369–374

[32] Criss, R. E.: *Principles of Stable Isotope Distribution.* Oxford University Press, USA, 1999

[33] Chacko, T. ; Cole, D. ; Horita, J.: Equilibrium oxygen, hydrogen and carbon isotope fractionation factors applicable to geologic systems. In: *Reviews in Mineralogy and Geochemistry* 43 (2001), P. 1–81

[34] Merlivat, L ; Nief, G: Fractionnement isotopique lors des changements d'état solide-vapeur et liquide-vapeur de l'eau à des températures inférieures à 0Â°C. In: *Tellus* 19 (1967), No. 1, 122–127

[35] Majoube, M.: Fractionnement en 18O entre la glace et la vapeur d'eau. In: *J. Chim. Phys.* 68 (1971), P. 625–636

[36] Majoube, M.: Fractionnement en Oxygène 18 et en Deutérium entre l'eau et sa vapeur. In: *J. Chim. Phys.* 10 (1971), P. 1423–1436

[37] Cappa, Christopher D.: Isotopic fractionation of water during evaporation. In: *Journal of Geophysical Research* 108 (2003), No. D16, 4525

[38] Luz, Boaz ; Barkan, Eugeni ; Yam, Ruth ; Shemesh, Aldo: Fractionation of oxygen and hydrogen isotopes in evaporating water. In: *Geochimica et Cosmochimica Acta* 73 (2009), No. 22, 6697–6703

[39] Jouzel, Jean ; Merlivat, Liliane: Deuterium and oxygen 18 in precipitation: Modeling of the isotopic effects during snow formation. In: *Journal of Geophysical Research: ...* 89 (1984), No. D7, 11749

[40] Merlivat, Liliane: Molecular diffusivities of H216O, HD16O, and H218O in gases. In: *The Journal of Chemical Physics* 69 (1978), No. 6, 2864

[41] Lorius, C. ; Merlivat, L. ; Hagemann, R.: Variation in the mean deuterium content of precipitations in Antarctica. In: *Journal of Geophysical Research* 74 (1969), No. 28, 7027–7031

[42] Jouzel, Jean ; Merlivat, Liliane ; Lorius, Claude: Deuterium excess in an East Antarctic ice core suggests higher relative humidity at the oceanic surface during the last glacial maximum. In: *Nature* 299 (1982), No. 5885, 688–691

[43] Vimeux, F ; Masson, V ; Jouzel, J ; Stievenard, M ; Petit, JR: Glacial-interglacial changes in ocean surface conditions in the southern hemisphere. In: *NATURE* 398 (1999), No. 6726, 410–413

[44] Barkan, Eugeni ; Luz, Boaz: High precision measurements of 17O/16O and 18O/16O ratios in H2O. In: *Rapid communications in mass spectrometry : RCM* 19 (2005), No. 24, 3737–42

[45] Barkan, Eugeni ; Luz, Boaz: Diffusivity fractionations of H2(16)O/H2(17)O and H2(16)O/H2(18)O in air and their implications for isotope hydrology. In: *Rapid communications in mass spectrometry : RCM* 21 (2007), No. 18, 2999–3005

[46] Landais, Amaelle ; Barkan, Eugeni ; Luz, Boaz: Record of δ 18 O and 17 O-excess in ice from Vostok Antarctica during the last 150,000 years. In: *Geophysical Research Letters* 35 (2008), No. 2, L02709

[47] Gat, J. R. ; Matsui, E.: Atmospheric water balance in the Amazon basin: An isotopic evapotranspiration model. In: *Journal of Geophysical Research* 96 (1991), No. D7, 13179

[48] Berman, Elena S F. ; Levin, Naomi E. ; Landais, Amaelle ; Li, Shuning ; Owano, Thomas: Measurement of δ18O, δ17O, and 17O-excess in water by off-axis integrated cavity output spectroscopy and isotope ratio mass spectrometry. In: *Analytical chemistry* 85 (2013), No. 21, 10392–8

[49] Steig, E. J. ; Gkinis, V. ; Schauer, a. J. ; Schoenemann, S. W. ; Samek, K. ; Hoffnagle, J. ; Dennis, K. J. ; Tan, S. M.: Calibrated high-precision 17Oexcess measurements using laser-current tuned cavity ring-down spectroscopy. In: *Atmospheric Measurement Techniques Discussions* 6 (2013), No. 6, 10191–10229

[50] Winkler, R. ; Landais, A. ; Sodemann, H. ; Dümbgen, L. ; Prié, F. ; Masson-Delmotte, V. ; Stenni, B. ; Jouzel, J.: Deglaciation records of 17O-excess in East Antarctica: reliable reconstruction of oceanic relative humidity from coastal sites. In: *Climate of the Past Discussions* 7 (2011), No. 3, 1845–1886

[51] Schoenemann, Spruce W. ; Steig, Eric J. ; Ding, Qinghua ; Markle, Bradley R. ; Schauer, Andrew J.: Triple water-isotopologue record from WAIS Divide, Antarctica: Controls on glacial-interglacial changes in 17-O(excess) of precipitation. In: *Journal of Geophysical Research: Atmospheres* 119 (2014), No. 14, 8741–8763

[52] Steen-Larsen, H. C. ; Sveinbjörnsdottir, a. E. ; Peters, a. J. ; Masson-Delmotte, V. ; Guishard, M. P. ; Hsiao, G. ; Jouzel, J. ; Noone, D. ; Warren, J. K. ; White, J. W. C.: Climatic controls on water vapor deuterium excess in the marine boundary layer of the North Atlantic based on 500 days of in situ, continuous measurements. In: *Atmospheric Chemistry and Physics Discussions* 14 (2014), No. 2, 2363–2401

[53] Kerstel, E R T. ; Meijer, H A J.: Optical Isotope Ratio Measurements in Hydrology (Chapter 9). In: Aggarwal, P.K. (Edt.) ; Gat, J. (Edt.) ; Froehlich, K. (Edt.): *Isotopes in the Water Cycle: past, present and future of a developing science.* 2005, P. 109–123

[54] J. Bigeleisen ; M.J., Perlman ; H., Prosser: Conversion of hydrogenic materials for hydrogen to isotopic analysis. In: *Anal. Chem1* 24 (1952), P. 1356–1357

[55] Gehre, M. ; Höfling, R. ; Kowski, P.: Sample preparation device for quantitative hydrogen isotope analysis using chromiun metal. In: *Anal. Chem.* 68 (1996), P. 4414

[56] Socki, R.A. ; Romanek, C.S. ; Gibson, E.K: On-line technique for measuring stable oxygen and hydrogen isotopes from microliter quantities of water. In: *Anal. Chem.1* 71 (1999), P. 2250–2253

[57] Begley, I.S. ; Scrimgeour, C.M.: High-precision d2H and d18O measurement for water and volatile organic compounds by continuous-flow pyrolysis isotope ratio mass spectrometry. In: *Anal. Chem.* 69 (1997), P. 1530–1535

[58] Phillips, A. ; Fourel, F. ; Morrison, J.: Oxygen-deuterium isotopic measurements using a variety of pyrolysis methods â€“ IRMS continuous-flow techniques. In: *Isotopes in Environ. Health Stud.* 36 (2000), P. 347

[59] Helliker, Brent R. ; Roden, John S. ; Cook, Craig ; Ehleringer, James R.: A rapid and precise method for sampling and determining the oxygen isotope ratio of atmospheric water vapor. In: *Rapid communications in mass spectrometry : RCM* 16 (2002), No. 10, 929–32

[60] Han, L-F ; Gröning, M ; Aggarwal, P. ; Helliker, B.R.: Reliable determination of oxygen and hydrogen isotope ratios in atmospheric water vapour adsorbed on 3A molecular sieve. In: *Rapid Communications in Mass Spectrometry* 20 (2006), No. 23, 3612–3618

[61] Rothman, L.S. ; Gordon, I.E. ; Babikov, Y. ; Barbe, A. ; Chris Benner, D. ; Bernath, P.F. ; Birk, M. ; Bizzocchi, L. ; Boudon, V. ; Brown, L.R. ; Campargue, A. ; Chance, K. ; Cohen, E.A. ; Coudert, L.H. ; Devi, V.M. ; Drouin, B.J. ; Fayt, A. ; Flaud, J.-M. ; Gamache, R.R. ; Harrison, J.J. ; Hartmann, J.-M. ; Hill, C. ; Hodges, J.T. ; Jacquemart, D. ; Jolly, A. ; Lamouroux, J. ; Le Roy, R.J. ; Li, G. ; Long, D.a. ; Lyulin, O.M. ; Mackie, C.J. ; Massie, S.T. ; Mikhailenko, S. ; Müller, H.S.P. ; Naumenko, O.V. ; Nikitin, A.V. ; Orphal, J. ; Perevalov, V. ; Perrin, A. ; Polovtseva, E.R. ; Richard, C. ; Smith, M.a.H. ; Starikova, E. ; Sung, K. ; Tashkun, S. ; Tennyson, J. ; Toon, G.C. ; Tyuterev, Vl.G. ; Wagner, G.: The HITRAN2012 molecular spectroscopic database. In: *Journal of Quantitative Spectroscopy and Radiative Transfer* (2013)

[62] *Chapter* IsotopeRat. In: Kerstel, E R T.: *Handbook of Stable Isotope Analytical Techniques*. Bd. 1. Elsevier, 2004, P. 759–787

[63] Rothman, L. S. ; Rinsland, C. P. ; Goldman, A. ; Massie, S. T. ; Edwards, D. P. ; Flaud, J. M. ; Perrin, A. ; Camy-Peyret, C. ; Dana, V. ; Mandin, J. Y. ; Schroeder, J. ; McCann, A. ; Gamache, R. R. ; Wattson, R. B. ; Yoshino, K. ; Chance, K. V. ; Jucks, K. W. ; Brown, L. R. ; Nemtchinov, V. ; Varanasi, P.: THE HITRAN MOLECULAR SPECTROSCOPIC DATABASE AND HAWKS (HITRAN ATMOSPHERIC WORKSTATION): 1996 EDITION (Reprint from J Quant Spectrosc Radiat Transfer, vol 60, pg 665-710, 1998). In: *JOURNAL OF QUANTITATIVE SPECTROSCOPY & RADIATIVE TRANSFER* 111 (2010), No. 11, 1568–1613

[64] Kerstel, E R T. ; Trigt, R van ; Dam, N ; J Reuss ; Meijer, H A J.: Simultaneous determination of the 2H/1H, 17O/16O, and 18O/16O isotope abundance ratios in water by means of laser spectrometry. In: *Anal. Chem.* 71 (1999), No. 23, P. 5297–5303

[65] Lee, X ; Sargent, S: In Situ Measurement of the Water Vapor 18 O/16 O Isotope Ratio for Atmospheric and Ecological Applications. In: *Journal of Atmospheric & ...* (2005), No. 1999, 555–566

[66] Wen, Xue-Fa ; Sun, Xiao-Min ; Zhang, Shi-Chun ; Yu, Gui-Rui ; Sargent, Steve D. ; Lee, Xuhui: Continuous measurement of water vapor D/H and 18O/16O isotope ratios in the atmosphere. In: *Journal of Hydrology* 349 (2008), No. 3-4, 489–500

[67] Lübken, Franz-Josef ; Dingler, Florian ; Lucke, Henrich von ; Anders, Joachim ; Riedel, Wolfgang J. ; Wolf, Helmut: MASERATI: a RocketBorne Tunable Diode Laser Absorption Spectrometer. In: *Applied Optics* 38 (1999), No. 25, 5338

[68] Buchholz, B. ; Kühnreich, B. ; Smit, H. G. J. ; Ebert, V.: Validation of an extractive, airborne, compact TDL spectrometer for atmospheric humidity sensing by blind intercomparison. In: *Applied Physics B* 110 (2012), No. 2, P. 249–262

[69] Gurlit, W ; Zimmermann, R ; Giesemann, C ; Fernholz, T ; Ebert, V ; Wolfrum, J ; Platt, U ; Burrows, JP: Lightweight diode laser spectrometer CHILD (Compact High-altitude In-situ Laser Diode) for balloonborne measurements of water vapor and methane. In: *APPLIED OPTICS* 44 (2005), No. 1, 91–102

[70] Huang, Haifeng ; Lehmann, Kevin K.: Sensitivity limits of continuous wave cavity ring-down spectroscopy. In: *The journal of physical chemistry. A* 117 (2013), No. 50, 13399–411

[71] Romanini, D ; Ventrillard, I ; Méjean, G ; Morville, J ; Kerstel, E: Introduction to cavity enhanced absorption spectroscopy 1 Introduction. Version: 2014. `http://dx.doi.org/10.1007/978-3-642-40003-2_1`. In: Gagliardi, G. (Edt.) ; Loock, H.-P. (Edt.): *Cavity-Enhanced Spectroscopy and Sensing (Vol. 179)*. Springer Berlin Heidelberg, 2014. – DOI 10.1007/978–3–642–40003–2_1, P. 1–51

[72] Paldus B. A. ; Zare R. N.: Absorption Spectroscopies: From Early Beginnings to Cavity-Ringdown Spectroscopy. Version: 1999. `http://dx.doi.org/10.1021/bk-1999-0720`. In: Busch, Kenneth W. (Edt.) ; Busch, Marianna A. (Edt.): *Cavity-Ringdown Spectroscopy* Bd. 720. Washington, DC : American Chemical Society, 1999. – DOI 10.1021/bk–1999–0720. – ISBN 0–8412–3600–3, 49–70

[73] Zee, Roger D. ; Hodges, Joseph T. ; Looney, J. P.: Pulsed, Single-Mode Cavity Ringdown Spectroscopy. In: *Applied Optics* 38 (1999), No. 18, 3951

[74] Demtröder, Wolfgang: *Laser Spectroscopy: Vol. 1: Basic Principles*. Bd. 9. Springer-Verlag, 2007. – ISBN 354073418X

[75] Paul, J B. ; Lapson, L ; Anderson, J G.: Ultrasensitive absorption spectroscopy with a high-finesse optical cavity and off-axis alignment. In: *Applied optics* 40 (2001), No. 27, 4904–10

[76] WEBSTER, CR ; MAY, RD ; TRIMBLE, CA ; CHAVE, RG ; KENDALL, J: AIRCRAFT (ER-2) LASER INFRARED-ABSORPTION SPECTROMETER (ALIAS) FOR IN-SITU STRATOSPHERIC MEASUREMENTS OF HCL, N2O, CH4, NO2, AND HNO3. In: *APPLIED OPTICS* 33 (1994), No. 3, 454–472

[77] Sturm, C ; Zhang, Q ; Noone, D: An introduction to stable water isotopes in climate models: benefits of forward proxy modelling for paleoclimatology. In: *Climate of the Past* 6 (2010), No. 1, 115–129

[78] Aemisegger, F. ; Sturm, P. ; Graf, P. ; Sodemann, H. ; Pfahl, S. ; Knohl, A. ; Wernli, H.: Measuring variations of d18O and d2H in atmospheric water vapour using laser spectroscopy: an instrument characterisation study. In: *Atmos. Meas. Tech.* 5 (2012), No. 7, 1491–1511

[79] Crosson, E.R.: A cavity ring-down analyzer for measuring atmospheric levels of methane, carbon dioxide, and water vapor. In: *Applied Physics B* 92 (2008), No. 3, 403–408

[80] Ye, Jun ; Ma, LS ; Hall, JL: Ultrasensitive detections in atomic and molecular physics: demonstration in molecular overtone spectroscopy. In: *JOSA B* 15 (1998), No. 1, 6–15

[81] Morville, Jérôme ; Romanini, Daniele ; Kerstel, Erik: Cavity Enhanced Absorption Spectroscopy with Optical Feedback. Version: 2014. `http://dx.doi.org/10.1007/978-3-642-40003-2_5`. In: Gagliardi, G. (Edt.) ; Loock, H.-P. (Edt.): *Cavity Enhanced Spectroscopy and Sensing (Vol. 179)*. Springer Berlin Heidelberg, 2014. – DOI 10.1007/978–3–642–40003–2_5, Chapter 13, P. 163–207

[82] Morville, J. ; Kassi, S. ; Chenevier, M. ; Romanini, D.: Fast, low-noise, mode-by-mode, cavity-enhanced absorption spectroscopy by diode-laser self-locking. In: *Appl. Phys. B* 80 (2005), No. 8, 1027–1038

[83] Iannone, Rosario Q. ; Kassi, Samir ; Jost, Hans-Jürg H.-J. ; Chenevier, Marc ; Romanini, Daniele ; Meijer, Harro A J. ; Dhaniyala, Suresh ; Snels, Marcel ; Kerstel, Erik R T.: Development and airborne operation of a compact water isotope ratio infrared spectrometer. In: *Isotopes Environ Health Stud.* 45 (2009), No. 4, 303–20

[84] Landsberg, J ; Romanini, D ; Kerstel, E: Very high finesse optical-feedback cavity-enhanced absorption spectrometer for low concentration water vapor isotope analyses. In: *Optics letters* 39 (2014), No. 7, 1795–8

[85] James, F. ; Roos, M.: Minuit - a system for function minimization and analysis of the parameter errors and correlations. In: *Computer Physics Communications* 10 (1975), No. 6, 343–367

[86] Brand, W A. ; Geilmann, H ; Crosson, E R. ; ; Rella, C W.: Cavity ring-down spectroscopy versus high-temperature conversion isotope ratio mass spectrometry and a case study on 25 à2H and à18O of pure water samples and alcohol/water mixtures. In: *Rapid Communications in Mass Spectrometry* 23 (2009), P. 1879–1884

[87] Habig, Jan C.: *Bestimmung von Wasserdampfpartialdrücken und Wasserisotopenverhältnissen mittels resonatorverstärkter Absorptionsspektroskopie - Entwicklung von Software und Spektrometer sowie die Anwendung für die Atmosphärenforschung*, Karlsruhe Institute of Technology / University of Heidelberg, Diss., 2013

[88] Demtröder, Wolfgang: 7. Emission und Absorption elektromagnetischer Strahlung durch Atome. In: *Exerimentalphysik 3 - Atome, Moleküle und Festkörper*. 2005, P. 231–238

[89] Tittel, Frank K. ; Richter, Dirk ; Fried, Alan: Mid-Infrared Laser Applications in Spectroscopy. Version: 2003. http://dx.doi.org/10.1007/3-540-36491-9. In: Sorokina, Irina T. (Edt.) ; Vodopyanov, Konstantin L. (Edt.): *Solid-State Mid-Infrared Laser Sources* Bd. 89. Berlin, Heidelberg : Springer Berlin Heidelberg, 2003. – DOI 10.1007/3–540–36491–9. – ISBN 978–3–540–00621–3, 458–529

[90] Lepère, Muriel: Line profile study with tunable diode laser spectrometers. In: *Spectrochimica acta. Part A, Molecular and biomolecular spectroscopy* 60 (2004), No. 14, 3249–58

[91] Huang, Xianglei ; Yung, YL: A common misunderstanding about the Voigt line profile. In: *Journal of the atmospheric sciences* 61 (2004), No. 13, 1630–1632

[92] Olivero, JJ ; Longbothum, RL: Empirical fits to the Voigt line width: a brief review. In: *Journal of Quantitative Spectroscopy and ...* 17 (1977), 233–236

[93] Rautian, S.G. ; Sobel'man, I.I.: The effect of collisions on the doppler broadening of spectral lines. In: *Sov. Phys. Usp. Engl. Transl.* 9 (1967), P. 701–716

[94] Galatry, L: Simultaneous effect of Doppler and foreign gas broadening on spectral lines. In: *Physical Review* 122 (1961), No. 4, P. 1218

[95] Leshchishina, O. ; Mikhailenko, S. ; Mondelain, D. ; Kassi, S. ; Campargue, A.: CRDS of water vapor at 0.1Torr between 6886 and 7406cm-1. In: *Journal of Quantitative Spectroscopy and Radiative Transfer* 113 (2012), No. 17, 2155–2166

[96] Campargue, A. ; Leshchishina, O. ; Wang, L. ; Mondelain, D. ; Kassi, S. ; Nikitin, A.V.: Refinements of the WKMC empirical line lists (5852-7919cm-1) for methane between 80K and 296K. In: *Journal of Quantitative Spectroscopy and Radiative Transfer* 113 (2012), No. 15, 1855–1873

[97] Allan, D.W.: STATISTICS OF ATOMIC FREQUENCY STANDARDS. 54 (1966), No. 2

[98] Werle, P: Accuracy and precision of laser spectrometers for trace gas sensing in the presence of optical fringes and atmospheric turbulence. In: *Applied Physics B - Lasers and Optics* 102 (2010), P. 313–329

[99] Romanini, D. ; Chenevier, M. ; Kassi, S. ; Schmidt, M. ; Valant, C. ; Ramonet, M. ; Lopez, J. ; Jost, H.-J.: Optical-feedback cavity-enhanced absorption: a compact

spectrometer for real-time measurement of atmospheric methane. In: *Appl. Phys. B* 83 (2006), No. 4, 659–667

[100] Nelson, D D. ; McManus, J B. ; Urbanski, S ; Herndon, S ; Zahniser, M S.: *High precision measurements of atmospheric nitrous oxide and methane using thermoelectrically cooled mid-infrared quantum cascade lasers and detectors*

[101] Gagliardi, G. ; Castrillo, a. ; Iannone, R.Q. ; Kerstel, E.R.T. ; Gianfrani, L.: High-precision determination of the 13CO2/12CO2 isotope ratio using a portable 2.008-?m diode-laser spectrometer. In: *Applied Physics B: Lasers and Optics* 77 (2003), No. 1, 119–124

[102] Kerstel, E R T. ; Gianfrani, L: Advances in laser-based isotope ratio measurements: Selected applications. In: *Appl. Phys. B* (2008)

[103] Giusfredi, G. ; Bartalini, S. ; Borri, S. ; Cancio, P. ; Galli, I. ; Mazzotti, D. ; De Natale, P.: Saturated-Absorption Cavity Ring-Down Spectroscopy. In: *Physical Review Letters* 104 (2010), No. 11, 110801

[104] Romanini, D ; Dupré, P ; Jost, R: Non-linear effects by continuous wave cavity ringdown spectroscopy in jet-cooled NO 2. In: *Vibrational spectroscopy* 19 (1999), No. 2, 93–106

[105] Nave, Carl R.: *HyperPhysics*. `http://hyperphysics.phy-astr.gsu.edu/hbase/kinetic/menfre.html`. Version: 2001

[106] Moretti, L ; Sasso, A ; Gianfrani, L ; Ciurylo, R: Collisional-Broadened and Dicke-Narrowed Lineshapes of H2_16O and H2_18O Transitions at 1.39 um. In: *Journal of molecular spectroscopy* 205 (2001), No. 1, 20–27

[107] Williams, David R.: *NASA - Earth Fact Sheet*. `http://nssdc.gsfc.nasa.gov/planetary/factsheet/earthfact.html`. Version: 2013

[108] R., Gonfiantini: The delta-notation and the mass-spectrometric measurement techniques. In: R., Gat J. (Edt.) ; Gonfiantini, R. (Edt.): *Stable Isotope Hydrology, Deuterium and Oxygen-18 in the Water Cycle*. Technical. Vienna : IAEA, 1981, Chapter 4, P. 35–84

[109] Tuzson, B ; Mohn, J ; Zeeman, M J. ; Werner, R A. ; Eugster, W ; Zahniser, M S. ; Nelson, D D. ; McManus, J B. ; Emmenegger, L: High precision and continuous field measurements of delta C-13 and delta O-18 in carbon dioxide with a cryogen-free QCLAS. In: *APPLIED PHYSICS B-LASERS AND OPTICS* 92 (2008), No. 3, P. 451–458

[110] Wen, X.-F. ; Meng, Y. ; Zhang, X.-Y. ; Sun, X.-M. ; Lee, X.: Evaluating calibration strategies for isotope ratio infrared spectroscopy for atmospheric 13CO2/12CO2 measurement. In: *Atmospheric Measurement Techniques Discussions* 6 (2013), No. 1, 795–823

[111] Schmidt, Markus ; Maseyk, Kadmiel ; Lett, Céline ; Biron, Philippe ; Richard, Patricia ; Bariac, Thierry ; Seibt, Ulli: Concentration effects on laser-based del O-18 and del H-2 measurements and implications for the calibration of vapour measurements with liquid standards. In: *Rapid Communications in Mass Spectrometry* 24 (2010), No. 24, P. 3553–3561

[112] Aemisegger, F. ; Pfahl, S. ; Sodemann, H. ; Lehner, I. ; Seneviratne, S. I. ; Wernli, H.: Deuterium excess as a proxy for continental moisture recycling and plant transpiration. In: *Atmospheric Chemistry and Physics* 13 (2013), No. 11, 29721–29784

[113] Lis, G ; Wassenaar, L I. ; Hendry, M J.: High-precision laser spectroscopy D/H and 18O/16O measurements of microliter natural water samples. In: *Analytical chemistry* 80 (2008), No. 1, 287–93

[114] Kurita, N. ; Newman, B. D. ; Araguas-Araguas, L. J. ; Aggarwal, P.: Evaluation of continuous water vapor δD and δ18O measurements by off-axis integrated cavity output spectroscopy. In: *Atmospheric Measurement Techniques Discussions* 5 (2012), No. 2, 2821–2855

[115] Franz, Peter ; Röckmann, Thomas: A new continuous flow isotope ratio mass spectrometry system for the analysis of delta2H, delta17O and delta18O of small (120 microg) water samples in atmospheric applications. In: *Rapid communications in mass spectrometry : RCM* 18 (2004), No. 13, 1429–35

[116] Wang, Lixin ; Caylor, Kelly K. ; Dragoni, Danilo: On the calibration of continuous, high-precision d18O and d2H measurements using an off-axis integrated cavity output spectrometer. In: *Rapid Communications in Mass Spectrometry* 23 (2009), No. 4, P. 530–536

[117] Gupta, Priya ; Noone, David ; Galewsky, Joseph ; Sweeney, Colm ; Vaughn, Bruce H.: Demonstration of high-precision continuous measurements of water vapor isotopologues in laboratory and remote field deployments using wavelength-scanned cavity ring-down spectroscopy (WS-CRDS) technology. In: *. . . in mass spectrometry* (2009), 2534–2542

[118] Iannone, Rosario Q.: *Development of a near-infrared Optical Feedback Cavity Enhanced Absorption Spectrometer (OF-CEAS) for atmospheric water vapor isotope ratio measurements*, Rijksuniversiteit Groningen, Diss., 2009

[119] Iannone, Rosario Q. ; Romanini, Daniele ; Kassi, Samir ; Meijer, Harro a. J. ; Kerstel, Erik R. T.: A Microdrop Generator for the Calibration of a Water Vapor Isotope Ratio Spectrometer. Journal of Atmospheric and Oceanic Technology. In: *J Atmos Ocean Technol* 26 (2009), No. 7, 1275–1288

[120] Sturm, P ; Knohl, A: Water vapor δ2H and δ18O measurements using off-axis integrated cavity output spectroscopy. In: *AMT* 3 (2009), P. 67–77

[121] Gkinis, Vasileios ; Popp, Trevor J. ; Johnsen, Sigfus J. ; Blunier, Thomas: A continuous stream flash evaporator for the calibration of an IR cavity ring-down spectrometer for the isotopic analysis of water. In: *Isotopes in environmental and health studies* 46 (2010), No. 4, 463–75

[122] Tremoy, Guillaume ; Vimeux, Françoise ; Cattani, Olivier ; Mayaki, Salla ; Souley, Ide ; Favreau, Guillaume: Measurements of water vapor isotope ratios with wavelength-scanned cavity ring-down spectroscopy technology: new insights and important caveats for deuterium excess measurements in tropical areas in comparison with isotope-ratio mass spectrometry. In: *Rapid communications in mass spectrometry : RCM* 25 (2011), No. 23, 3469–80

[123] Clair, J M S. ; Hanisco, T F. ; Weinstock, E M. ; Moyer, E J. ; Sayres, D S. ; Keutsch, F N. ; Kroll, J H. ; Demusz, J N. ; Allen, N T. ; Smith, J B. ; J. R. Spackman ; Anderson, J G. ; St Clair, J M. ; Spackman, J R.: A new photolysis laser-induced fluorescence instrument for the detection of H2O and HDO in the lower stratosphere. In: *The Review of scientific instruments* 79 (2008), No. 6, 064101

[124] Iannone, Rosario Q. ; Romanini, Daniele ; Cattani, Olivier ; Meijer, Harro a. J. ; Kerstel, Erik R. T.: Water isotope ratio (δ 2 H and δ 18 O) measurements in atmospheric moisture using an optical feedback cavity enhanced absorption laser spectrometer. In: *Journal of Geophysical Research* 115 (2010), No. D10, D10111

[125] Johnson, L R. ; Sharp, Z D. ; Galewsky, J ; Strong, M ; Van Pelt, a D. ; Dong, F ; Noone, D: Hydrogen isotope correction for laser instrument measurement bias at low water vapor concentration using conventional isotope analyses: application to measurements from Mauna Loa Observatory, Hawaii. In: *Rapid communications in mass spectrometry : RCM* 25 (2011), No. 5, 608–16

[126] Wen, Xue-Fa ; Lee, Xuhui ; Sun, Xiao-Min ; Wang, Jian-Lin ; Tang, Ya-Kun ; Li, Sheng-Gong ; Yu, Gui-Rui ; Haven, New: Intercomparison of Four Commercial Analyzers for Water Vapor Isotope Measurement. In: *Journal of Atmospheric and Oceanic Technology* 29 (2012), No. 2, 235–247

[127] Ellehoj, M D. ; Steen-Larsen, H C. ; Johnsen, S J. ; Madsen, M B.: Ice-vapor equilibrium fractionation factor of hydrogen and oxygen isotopes: experimental investigations and implications for stable water isotope studies. In: *Rapid communications in mass spectrometry : RCM* 27 (2013), No. 19, 2149–58

[128] Picarro: *High-Precision Vaporizer*. `http://www.picarro.com/products_solutions/peripherals/high_precision_vaporizer`. Version: 2014

[129] Gkinis, Vasileios ; Morrie, Valerie ; Jones, Tyler ; Vaughn, Bruce ; White, James: High resolution , high precision , simultaneous measurements of δD and δ18 O using a CRDS analyzer with an ultrasonic nebulizer sample preparation module . 15 (2013)

[130] Lee, Eric R.: *Microdrop Generation.* Boca Raton, FL : CRC Press, 2003. – 272 P. – ISBN 0–8493–1559–X

[131] Iannone, R. ; Romanini, D. ; Meijer, H. ; Kerstel, E.: Calibration of a diode laser water isotope ratio spectrometer for in-situ measurements in the troposphere and lower stratosphere : Using a piezo-injector to produce water with know concentration and isotopic signature in the laboratory. In: *Geophysical Research Abstracts (Vol. 9, p. 02398)*, 2007

[132] Gans, Berend-Jan de ; Schubert, Ulrich S.: Inkjet printing of well-defined polymer dots and arrays. In: *Langmuir : the ACS journal of surfaces and colloids* 20 (2004), No. 18, 7789–93

[133] Meinhart, C.D. ; Zhang, H.: The flow structure inside a microfabricated inkjet printhead. In: *Journal of Microelectromechanical Systems* 9 (2000), No. 1, 67–75

[134] Bird, R.Byron ; Stewart, Warren E. ; Lightfoot, Edwin N.: *Transport Phenomena (Second Edition).* John Wiley & sons, 2002

[135] Horita, J. ; Cole, D. R.: Stable isotope partitioning in aqueous and hydrothermal systems to elevated temperatures. In: Palmer, D. A. (Edt.) ; Fernández-Prini, R. (Edt.) ; Harvey, A. H. (Edt.): *Aqueous systems at elevated temperatures and pressures: Physical chemistry in water, steam and hydrothermal solutions.* Elsevier, 2004, P. 277–319

[136] Harvard Apparatus: User's Manual - Pump 11 Pico Plus Elite. 2012. – Scientific report. – 8 P.

[137] Rothman, L.S. ; Jacquemart, D. ; Barbe, A. ; Chris Benner, D. ; Birk, M. ; Brown, L.R. ; Carleer, M.R. ; Chackerian, C. ; Chance, K. ; Coudert, L.H. ; Dana, V. ; Devi, V.M. ; Flaud, J.-M. ; Gamache, R.R. ; Goldman, A. ; Hartmann, J.-M. ; Jucks, K.W. ; Maki, A.G. ; Mandin, J.-Y. ; Massie, S.T. ; Orphal, J. ; Perrin, A. ; Rinsland, C.P. ; Smith, M.A.H. ; Tennyson, J. ; Tolchenov, R.N. ; Toth, R.A. ; Vander Auwera, J. ; Varanasi, P. ; Wagner, G.: The HITRAN 2004 molecular spectroscopic database. In: *Journal of Quantitative Spectroscopy and Radiative Transfer* 96 (2005), No. 2, 139–204

[138] Bronkhorst High-Tech B.V.: *Datasheet F-201CV, Mass Flow Controller for Gases.* `http://www.bronkhorst.com/files/downloads/datasheets/el-flow/f-201cv.pdf`. Version: 2014

[139] Harvard Apparatus: *Harvard Apparatus - Pico Plus Elite.* http://www.harvardapparatus.com/webapp/wcs/stores/servlet/product_11051_10001_64201_-1_HAI_ProductDetail___#specificationstab. Version: 2014

[140] IPCC ; Solomon, S. (Edt.) ; Qin, D. (Edt.) ; Manning, M. (Edt.) ; Chen, Z. (Edt.) ; Marquis, M. (Edt.) ; Averyt, K.B. (Edt.) ; Tignor, M. (Edt.) ; Miller, H.L. (Edt.): *Climate Change 2007: The Physical Science Basis. Contribution of Working Group I to the Fourth Assessment Report of the Intergovernmental Panel on Climate Change.* Cambridge, United Kingdom and New York, NY, USA. : Cambridge University Press, 2007. – 996 P.

[141] Jouzel, J ; Masson-Delmotte, V: Paleoclimates: what do we learn from deep ice cores? In: *Wiley Interdisciplinary Reviews-Climate Change* 1 (2010), No. 5, P. 654–669

[142] Hansen, G. ; Aspmo, K. ; Berg, T. ; Edvardsen, K. ; Fiebig, M. ; Kallenborn, R. ; Krognes, T. ; Lunder, C. ; Stebel, K. ; Schmidbauer, N. ; Solberg, S. ; Yttri, K.E.: Atmospheric monitoring at the Norwegian Antarctic station Troll: measurement programme and first results. In: *Polar Research* 28 (2009), No. 3, 353–363

[143] Trigas FI: *No Title.* http://www.trigasfi.de/pdf/Sonic-Nozzle-Brochure.pdf. Version: 2014

[144] Horita, J ; Wesolowski, DJ J.: Liquid-vapor fractionation of oxygen and hydrogen isotopes of water from the freezing to the critical temperature. In: *GEOCHIMICA ET COSMOCHIMICA ACTA* 58 (1994), No. 16, 3425–3437

[145] Mook, Willem G.: V1 - Introduction - Theory , methods, review. In: *Environmental Isotopes in the Hydrological Cycle - Principles and Applications.* International Atomic Energy Agency and United Nations Educational, Scientific and Cultural Organization, 2001, P. 1–165

[146] Draxler, R.R. ; Rolph, G.D.: *HYSPLIT (HYbrid Single-Particle Lagrangian Integrated Trajectory) Model access via NOAA ARL READY Website.* (http://ready.arl.noaa.gov/HYSPLIT.php. Version: 2013

[147] Draxler, R.R. ; Hess, G.D.: An overview of the HYSPLIT_4 modeling system of trajectories, dispersion, and deposition. In: *Aust. Meteor. Mag.* 47 (1998), P. 295–308

[148] *Institut Polaire Francais - Dome Concordia.* http://www.institut-polaire.fr/ipev/bases_et_navires/station_concordia_dome_c

[149] Keller, Linda M. ; Lazzara, Matthew A. ; Thom, Jonathan E. ; Weidner, George A. ; Stearns, Charles R.: Antarctic Automatic Weather Station Data for the calendar year 2009. (2010)

[150] Krämer, M ; Schiller, C ; Afchine, A ; Bauer, R ; Gensch, I ; Mangold, A ; Schlicht, S ; Spelten, N ; Sitnikov, N ; Borrmann, S ; Reus, M de ; Spichtinger, P: Ice supersaturations and cirrus cloud crystal numbers. In: *ATMOSPHERIC CHEMISTRY AND PHYSICS* 9 (2009), P. 3505–3522

[151] Kärcher, B: Supersaturation, dehydration, and denitrification in Arctic cirrus. In: *ATMOSPHERIC CHEMISTRY AND PHYSICS* 5 (2005), P. 1757–1772

[152] Korolev, Alexei V. ; Mazin, Ilia P.: Supersaturation of Water Vapor in Clouds. In: *Journal of Atmospheric Science* 60 (2003), No. 24, P. 2957–2974

[153] Moyer, E.J.: International Collaboration in Chemistry: Improving understanding of ice nucleation and growth inhibition mechanisms via new isotopic tracer studies in the AIDA aerosol chamber. In: *Application for a Research Grant: Project Description* (2010)

[154] Gallavardin, S J. ; Froyd, K D. ; Lohmann, U ; Moehler, O ; Murphy, D M. ; Cziczo, D J.: Single particle laser mass spectrometry applied to differential ice nucleation experiments at the AIDA Chamber. In: *Aerosol Science and Technology* 42 (2008), P. 773–791

[155] Fahey, D. W. ; Gao, R. S. ; Möhler, O.: Summary of the AquaVIT Water Vapor Intercomparison : Static Experiments. 2009 (October). – Scientific report. – 102 P.

[156] Hiranuma, N. ; Kohn, M. ; Pekour, M. S. ; Nelson, D. a. ; Shilling, J. E. ; Cziczo, D. J.: Droplet activation, separation, and compositional analysis: laboratory studies and atmospheric measurements. In: *Atmospheric Measurement Techniques* 4 (2011), No. 10, 2333–2343

[157] Boulter, J E. ; Cziczo, D J. ; Middlebrook, A M. ; Thomson, D S. ; Murphy, D M.: Design and Performance of a Pumped Counterflow Virtual Impactor. In: *Aerosol Science and Technology* 40 (2006), No. 11, P. 969–976

[158] Kulkarni, Gourihar ; Pekoura, Mikhail ; Afchineb, Armin ; Murphyc, Daniel M. ; Cziczoa, Daniel J. ; Pekour, Mikhail ; Afchine, Armin ; Murphy, Daniel M. ; Cziczo, Daniel J.: Comparison of Experimental and Numerical Studies of the Performance Characteristics of a Pumped Counterflow Virtual Impactor. In: *Aerosol Science and Technology* 45 (2011), No. 3, 382–392

[159] Möhler, O. ; Büttner, S. ; Linke, C. ; Schnaiter, M. ; Saathoff, H. ; Stetzer, O. ; Wagner, R. ; Krämer, M. ; Mangold, A. ; Ebert, V. ; Schurath, U.: Effect of sulfuric acid coating on heterogeneous ice nucleation by soot aerosol particles. In: *Journal of Geophysical Research* 110 (2005), No. D11, D11210

[160] Fahey, D. W. ; Gao, R.-S. ; Möhler, O. ; Saathoff, H. ; Schiller, C. ; Ebert, V. ; Krämer, M. ; Peter, T. ; Amarouche, N. ; Avallone, L. M. ; Bauer, R. ; Bozóki, Z. ; Christensen, L. E. ; Davis, S. M. ; Durry, G. ; Dyroff, C. ; Herman, R. L. ; Hunsmann, S. ; Khaykin, S. M. ; Mackrodt, P. ; Meyer, J. ; Smith, J. B. ; Spelten, N. ; Troy, R. F. ; Vömel, H. ; Wagner, S. ; Wienhold, F. G.: The AquaVIT-1 intercomparison of atmospheric water vapor measurement techniques. In: *Atmospheric Measurement Techniques Discussions* 7 (2014), No. 4, 3159–3251

[161] Saathoff, H.: *No Title*. 2013

[162] Lamb, Kara D. ; Clouser, Ben ; Sarkozy, Laszlo ; Stutz, Eric ; Kühnreich, Benjamin ; Landsberg, Janek ; Habig, Jan ; Hiranuma, Naruki ; Wagner, Steven ; Ebert, Volker ; Kerstel, Erik ; Möhler, Ottmar ; Saathoff, Harald ; Moyer, Elisabeth: Direct Measurements of Isotopic Fractionation Factors of Water Vapor over Ice for T $<$ 235 K. In: *Goldschmidt conference* (2013)

[163] Ellehø j, Mads D.: *Ice-vapor equilibrium fractionation factor*, Niels Bohr Institute, Diss., 2011

[164] Matsuo, Sadao ; Kuniyoshi, Hideko ; Miyake, Yasuo: Vapor pressure of ice containing d2o. In: *Science* 145 (1964), No. 3639, P. 1454–1455

[165] Johansson, M. ; Holmberg., K. E.: Separation of heavy water in phase equilibria involving pure water or salt-water systems. In: *Acta Chemica Scandinavica* 23 (1969), No. 3, P. 765

[166] Van Hook, W. Alexander V.: Vapor pressures of the isotopic waters and ices. In: *The Journal of Physical Chemistry* 72 (1968), No. 4, P. 1234–1244

[167] Pupezin, Jovan D. ; Jakli, Gyorgy ; Jancso, Gabor ; Van Hook, W. A.: Vapor pressure isotope efect in aqueous systems. i. water-water-d2 (-64.deg. to 100.deg.) and BIBLIOGRAPHY 154 water-water18-0 (-17.deg. to 16.deg.). ice and liquid. ii. alkali metal chloride solution in water and water-d2 (-5.deg. to 100.deg.). In: *The Journal of Physical Chemistry* 76 (1972), No. 5, P. 743–762

[168] Méheut, Merlin ; Lazzeri, Michele ; Balan, Etienne ; Mauri, Francesco: Equilibrium isotopic fractionation in the kaolinite, quartz, water system: Prediction from first-principles density-functional theory. In: *Geochimica et Cosmochimica Acta* 71 (2007), No. 13, P. 3170–3181

[169] *Antarctic Meteorology Research at the University of Wisconsin-Madison (AMRC & AWS)*. `http://amrc.ssec.wisc.edu/data/view-data.php?action=list&product=surface/plot`. Version: 2014

[170] Casado, Mathieu ; Cauquoin, Alexandre ; Landais, Amaelle ; Landsberg, Janek ; Kerstel, Erik ; Doussin, Jean-François: Experimental determination for kinetic fractionation during solide condensation at low temperature and theoretical framework. In: *Geophysical Research Abstracts, Vol. 16*, 2014

[171] Burkart, Johannes ; Romanini, Daniele ; Kassi, Samir: Optical feedback stabilized laser tuned by single-sideband modulation. In: *Optics letters* 38 (2013), No. 12, 2062–4

[172] Harris, J. W. ; Stocker, H.: Spherical Segment (Spherical Cap). In: *Handbook of Numerical Analysis. Special Volume: Foundations of Computational Mathematics.* 1998, P. 107

[173] Noone, D. ; Risi, C. ; Bailey, A. ; Berkelhammer, M. ; Brown, D. P. ; Buenning, N. ; Gregory, S. ; Nusbaumer, J. ; Schneider, D. ; Sykes, J. ; Vanderwende, B. ; Wong, J. ; Meillier, Y. ; Wolfe, D.: Determining water sources in the boundary layer from tall tower profiles of water vapor and surface water isotope ratios after a snowstorm in Colorado. In: *Atmospheric Chemistry and Physics* 13 (2013), No. 3, 1607–1623

[174] Bolot, M. ; Legras, B. ; Moyer, E. J.: Modelling and interpreting the isotopic composition of water vapour in convective updrafts. In: *Atmospheric Chemistry and Physics* 13 (2013), No. 16, 7903–7935

[175] Moyer, E.J. ; Sayres, D.S. ; Engel, G.S. ; St. Clair, J.M. ; Keutsch, F.N. ; Allen, N.T. ; Kroll, J.H. ; Anderson, J.G.: Design considerations in high-sensitivity off-axis integrated cavity output spectroscopy. In: *Applied Physics B* 92 (2008), No. 3, 467–474

[176] Romanini, D. ; Lehmann, K. K.: Ring-down cavity absorption spectroscopy of the very weak HCN overtone bands with six, seven, and eight stretching quanta. In: *The Journal of Chemical Physics* 99 (1993), No. 9, 6287

[177] Ehlers, Patrick ; Silander, Isak ; Wang, Junyang ; Axner, Ove: Fiber-laser-based noise-immune cavity-enhanced optical heterodyne molecular spectrometry instrumentation for Doppler-broadened detection in the 10ˆâˆ'12â€‰â€‰cmˆâˆ'1â€‰Hzˆâˆ'1/2 region. In: *Journal of the Optical Society of America B* 29 (2012), No. 6, 1305

[178] Laurent, P ; Clairon, A ; Breant, C: Frequency noise analysis of optically self-locked diode lasers. In: *Quantum Electronics, IEEE ...* 25 (1989), No. 6

[179] Gianfrani, L ; Gagliardi, G ; Burgel, M van ; Kerstel, E R T.: Isotope analysis of water by means of near-infrared dual-wavelength diode laser spectroscopy. In: *Optics Express* 11 (2003), P. 1566–1576

Nomenclature

APeT AIDA PCI extractive TDL

CEAS Cavity Enhanced Absorption Spectroscopy

CRDS Cavity Ring Down Spectroscopy

CW Continuous Wave

FFT Fast Fourier Transform

FSR Free Spectral Range

FWHM Full Width Half Maximum

HYSPLIT Hybrid Single Particle Lagrangian Integrated Trajectory Model

IAEA International Atomic Energy Agency

ICOS Integrated Cavity Output Spectroscopy

IRMS Isotope-Ratio Mass Spectrometry

ISO-APicT Isotope AIDA-PCI-in-cloud-TDL

MFP Mean Free Path

NEA Noise-Equivalent Absorption

NILU Norwegian Institute for Air Research

OA-ICOS Off-axis Integrated Cavity Output Spectroscopy

OF-CEAS Optical Feedback Cavity Enhanced Absorption Spectroscopy

OFFS-CRDS Optical Feedback Frequency Stabilized Cavity Ring-Down Spectroscopy

OPC Optical Particle Counter

QCL Quantum cascade laser

RD Ring-Down

RMS Root Mean Square

SIRI Spectromètre Infrarouge des Rapports Isotopiques

SLAP Standard Light Antarctic Precipitation

SNICS Syringe Nanoliter Injection Calibration System

standard liters per minute slm

TDLAS Tunable Diode Laser Absorption Spectroscopy

TEM Transverse Electromagnetic Mode

UTLS Upper Troposphere Lower Stratosphere

vmr Volume mixing ration

VSMOW Vienna Standard Mean Ocean Water

Appendix A

Isotope standards used in this work

Standard	δ^2H	δ^{18}O	δ^{17}O
GS48	-43.3 ± 0.3‰	-6.52 ± 0.03‰	-3.45 ± 0.02‰
GS50	-276.7 ± 0.3‰	-35.01 ± 0.03‰	-18.64 ± 0.02‰
GS22	-113.5 ± 0.3‰	-15.29 ± 0.03‰	-8.1 ± 0.02‰
BEW1	880‰	111.9‰	-
BEW2	1374‰	175.4‰	-

Table A.1: Isotope standards used in this work

Appendix B

Modeling of SNICS injection

Instead of an isotope ratio gradient inside the droplet, we assume an enriched surface layer volume and a core volume with the isotope ratio of the water standard (figure B.2). This means that the syringe calibration system is built of three different water volumes:
1) the syringe reservoir with constant isotope ratio R_0 of the given water standard and a flow rate $\Phi_0(t)$, which is determined by the injection speed of the syringe pump.
2) the core volume of the droplet, which has a time dependent volume $V_C(t)$ and constant isotope ratio $R_C(t) = R_0$.
3) The surface layer of the droplet with volume $V_S(t)$ and isotope ratio $R_S(t)$, which is influenced by the evaporation from the surface layer and a continuous supply of the isotope standard from the core volume V_C. For the surface volume, we assume a constant thickness d, which is determined by the diffusion of water molecules in the surface layer. For small d, we can approximate V_C to be the surface area A_S multiplied with the thickness of the layer:

$$V_S(t) = A_S(t) * d \tag{B.1}$$

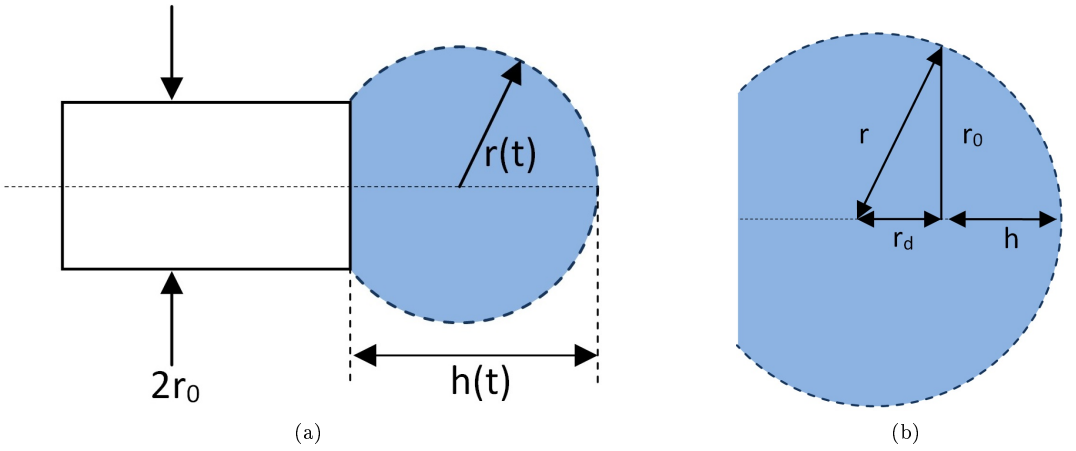

Figure B.1: Illustration of the dimensions of a droplet formed during water injection with SNICS. (a) The syringe needle has a diameter of $2r_0$ and the height of the droplet is $h(t)$. (b) Quantities used to compute the volume of the droplet over time

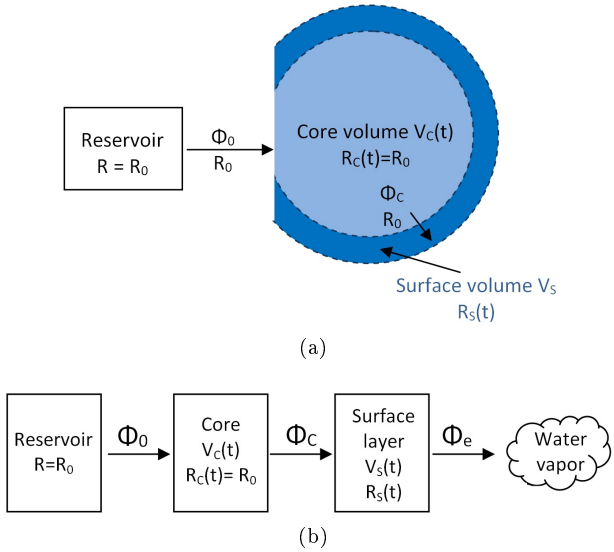

Figure B.2: (a) The droplet is assumed to have an enriched surface with volume $V_s(t)$ and a core volume $V_c(t)$ with isotopic composition as the water in the reservoir (b) The different volumes of water in the model approach. Water from the reservoir is injected to the core volume V_c, travels into the surface layer volume V_s and is evaporated.

The flow from the reservoir to the core is Φ_0, the flow from the core to the surface layer Φ_C, and the flow of evaporated water Φ_e.

Before we look in detail into the behavior of the isotopes, we investigate the behavior of total water in this model, which allows us to derive an expression for the droplet size, as well as the evaporated water flow, as a function of time. Combining the latter with the dry air flow, we then obtain an expression for the water volume mixing ratio as a function of time.

The volume of the droplet equals the flow towards the droplet minus the flow out of the droplet. In discrete time one obtains the following integration formula:

$$V_{drop}(t + \Delta t) = V_{drop}(t) + (\Phi_0(t) - \Phi_e(t)) \cdot \Delta t \tag{B.2}$$

The volume of a spherical cap is given by [172]:

$$V = \frac{\pi}{6} \cdot h \left(3r_0^2 + h^2\right) \tag{B.3}$$

and the surface area

$$A_S = 2\pi r h \tag{B.4}$$

for $0 \leq h \leq 2r$
With $r^2 = r_0^2 + r_d^2$ and $r_d = r - h$ (cf. figure B.1b), A_S can also be written as

$$A_S = \pi \left(r_0^2 + h^2\right) \tag{B.5}$$

We now want to express the cap height in terms of the droplet volume V_{drop}. Rearranging equation B.3, we can write

$$h^3 + 3r_0^2 h - \frac{6V}{\pi} = 0 \tag{B.6}$$

We find three solutions of which only one is real:

$$h = \frac{\alpha^2 - 36 \cdot r_0^2}{6 \cdot \alpha} \tag{B.7}$$

with

$$\alpha := 6 \left\{ \frac{3V}{\pi} + \left(r_0^6 + 9 \left(\frac{V}{\pi} \right)^2 \right)^{1/2} \right\}^{1/3}$$

We now assume that the evaporation rate $\Phi_e(t)$ is proportional to the (exposed) surface of the water droplet:

$$\Phi_e(t) := k_e \cdot A_s(t) \tag{B.8}$$

with k_e a constant evaporation factor.
With this and the injection rate $\Phi_0(t)$, the iteration step yields

$$V_{drop}(t + \Delta t) = V_{drop}(t) + (\Phi_0(t) - \Phi_e(t)) \cdot \Delta t \tag{B.9}$$

$$A_s(t + \Delta t) = \pi \left(r_0^2 + h^2 \left(V_{drop}(t + \Delta t); r_0\right)\right) \tag{B.10}$$

for the droplet volume and the exposed surface area of the droplet.
For the study of the isotopic behavior, we have to differentiate between the two volumes V_C and V_S of the droplet. The change of the surface volume V_S is determined by the flow from the core volume (Φ_C) and the evaporation flow Φ_e:

$$V_S(t + \Delta t) = V_S(t) + (\Phi_C(t) - \Phi_e(t)) \cdot \Delta t \tag{B.11}$$

The core volume is determined by the supply flow from the syringe pump $\Phi_0(t)$ and the flow $\Phi_C(t)$ to the surface layer:

$$V_C(t + \Delta t) = V_C(t) + (\Phi_0 - \Phi_C) \cdot \Delta t \tag{B.12}$$

Alternatively, we can also express $V_C(t)$ as the difference between the total droplet volume $V_{drop}(t)$ and the surface layer volume $V_S(t)$:

$$V_C(t) = V_{drop}(t) - V_S(t) \tag{B.13}$$

$$\Delta V_C(t) = \Delta V_{drop}(t) - \Delta V_S(t) \tag{B.14}$$

In a volume V with constant density, the isotope ratio can be calculated as

$$R = \frac{V''}{V'} \approx \frac{V''}{V - V''} \tag{B.15}$$

with V' indicating the volume of the most abundant and V'' the volume of a rare isotope. For V'', this leads to

$$V'' = V \cdot \frac{R}{1+R} \tag{B.16}$$

The rare isotope in the surface layer can thus be described by the following relation:

$$V_S''(t+\Delta t) = V_S(t+\Delta t) \cdot \frac{R_S(t+\Delta t)}{1+R_S(t+\Delta t)} \tag{B.17}$$

which leads together with equation (B.11) to:

$$V_S(t+\Delta t) \cdot \frac{R_S(t+\Delta t)}{1+R_S(t+\Delta t)} = V_S(t)\frac{R_S(t)}{1+R_S(t)} + \left[\Phi_C(t)\frac{R_0}{1+R_0} - \Phi_e''(t)\right] \cdot \Delta t \tag{B.18}$$

with

$$\Phi_C(t) = \Phi_0(t) - \frac{\Delta V_C(t)}{\Delta t} \tag{B.19}$$

$$= \Phi_0(t) - \frac{\Delta V_{drop}(t) - \Delta V_S(t)}{\Delta t} \tag{B.20}$$

this gives

$$V_S(t+\Delta t) \cdot \frac{R_S(t+\Delta t)}{1+R_S(t+\Delta t)} = V_S(t) \cdot \frac{R_S(t)}{1+R_S(t)} + \left(\Delta V_S(t) - \Delta V_{drop}(t)\right) \cdot \frac{R_0}{1+R_0} + \left[\Phi_0(t)\frac{R_0}{1+R_0} - \Phi_e''(t)\right]\Delta t \tag{B.21}$$

Substituting $\psi(t) := \frac{R_S(t)}{1+R_S(t)}$, we can write

$$\psi(t+\Delta t) = \frac{1}{V_S(t+\Delta t)} \cdot \left\{V_S(t)\psi(t) + \left[\Delta V_S(t) - \Delta V_{drop}(t)\right]\frac{R_0}{1+R_0} + \left[\Phi_0(t)\frac{R_0}{1+R_0} - \Phi_e''(t)\right]\Delta t\right\} \tag{B.22}$$

$\Phi_e''(t)$ can be written as

$$\Phi_e''(t) = \Phi_e(t)\frac{R_{VSMOW}(1+\delta_S)\cdot\alpha_V}{1+R_{VSMOW}(1+\delta_S)\cdot\alpha_V} \tag{B.23}$$

Since $R_{VSMOW} \ll 1$, we can approximate

$$\frac{1}{1 + R_{VSMOW}(1+\delta_S) \cdot \alpha_V} \approx \frac{1}{1 + R_{VSMOW}(1+\delta_S)}$$

$$\begin{aligned} \Phi_e''(t) &\approx \Phi_e(t) \frac{R_{VSMOW}(1+\delta_S)}{1 + R_{VSMOW}(1+\delta_S)} \cdot \alpha_V \\ &= \Phi_e(t) \cdot \psi(t) \cdot \alpha_V \end{aligned} \tag{B.24}$$

Thus, we finally get

$$\psi(t+\Delta t) = \frac{1}{V_S(t+\Delta t)} \cdot \Big\{ V_S(t)\psi(t) + \left[\Delta V_S(t) - \Delta V_{drop}(t)\right] \frac{R_0}{1+R_0} \tag{B.25}$$

$$+ \left[\Phi_0(t) \frac{R_0}{1+R_0} - \Phi_e(t) \cdot \psi(t) \cdot \alpha_V \right] \Delta t \Big\} \tag{B.26}$$

With eq. B.1, B.8-B.10, we can now calculate the isotope ratio in the surface layer and the evaporated water. The isotope ratio of the enriched surface layer can be calculated by

$$R_S(t) = \frac{\psi(t)}{1 + \psi(t)} \tag{B.27}$$

and the isotope ratio of the vapor phase with

$$R_e(t) = R_S(t) \cdot \alpha_V \tag{B.28}$$

Appendix C

Very high finesse optical-feedback cavity-enhanced absorption spectrometer for low concentration water vapor isotope analyses

Reproduction of an Optics Letter [84] in the formatting of the thesis.
http://www.opticsinfobase.org/ol/abstract.cfm?uri=ol-39-7-1795

J. Landsberg, D. Romanini, and E. Kerstel

So far, cavity-enhanced absorption spectroscopy (CEAS) has been based on optical cavities with a high finesse $\mathcal{F}$ that, however, has been limited by mirror reflectivity and by cavity transmission considerations to a few times 10,000. Here, we demonstrate a compact near-infrared optical-feedback CEAS instrument for water vapor isotope ratio measurements, with $\mathcal{F} > 140,000$. We show that this very high finesse can be effectively exploited to improve the detection sensitivity to the full extent predicted by the increased effective path length to reach a noise equivalent absorption sensitivity of $5.7 \times 10^{-11}\text{cm}^{-1}$ $\text{Hz}^{-1/2}$ for a full spectrum registration (including possible effects of interference fringes and fit model inadequacies).

In recent years, gas concentration and isotope ratio analyzers based on near-infrared, cavity-enhanced absorption (CEAS; characterized by a measurement of the light intensity transmitted by the cavity) or cavity ringdown spectroscopies (CRDS; characterized by a time-resolved measurement of the light intensity decay) have experienced an increase in acceptance by the scientific community [71]. Compared with their conventional mass spectrometer counterparts, optical instruments are easier to handle and enable continuous and in situ measurements with high temporal resolution. Arguably, water vapor isotope measurements have benefited the most, as evidenced by, e.g., [10, 78, 173].

However, there is a number of applications for which higher detection sensitivity is imperative. For example, some of the most interesting isotopic processes involving atmospheric water occur at water abundances well below the range accessible with commonly available laser spectrometers. In the Antarctic atmosphere, water concentration does not normally exceed a few hundred parts per million by volume (ppmv), whereas in the lower stratosphere it reaches lows of just a few ppmv. Isotope studies in these environments are relevant for the validation of the

water isotope paleothermometer [77] and for the understanding of cirrus cloud formation and troposphere-stratosphere exchanges [3, 174], respectively.
Until now, a small number of optical instruments have been developed with the aim to measure in situ water isotopes with high precision at very low water abundances [5–7, 10, 83, 118, 175]. Unfortunately, resolving the details of isotope fractionation effects at these low water concentrations requires even higher levels of sensitivity and precision.
A standard quantification of the sensitivity of an absorption spectrometer is given by the noise equivalent absorption sensitivity (NEAS) [175, 176], which gives the minimum detectable absorption per unit path length normalized to the measurement rate MR (the inverse of the time required to record a full spectrum). If δI represents the uncertainty (1σ) of the detected light transmission of intensity I over an effective absorption path length L_{eff} , the NEAS is given by

$$\text{NEAS} = \frac{\delta I}{I} \frac{1}{L_{\text{eff}}} \frac{1}{\sqrt{MR}} \tag{C.1}$$

One possible way to increase the sensitivity of a CEAS spectrometer is to combine it with a high-frequency modulation technique in order to reduce δI. This is exploited in noise-immune cavity-enhanced optical heterodyne molecular spectroscopy (NICE-OHMS) which, however, is experimentally highly complex [80]. In addition, its full sensitivity potential has never been approached in applications where complete Doppler-broadened rovibrational features need to be recorded [177]. A compelling alternative is to "simply" increase L_{eff} by increasing the finesse $\mathcal{F}$ of the optical cavity through the use of very high-reflectivity mirror coatings. There are two obvious disadvantages to this approach. First, the time required to reach the full build-up of light intensity inside the cavity, as well as the subsequent decay of the light leaking out of the cavity (τ), are also proportional to $\mathcal{F}$. This increases the time required to record the spectrum, thus lowering MR. Second, a higher finesse tends to reduce the detected signal by reducing the coupling efficiency of the relatively broad laser emission (the free-running linewidth of a DFB laser as used in this study is several MHz on a 1 s timescale) to the exceedingly narrow cavity mode width ($\sim$ 1 kHz for the high-finesse cavity). In addition, an increase of the mirror reflectivity is almost inevitably accompanied by a reduction of the mirror transmission (as there is a technical lower limit to the losses caused by coating absorption and scattering) which reduces the cavity throughput at resonance [71]. Thus, for "normal" CEAS or CRDS one expects to gain sensitivity proportional to finesse due to a cause of a lower cavity transmission, either proportional to $\mathcal{F}$, when the system is limited by detector noise, or by $\mathcal{F}$ in the case of shot-noise limited detection. Longer averaging may compensate for slower spectrum acquisition. However, the maximum averaging time is, in all practical situations, determined by variations in environmental factors that limit the stability time of the spectrometer (T_{opt}, as determined, e.g., by the minimum in an Allan-Werle plot [98]). Beyond this time, drift will start degrading the detection limit. Moreover, many systems are not limited by technical noise but rather by optical interference fringes ("etaloning") which may not be equally susceptible to averaging.

The effect of increasing $\mathcal{F}$ is quite different in the case of optical-feedback cavity-enhanced absorption spectroscopy (OFCEAS), as this technique enables optimal and rapid coupling of the laser radiation to the transmission modes of the high-finesse cavity [81]. In fact, in this Letter we demonstrate an OFCEAS spectrometer with $\mathcal{F} \approx 144,000$. It realizes a high level of light injection and cavity-throughput and a gain in sensitivity proportional to the finesse for a given measurement time. In addition, we were able to increase T_{opt} compared to a previous lower finesse setup.

In order to record absorption spectra with the OFCEAS technique, a laser is approximately mode-matched, then optically locked to successive longitudinal, TEM_{00} modes of a three-mirror V-shaped cavity. This geometry returns a portion of the light resonating inside the cavity as optical feedback to the laser source. At the same time, it avoids unfiltered feedback of the direct reflection from the input mirror, as described in, e.g., [81]. The aforementioned high light throughput is predominantly due to a narrowing of the laser linewidth to below the cavity transmission mode width ($\sim \text{FSR}/\mathcal{F}$) [81, 82, 178]. Thus, OFCEAS, in contrast to other CEAS or CRDS techniques, does not suffer from an inadequate light transmission at very high mirror reflectivity. In fact, no diminution of the light intensity after the cavity is observed, despite a seven-fold augmentation of $\mathcal{F}$.

The instrument presented in this Letter is compared to a previous instrument developed in our group. This older instrument, called isotope ratio infrared spectrometer (IRIS) participated in airborne campaigns to study the upper troposphere and lower stratosphere and is described in detail in [6, 83, 118]. IRIS was equipped with high-reflectivity mirrors resulting in a ring-down time of $\tau_0 = 21$ µs and a NEAS of 4×10^{-10} cm^{-1} Hz$^{-1/2}$. The new high-finesse isotope ratio instrument ("HiFI") is equipped with mirrors of reflectivity 99.9989% (1 - R = 11 ppm and roughly equal losses and transmission; Layertec GmbH), resulting in $\tau_0 = 150$ µs. The finesse of a V-shaped cavity with arms of length L_1 and L_2 is given by $\mathcal{F} = \pi\mathcal{R}/(1-\mathcal{R}^2) = \pi c\tau_0/(L_1+L_2)$ [82]. In this case, with $L_1 = L_2 = 489$ mm, $\mathcal{F} \approx 144,000$ (a standard linear cavity of the same external length using the same mirrors would have $\mathcal{F} = 288,000$, and twice as large FSR, for the same ring-down time).

As IRIS, HiFI measures the four water vapor isotopologues $H_2\,{}^{16}O$, $H_2\,{}^{18}O$, $H_2\,{}^{17}O$ and $HD\,{}^{16}O$ in the spectral range near 7184 cm^{-1}. A deliberate choice was made to work in the near-infrared region of the spectrum, where state-of-the-art mirror coatings allow for a more than ten times increase in finesse compared to the mid-infrared (MIR) regions around 2.7 and 6.7 µm. The associated longer L_{eff} is expected to outweigh the roughly one order of magnitude higher absorption band strength in the MIR, without even considering the lower performance of MIR detectors and other optical components.

Figure C.1 shows a typical HiFI spectrum. At water concentrations below 500 ppmv, the NEAS is typically 6×10^{-11} cm^{-1} Hz$^{-1/2}$, an improvement by a factor of almost 7 compared to IRIS which is equal to the ratio of the finesses. Clearly, the penalty of the slower scan rate is not as severe as might have been expected, mostly because the scan time is still used effectively (see

below) to better define the cavity mode transmission maxima needed to calculate the absorption spectrum. Thus, the product of the first and last factors in Eq. C.1 remains unchanged, and the improvement in NEAS appears to be determined by the increase in L_{eff}. Although in both instruments no fringes are visible on the spectrum baseline, we cannot completely exclude that part of the improvement is due to a reduction of the fringes underneath the noise structure. It is noted that our NEAS values are based on the RMS noise of the fit residuals of a single spectrum. Thus, they would also include possible effects of fit imperfections and fringes.

In the following, we briefly discuss the improvements that were necessary to accommodate the

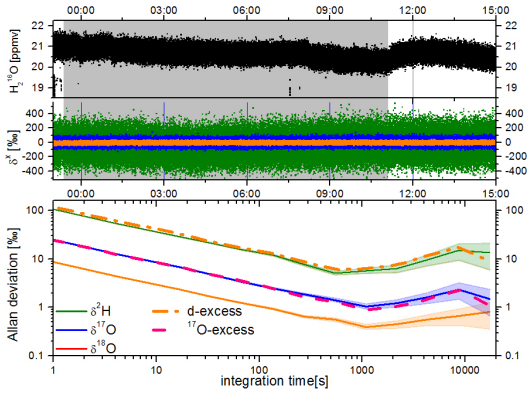

Figure C.1: Single spectrum recorded with HiFI at 500 ppmv H_2 ^{16}O and a 2 Hz measurement rate. The RMS of the residuals is 8×10^{-11} cm^{-1}.

new ultrahigh-finesse cavity and increase T_{opt}, and we present our first results illustrating instrument stability and performance. HiFI is mounted in a thermally insulated 19 in. rack housing. The V-shaped cavity has an internal volume ∼25 mL that is electro-polished and coated with a fluoroaliphatic polymer (Cytonix FluoroPel 800A). Air inside the instrument housing is ventilated and regulated to 38±0.1°C with a thermo-electric air-air heat exchanger (Supercool). The temperature of the optical breadboard is stabilized at 45°C using adhesive heater tapes (Minco), regulated with a proportional-integral-differential feedback-loop implemented in software. The sample pressure inside the cavity is regulated to 35 mbar by a custom Siltek-treated (Restek) pressure controller (Bronkhorst) at a flow rate of 150 standard mL/min for a calculated gas exchange time of 0.35 s. Over a period of 3.6 h, the drift of the cavity temperature is smaller than 0.5 mK and the drift of the pressure smaller than 10 µbar, as measured with sensors not used in the control loops. The signal and reference photodiode outputs are digitized by a 2 channel, 16 bit A/D converter with a record length of 60k points and 8 µs step size (125 kHz). Note that, compared to the previous spectrometer, about 4 times as many datapoints are acquired per spectral scan, while the detector bandwidth (48 kHz) is matched to the Nyquist limit associated with the data acquisition rate, enabling an improved definition of the cavity transmission signal. In view of the long cavity ring-down time, the scanning frequency is set to 2 spectra per second (∼10 for IRIS) and the laser tuning speed to one cavity FSR (153.2 MHz) in 3.5 ms (∼0.5 ms

for IRIS [6]). A single spectrum spans about 110 successive cavity modes, corresponding to a spectral window of 0.6 cm^{-1}. At the end of each scan, the laser is interrupted for 3.2 ms in order to record a ring-down event on the last cavity mode with a typical shot-to-shot RMS fractional variation of 1.7×10^{-4}. This measurement allows for an absolute calibration of the absorption scale [6, 81].

For the analysis, a spectrum composed of Rautian line profiles [93] is fit to each individual retrieved spectrum, and the isotope ratios are calculated using the integrated line intensities [6] before being averaged. Absorption lines of methane in the same spectral region are introduced in the fit since methane absorption becomes an important factor at water concentrations below ~500 ppmv. The baseline is fit by two strong water absorption lines outside the measurement range, which are grouped with the $H_2\,^{16}O$ lines inside the measurement range, and an additional third-order polynomial.

To determine the precision of the isotope ratio measurements, a gas bottle was repeatedly

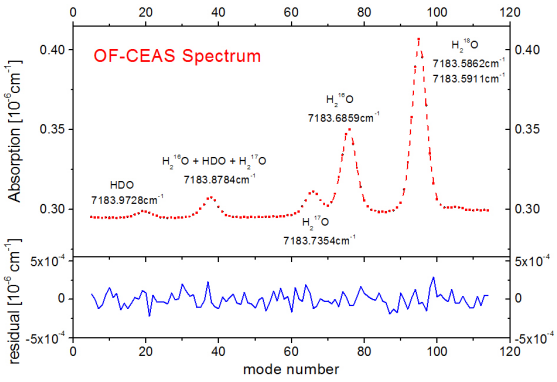

Figure C.2: Time series of $H_2\,^{16}O$ and its isotope ratios (two top panels) and the corresponding Allan plots (bottom panel) for the selected data for $H_2\,^{18}O$, $H_2\,^{17}O$, and HD ^{16}O, as well as the deuterium- and ^{17}O-excesses, as a function of averaging time T at a water mixing ratio of 20 ppmv.

prepared with a mixture of dry synthetic air and a local water standard for different water concentrations. This standard gas bottle was then connected to the OF-CEAS instrument for longterm stability measurements (>8 h). Previous studies comparing this method with a microdroplet injector indicate that isotopic fractionation using a standard 50 L tank is undetectable [118]. Figure C.2 shows an Allan-Werle plot of the $H_2\,^{18}O$, $H_2\,^{17}O$ and HD ^{16}O isotope ratios from measurements at the lowest sample concentration of 20 ppmv. The figure also includes the Allan deviations for the deuterium excess $d = \delta^2H - 8\,\delta^{18}O$ [14] and the ^{17}O-excess $= \ln(1 + \delta^{17}O) - 0.528\ln(1 + \delta^{18}O)$ [44] which, however, are practically indistinguishable from the δ^2H and δ^{17}O Allan deviation curves, respectively.

Dependent on the water concentration, the optimum integration time for the isotope ratio determination is up to ~70 min. For longer integration times, drift degrades the precision. The

stability of HiFI is thus much higher than that of IRIS, for which the longest optimum integration time was ∼5 min [118], mostly due to the better temperature stabilization (cf. chapter 3). The best precision for δ^2H and δ^{17}O is obtained at around 1500 ppmv. For δ^2H, 70 min averaging gives a precision $\sigma(^2H) = 0.12‰$, while averaging of 3 min results in $\sigma(^{17}O) = 0.07‰$ and $\sigma(^{18}O) = 0.05‰$. However, the optimum for δ^{18}O, with $\sigma(^{18}O) = 0.02‰$, is obtained at a lower water concentration of ∼600 ppmv (in about 30 min). In fact, cavity transmission at the peak of the $H_2\,^{18}O$ absorption line drops to 10% at 1500 ppmv, giving a signal-to-noise ratio far from optimal.

In table C.1, the precisions at different water concentrations are given for $T = 4$ s (8 data points) averaging and for the Allan optimum $\sigma(T_{\mathrm{opt}})$. With 4 s averaging, the time resolution is still sufficient to study fast isotopic processes, but the precision is nearly a factor of three better than for nonaveraged (0.5 s) measurements.

In conclusion, the new instrument achieves similar or better results in terms of measurement precision compared to our previous OFCEAS water isotope spectrometer, as well as compared to most commercial water vapor spectrometers but at a water concentration that is approximately an order of magnitude lower. The NEAS of 5.7×10^{-11} cm^{-1} Hz$^{-1/2}$ (or 5.4×10^{-12} cm^{-1} Hz$^{-1/2}$ when normalized per spectral element) is among the lowest values reported for near-infrared CEAS so far, with the exception of NICE-OHMS (with its much smaller tuning range) and the lowest for CEAS with a base length below 50 cm. Here, the instrument offers the possibility to record useful isotopic signals in dry Antarctic or upper tropospheric air and eventually even in stratospheric air. The improved stability time can be used to increase the precision on a single measurement before drift starts dominating the noise. It also enables longer uninterrupted recording before recalibration needs to be carried out [98].

The instrument is capable of even higher precision or higher sensitivity isotopic measurements,

$H_2\,^{16}O$ (ppmv)	$\sigma(^2H)$ (4 s) [‰]	$\sigma(^2H)$ (T_{opt}) [‰]	$\sigma(^{18}O)$ (4 s) [‰]	$\sigma(^{18}O)$ (T_{opt}) [‰]	$\sigma(^{17}O)$ (4 s) [‰]	$\sigma(^{17}O)$ (T_{opt}) [‰]
20	54	5	4.4	0.5	12	1.1
80	12	0.8	1.1	0.1	3.2	0.2
190	5.5	0.6	0.5	0.07	1.4	0.19
420	2.7	0.5	0.27	0.05	0.7	0.16
610	1.7	0.5	0.18	0.02	0.4	0.1
770	1.1	0.28	0.18	0.04	0.3	0.07
1470	0.7	0.12	0.17	0.05	0.22	0.07

Table C.1: Measurement Precision as a Function of the Water Mixing Ratio for Different Averaging Times.

when only one or two isotopic ratios need to be determined. In a previously identified range around 7200 cm^{-1} [179], the spectral lines are better separated and the isotopologues, excluding δ^{17}O, can be measured with modestly better precision. Alternatively, we recently demonstrated

that near 7286 cm^{-1}, $\delta^{18}O$ can be measured almost one order of magnitude better with a minimal Allan deviation of 0.4% in 30 min at only 4 ppmv $H_2\,^{16}O$ (cf. chapter 8). By temperature tuning of the same laser, it is also possible to measure δ^2H at 7289 or 7280 cm^{-1}, with a comparable performance to what is shown here at 7184 cm^{-1}. Finally, nearby $H_2\,^{16}O$ lines at 7299.43 and 7181.17 cm^{-1} may be used for water detection below 0.1 ppbv.

Especially in the case of a molecule in which a (anharmonic) hydrogen oscillator is excited, such as water, our approach may avoid the need to use more complex MIR light sources and optics, given that line strengths may differ by only one order of magnitude, easily compensated by the higher finesse available in the NIR.

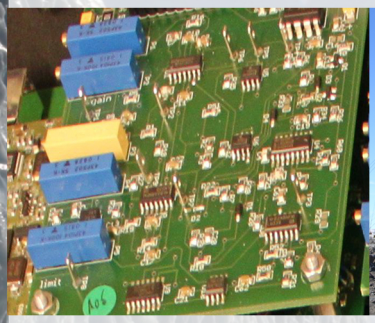


TROLL STATION

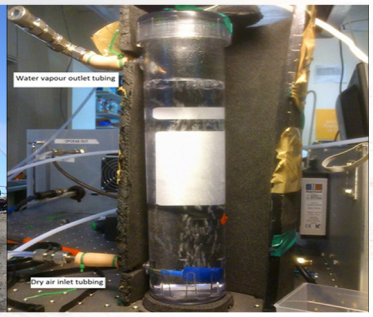
Water vapour outlet tubing
Dry air inlet tubbing